# Chemical Controls on the Dissolution Kinetics of Calcite in Seawater

Thesis by
Adam Vinay Subhas

In Partial Fulfillment of the Requirements for the
degree of
Doctor of Philosophy in Geochemistry

**Caltech**

CALIFORNIA INSTITUTE OF TECHNOLOGY
Pasadena, California

2017
Defended May 15, 2017

ORCID: 0000-0002-7688-6624

# ACKNOWLEDGEMENTS

To you guys: leaving LA will be leaving a piece of my creativity behind. I'll miss it dearly.

Thanks to the rest of the Pit – first year would have not been nearly as tolerable if it weren't for you guys. Ted, Vicky, Luca, Jason, Renata, Jen, Kirsten, Frank...the pit couldn't contain us. No one will ever host a Tuesday morning coffee hour like we did. Thanks also to my friends in other lab groups. Stephen and I suffered through Stat Mech together and ended up running a fun course on U-series decay chains. Hayden and Max are always up for an adventure. My current office mates Xiaozhou, Georgy, Emily, Zach, and Giuliana seem to manage the perfect balance between actually getting work done and keeping the office lively and fun.

Thanks also the rest of the Adkins lab, including Nithya, Anna, Madeline, Nele, Stacy, Seth, Morgan, and John. Nele first brought me to The Edison. Nithya, Madeline, and I had an Adventure Hike I will never forget. Anna will forever be the most "tantankerous" group member. Morgan and I bonded over music and science...I'm glad we got to play a couple of shows together! I am so excited that John is carrying on the carbonate dissolution torch. I could not have asked for better friends and lab-mates.

Thanks to my Haverford friends – Sean and Shea host a great game night. No matter how many kids we all end up with, I assume I will be gaming with the A8K crew for a long time to come. And thanks to the members of all itertations of Show Your Junk - West Coast Crew, with a big shout-out to Maddie as my co-conspirator. Frisbee on the beach in January simply cannot be beat!

And to the two main ladies in my life, Sophie and Kali – you're the best!! Sophie is my best friend, an inspiration, and a truly badass role model. Kali is the best dog ever. That pretty much sums it up.

Also thanks to my aunt Malathi and Uncle Shankar. It has been great getting to spend time with them this past eight years. I know I can come to the house, enjoy their company, a tasty home-cooked meal, and if the season is right, come home with some tasty fruits. I will miss those guava trees!

Of course, I would not be here at all if it weren't for my parents. They have loved and supported me so unconditionally, even from the other side of the country, during my time as a technician and graduate student at Caltech. I knew from an early age that I wanted to do science, and despite neither of them having careers in science they encouraged me to pursue that dream. For that gift of confidence and freedom I

v

am truly blessed.

My sister, although also not a scientist (although there is some streak of the scientific method in her approach to baking), has also been there to talk to about whatever has been an issue for me – and for her – over the last 8 years. We have only become closer over the years, despite our different careers and places of living. Perhaps some day we will live in the same city!

# ABSTRACT

Calcium carbonate minerals are abundant on the earth's surface. Delivery of alkalinity to the oceans is balanced by the production and burial of calcium carbonate in marine sediments, which results in a large reservoir of sedimentary $CaCO_3$ both in the ocean and in terrestrial rocks. Alkalinity also provides oceanic buffering capacity, which today results in about 60 times more dissolved $CO_2$ in the world oceans than is present as $CO_2$ gas in the atmosphere. Because calcium carbonate formation removes alkalinity from the oceans, $CaCO_3$ precipitation leads to the outgassing of $CO_2$ from the ocean into the atmosphere. Likewise, the dissolution of $CaCO_3$ adds alkalinity to the oceans, leading to an increased buffering capacity and a drawdown of atmospheric $pCO_2$.

Calcium carbonate precipitation in the form of calcite and aragonite is almost exclusively mediated by biological organisms such as corals, coccoliths, and foraminifera, which use these minerals as components in their shells. $CaCO_3$ is overproduced by organisms in the ocean relative to the flux of alkalinity delivered to the oceans by rivers. Thus, a significant portion of $CaCO_3$ must be dissolved back into seawater for the ocean alkalinity cycle to come into steady state. Because of the link between alkalinity and $CO_2$, the ocean alkalinity cycle has a direct effect on atmospheric $pCO_2$ especially on timescales less than 100,000 years.

How fast $CaCO_3$ dissolves back into seawater is thus a crucial rate in determining the response of the oceanic system to perturbations in either alkalinity or $CO_2$ input to the ocean-atmosphere system. We are testing the kinetics of this system with the large amount of $CO_2$ emitted from fossil fuel burning, about a third of which has dissolved into the surface ocean. This process is known as ocean acidification, as $CO_2$ is an acid, soaking up buffering capacity and dropping ocean pH. This $CO_2$ will eventually be neutralized through the dissolution of carbonate rich deep-sea sediments, but the process will take a long time. This thesis makes new measurements of calcite dissolution in seawater, in an attempt to build an understanding of the chemical processes responsible for dissolution kinetics.

I first introduce the new method, in which $Ca^{13}CO_3$ is dissolved in undersaturated seawater. Mass loss is directly traced by measuring the appearance of $^{13}C$ in seawater over time. The dissolution rate of calcite is a highly nonlinear function of calcite saturation state, typically defined as $\Omega = \frac{[Ca^{2+}][CO_3^{2-}]}{K'_{sp}}$, where the numerator is the

product of dissolved calcium and carbonate ions and the denominator is the apparent solubility for calcite in seawater.

Next, I show that this tracer can tell us about the balance of precipitation and dissolution at the mineral surface. I use this balance to constrain mass fluxes due to precipitation and dissolution as a function of saturation state. I also show that the enzyme Carbonic Anhydrase (CA), which rapidly equilibrates $CO_2$ and $H_2CO_3$, greatly enhances the rate of calcite dissolution especially near equilibrium. A model of dissolution is presented in which CA is most effective in the region where dissolution proceeds via etch pit nucleation at surface defects.

The dissolution behavior of biogenic carbonates is also investigated using the $^{13}C$ method. I cultured coccoliths, foraminifera, and soft corals in $^{13}C$-labeled seawater so that their skeletons incorporated the $^{13}C$ tracer. These skeletons were then used in dissolution experiments. I show that both magnesium and organic matter contained within the calcite lattice have large effects on the dissolution behavior of biogenic carbonates. Magnesium content generally increases dissolution rate, and it is hypothesized that highly soluble magnesium-rich phases are preferentially removed from dissolving carbonates. Organic content generally decreases dissolution rate. It is hypothesized that organic matrices within the calcite lattice promote re-precipitation reactions, due to the balance of dissolution and precipitation rates in our data, and their promotion of precipitation during biomineralization.

I then analyze, in 2- and 3-dimensions, dissolved foraminiferal tests to locate where and how mass is being lost. It is shown that dissolution proceeds along specific layers, that are consistent with the size and location of Mg-rich carbonate spherules that are initially deposited during chamber formation. Surface topography generation of foraminiferal tests shows that sub-micron features are formed rapidly and then quickly eroded into larger pits and channels. These larger channels then propagate and cover the test surface at higher amounts of mass loss.

Finally, the involvement of CA in carbonate dissolution necessitates the measurement of CA activity in the environment, especially in carbonate-rich ecosystems such as reefs, carbonate-rich sediments, and carbonate-rich marine particles. To this end, I survey a number of available techniques for measuring CA activity. In the end, it is shown that the most effective method is based on measuring the depletion of $^{18}O$ from $^{13}C$- and $^{18}O$- labeled DIC, as measured by membrane inlet mass spectrometry (MIMS). This method is promising and shows about 0.1 nM CA present in unfiltered surface seawater collected from San Pedro Basin.

# PUBLISHED CONTENT AND CONTRIBUTIONS

Subhas, A.V., J.F. Adkins, J. Erez, N.E. Rollins, et al. (Under Review). "Catalysis and Chemical Mechanisms of Calcite Dissolution in Seawater". In: *Under Review at the Proceedings of the National Academy of Sciences*.
A.V.S. conducted the research, wrote model code, analyzed all of the data, and wrote the manuscript for this publication.

Subhas, A.V., J.F. Adkins, J. Erez, P. Ziveri, et al. (in prep.). "Controls on the Dissolution Kinetics of Biogenic Calcites in Seawater". In: *in preparation*.
A.V.S. conducted the research, analyzed data, and wrote the manuscript for this publication.

Haynes, L.L et al. (Accepted). "Calibration of the B/Ca Proxy in the Planktic Foraminifer *O. universa* to Paleocene Seawater Conditions". In: *Accepted in Paleoceanography*.
A.V.S. conducted BET surface area measurements for this study, and contributed to the writing of the manuscript.

Subhas, Adam V et al. (2015). "A novel determination of calcite dissolution kinetics in seawater". In: *Geochimica et Cosmochimica Acta* 170.C, pp. 51–68.

# TABLE OF CONTENTS

LIST OF ILLUSTRATIONS

# LIST OF TABLES

# NOMENCLATURE

**Alkalinity.** Alkalinity is defined as either the net negative charge in seawater after accounting for all major constituents, or by a more chemical definition, the total charge equivalents of acid/base-reactive species at the $CO_2$ equivalence point. In Morel's "Tableau" method, alkalinity is equivalent to $-TOT_{H^+}$. Seawater contains several chemical species which can contribute to alkalinity. The most abundant is the carbonate system, where $HCO_3^-$ and $CO_3^{2-}$ contribute 1 and 2 units of alkalinity, respectively. Borate ion also contributes significant alkalinity as the total borate concentration in seawater is on the order of 100 $\mu$m. Both sulfate and chloride ions, while abundant in seawater, do not contribute to alaklinity because they are conjugate bases of very strong acids with $pK_a$ values significantly below the $CO_2$ equivalence point (pH ~4.5).

**Calcite Compensation Depth (CCD).** The CCD is the globally integrated depth of the ocean where the rate of burial is exactly matched by the rate of dissolution such that there is zero accumulation of $CaCO_3$ in the sediment. This depth reflects the balance of ocean hypsometry and $CaCO_3$ production and burial. As such, it represents the steady-state balance of alkalinity being returned to the ocean and alkalinity being buried in sediments. The CCD is often operationally defined for specific sediment locations or ocean basins, and often takes on a more practical definition as the depth at which $\%CaCO_3$ goes to zero.

**Calcite Lysocline.** The lysocline is the depth interval in the ocean over which sedimentary $\%CaCO_3$ drops rapidly, typically from 80% to less than 5%. It is often very thick, spanning 1,000 meters of water depth in some locations. The position of the lysocline can also become decoupled from the saturation horizon through the ratio of organic carbon to carbonate particles raining onto sediments. The lysocline can start at the saturation horizon or above it, if there is significant respiration of organic carbon.

**Coccolithophores.** Coccolithophores are marine eukaryotic algae that make their shells out of calcite. Unlike many other marine calcifiers, coccoliths make their hard parts internally and then extrude them to the cell's surface once complete.

**DIC.** Dissolved Inorganic Carbon is defined as the sum of all inorganic carbon species in seawater: $DIC=[CO_{2(aq)}] + [H_2CO_3] + [HCO_3^-] + [CO_3^{2-}]$. The terms $CO_{2(aq)}$ and $H_2CO_3$ are often grouped together as $H_2CO_3*$. The concentration of $H_2CO_3$ is about 700 times lower than the concentration of $CO_{2(aq)}$, due to the slow rate of $CO_2$ hydration to form $H_2CO_3$, relative to the rapid rate of dehydration. Ths hydration of $CO_2$ is considered the rate-limiting step for equilibrating DIC species in seawater.

**Foraminifera.** Foraminifera are marine amoeboids that precipitate calcium carbonate skeletons. They are animals and must thus consume food for energy. However, many species of planktonic and benthic foraminifera host symbiotic algae, which move within the cytoplasm and can be found draped along the foraminiferal spines when an individual is illuminated and healthy..

**Saturation Horizon.** The depth in the ocean at which $\Omega=1$. The saturation horizon is different for calcite and aragonite, as aragonite is more soluble. Its saturation horizon is shallower than calcite's. Above the saturation horizon, $\Omega > 1$ and therefore precipitation is predicted. Below the saturation horizon, $\Omega < 1$ and dissolution is predicted.

**Test.** The test refers to the shell of a marine microorganism. It is most often used when referring to foraminifera.

*Chapter 1*

# INTRODUCTION: THE ROLE OF CACO₃ DISSOLUTION AND ITS KINETICS IN THE GLOBAL ALKALINITY CYCLE

Calcium carbonate minerals are abundant on the earth's surface, and have been used extensively to interpret the geological history of the oceans and the earth's surface (John W Morse and Mackenzie, 1990; John W Morse, Rolf S Arvidson, and Lüttge, 2007). The formation of carbonate rocks on long timescales is canonically driven by the interaction of aqueous $CO_2$ and the cationic products of silicate rock weathering (R E Zeebe and Westbroek, 2003; A Ridgwell and R E Zeebe, 2005). Rivers deliver dissolved weathering products to the oceans in the form of alkalinity, which at steady state is removed via the production and burial of calcite and aragonite minerals:

$$Ca^{2+} + 2HCO_3^- \rightleftharpoons CaCO_3 + H_2CO_3. \tag{1.1}$$

Whole ocean alkalinity inputs and outputs are hard to constrain, and over the Pleistocene based on budgets and sea level changes it is unclear how long the system needs to reach steady state (Milliman, 1993; Milliman and Droxler, 1995). When considering just the deep ocean, the inputs and outputs are slightly better understood, with about 0.1 GT of inorganic carbon coming in as alkalinity (Milliman, Troy, et al., 1999), and a similar amount coming out as $CaCO_3$ in deep-sea sediments (Milliman, Troy, et al., 1999; Berelson et al., 2007).

Today, almost all calcium carbonate precipitation is mediated by organisms living in the ocean (Andy Ridgwell, 2005). About 30% of $CaCO_3$ is produced on coral reef complexes, and the rests occurs in the open ocean by pelagic organisms such as foraminifera and coccolithophores (J Erez, 2003; Milliman, 1993). While the relative proportion of shelf to open-ocean calcification might have been different in the past, the current situation decouples carbonate production (at the ocean's surface) and carbonate burial (in deep ocean sediments) both spatially and temporally. Models of ocean circulation that include carbonate export and burial suggest that the open ocean $CaCO_3$ system has an e-folding time of about 5700 years (D. Archer, 1991; Ilyina and R E Zeebe, 2012).

This multi-thousand year decoupling leads to an active ocean alkalinity cycle, by

which alkalinity is consumed in the surface ocean by $CaCO_3$ precipitation (left to right in Eq.(1.1)) and produced in the deep ocean by $CaCO_3$ dissolution (right to left in Eq.(1.1)). Open ocean calcification is hard to measure globally, and estimates range between 0.2 and 0.6 GT of inorganic carbon (Milliman, 1993; Milliman and Droxler, 1995; Berelson et al., 2007). If only 0.1 GT of $CaCO_3$ must be buried to reach steady state, somewhere between 50 and 83% of the $CaCO_3$ produced in the surface ocean must be dissolved either in the water column or in ocean sediments.

The location of $CaCO_3$ dissolution – and thus alkalinity return to the ocean system – is also underconstrained. There is significant uncertainty about how much dissolution happens in the water column versus sediments, and water column dissolution, especially in the upper ocean, seems crucial to bring the alkalinity and particle budgets into agreement. The flux of particles between the surface ocean and 1000 and 2000 m traps, for instance, indicates that up to 60% of produced carbonate dissolves in the top 1000-2000 m of the ocean (Milliman, Troy, et al., 1999; Berelson et al., 2007). The alkalinity excess due to carbonate dissolution, known as TA*, also suggests that a significant amount of dissolution happens at intermediate depth (R A Feely, 2004). However, Friis et al. (2006) incorporated water column and sedimentary $CaCO_3$ dissolution in a GCM to show that this excess TA* anomaly could be transported from dissolving sediments along isopycnals relatively rapidly.

Much of the uncertainty about controls on the dissolution rate of $CaCO_3$ exists because the fundamentals of how fast $CaCO_3$ responds to a thermodynamic driving force are poorly understood. There are a few pieces that we know well. For instance, the saturation state of calcite, $\Omega_{calc}$ is related to the ion activity product of calcium and carbonate ions divided by the apparent solubility constant of calcite in seawater:

$$\Omega_{calc} = \frac{[Ca^{2+}][CaCO_3]}{K'_{sp}}. \tag{1.2}$$

The solubility product for calcite in seawater is a function of temperature, pressure, and salinity. The best determinations of $K'_{sp}$ were made from both sides of equilibrium in months-long experiments conducted by J W Morse, Mucci, and Millero, 1980. We also know the relationships between $K'_{sp}$ and T,P, and S to about 10 % (Millero, 1995).

One reason why shallow ocean carbonate dissolution presents such a conundrum is that calcite solubility increases with pressure. The deep ocean is more undersaturated with respect to carbonate minerals due to the pressure effect on the $K'_{sp}$, such that the saturation horizon occurs at roughly 4,000 meters in the Pacific and 5,000

meters in the Altantic (R Oxburgh and W S Broecker, 1993). Above this depth, calcite is thermodynamically stable. Below this depth, calcite is thermodynamically unstable and is predicted to dissolve. Deep ocean waters are also rich in respired $CO_2$, which shifts the equilibrium distribution of dissolved inorganic carbon species to greater $CO_{2aq}$ and lower $CO_3^{2-}$ concentration, further decreasing saturation state.

It is thus doubly strange that so much dissolution should happen in the upper ocean: there is neither the pressure effect to drive calcite solubility, nor is there enough respired $CO_2$ to decrease carbonate ion concentration significantly. Hypotheses for driving shallow dissolution have therefore primarily focused on the extreme proximity of organic matter respiration to carbonate grains. Sinking particle aggregates, the guts of zooplankton, or organic-rich sediments all might have enough locally respired $CO_2$ to decrease $\Omega$ and promote dissolution, even when surrounded by supersaturated ocean water (Steven Emerson and M. Bender, 1981; Milliman, Troy, et al., 1999; Burke Hales, 2003; Dunne, Burke Hales, and Toggweiler, 2012).

We still do not fully understand the relationship between $\Omega$ and the rate of carbonate dissolution. Early determinations of the dissolution rate in seawater by Keir (1980) and R A Berner and J W Morse (1974) documented a highly nonlinear response to saturation state by fitting their data through the log-transform of the equation

$$R = k(1 - \Omega)^n, \tag{1.3}$$

where R is the rate of dissolution normalized by surface area, $k$ is the specific dissolution rate constant, $\Omega = \frac{[Ca^{2+}][CaCO_3]}{K'_{sp}}$ is the saturation state of seawater, and $n$ is the reaction "order". Keir (1980) obtained an $n$ of 4.5 and a $k$ of 1300% day$^{-1}$, implying that the dissolution rate was very fast and highly sensitive to saturation state. This result underscores our lack of physical understanding of the relationship between dissolution kinetics and its thermodynamic driving force. In addition, *in situ* dissolution studies appear to be slow relative to laboratory rates by orders of magnitude (Honjo and J Erez, 1978). For example, the models of Friis et al. (2006) and Jokulsdottir and D. Archer (2016) use a highly nonlinear response to saturation state (Rate $\propto (1 - \Omega)^{4.5}$) based on the original determination of Keir (1980), but use very different $k_\%$ values of 7 and 500, respectively.

This is an issue that has frustrated oceanographers for decades. Initially, many studies assumed linear ($n = 1$) kinetics so sedimentary diagenesis models could be solved analytically (Steven Emerson and M. Bender, 1981). This assumption has since led to the forcing of data through a linear fit in order to make dissolution work
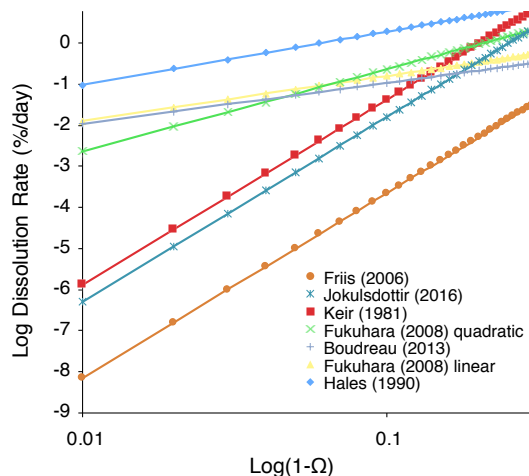
**Figure 1.1:** A comparison of mulitple determinations of a "rate law" for $CaCO_3$ dissolution in natural seawater (Friis et al., 2006; Keir, 1980; Fukuhara et al., 2008; B Hales and S Emerson, 1997b; Jokulsdottir and D. Archer, 2016; Boudreau, 2013). These dissolution rates, normalized by mass, span almost 10 orders of magnitude and exhibit several different slopes in log-log space, from $(1-\Omega)^{4.5}$ (Friis et al., 2006; Keir, 1980; Jokulsdottir and D. Archer, 2016) to linear (B Hales and S Emerson, 1997b; Boudreau, 2013).

well in simple models of deep sea sediments. For example, B Hales and S Emerson (1997b) reinterpreted the data of Keir (1980) to argue for near-linear ($n = 1.3$) kinetics. Later, Boudreau (2013) reinterpreted the data of Keir (1983) to argue for completely linear kinetics, although in many cases the data refit did not pass through the origin. Figure 1.1 plots a number of $CaCO_3$ dissolution studies' fits to Eq.(1.3). It is clear from this plot that one could basically pick any dissolution rate at any saturation state, and find a study that agreed with your choice.

In addition to the lack of agreement between studies, a simple % dissolved framework is inappropriate for the wide diversity of biogenic carbonates that are produced. For instance, coccoliths and foraminifera have very different specific surface areas (Honjo and J Erez, 1978). For the same mass, they therefore have a different area of calcite exposed to seawater. The most widely used surface area measurement is by gas adsorption (Brunauer, Emmett, and Teller, 1938; Kanel and J W Morse, 1979), and yet dissolution rates normalized by this technique still do not agree with each other within a single study (Honjo and J Erez, 1978; Keir, 1980; Walter and J W Morse, 1985). Uncertainty in the applicability of gas adsorption-based surface areas have led some authors to conclude that shell size alone is a better measure of reactivity (Cubillas et al., 2005), while others have argued that adsorption by gases does not reflect adsorption by the specific species responsible for dissolution

reactions at the mineral surface (John W Morse, Rolf S Arvidson, and Lüttge, 2007).

Two other important components of biogenic carbonates should be mentioned. First, biogenic carbonates possess a wide range of magnesium contents, from basically zero magnesium (coccoliths at Mg/Ca = 0.0001 and foraminifera at 0.005) to high-magnesium calcite coralline algae and soft corals (Mg/Ca = 0.1-0.15). Magnesium content above about 0.04 has a strong impact on the solubility of calcite (John W Morse and Mackenzie, 1990), such that at about 15 mole % Mg, calcite is 50% more soluble than Mg-free calcite.. In foraminifera, $Mg^{2+}$ is also hetergeneously distributed in the test, which means that certain layers of foraminiferal calcite may be more susceptible to dissolution than others (A. Y. Sadekov, Stephen M Eggins, and Patrick De Deckker, 2005; Johnstone, Jimin Yu, et al., 2011).

Secondly, organic matrices play an active role in the templating and nucleation of calcite in many organisms (Drake et al., 2013; Gal et al., 2016; S Bentov and J Erez, 2005; Mass et al., 2014; Hamm et al., 2014). A template's role in precipitation implies that it should retard dissolution by promoting the back precipitation reaction. The organic coatings surrounding coccolithophores have also been hypothesized to retard dissolution, through an as-yet unexplained mechanism (Honjo and J Erez, 1978; Keir, 1980).

Flying in the face of this confusing seawater data is the relatively well-described set of reactions controlling the dissolution kinetics of calcite in freshwater. L N Plummer and Wigley (1976) and L N Plummer, Wigley, and Parkhurst (1978) used a pH-stat technique to measure freshwater calcite dissolution rates, and developed a framework based on three key chemical reactions:

$$CaCO_3 + H_2O \rightleftharpoons Ca^{2+} + CO_3^{2-} + H_2O. \qquad (1.4a)$$

$$CaCO_3 + H_2CO_3 \rightleftharpoons Ca^{2+} + 2HCO_3^-; \qquad (1.4b)$$

$$CaCO_3 + H^+ \rightleftharpoons Ca^{2+} + HCO_3^-; \qquad (1.4c)$$
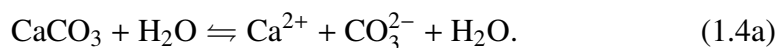
In general, Eq.(1.4c) is effective at high $H^+$ concentration (low pH $\leq$ 5.5). Eq.(1.4a) is effective near equilibrium and involves the hydrolysis of $CaCO_3$ into $Ca^{2+}$ and $CO_3^{2-}$. Eq.(1.4b) was shown to only be effective at very high $pCO_2$, where there was a substantial concentration of $H_2CO_3$. Later, Arakaki and Mucci (1995) combined this dissolution model with the surface speciation model of Van Cappellen, Charlet, and Stumm (1993) and developed a kinetic framework for freshwater dissolution

that was sensitive to both aqueous and surface speciation:

$$\text{Rate} = k_1 > CO_3^- (a_{H^+})^2 + (k_2 - k_5) > Ca^+ a_{H_2CO_3^*}$$
$$+ k_4 - (k_6 - k_3) > CO_3H^0 a_{CaHCO_3^+} \tag{1.5}$$
$$- k_7 > Ca^+ a_{H_2CO_3^*} a_{CaCO_3^0} - k_8 a_{CaCO_3^0}.$$

Here, $k$ are rate constants associated with chemical transformations based on surface speciation and the reactions of Eq.(1.4). The ">" denote densities of surface complexes; charges are reduced by half to indicate that half of these surface species' charges are distributed in the calcite lattice. Again, this reaction scheme includes terms for $H^+$ (first term), carbonic acid (second and fifth terms), and water/calcite alone (third and sixth terms). The fourth term describes reactions between calcite and calcium-complexed $HCO_3^-$. Arakaki and Mucci (1995) successfully showed that such a model was able to reproduce the dissolution behavior of calcite, and the transition from dissolution to precipitation. Their formulation also reduces to a linear relationship between dissolution rate and saturation state near equilibrium. This linear decrease in dissolution rate is exclusively due to a linearly increasing precipitation flux, which, given a constant dissolution flux, decreases the net rate approaching equilibrium. Similar descriptions of dissolution kinetics are abundant in the literature, and the general trends of dissolution as a function of these various species is borne out in many studies (Shiraki, Rock, and Casey, 2000; Chou, Garrels, and Wollast, 1989; Cubillas et al., 2005; Sjöberg and Rickard, 1984).

The fact that calcite dissolution in seawater is so hard to characterize is surprising. Many freshwater studies take for granted that seawater should be as simple as dilute solution dissolution (e.g. Sjöberg, 1976). Even Arakaki says at the end of their paper: "Furthermore, in a forthcoming paper, the validity of our model will be demonstrated for the same reactions in strong electrolyte solutions, including seawater" (Arakaki and Mucci, 1995). Such a paper never materialized.

In this way, calcite dissolution in seawater bears greater resemblance to the behavior of silicate mineral dissolution, which is often highly nonlinear (P M Dove, Han, and J J De Yoreo, 2005; Patricia M Dove et al., 2008; Dixit and Carroll, 2007). Studies on silicate mineral dissolution have successfully described their data using models which incorporate not only saturation state, but also geometric constraints on the location of dissolution features at the mineral surface. For instance, P M Dove, Han, and J J De Yoreo (2005) applied the crystal growth model of W. K. Burton, Cabrera, and Frank (1951) and found that quartz dissolution occupies three distinct regimes

**Table 1.1:** A comparison of different experimental techniques and their precision for measuring the dissolution rate of CaCO$_3$ in solution. All quoted precisions from the cited studies are converted to effective alkalinity increases for a more direct comparison. The $\delta^{13}$C method has a better precision by one order of magnitude compared to previous techniques.

| Method | Precision | Alkalinity Eq. ($\mu$eq kg$^{-1}$) | Study |
|---|---|---|---|
| pH | 0.001 | 0.5 | L N Plummer, Wigley, and Parkhurst (1978) |
| Alkalinity | 0.5 $\mu$eq kg$^{-1}$ | 0.5 | Pickett and A J Andersson (2014) |
| Ca$^{2+}$ | 21 $\mu$mol kg$^{-1}$ | 42 | Shiraki, Rock, and Casey (2000) |
| $\delta^{13}$C | 1 ‰ | 0.05 | This thesis |

of surface modification through dissolution. In some solution compositions, quartz dissolved by the retreat of crystal steps. In others, quartz dissolved by the formation of 2D-pits at crystal defects, followed by the nucleation of such pits everywhere on the crystal surface.

Surface feature models have also been applied to calcites in an attempt to apply dissolution rate data to the complexity of surface geometries expressed in natural carbonates (Lasaga and Luttge, 2001; H Henry Teng, 2004). However many have hypothesized that such surface diversity is an almost insurmountable challenge to predicting how fast calcites will dissolve in the natural environment (John W Morse, Rolf S Arvidson, and Lüttge, 2007; Luttge, R S Arvidson, and C Fischer, 2013). As a final note, crystal growth models, while descriptive, have yet to be predictive for either silicate or carbonate mineral dissolution.

This thesis makes new measurements of calcite dissolution kinetics in seawater. We use a new technique which is much more sensitive than previous techniques. We do not measure a bulk chemistry change such as an increase in Ca$^{2+}$ or alkalinity. Instead, mass loss from $^{13}$C-labeled calcite is traced by measuring the increase in seawater $\delta^{13}$C over time. This technique is an order of magnitude, or greater, more sensitive than other methods currently being used for calcite dissolution studies (Table 1.1). Here we quote an analytical precision of 1 ‰ for $\delta^{13}$C measurements, which, if using a 100%-labeled mineral in our experimental system, corresponds to an alkalinity increase of only 0.05 $\mu$eq kg$^{-1}$. Alkalinity measurements on their own have a precision of at best 0.5 $\mu$eq kg$^{-1}$.

In Chapter 2, I present the new method to measure the dissolution rate of carbonates in seawater. Pure $^{13}$C calcite is dissolved in undersaturated seawater, and the transfer of mass between solid and solution is traced by measuring the increase of seawater $\delta^{13}$C over time. The development of this method included:

- The building and calibration of a high-precision alkalinity titration system for small (16 gram) seawater samples;

- The modification of a Picarro cavity ringdown spectrometer to measure sea-water DIC concentration to about 0.2 % and DIC $\delta^{13}C$ to better than 0.1‰;

- The measurement of specific surface area on small samples with BET gas adsorption and Krypton gas;

- The development of the dissolution experimental procedure;

- The characterization of commercially purchased $Ca^{13}CO_3$ and the synthesis of large-grain $^{13}C$-calcite in the laboratory using a gel-diffusion technique first published by Nickl and Henisch (1969).

Calcite dissolution rates measured in this way scale inversely with grain size, and give a highly nonlinear dependence of dissolution rate on saturation state:

$$\text{Rate(g/cm}^2\text{/day)} = 7.2 \pm 0.6 \cdot 10^{-4}(1 - \Omega)^{3.9\pm0.1}.$$

The far-from-equilibrium dissolution rate constant (i.e. the dissolution rate when $\Omega = 0$) is consistent with the dissolution rates measured in dilute solution, giving us confidence in our method. This highly nonlinear dissolution rate speaks to the lack of a direct physical link between saturation state and dissolution rate. The dissolution rate is very slow near equilibrium. In fact, it is slower than the rate of diffusion of carbonate ion out of sediments, which brings back the idea that the distribution of calcite in seafloor sediments is to some extent kinetically controlled.

In Chapter 3, I investigate in more detail our tracer technique, and show that in addition to information about the net rate of dissolution, the $^{13}C$ tracer gives us information about the balance of gross dissolution and precipitation fluxes at the mineral surface. The trace of $\delta^{13}C$ versus time is sensitive to the relative rates of dissolution and precipitation, and the volume of calcite that is in contact with seawater. We probe this solid volume by making vertical secondary ion mass spectrometry (SIMS) profiles of $^{13}C/^{12}C$ and Mg/Ca ratios through the calcite's reactive surface layer. We then use a box model of gross dissolution and precipitation to show that there is a change in the balance of dissolution to precipitation at about $\Omega = 0.7$, suggesting a mechanism shift. Finally, we show that the enzyme Carbonic Anhydrase (CA) can catalyze the dissolution of calcium carbonate, which

implicates $H_2CO_3$ directly in the dissolution mechanism. This species is not explicit in the standard $1 - \Omega$ framework adopted by oceanographers, and forces us to reconsider how we parameterize dissolution in seawater. Finally, we show that a model adopted from crystal growth theory also describes a large mechanism change at $\Omega = 0.7$. Previous authors have suggested this change is a switch from defect-assisted nucleation of etch pits near equilibrium to homogeneous nucleation of etch pits everywhere on the crystal surface farther from equilibrium. The enzyme CA has a large effect in the defect-assisted region of dissolution, and seems to have a smaller effect farther away from equilibrium.

In Chapter 4, I use the $^{13}$C-dissolution technique to measure the dissolution kinetics of several biogenic calcites. I cultured several marine calcifiers in $^{13}$C-labeled seawater such that their skeletons took on the $^{13}$C label via calcification in culture. Planktonic and benthic foraminifera, a soft coral producing high-magnesium calcite spicules, and coccoliths were dissolved under a range of saturation states. Per gram, planktonic foraminifera have the highest dissolution rate, followed closely by coccoliths. The similarity of these dissolution rates suggests that per gram of sediment, coccolith and foraminiferal oozes deliver a similar amount of alkalinity back to the ocean. Normalized by surface area, benthic foraminifera dissolution rates are the fastest. Near-equilibrium specific dissolution rates are shown to scale with mangesium content, and far-from equilibrium dissolution rates are shown to scale negatively with increasing organic matter content. Magnesium is hypothesized to dissolve out preferentially from biogenic calcites, since high-Mg calcites are much more soluble than low-Mg calcites. Organic carbon is hypothesized to supress dissolution through active reprecipitation reactions. The organic molecules responsible for this reaction were not removed by surficial bleaching, and are thus hypothesized to be internally bound in the calcite lattice, possibly as templating or matrix molecules left over from the biomineralization process. Finally, we apply the dissolution model of Chapter 3 and P M Dove, Han, and J J De Yoreo (2005) to show that three regimes are evident in inorganic, benthic foraminiferal, and coccolith calcite dissolution rates. These regimes do not directly correspond to magnesium or organic carbon content, although the geometric model does not explicitly include these terms in its derivation.

In Chapter 5, I investigate the benthic foraminifera *Amphistegina* under different stages of dissolution using SEM imaging and micro-CT scans. The smooth top of the *Amphistegina* test is an ideal place to track surface features generated by

dissolution. A power spectrum of the surface roughness shows generation and subsequent disappearance of sub-micron features, and also the generation of larger micron-sized features such as pits and channels. Power spectra of SEM images taken of foraminifera suspended in the deep ocean show a similar pattern. High-resolution CT scans also allow for the 3D reconstruction of intact and dissolved *Amphistegina* tests. These scans show that dissolution preferentially affects specific layers which run parallel to the test surface. These dissolution features then destabilize the intact layers above them, which then detach or slough off. The dissolution layers observed appear to correspond to the size and location of high-Mg spherules that are initially precipitated during *Amphistegina* biomineralization (e.g. S Bentov and J Erez (2005)).

In Chapter 6, I investigate the natural occurrence of the enzyme Carbonic Anhydrase (CA) using several analytical techniques. The classic pH-drop, esterase activity, and $^{18}$O-MIMS techniques are utilized, as well as a new $^{13}$C-based technique using a Picarro cavity ringdown spectrometer. I demonstrate that $^{18}$O-MIMS is the best candidate for measuring CA activity in natural samples, and show CA activity in oyster larvae, *Picocystis* isolated from Mono Lake, and also in unfiltered natural seawater from the San Pedro Basin.

*Chapter 2*

# A NOVEL DETERMINATION OF CALCITE DISSOLUTION KINETICS IN SEAWATER

## 2.1  Introduction

Calcium carbonate minerals are a major component of the global carbon cycle. At steady state, alkalinity input to the oceans from terrestrial weathering and rivers is ultimately balanced by calcium carbonate burial in marine sediments. In the modern ocean, marine calcifiers produce four times more calcium carbonate than is needed to balance the terrestrial alkalinity source (Sarmiento and Gruber, 2006; Sigman and Boyle, 2000). This imbalance results in a large dissolution flux back into the ocean, both in the water column and in sediments. Dissolution acts as a filter between calcium carbonate production and its eventual long-term preservation, and is the link between calcium carbonate cycling and the global alkalinity cycle. Today, atmospheric $CO_2$ concentrations are rising at geologically unprecedented rates (Stockner et al., 2013). The response and feedback of calcium carbonates to this perturbation is of major significance to our climate and environment. In the oceans, invasion of $CO_2$ leads to an increase of dissolved inorganic carbon (DIC), without a concomitant change in alkalinity. This shift in the DIC:Alkalinity ratio decreases surface ocean $[CO_3^{2-}]$; a decrease that will eventually propagate into the deep ocean. Marine calcifiers currently precipitate about 1 gigaton (GT) of carbon per year from the surface ocean, and the sedimentary reservoir of $CaCO_3$ is about $48 \cdot 10^6$ GT of carbon (Sigman and Boyle, 2000). Supression of calcification in the surface ocean, and carbonate dissolution throughout the water column and in the sediments, are two ways in which calcium carbonate buffers rising atmospheric $p$CO$_2$. With ~250 GT of anthropogenic carbon emitted since the preindustrial era (about one third of which has invaded the oceans, Sabine et al., 2004), we are already significantly altering the surface ocean carbon cycle (Richard A Feely et al., 2012; Bednarsek et al., 2014).

Calcium carbonate dissolution will potentially neutralize all fossil fuel-derived $CO_2$ introduced into the ocean. The neutralization timescale is a subject of some debate (Boudreau, Middelburg, Hofmann, et al., 2010; D. Archer, Kheshgi, and Maier-Reimer, 1998; Ilyina and R E Zeebe, 2012), and is coupled to the timescale of ocean

circulation, sediment bioturbation, and the kinetics of dissolution itself. Since ocean acidification is occurring more rapidly than ever documented in geological history, we must consider how best to establish the kinetics of calcium carbonate dissolution, and its role in the buffering of anthropogenic $CO_2$ emissions, to best predict the fate of fossil fuel $CO_2$ that invades the ocean.

It is surprising that despite the quantity and caliber of research on calcium carbonate dissolution, there is still a major debate over the basic formulation of a dissolution rate law. The kinetics of calcium carbonate dissolution are typically described by the equation:

$$Rate = k(1 - \Omega)^n. \tag{2.1}$$

The dissolution rate is driven by a thermodynamic potential $(1 - \Omega)$. A mineral's saturation state, $\Omega$, is defined as the *in situ* calcium and carbonate ion concentrations divided by the apparent solubility product for that mineral ($[Ca^{2+}][CO_3^{2-}]/K'_{sp}$). Undersaturation is related to the dissolution rate by a rate constant, $k$, and a reaction "order", $n$. This reaction order is of ambiguous significance; in this case it solely describes the empirical relationship between the saturation state and the dissolution rate. Global modeling efforts have focused on a linear ($n$=1) formulation, since it is relatively easy to implement (B Hales and S Emerson, 1997b; Boudreau, 2013; Ilyina and R E Zeebe, 2012; Dunne, Burke Hales, and Toggweiler, 2012). However, many experimental and *in situ* studies suggest nonlinear relationships between undersaturation and dissolution rate (Keir, 1980; Gehlen et al., 2005b; R A Berner and J W Morse, 1974; Cubillas et al., 2005; Fukuhara et al., 2008; Honjo and J Erez, 1978; Berelson et al., 2007). In one of the most influential studies, Keir (1980) found carbonate dissolution kinetics to be both very nonlinear and very fast (n=4.5, $k$=1300%/day). Keir's experimental dissolution rate is about an order of magnitude faster than those determined *in situ* (Honjo and J Erez, 1978). In fact, almost all laboratory dissolution studies outpace rates determined in the water column.

While a few other dissolution rate studies have been performed in natural seawater (Gehlen et al., 2005b; J W Morse and R A Berner, 1972), the applicability of many dissolution rate determinations to oceanographic conditions is extremely limited, due to solution chemistry and distance from equilibrium. For instance, most of the mechanistic work performed on calcite is far from equilibrium in dilute or

non-seawater solutions (Arakaki and Mucci, 1995; MacInnis and Brantley, 1992; Shiraki, Rock, and Casey, 2000, Cornelius Fischer, Rolf S Arvidson, and Lüttge, 2012 and references therein). Moreover, mechanistic studies are typically performed on a small area on individual grain surfaces, while the oceans interact with entire, complex particles. Thus, the real quantity of interest is a bulk dissolution rate. The disagreement among laboratory determinations, and the large discrepancy between lab and *in situ* results, lead to limited understanding of the dissolution process, and uncertainties in the implementation of a dissolution rate law in earth system models and projections.

Here, we present novel measurements of calcium carbonate dissolution that rely on a closed system dissolution measurement. We can perform these experiments in natural seawater close to equilibrium, capturing the range of undersaturations experienced by carbonates in the ocean. Using this method, we are able to completely constrain and maintain experimental saturation state, and also maintain near-constant surface area throughout the experiment. Our bulk dissolution study thus represents a potential link to detailed, mechanistic studies of solid-solution interfaces.

## 2.2 Materials and Methods

The method we employ here takes advantage of high precision stable isotope ratio measurements. We exploit the stable isotope of carbon, $^{13}C$, as a direct tracer of mass transfer from mineral to solution. In general, calcium carbonates enriched in $^{13}C$ are placed in a closed system of undersaturated seawater. We then measure the evolving $\delta^{13}C$ of this seawater over time by discrete sampling, obtaining curves of moles dissolved over time. The slope of these curves is a direct measure of mass loss rate from the mineral. First, we present the synthesis and characterization of the materials used in this study. Second, we describe our measurements of the carbonate system during an experiment – dissolved inorganic carbon (DIC), and total alkalinity (TA) – and the subsequent calculation of experimental saturation state. Finally, we describe the setup and execution of our dissolution rate experiments, $\delta^{13}C$ measurement, data fitting techniques, and analysis of uncertainty.

### Labeled calcium carbonates

Calcium carbonates enriched in $^{13}C$ are not produced naturally. Therefore, all of the materials used in this study were either purchased or prepared in the laboratory. We confirmed mineralogy with XRD and/or Raman spectroscopy, and measured specific surface area using either nitrogen, argon, or krypton adsorption isotherms, fitting

the curves following the BET method (Brunauer, Emmett, and Teller, 1938). SEM imagery was also obtained, using a Hitachi TM-1000 environmental SEM. Mineralogical determinations with XRD and Raman spectroscopy both have detection limits of $\sim$ 1% for calcium carbonate polymorphs (calcite, aragonite, and vaterite; Kontoyannis and Vagenas, 2000). Thus, we are confident in our mineralogies to 99% purity.

Synthetic $Ca^{13}CO_3$ was purchased from Sigma Aldrich (SKU 492027, $\geq$ 99 atom %). In all experiments performed with Aldrich calcite, this stock powder was wet-sieved to a grain size of 70-100 $\mu$m using 18.2 M$\Omega$ water adjusted to a pH of $\sim$ 8 using ammonium hydroxide.

The above material, while inexpensive and plentiful, is not ideal due to its sintered nature. We also needed a well-formed material that can be manipulated as an inorganic solid in a range of grain sizes. To this end, we grew our own calcium carbonates in the laboratory, using a gel-diffusion method first described by Nickl and Henisch, 1969. In this method, a 120 mL glass U-shaped tube was filled with 50 mL hydrous gel (0.17 M sodium metasilicate, adjusted to pH 8), separating 30 mL reservoirs of $CaCl_2$ and $Na_2^{13}CO_3$ (both 0.15 M) in each arm of the tube. The ends of the tube were sealed using Parafilm and rubber stoppers. Nucleation of calcium carbonate crystals was limited by diffusion and the gel pore spacing, allowing for slow growth of large grains. Grains were harvested after 3-6 months of reaction time by pouring off the spent reservoir solutions followed by physical break-up, sonication, and decantation of the less dense gel matrix from the calcium carbonate grains. Grains were then triply washed in DDW and dried at 60 °C. In this study, we present data from Aldrich-supplied and gel-grown calcite, dry-sieved to several size fractions. The degree of isotopic labeling was measured using a Picarro CRDS on small (0.2 mg) aliquots of material, pre-acidified, and introduced to the Picarro using the AutoMate Liaison autosampler. Raw isotopic abundances were used, and compared against a standard curve, prepared by sequentially diluting fine-sieved pure $^{13}C$ Aldrich calcite into natural abundance optical calcite.

**Surface area determination**

Surface areas were determined using two different methods. First, the specific geometric surface area of the calcites were calculated using the mean sieving size and assuming cubic geometry:

$$S.A._{geom} = \frac{6}{\rho \cdot \bar{d}},\tag{2.2}$$

where $\rho = 2.63$ g/cm$^3$ is the assumed density of calcite and $\bar{d}$ is the mean grain diameter of the sieving fraction. Secondly, "total" specific surface areas were determined by the BET method (Brunauer, Emmett, and Teller, 1938), using Ar, N$_2$, and/or Kr gases. Raw data (pressure ($p$),reference pressure ($p_0$), and volume ($V$)) were plotted as $\frac{p}{V(p-p_0)}$ vs $\frac{p}{p_0}$, in the linear region of $0.04 < p < 0.5$, fitted using a linear regression, and the surface area was calculated as in Brunauer, Emmett, and Teller (1938) These regressions typically gave relative errors of 1-3%.

**Carbonate system parameters**

We constrained calcite saturation state using DIC-TA pairs. All of our experiments were performed in Dickson seawater reference material (poisoned with mercuric chloride, final concentration $\sim 0.0015\%$ by weight or 55$\mu$M). The phosphate concentrations in all Dickson batches used were between 0.55 and 0.58 $\mu$mol/kg. We first made up large batches of undersaturated water for use in dissolution experiments. About 2-3 L of Dickson seawater standard was siphoned to 5 L Supelco gastight foil bags (Part no. 30228-U). Undersaturation was achieved by titrating negative alkalinity via injection of HCl (0.1 M) through the sampling port septum of the foil bag. No DIC was lost during acid addition. DIC did change slightly, but only due to dilution by the added HCl solution. These reservoirs could be used for 6-10 experiments, allowing for replicate experiments at the same degree of undersaturation.

Alkalinity, determined by open-system Gran titration, was performed on a custom-built instrument. We used a Metrohm Ecotrode (part no. 6.0262.100) electrode connected to a Mettler Toledo SevenCompact pH meter. The titrant (0.05-0.1 M HCl in natural seawater medium) was delivered by a Metrohm 876 Dosimat Plus titrator with a 5 mL burette. Titrant concentration was determined by calibration to seawater standard reference materials. To run a sample, ~16 mL of seawater was filtered and weighed into a plastic sample container, which was placed into a 21.0±0.1 °C water bath. The sample was stirred with a Teflon-coated stir bar and bubbled with air throughout the measurement. The titration was controlled from a Windows laptop using a home-coded MATLAB script. Initial acid injection and stabilization took about 5 minutes; then, the titration dosed 0.01 mL of acid and measured pH at 20 second intervals. After a total of 12 time points, alkalinity
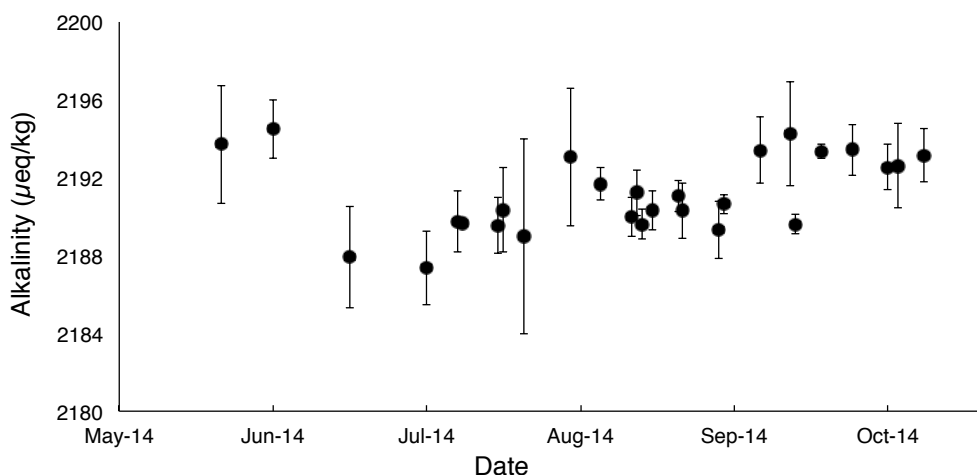
**Figure 2.1:** Long-term precision and drift of our in-house alkalinity standard. Data points are the mean of the standard replicates collected during the analytical session that day; error bars are the $1\sigma$ standard deviation of the replicates.

was determined using a nonlinear least- squares approach as outlined in the best practices guide (Riebesell et al., 2010). Dickson standard reference materials, as well as an in-house seawater alkalinity standard, were run at the beginning and end of every session to ensure analytical consistency and to monitor acid and electrode drift. Long-term alkalinity precision is about 2.0 $\mu$eq/kg ($1\sigma$, Figure 2.1) over several months, based on our internal standard. There is also a slight decrease in replicate standard deviation over this measurement period; this mainly represents the increasing experience of the analyst, rather than a true decrease in the variance of the standard. Long-term accuracy is about the same as precision; thus total alkalinity error over the long-term is on the order of 2 $\mu$mol/kg (Table 2.1).

|  | Alkalkinity ($\mu$eq/kg) | DIC ($\mu$mol/kg) | $\Omega$ |
|---|---|---|---|
| Mean Value | 1960-2200 | $\sim 2000$ | 0.6-3.0 |
| Internal Error ($1\sigma$) | 2.5 | 5.1 | – |
| Intermediate Error ($1\sigma$) | 2.0 | 5.6 | – |
| External Error ($1\sigma$) | 2.0 | 5.2 | 0.01-0.025 |

**Table 2.1:** Error analysis of alkalinity, DIC, and $\Omega$ in this study. Internal errors are due to the goodness of data fit and precision of mass flow for alkalinity and DIC, respectively. Intermediate errors are the standard deviation of replicates run in a single analytical session. External errors are the standard deviation of replicates run over multiple analytical sessions. Note the similarity in values between all of these values, indicating that errors are traceable to the initial measurement error.

Dissolved Inorganic Carbon (DIC) and seawater $\delta^{13}C$ were determined using a Picarro cavity ring down spectrometer (G2131-i) coupled to Picarro Liason interface and a modified AutoMate autosampler. About 7 mL of filtered seawater was injected into an evacuated, pre-weighed, 12 mL AutoMate vial from a syringe through the rubber septum screw-cap. The net sample weight was recorded. The AutoMate acidifies these samples on-line using 10% phosphoric acid, and the resulting $CO_2$ is carried in a nitrogen stream, through a Nafion desolvating line, to the Picarro Liaison sampling bags. The flow of gas from the AutoMate into the Picarro Liason's discrete sample bag was mass-flow controlled such that every bag had precisely the same mass of $N_2 + CO_2$. Each bag was then introduced to the Picarro CRDS for continuous analysis over an 8 minute interval.

Averaging statistics on each of these sample peaks were taken to give final $CO_2$ concentrations and isotopic compositions. Drift in both DIC and $\delta^{13}C$ was monitored over the course of the run, and also over longer time periods. DIC values were normalized to reference material values, and samples were both blank-and standard-corrected. Since we do not care about absolute $\delta^{13}C$ values, only relative changes, and because there are no available seawater $\delta^{13}C$ reference materials, standard $\delta^{13}C$ values were normalized to an arbitrary value of 1‰ (VPDB). Samples were corrected for instrumental drift using linear interpolation between bracketing standards (at the beginning, middle and end of the run, typically 7-10 hours). We also have documented a negative correlation between water content and $[^{12}CO_2]$ (and thus $\delta^{13}C$). Although most water is removed via Nafion reverse flow partitioning, we monitored water content in our samples, and made a water correction if necessary. Drift over the course of a run (~10 hours) was almost never above a few tenths of a permil, and resulting Picarro standards (Dickson standard seawater) typically had a standard deviation of under 0.1‰. The error in our DIC values can be entirely traced to fluctuations in flow rate: the standard deviation of replicate seawater samples has a relative error of 0.2/80 standard cubic centimeters per minute (SCCM), or $\sim 5.1 \mu mol/kg$ (Table 2.1). We were able to take advantage of replicate DIC and Alkalinity analyses to use standard errors when calculating experimental $\Omega$ and its uncertainty.

Alkalinity and DIC pairs were then converted to saturation state using CO2SYS (v1.1, 2011) run through MATLAB. We used the acid dissociation constants of Mehrbach et al., 1973 and the solubility product data from Mucci, 1983. The errors in alkalinity and DIC were propagated to $\Omega_{calcite}$ by a Monte Carlo approach: Alk-

DIC pairs were sampled randomly from normal distributions with their associated standard errors as the standard deviations, and the resulting $\Omega$ values were averaged. Errors on $\Omega$, calculated this way, are between 0.01 and 0.04 units. The calcite solubility data from Mucci (1983) were used for calculation of $\Omega$ in CO2SYS. We later discuss the experimental evidence in support of Mucci (1983) solubilities.

**Dissolution Rate Experiments**

All dissolution rate experiments presented here were performed on the benchtop at ambient temperature ($20 - 22°C$). We evaluated several different materials for their effect on DIC and alkalinity to construct our experimental apparatus, since we needed excellent control on saturation state.

**Unacceptable materials**

Our first experiments were performed in Tedlar bags, which proved permeable to $CO_2$. In Tedlar, undersaturated seawater with a $pCO_2$ of over 2000 ppm lost an average of 1 $\mu$mol/kg DIC per day over a 10-day period. We then switched to Supelco inert foil bags, which demonstrated a stable DIC and did not add or remove alkalinity. Secondly, we needed a material that would retain our labeled carbonate grains during an incubation experiment. We initially sealed our grains in nylon mesh bags. However, we found that this amide polymer slowly increased the alkalinity of the experimental seawater over time. No amount of washing or pre-conditioning changed this alkalinity increase. Additionally, as our mesh bags were constantly moving and bending, this alkalinity increase did not happen all at once, but slowly over time, by 10-15 $\mu$eq/kg over 5 days (Figure 2.2). Heat-sealing the nylon – crucial for retaining grains – further increased alkalinity contamination. presumably due to disintegration of the nylon polymer.

Instead of sealing our grains in nylon mesh, we placed grains directly into the foil bag and used specially fabricated polycarbonate sampling ports. These ports have a built-in filter housing, such that sampled water is filtered through Nucleopore membrane filters ($\sim 0.2\mu$m, Figure 2.3). The port was fitted onto the bag through a punched hole, hand-tightened, and sealed with a Viton o-ring. Using this setup, both alkalinity and DIC blank experiments showed no change over days to weeks.
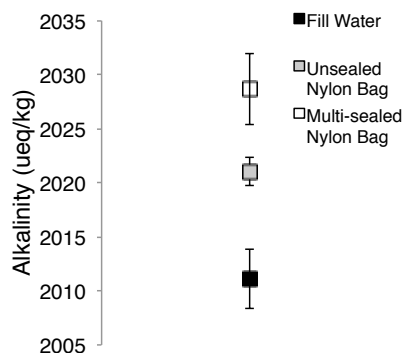
**Figure 2.2:** Documented alkalinity increase in a Supeclo inert foil bag over 5 days with (black symbol) no nylon mesh, (grey symbol) unsealed nylon mesh, and (open symbol) multiply-sealed nylon mesh.
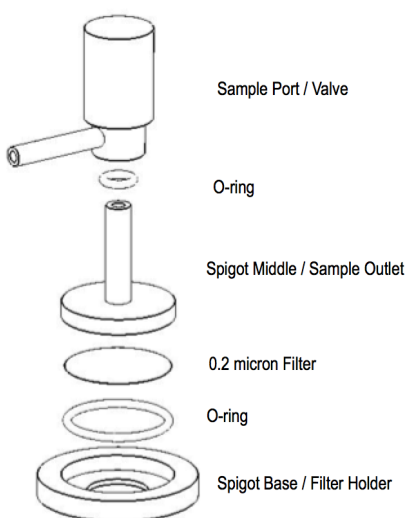


**Figure 2.3:** A diagram of the custom-made sampling port used in our experiments. Filter is an 0.2 $\mu$m Nucleopore membrane filter. The foil bag wall sits between the sample port and spigot middle, sealed by a Viton o-ring.

## Experimental setup

Experiments were prepared in the following way: 1 L Supelco bags (part no. 30336-U) were cut open, and the sampling ports were fitted through the foil. Labeled material (3-5 mg) was weighed out and quantitatively poured into the foil bag. The open bag was then heat-sealed shut, twice, creating a double seam. These bags were then evacuated to remove all headspace. Undersaturated fill water was siphoned from the large foil reservoirs into these experimental bags. First, about 50 grams was siphoned in, and grains were agitated and rinsed. This water was then removed

through the sampling port via syringe and discarded. Then, about 300 grams of fill water was siphoned in, the bag was weighed to obtain the exact mass of water added, and the experiment was considered started once the bags were placed on a shaker table at 60 rpm. We have tested the shaking rate and found that at speeds above 60 rpm the dissolution rate is the same as the rate at 60 rpm. Below 60 rpm rates slowed significantly, presumably due to stagnation and the formation of boundary layers around the grains. At each sampling point, the experimental bags were weighed. Samples were withdrawn through the sampling port via a Tygon tube attached to a plastic syringe. The syringe was washed with about 2 mL of sample water, and then a full 7 mL sample was taken, carefully avoiding headspace. This sample was injected through a 0.45 $\mu$m filter into a pre-evacuated, pre-weighted AutoMate vial for Picarro analysis. Initially, sampling occured either two or three times daily. As the experiment proceeded, however, sampling became more infrequent. Total experiment duration lasted six to twelve samplings over three to ten days. Since we measured DIC and $\delta^{13}$C simultaneously, DIC was monitored over the course of the run. Post-experiment alkalinity measurements were also taken to check for alkalinity consistency.

**Data processing**

Data processing required manipulating the raw Picarro data to generate DIC and $\delta^{13}$C values. Total $CO_2$ concentrations were blank-corrected (typically $15 \pm 4$ ppm in $\sim$ 1200 ppm), mass-normalized, and corrected using a multiplication factor determined by reference material standards run in the same analytical session. We converted $\delta^{13}$C signals over time into a mass loss rate, or moles dissolved over time. This is done by first converting $\delta^{13}$C into moles dissolved. The $^{13}$C/$^{12}$C ratio of seawater, $R^{13}_{sw}$, is related to $\delta^{13}C_{sw}$ by:

$$R^{13}_{sw} = (\delta^{13}C_{sw}/1000 + 1) \cdot R^{13}_{PDB}, \tag{2.3}$$

where $R^{13}_{PDB}$ is the standard isotopic ratio of Pee Dee Belemnite (0.0112372). Assuming no addition of $^{12}$C, the isotopic ratio change from sample to sample of the seawater was converted into a change in the moles of $^{13}$C added to the solution, modified by the change in mass due to sampling:

$$\Delta^{13}C_{2-1} = m_1 \cdot [^{12}C]_{init} \cdot (R^{13}_2 - R^{13}_1), \tag{2.4}$$

where $m_1$ is the seawater mass of time point 1, $[^{12}C]_{init}$ is the initial $^{12}C$ concentration of the seawater (which remains unchanged while dissolving 100% labeled materials) and $R^{13}_i$ is the isotopic ratio measured at time point $i$. $\Delta^{13}C_{2-1}$ is then the change in moles of $^{13}C$ between time points 1 and 2. These incremental changes are cumulative, so that the total moles dissolved are summed over the time course. Typical dissolution experiments that use a carbonate mass of 5 mg and a bag volume of 300 mL yield a $\delta^{13}C$ change of about 20‰ for every 1 $\mu$eq/kg change in alkalinity in the reaction chamber. As an experiment proceeds and seawater is removed for sampling, a constant dissolution rate will have a larger impact on this smaller reservoir. Due to this diminishing reservoir effect, our sensitivity is closer to 10‰ per $\mu$eq/kg alkalinity change by the end of an experiment. When alkalinity changes were large, we used the mean bag alkalinity to calculate $\Omega$, and used a standard deviation instead of standard error to calculate the error on $\Omega$.

## 2.3 Results

**Solid characterization**

The solid-phase carbonate minerals we use in our experiments, highly enriched in $^{13}C$, come from two different sources: Aldrich and homegrown (Figure 2.4). The composition of Aldrich calcite was confirmed to be 100% calcite via XRD. Aldrich calcite came as a fine powder which, upon closer inspection, was composed of sintered clumps of grains about 20 $\mu$m in diameter (Figure 2.4). Gel-grown calcium carbonate was formed in a range of grain sizes and morphologies; predominantly as well-formed rhombs. Additionally, a vaterite phase was formed in the shape of rough spherules of various sizes, as first observed by Schwartz et al., 1971. These two polymorphs were separated manually. The larger, homegrown rhombs were confirmed as 100±2% calcite by Raman spectroscopy. We also confirmed that these grains are 100% $Ca^{13}CO_3$ by measurement on the Picarro, as described above. Grain surfaces, however, revealed two distinct surface types. There were smooth, terraced features, as well as rough, poorly formed surfaces (Figure 2.4f). Raman spectroscopy on both of these surfaces confirmed that, despite very different morphology, they were both calcite. As shown in Nickl and Henisch, 1969, gel-grown grains retain some of the gel matrix during crystal growth. Thus, these differences in morphology could be guided by interaction with the gel matrix rather than any true mineralogical difference. Vaterite was present as separate crystalline units, so we cannot rule out that vaterite was present on our grains below our detection limit of $\sim 1 - 2\%$ compositional purity.
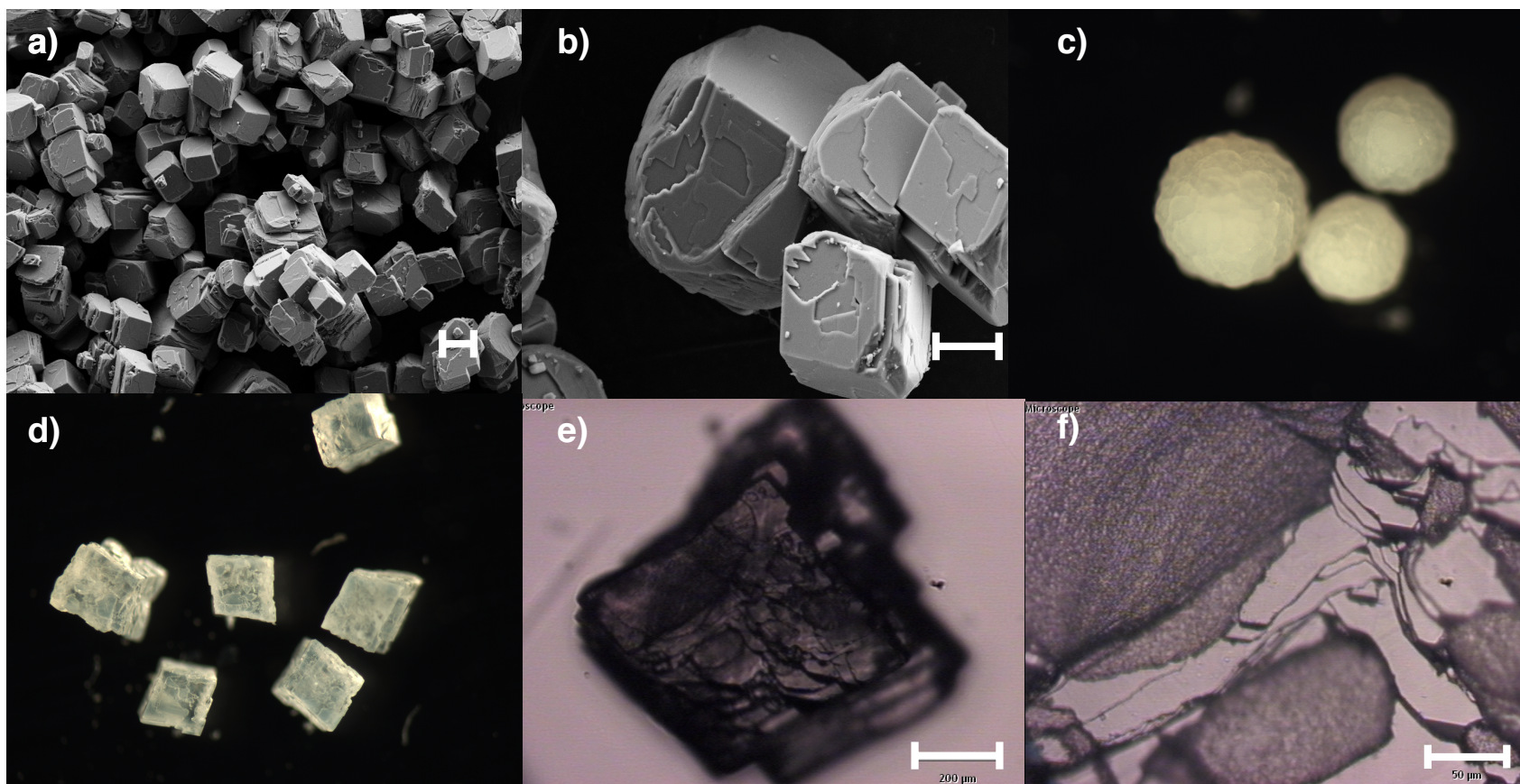
**Figure 2.4:** Materials used in this study. **a-b)** SEM images of the Aldrich $^{13}$C-calcite, sieved to 70-100 $\mu$m. Notice the clumps of sintered grains, each about 20$\mu$m in size. Scale bars are 20 and 10 $\mu$m, respectively. **c)** vaterite spherules at 6x magnification. Mineralogy confirmed by Raman spectroscopy. **d)** Transmitted light micrographs of the homegrown calcite, sieved to 500-700 $\mu$m, at 6x magnification. **e-f)** Reflected light micrographs of the same homegrown calcite grains. Notice the different textures, from a rough, sandpapery texture to smooth terraces. Both surfaces are confirmed to be calcite. Scale bars are 200 and 50 $\mu$m, respectively.

Various estimates of grain surface areas (Table 2.2) were compiled to compare methodologies. BET surface areas measured with $N_2$ and/or Argon are two to three orders of magnitude larger than corresponding geometric surface areas. Krypton has more promise as an adsorbate, as it has been demonstrated to give accurate surface areas down to 0.05 $m^2$ total area (Kanel and J W Morse, 1979). We measured Kr-BET surface areas with different amounts of Aldrich calcite sieved to 70-100 $\mu$m, and found that the measured surface area is also strongly dependent on the sample size (Table 2.2). At lower sample sizes, the BET-measured specific surface area is much larger. Measurements agree well within error at a single mass, while increasing sample size decreases the measured surface area to a threshold level of about 0.087 $m^2$/g for Aldrich calcite. We interpret the $\sim$ 3x difference between geometric and Kr-BET areas as a measure of the surface roughness of the Aldrich calcite. We have chosen to normalize all of our dissolution rate data to geometric surface area because of inaccuracies in our $N_2$ and Ar BET data.

| Material | Mass (g) | Method | Surface Area ($m^2$/g) | Error |
|---|---|---|---|---|
| Aldrich 70-100 $\mu$m | | Eq.(2.2) | 0.027 | |
| | 0.136 | Ar-BET | 4.514 | 0.126 |
| | 0.585 | $N_2$-BET | 0.536 | 0.013 |
| | 0.172 | Kr-BET | 0.150 | 0.015 |
| | 0.172 | Kr-BET | 0.136 | 0.013 |
| | 0.585 | Kr-BET | 0.095 | 0.006 |
| | 0.585 | Kr-BET | 0.090 | 0.004 |
| | 0.806 | Kr-BET | 0.085 | 0.004 |
| | 0.806 | Kr-BET | 0.089 | 0.005 |
| Homegrown 300-500 $\mu$m | | Eq.(2.2) | 0.0057 | |
| | 0.085 | Ar-BET | 0.513 | 0.03 |
| Homegrown 500-700 $\mu$m | | Eq.(2.2) | 0.0038 | |
| | 0.187 | Ar-BET | 7.65 | 0.23 |

**Table 2.2:** A summary of the specific surface areas determined in this study. Method is either calculating a geometric surface area using Eq.(2.2) or determined through BET using argon, nitrogen, or krypton as the analysis gas. The mass refers to the amount of sample used in the BET determination.

**Dissolution Experiments**

The first step in converting raw $\delta^{13}$C vs. time (Figure 2.5a) to the number of moles dissolved is to fit straight lines and calculate the experiment's slope (Figure 2.5b). This quantity is normalized to the mass of the solid used in each experiment. As shown in Figure 2.5, there is always a change in slope at about 24 hours. We use this second slope to calculate dissolution rates. The choice of using the second

slope is discussed in Section 4.1. Slopes, intercepts, and the goodness of fits are obtained using the LINEST function in Microscoft Excel. R-squared values on these slopes range from 0.98 to 1.00. These linear regressions, while quite strong, are not as strong as those predicted from scatter on individual $\delta^{13}$C measurements alone. Thus, the error in the fit here is indicative of not only instrumental precision, but experimental conditions as well.
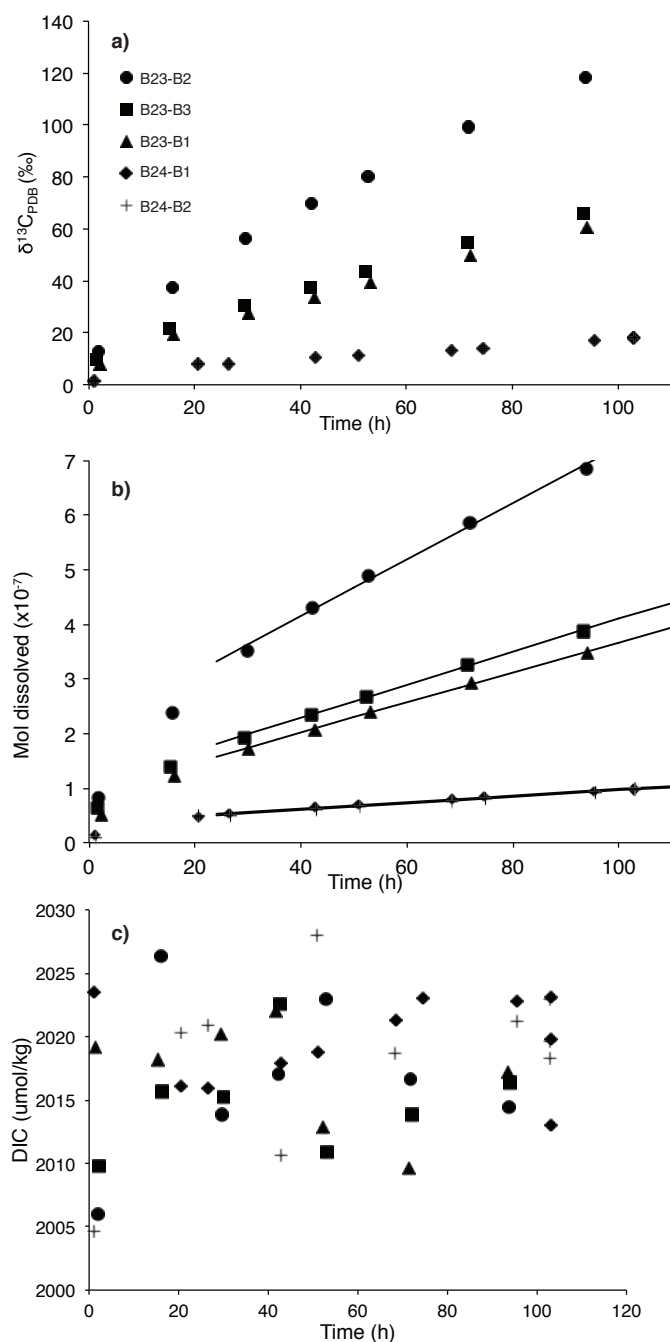
**Figure 2.5:** Raw data from experiments B23 and B24. Each symbol type represents a single dissolution experiment, with discrete samples collected over the time displayed. Steeper slopes are measured in bags with greater undersaturation. **a)** Raw isotopic $CO_2$ data. Each point is a single Picarro measurement of $\delta^{13}C$. **b)** The data from **a)** converted to the moles of labeled carbonate dissolved based on Eq.(2.4). Lines plotted are fits to the data after 24 h. **c)** the DIC data over time for each experiment. Statistics on these data, rate calculations, and final undersaturations are presented in Table 2.3.

| Material | Expt. | DIC | | Alkalinity | | | | Ω | | Rate | |
|---|---|---|---|---|---|---|---|---|---|---|---|
| | | *in situ* ($\mu$mol/kg) | s.e. (1$\sigma$) | *initial* ($\mu$eq/kg) | *final,calc.* ($\mu$eq/kg) | *final,meas.* ($\mu$eq/kg) | s.e. (1$\sigma$) | *calc.* | Error (1$\sigma$) | $\cdot 10^{-3}$ (g/g/day) | Error |
| Aldrich | B20-B1a | 2026 | 1 (10) | 1984 | 1985 | 1982 | 1 (4) | 0.75 | 0.01 | 0.450 | 0.028 |
| 70-100 $\mu$m | B20-B1b | 2018 | 2 (10) | 1984 | 1986 | 1982 | 1 (4) | 0.81 | 0.02 | 0.192 | 0.014 |
| | B20-B2 | 2023 | 1 (20) | 2004 | 2005 | 2002 | 1 (4) | 0.90 | 0.01 | 0.048 | 0.004 |
| | B22-B1 | 2011 | 2 (12) | 1986 | 1987 | 1986 | 1 (3) | 0.85 | 0.01 | 0.947 | 0.005 |
| | B22-B2 | 2016 | 2 (12) | 1987 | 1989 | 1991 | 2 (4) | 0.83 | 0.01 | 0.215 | 0.009 |
| | B23-B1 | 2017 | 2 (6) | 1963 | 1966 | 1965 | 1 (4) | 0.68 | 0.01 | 1.757 | 0.063 |
| | B23-B2 | 2017 | 2 (5) | 1957 | 1963 | 1963 | 2 (4) | 0.66 | 0.01 | 3.935 | 0.304 |
| | B23-B3 | 2016 | 2 (5) | 1962 | 1968 | 1968 | 1 (3) | 0.69 | 0.01 | 1.793 | 0.088 |
| | B23-B4 | 2013 | 1 (5) | 1973 | 1974 | 1973 | 0.2 (3) | 0.75 | 0.01 | 0.549 | 0.078 |
| | B24-B1 | 2020 | 2 (8) | 1985 | 1986 | 1986 | 1 (4) | 0.79 | 0.01 | 0.327 | 0.012 |
| | B24-B2 | 2020 | 1 (9) | 1985 | 1986 | 1988 | 0.3 (4) | 0.81 | 0.01 | 0.367 | 0.005 |
| | B30-B4 | 2027 | 3 (3) | 2004 | 2005 | 2008 | 1 (3) | 0.87 | 0.02 | 0.074 | 0.002 |
| Low Ω | B35-B1 | 1967 | 5 (6) | 939 | 999 | 983 | 21 | 0.017 | 0.001 | 87.51 | 4.47 |
| | B36-B1 | 2051 | 4 (6) | 1660 | 1680 | 1674 | 6 | 0.127 | 0.003 | 31.02 | 1.25 |
| High Ω | B31-B1 | 2013 | 7 (4) | 2046 | 2046 | 2046 | 0.1 (3) | 1.33 | 0.06 | N/A | N/A |
| | B31-B2 | 2022 | 2 (4) | 2046 | 2046 | 2045 | 1 (3) | 1.26 | 0.02 | N/A | N/A |
| | B31-B3 | 2020 | 4 (4) | 2054 | 2054 | 2055 | 1 (3) | 1.27 | 0.04 | N/A | N/A |
| | P13 | 2018 | 1 (10) | 2022 | 2022 | 2022 | 1 (3) | 1.07 | 0.02 | 0.017 | 0.002 |
| Homegrown | B27-B1 | 2009 | 4 (6) | 1971 | 1972 | 1974 | 1 (4) | 0.78 | 0.02 | 0.147 | 0.010 |
| 300-500$\mu$m | B27-B2 | 2020 | 2 (5) | 1995 | 1995 | 1993 | 1 (3) | 0.84 | 0.02 | 0.068 | 0.007 |
| | B27-B3 | 2017 | 3 (6) | 1987 | 1988 | 1987 | 1 (4) | 0.82 | 0.02 | 0.089 | 0.011 |
| | B27-B4 | 2020 | 4 (6) | 1977 | 1978 | 1976 | 0.2 (3) | 0.74 | 0.02 | 0.310 | 0.036 |
| Homegrown | B26-B1 | 2025 | 3 (7) | 1985 | 1985 | 1989 | 1 (4) | 0.76 | 0.01 | 0.127 | 0.007 |
| 500-700$\mu$m | B26-B2 | 2018 | 4 (7) | 1963 | 1964 | 1968 | 1 (3) | 0.70 | 0.02 | 0.344 | 0.013 |
| | B26-B3 | 2020 | 3 (7) | 1957 | 1959 | 1960 | 1 (4) | 0.64 | 0.02 | 0.629 | 0.016 |
| | B26-B4 | 2012 | 1 (5) | 1962 | 1964 | n.c. | n.c. | 0.70 | 0.01 | 0.516 | 0.015 |
| | B26-B5 | 2022 | 1 (5) | 1973 | 1974 | 1977 | 1 (4) | 0.70 | 0.01 | 0.205 | 0.005 |

**Table 2.3:** Carbonate system parameters and mass-normalized dissolution rates for all of the experiments presented in this study. Standard errors are accompanied by the number of replicates, in parentheses. Saturation state is calculated via Monte-Carlo error analysis of final (or average) alkalinity and *in situ* DIC pairs for each experiment (see text for more details; n.c. = not collected.)

We measured the alkalinity of the fill-waters and of the individual bag-waters once an experiment finished. Samples for DIC are taken throughout the course of an experiment, so $CO_2$ loss is monitored. We find that after filling an experimental bag, DIC values are about 5-10 $\mu$mol/kg lower than the original fill water used. This DIC loss is attributed to $CO_2$ adsorption and diffusion into and through the tygon tubing used for solution transfer. Once the siphon is complete and the experiment underway, DIC loss is imperceptible given our measurement error (Figure 2.5c). All pre-and post DIC and alkalinity values are presented in Table 2.3. The calculated saturation states from these Alk-DIC pairs are also presented, along with their Monte Carlo-estimated errors. Since we know quantitatively how many moles of carbon have been added to solution, we can calculate a final alkalinity change due to carbonate dissolution, and compare this to the measured alkalinity after an experiment is finished. We use the final alkalinity value and experiment bag-DIC value to calculate saturation state, since the initial and final (calculated and measured) alkalinity values never differ more than 6 $\mu$eq/kg from each other. When the final and initial alkalinities differ by more than 5 $\mu$eq/kg, we use the average alkalinity in the bag over the course of the experiment, calculated using the changing bag mass and cumulative moles of carbonate ion added at each time point.

Saturation state and dissolution rates are plotted against each other (1-$\Omega$; Figure 2.6). Data are fitted using a log-linear formulation of Eq.(2.1) and a log-linear regression which includes errors on both dissolution rate and $\Omega$:

$$\log(Rate) = \log(k) + n \cdot \log(1 - \Omega), \tag{2.5}$$

where $\log(k)$, the intercept, is the logarithmic dissolution rate constant in g/g/day or g/cm$^2$/day, and n, the slope, is the reaction order. This form of linear regression was first described in the geochemical community by York, 1966, and explicitly includes errors in the x-variable as well as the y-variable. These data are presented for Aldrich calcite and two grain sizes of homegrown calcite, in Table 2.4 and Figure 2.7.

## 2.4 Discussion

**Choice of thermodynamic constants**

Accurate measurements of the carbonate system in seawater are dependent on the appropriate choice of thermodynamic constants, and calcite dissolution is no exception. We chose to use the Dickson and Millero (1987) refit of Mehrbach's data (Mehrbach et al., 1973). We also tested sensitivity to the choice of dissociation con-

stants on calculation of $\Omega$, and found that the use of constants from Lueker, Dickson, and Keeling (2000) change the calculated value of $\Omega$ by only as much as 0.002 units, well below the measurement error of $\Omega$. The other important constant is the value of $K'_{sp}$ for calcite in seawater. If the calcite $K'_{sp}$ value used in our study is too small, then a plot of dissolution rate versus undersaturation (1-$\Omega$) will shift towards equilibrium, making it appear more linear. B Hales and S Emerson (1997b) recast the original dissolution data from Keir (1980) using updated carbonic acid dissociation constants and extrapolated to zero-dissolution to find a saturated ion activity product. These recalculations found dissolution rate to be essentially linearly dependent on undersaturation. Current estimates for a calcite solubility product by Gehlen et al. (2005a) are either the same as or larger than that of Mucci (1983) (the value used in our $\Omega$ calculations). Using the values of Gehlen et al. (2005a), our curves would shift towards higher undersaturation, rather than towards equilibrium. Furthermore, Gehlen et al. (2005b) show that their updated values of $K'_{sp}$ also produce a nonlinear relationship in Keir's data. Finally, our own data indicate that the $K'_{sp}$ Gehlen et al. (2005a) may be more accurate than that of Mucci, 1983. In a long-term dissolution experiment of our Aldrich calcite, we measured DIC and alkalinity after about two months, and found that the carbonate ion concentration indicated an IAP for our Aldrich calcite to be 1-10% higher than that of Mucci (1983). We cannot give a more accurate estimate of the $K'_{sp}$ for our calcite, since we suspect there might have been a small amount of DIC loss during this long-term incubation. Shorter-term solubility experiments using aragonite indicate that a larger solubility product is reached in under two months. We could choose to use a different "short-term" $K'_{sp}$ that might be more appropriate for our day-to-week-long experiments, but it is difficult to determine if such a quantity would be truly a thermodynamically stable solubility product, or if there are still unbalanced kinetic processes occurring.

In order to further confirm our choice of $K'_{sp}$, we performed several short-term experiments in supersaturated seawater very close to equilibrium (Figure 2.8). Experiments performed in 30% supersaturated seawater ($\Omega$ = 1.3) showed no appreciable exchange over 10 days. A supersaturated experiment closer to equilibrium ($\Omega$ = 1.07) shows definite isotopic enrichment over 7 days (Figure 2.8b). This near-equilibrium ($\Omega$ = 1.07) enrichment could be due to isotopic exchange, or it could be due to actual carbonate dissolution. Solid-solution exchange has been investigated before, and typically models partition the solid into labile and trapped reservoirs of calcium and carbonate groups on the calcite surface (Badillo-Almaraz and Ly, 2003; Tertre et al., 2010). Using radiolabeled calcium and bicarbonate,

Tertre et al., 2010 showed immediate (minutes to hours) exchange of the labile solid surface with the solution; after this initial equilibrium was reached, the solid maintained equilibrium for up to 10 days. Thus, exchange on the multi-day timescale is an unlikely contributor to our observed isotopic increases. We can confirm this hypothesis using a simple geometric calculation. If we assume a calcite mass of 5 mg in an experiment, and a surface area of 0.09 m$^2$/g, this gives a total surface area of 4.5·10$^{-4}$ m$^2$ of calcite per experiment. Furthermore, if we assume that a unit cell of calcite is 0.5 nm deep, this gives a total volume of 2.25·10$^{-13}$ m$^3$, or 6.7·10$^{-9}$ mol in a monolayer on the total calcite surface. A 300g seawater solution contains about 6·10$^{-4}$ mol DIC. If all of this surface monolayer were to exchange with seawater, this would lead to an isotopic increase of 1 part in $\sim$ 10$^5$, or 0.01‰. This is a negligible increase in $\delta^{13}$C relative to our measurement precision. On the other hand, if this enrichment is indeed dissolution, we would need to adjust our $\Omega$ by choosing a new K$'_{sp}$ (see discussion below). The calculated dissolution rate of this experiment (Table 2.3) is about 35% of the dissolution rate at $\Omega$ = 0.90. Assuming that the entire isotopic signal in this experiment is due to exchange, this would also be the maximum contribution of exchange to any of our reported dissolution rates. Our own determinations of K$'_{sp}$, in addition to the arguments against exchange made here, strongly support this near-equilibrium behavior being dissolution. We do not have direct measurements of K$'_{sp}$ for our homegrown calcite. In order to be consistent across our two materials in this study, we do all calculations of dissolution parameters using the K$'_{sp}$ estimate from Mucci, 1983, and discuss this very near equilibrium dissolution data in the context of potential mechanisms of dissolution.

**Surface area corrections**

In all of our experiments, there are two stages of $\delta^{13}$C accumulation in the bags (Figure 2.5). In the first 24 hours, rates are faster than thereafter. Following the first 24 hours, rates remain constant over several days. There are several explanations for this increased initial rate. First, since our detection limits in determining mineralogy are at best 1%, this initial rate could be due to dissolution of a more soluble or hydrated calcium carbonate polymorph on the mineral surface. Secondly, this increased rate could reflect the mineral surface reaching steady state with the solution composition. These effects could be substantial, since calcium carbonates in all cases were precipitated from pure calcium chloride solutions. Thus, the calcite surface could be equilibrating with seawater Mg/Ca; it could be hydrating to adjust its water activity; and it could be adsorbing species such as dissolved organic carbon or

phosphate ion. Finally, although we rinsed our grains with pH-adjusted DIW, these increased rates could be due to dissolution of fine-grained material and/or desorption of loosely bound carbonate ions from the mineral surface. We did not systematically test these various hypotheses, and we choose the later rates as representing the bulk crystal dissolution rates. We choose 24 hours as an arbitrary cutoff between these slopes, since this effect never lasted longer than one full day. In no experiment was this period long enough to significantly change the experimental saturation state.

The fact that we see no further change in slope indicates that these are bulk dissolution rates, and that our system is remaining closed to any alkalinity or DIC change. Based on the number of moles dissolved at the end of our experiments, a maximum of 2% of the solid is consumed over the duration of an experiment. In most cases, $< 1\%$ dissolves. As above, there are $6.7 \cdot 10^{-9}$ mol in a monolayer on the calcite surface in our experiments. A $40\permil$ solution enrichment – $\sim 2 \cdot 10^{-7}$ moles of carbonate dissolved – corresponds to about 30 monolayers of calcite dissolved, or a 15 nm change in surface height. This surface height is consistent with surface height changes measured in AFM studies of calcite dissolutions (Rolf S Arvidson and Lüttge, 2010; Tang, Orme, and George H Nancollas, 2004) and are on the order of AFM tip sizes used in these experiments (4-50 nm; H Henry Teng, 2004). Thus, changes in surface area in our experiments are no greater than those observed in surface-based dissolution studies, and we can treat the surface area as constant throughout an experiment. Our tight control of surface area and bulk chemistry bridges the gap between detailed surface examinations of calcite dissolution, and bulk mineral dissolution studies.

Compiling the rate data (per gram) as a function of undersaturation (Figure 2.6a) shows differences between the grains used in our experiments. As expected from an inverse-diameter relationship, the larger-grained material dissolves more slowly per gram than the Aldrich calcite. Indeed, when the data are normalized to geometric surface area, they collapse to a single curve (Figures 2.6b and 2.7d). This agreement could be coincidental, due to the differences observed in surface morphology. It is also not unprecedented for different materials to have different dissolution rate constants (e.g. Carrara marble and Iceland spar; Sjöberg and Rickard, 1984). Data plotted in log-log space (Figure 2.7d) indicate a slight offset between our homegrown calcites and the Aldrich grains. This offset could be due to differences in grain surfaces and crystal microstructure that are not captured by our geometry normalization, or small differences between the $K'_{sp}$ of the two materials. The

empirical fits also provide slightly different k and n values (Table 2.4 discussed below). The fact that our geometry normalization works across three grain sizes and two material types indicates that grain size plays a role in controlling dissolution rate. Since grain size correction alone normalizes our data quite well, it seems that the microstructural differences we observe are not of primary importance for dissolution rate.

We present data normalized by geometric, not BET, surface area (Table 2.4, figures 2.6-2.9). The BET method accounts for surface roughness and heterogeneity, whereas geometric normalizations simply treat grains using an average grain size and a model grain shape (in our case a cube). Nitrogen and Argon BET overestimate surface area significantly at total surface areas less than $1m^2$,: in our case, by factors of 20 and 167, respectively (Table 2.2). Kanel and J W Morse (1979) report accurate and precise results for calcium carbonates down to only 0.03 $m^2$ using Kr-BET. For Aldrich calcite, our Kr BET result provides a maximum surface roughness that increases surface area over the geometric estimate by a factor of ~3. We lack sufficient sample to analyze our homegrown material's surface area using Kr-BET. Normalizing to geometric surface area means the absolute dissolution rates presented in this study could be systematically high by a factor of 3. This is a large source of uncertainty in our method, but is hard to deal with for small quantities of materials. The use of geometric surface area is not unprecedented (L N Plummer and Wigley, 1976, Shiraki, Rock, and Casey, 2000, Cubillas et al., 2005, Sjöberg, 1976, Sjöberg and Rickard, 1985), and with the exception of Keir, 1980 and Honjo and J Erez, 1978, we restrict any quantitative rate comparison to other studies which normalized to geometric surface area.

**Data workup and fitting**

The near-equilibrium log-log dissolution data plotted versus undersaturation, and their York fits, are presented in Figure 2.7. Dissolution rates at replicate saturation states agree within error of each other. We fit the log-transformed data to the empirical relationship of Eq.(2.1). Goodness of fit is quantified using the MSWD (mean square weighted deviate) statistic. The MSWD determines how much of the scatter in the data can be accounted for by the internal errors. Since a York-regression calculates the best fit line accounting for errors in both x and y, we can use an MSWD to calculate the relative goodness of fit (compared to the internal errors) in the x-direction, the y-direction, and normal to the fit:

$$\text{MSWD}_y = \frac{1}{N-1} \frac{\sum_i (y_i - \bar{y}_i)^2}{\sum_i \sigma_{y_i}^2},$$

$$\text{MSWD}_x = \frac{1}{N-1} \frac{\sum_i (x_i - \bar{x}_i)^2}{\sum_i \sigma_{x_i}^2}, \tag{2.6}$$

$$\text{MSWD}_{xy} = \frac{1}{N-1} \frac{\sum_i (y_i - \bar{y}_i + x_i - \bar{x}_i)^2}{(\sigma_{x_i} + \sigma_{y_i})^2},$$

where $x_i$, $y_i$ are the $i$ data pairs of $log(1 - \Omega)$ and $log(\text{Rate})$, respectively, and $N$ is the number of points used for the fit. The York regression parameters give a line $y = a + bx$, so the calculated $x$ and $y$ values from the regression are $\bar{x}_i = (y_i - a)b$ and $\bar{y}_i = a + bx_i$. Individual errors are defined as $\sigma_{x_i}$ and $\sigma_{y_i}$. The MSWD values calculated in this way are shown in Table 2.4. Interestingly, almost all MSWD values are below 1, suggesting that the scatter about the line is much smaller than that predicted by the internal errors. Part of this large discrepancy is due to the number of points we use to do the fitting – an artifact of the small range of undersaturations over which we perform the fit. One other explanation for our small MSWD statistics is that we have overestimated errors in $\Omega$ and dissolution rate. These errors should not be correlated, since they are determined by completely independent methods. Errors in the dissolution rate should not be overestimated at all. There is virtually no error in our x-axis (time), so all error is from scatter in the y-axis ($\delta^{13}$C or moles dissolved). Errors in measured DIC-alkalinity pairs should also not lead to an overestimation of error in $\Omega$. We accept the errors on this empirical fit, and acknowledge that they might be an overestimate of our uncertainty on $\Omega$, and the resulting uncertainty on our empirical fits.

**The nonlinearity of calcite dissolution in seawater**

Several arguments have been made for a linear relationship between dissolution rate and saturation state in seawater (Steven Emerson and M. Bender, 1981; B Hales and S Emerson, 1997b; Boudreau, 2013). A majority of these studies have either been modeling attempts or refits of older experimental data (specifically from Keir, 1980 and Keir, 1983). The first argument against a linear fit to our data is statistical. Fitting our data with a linear regression gives a poor r-squared value (0.72, not shown), and a significant negative y-intercept. A negative intercept would imply a large quantity of more soluble calcium carbonate, but none were detected given the

detection limits of our methods (see above). Thus, a negative intercept must imply a large shift of calcite solubility towards numbers smaller than those determined by J W Morse, Mucci, and Millero, 1980, for which there has been no recent experimental evidence. In contrast to model fits of deep-sea sediments, most laboratory calcite dissolution data shows a strongly nonlinear dissolution rate, dating from as early as 1972 (J W Morse and R A Berner, 1972; Keir, 1980; Gehlen et al., 2005b; J. Xu, Fan, and H Henry Teng, 2012; H Henry Teng, 2004). This nonlinearity is also not unique to calcite: similar results have been shown for near-equilibrium albite dissolution as well (Rolf S Arvidson and Lüttge, 2010).

Our results give fitted values of *n* varying from 2.92 - 3.85 (Table 2.4). These large *n* values demonstrate a strongly nonlinear relationship between dissolution rate and undersaturation. This nonlinearity is more evident when rates over a larger range of undersaturation are considered. In Figure 2.9, we show near-equilibrium dissolution data plotted with two far-from-equilibrium experiments, along with the very near-equilibrium point discussed in Section 2.4. In order to plot all of these data, we have adjusted the undersaturation to make this near-equilibrium point undersaturated (changing $\Omega$ from 1.07 to 0.995). Dissolution rates are plotted versus free energy, using $\Delta G = RT\ln(\Omega)$ (Figure 2.9). The temperature used was 294 K. When plotted as an ensemble a definite curvature is noticeable, both far from equilibrium and, in the figure inset, very close to equilibrium as well. This is exactly the type of curvature described by Rolf S Arvidson and Lüttge (2010) and J. Xu, Fan, and H Henry Teng (2012). This curvature is further supported by fitting our data over narrow ranges of undersaturation: closer to equilibrium, a log-log regression gives a smaller *n*. Further from equilibrium, *n* grows larger. A similar feature is also noticeable in data from Keir, 1980, especially in his reagent calcite and small size-fraction sedimentary data.

This curvature helps explain the range of *n* values determined for our three materials. It is also evidence for multiple dissolution mechanisms. Similar curvature has also been documented before by other mechanistic studies (R A Berner and J W Morse, 1974; J. Xu, Fan, and H Henry Teng, 2012; H Henry Teng, 2004; Rolf S Arvidson and Lüttge, 2010), and has been the subject of some debate. There is general agreement that strongly nonlinear dissolution behavior must be related to criticality in the mineral-solution system. In this scheme, there is some critical undersaturation, $\Omega_c$, that once surpassed, allows dissolution to occur very rapidly. In a seminal study, R A Berner and J W Morse (1974) argued that near-equilibrium criticality was

related to the abundance of phosphate ion adsorbed to the mineral surface. Berner and Morse hypothesized that these adsorbed ions prevent dissolution steps from propagating. Once below a certain threshold saturation state, however, dissolution is able to overcome these adsorbed barriers and a dissolution kink or step propagates very rapidly. Indeed, the zeta-potential of calcite is quite high (~9 at atmospheric $p$CO$_2$, Heberling et al. (2011)), which would implicate negatively charged ions as the barrier-forming species. This study represents new evidence for criticality at $\Delta$G $\sim$ 0.4-0.6 kJ/mol (Figure 2.9). This criticality at very low free energy seems to be unique to seawater. The $\Omega_c$ given for step-edge propagation in freshwater (H Henry Teng, 2004; J. Xu, Fan, and H Henry Teng, 2012) is around 0.3 (-2.9 kJ/mol), which is quite different from our findings. We calculate $\Omega_c$ using the equation from R A Berner and J W Morse (1974), which assumes that phosphate adsorption poisons the calcite surface and prevents step propagation. This calculation gives $\Omega_c \sim$ 0.9, which is consistent with our curvature, phosphate ion concentration, and solid:solution ratio of our experiments. Although Walter and E. A. Burton (1986) showed little dependence of curvature on phosphate ion concentration, further work should be done on the role of low phosphate concentrations in calcite dissolution kinetics.

Dickson standard seawater is poisoned with mercuric chloride, so Hg$^{2+}$ could also poison the calcite surface. There is evidence that Hg$^{2+}$ does not appreciably adsorb onto calcite (Bilinski et al., 1991), and thus should not interfere with dissolution kinetics. There is also some evidence that magnesium ion could play a role in inhibiting step edge formation and propagation close to equilibrium (M. Xu and Higgins, 2011). These authors report an inhibitory effect at $\Omega_c = 0.2$, although their $\Omega$ is poorly constrained due to gas exchange considerations. There are two effects of magnesium on dissolution rate. The first is its effect on K$'_{sp}$. Overgrowth of calcite from seawater onto pure calcium carbonate would contain $\sim$ 8 mole% magnesium (Mucci and J W Morse, 1984). This resulting overgrowth could have a different solubility than the original crystal. The second is an actual relationship with $\Omega_c$ through surface poisoning. Chemisorption of magnesium onto calcite could either prevent other species from attacking the mineral surface, or prevent steps from retreating (M. Xu and Higgins, 2011). If magnesium were the cause of our observed criticality, this would imply that at seawater Mg concentrations (53 mmol/kg), $\Omega_c$ must shift towards equilibrium. This inference is rather counterintuitive, as it implies that magnesium ion's inhibitory effect changes sign somewhere between 1 and 50 mmol/kg. The solubility of magnesian carbonates goes through a minimum at 4

mole %, and if the equilibrium composition of the solid displays such a reversal in seawater solutions of various Mg:Ca ratio, the multiple effects of Mg concentration on the calcite-seawater system could lead to such a sign reversal in the dissolution kinetics as well.

Finally, Zhang and G H Nancollas (1998), through a kinetic treatment of an ideal AB (i.e. two component) crystal, indicate that dissolution rates should also be strongly dependent on the ratio of calcium to carbonate ions. Over the range of undersaturations we explore here, that ratio does not vary much; it is fixed at around $[Ca^{2+}] : [CO_3^{2-}]$ ~300. At a solution ratio of 100, Zhang and G H Nancollas, 1998 showed a 40% change in the calcium-carbonate ion ratio correction function to their dissolution rate expression over a saturation range from 0 to 1. This change is small compared to the orders of magnitude change in rates we observe here. The solution ratio might be important in solutions with a wide range of calcium and carbonate ion concentrations, and could be worth further investigation with our method. But it is not an important factor in the nonlinearity of our dissolution rates close to equilibrium. We have not attempted to determine the underlying controls on criticality in the calcite-seawater system. An understanding of this criticality should elucidate the underlying mechanisms of calcite dissolution.
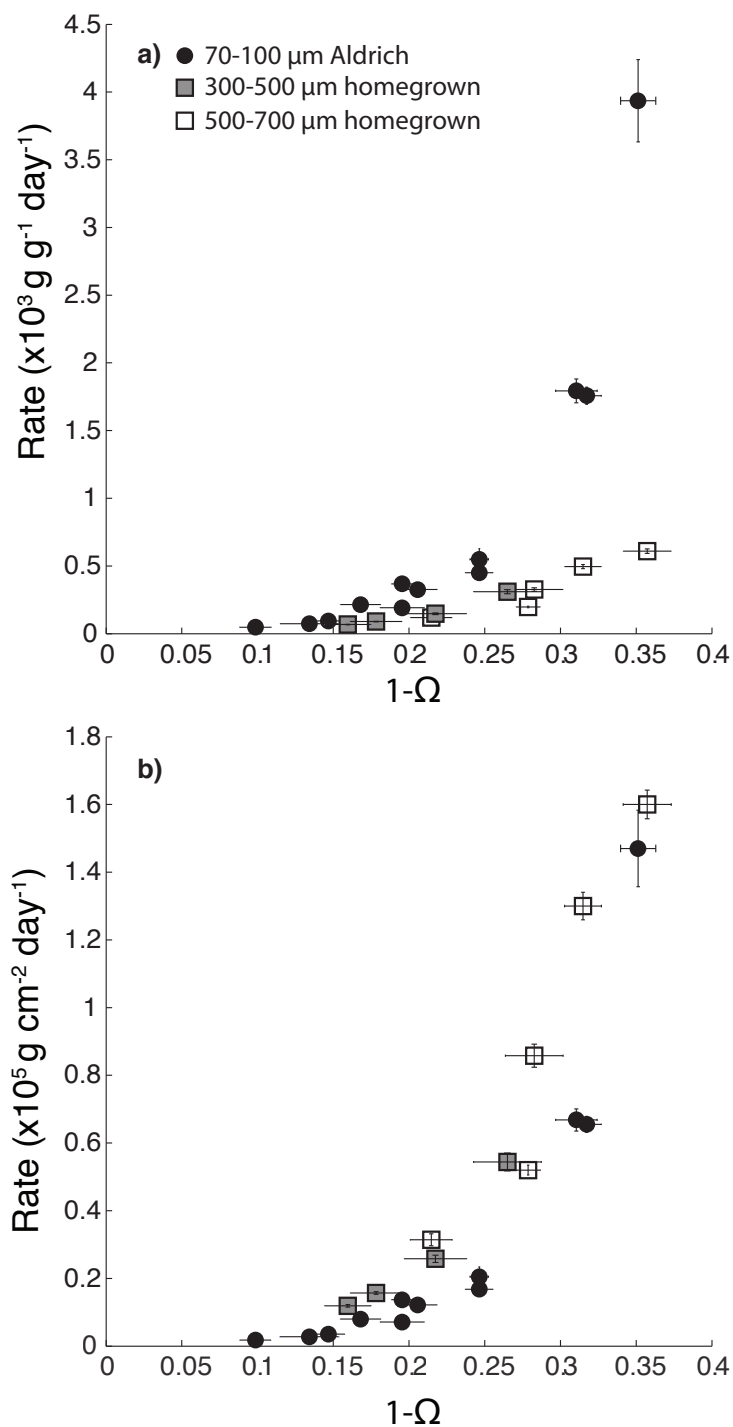
**Figure 2.6:** Dissolution rates versus undersaturation (1-Ω) for Aldrich and Homegrown materials. **a)** Rates normalized to mass of carbonate. **b)** Rates normalized to mass and specific geometric surface area. Note the rate unit and scale differences. Solid circles: 700-100μm Aldrich calcite. Gray squares: 300-500 μm homegrown calcite. Open squares: 500-700 μm homegrown calcite.

**Figure 2.7:** Log-log plots of undersaturation versus geometry-normalized rate data for all materials presented. **a)** 70-100 $\mu$m Aldrich calcite. **b)** 300-500 $\mu$m homegrown calcite. **c)** 500-700 $\mu$m homegrown calcite. **d)** geometry-normalized rate data for all minerals, fit as an ensemble. Symbols are the same as in Figure 2.6. Slopes (log$k$) and intercepts ($n$) for these fits, along with the accompanying error analysis, are presented in Table 2.4.
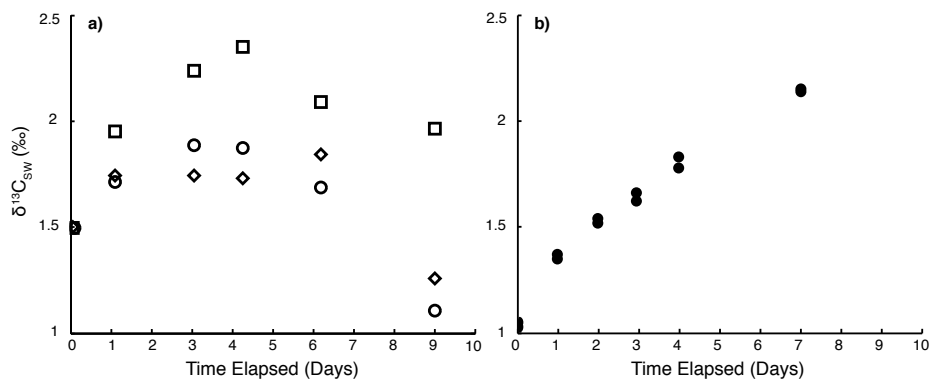
**Figure 2.8:** Seawater isotopic data versus time for four experiments conducted at super-saturation ($\Omega \sim 1.3$) to test for isotopic exchange between solid and solution. **a)** Three experiments conducted at $\Omega \sim 1.3$. These experiments show no significant isotopic enrichment over time. Each symbol type is an individual dissolution experiment. **b)** One dissolution experiment conducted at $\Omega = 1.07$. There is some isotopic enrichment over 7 days.
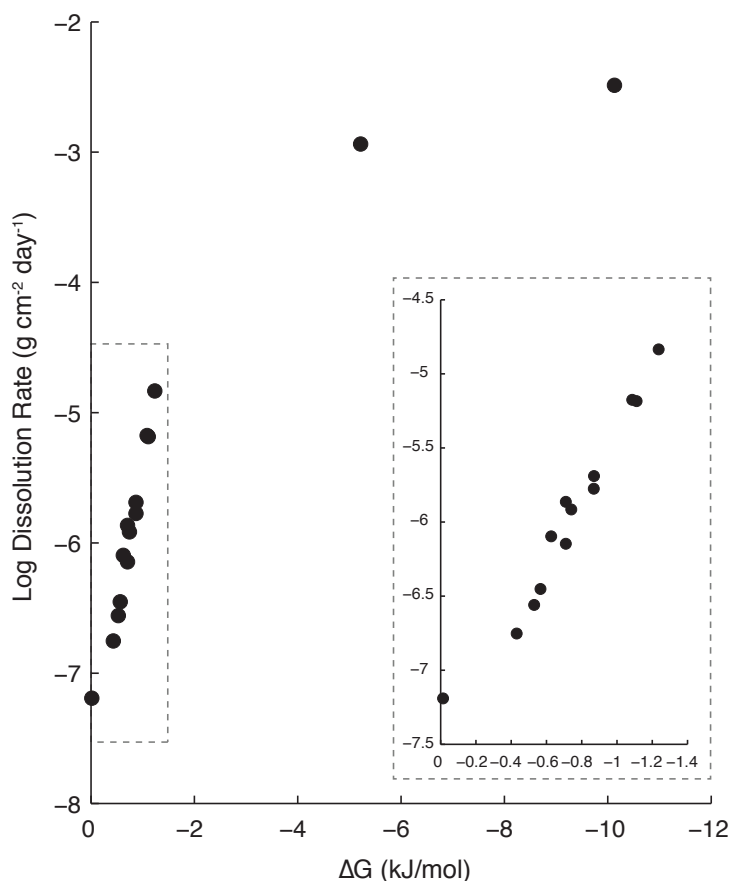


**Figure 2.9:** Aldrich calcite dissolution rate data versus $\Delta G = RT\ln(\Omega)$. The lower right inset plots the very near-equilibrium data, illustrating curvature both near and far from equilibrium.

| Material | $\log k_{geom} \pm \sigma_{\log k}$ | $k_{geom} \pm \sigma_k$ | $n \pm \sigma_n$ | $\text{MSWD}_x$ | $\text{MSWD}_y$ | $\text{MSWD}_{xy}$ |
|---|---|---|---|---|---|---|
| | $(\text{g cm}^{-2}\ \text{day}^{-1})$ | $(\text{g cm}^{-2}\ \text{day}^{-1})$ | | | | |
| Aldrich calcite 70-100 $\mu$m | -3.4±0.1 | $3.7\pm0.4 \cdot 10^{-4}$ | 3.5±0.2 | 0.6 | 0.4 | 0.1 |
| Homegrown calcite 300-500 $\mu$m | -3.6±0.4 | $2.4\pm0.9 \cdot 10^{-4}$ | 2.9±0.5 | 0.04 | 0.02 | 0.01 |
| Homegrown calcite 500-700 $\mu$m | -3.0±0.3 | $1.0\pm0.3 \cdot 10^{-3}$ | 4.0±0.6 | 0.3 | 1.3 | 0.3 |
| All Inorganic Data | -3.1±0.1 | $7.2\pm0.6 \cdot 10^{-4}$ | 3.9±0.1 | 0.3 | 0.3 | 0.1 |

**Table 2.4:** Each material's rate law parameters in this study. Geometric surface areas calculated using Eq.(2.2). Errors ($1\sigma$) are calculated from a York regression accounting for errors in both rate and undersaturation.

**Specific rate constant ,$k$**

Our York-regression fits (Figure 2.7, Table 2.4) show k-values ranging from 0.3 -1.0·$10^{-3}$ g cm$^{-2}$ day$^{-1}$ for the different material types measured. Our specific rate constant, $k_{geom}$, is a measure of the far-from-equilibrium bulk dissolution rate in natural seawater, where $\Omega$ approaches 0, i.e. Rate = $k(1-0)^n$ = $k$. We have two independent estimates of $k_{geom}$: a fit to our near-equilibrium data, extrapolated to $\Omega = 0$, and a true, far-from-equilibrium dissolution rate experiment run at $\Omega$ ~ 0.01. These data are plotted along with the near-equilibrium results in Figure 2.9. A comparison of these two estimates of the rate constant to other measured dissolution rates in dilute solution is presented in Table 2.5. Surprisingly, all of these measured dissolution rates are within an order of magnitude of each other, and many even agree within error. These studies were all performed in different solutions, suggesting similar dissolution mechanisms far enough from equilibrium, regardless of ionic strength and other solution considerations. These studies also employ a wide range of measurement techniques. The pH-stat method, first employed by J W Morse and R A Berner (1972), was also employed by L N Plummer and Wigley (1976) in dilute solution. At near-neutral pH, they found no dependence of dissolution rate on pH. The closest analog to our experiments are those performed in seawater by Keir (1980), whose $k$ is also presented in Table 2.5. With the exception of Keir's data, all rate constants here are normalized to geometric, not BET, surface area.

| Study | Method | pH | [Ca$^{2+}$] (mmol kg$^{-1}$) | Dissolution Rate (mol cm$^{-2}$ s$^{-1}$) |
|---|---|---|---|---|
| L N Plummer and Wigley, 1976 | pH-stat | 5.5-7.0 | 0 | 3.2·$10^{-10}$ |
| Sjöberg and Rickard, 1985 | Rotating disk reactor | 6-8 | 0 | 6.9·$10^{-10}$ |
| Sjöberg and Rickard, 1985 | Rotating disk reactor | 6-8 | 10 | 8.7·$10^{-11}$ |
| Shiraki, Rock, and Casey, 2000 | *in situ* AFM | 7.6 | 0 | 1.8·$10^{-10}$ |
| Shiraki, Rock, and Casey, 2000 | Ca$^{2+}$ Flux | 7.6 | 0-0.01 | 3.1·$10^{-10}$ |
| Cubillas et al., 2005 | Stirred-flow reactor | 5.1-9.8 | 0.1 | 1.8·$10^{-10}$ |
| Keir, 1980 | Flow-through reactor | 7.1-7.3 | 10 | 5.1·$10^{-10}$ |
| This study | $k_{geom}$ | 7.1-7.3 | 10 | 8.5·$10^{-11}$ |
| | Low $\Omega$ expt. | 5.5 | 10 | 3.8·$10^{-10}$ |

**Table 2.5:** A comparison of normalized, far from equilibrium, calcite dissolution rates. Details of the studies are listed. The dissolution rates presented for this study, Cubillas et al., 2005, and Keir, 1980, are the far-from-equilibrium dissolution rate (the extrapolated dissolution rate constant from the data in the listed pH range). We also present our own measurements of the zero $\Omega$ dissolution rate.

Our $k$ does not agree well with that of Keir (1980) by at least a factor of 6; his rates, by his own admission, are quite fast (Keir, 1983) and do not compare well with *in situ* results (e.g. Honjo and J Erez (1978)). This discrepancy could be due to incorrectly defined carbonate system parameters, although a refit of the data by

B Hales and S Emerson (1997b) still gives a very large dissolution rate. Instead, the difference could be due to a difference in measured and actual saturation state. One other difference could be that once steady state was reached in Keir's flow-through reactor, the surface had dissolved enough to significantly change the mineral's surface area. This would lead to enhanced rates, since specific surface area increases as dissolution proceeds (Honjo and J Erez, 1978), and dissolution rates can vary by orders of magnitude as the surface evolves in dissolution simulations (Luttge, R S Arvidson, and C Fischer, 2013). Our measured far-from-equlibrium dissolution rate, on the other hand, is slightly on the upper end, but around the mean value of the dissolution rates in Table 2.5. An explanation for our elevated rate constant is that this experiment was conducted at a pH of about 5.5. At this pH, dissolution through direct hydrogen ion attack is proposed as a significant contributor to the overall dissolution rate, which could explain the elevated rate compared to that extrapolated from our near-equilibrium results (at pH ~7; L N Plummer and Wigley (1976) and Sjöberg (1976)).

In the rotating disk experiments of Sjöberg and Rickard (1985), a strong dependence on calcium ion concentration is noted; they attribute this dependence to transport of calcium ion from the reacting mineral surface to the bulk solution. Their calculated dissolution rate at seawater-like calcium concentration (10 mM) is in excellent agreement with our calculated value of $k$. We will need to further investigate the effect of calcium ion concentration on dissolution rate if we are to determine if it plays a role in the chemical kinetics, above and beyond its effect on transport of calcium away from the mineral surface.

**Implications for the calcite lysocline**

Ideally, calcite dissolution rate measurements determined in the laboratory should be able to explain variations of calcite reactivity in the natural environment, and help explain the distribution of calcitic sediments in the ocean. However, there has been a long-standing disagreement between laboratory measurements and field-based observations. Our near-equilibrium dissolution rate constant determined for 70-100 $\mu$m Aldrich calcite (8.5%/day; Table 2.4) is within the range proposed by both W. R. Martin and Sayles, 1996 and B Hales and S Emerson, 1997a for use in lysocline models with a nonlinear rate law. It is also close to the value obtained by Keir, 1983 (16%/day) during his sediment bed experiments and a strongly nonlinear (n=4.5) rate law formulation. It is in very close agreement with the rate constant used by Friis et al., 2006 to match global alkalinity distributions in a GCM simulation.

Our dissolution rates also match quite well with those determined by Honjo and J Erez, 1978, measured in flow-through reactors suspended in the water column. At $\Omega = 0.75$, we calculate a dissolution rate of $3.4 \cdot 10^{-6}$ g/cm$^2$/day. Honjo and Erez measured a dissolution rate of $2.1 \cdot 10^{-6}$ g/cm$^2$/day. These agreements lend strong support to our rate determinations, and the application of our rate constant to dissolution kinetics in natural environments. Below, we apply our rate formulation to the natural environment, using a simple model.
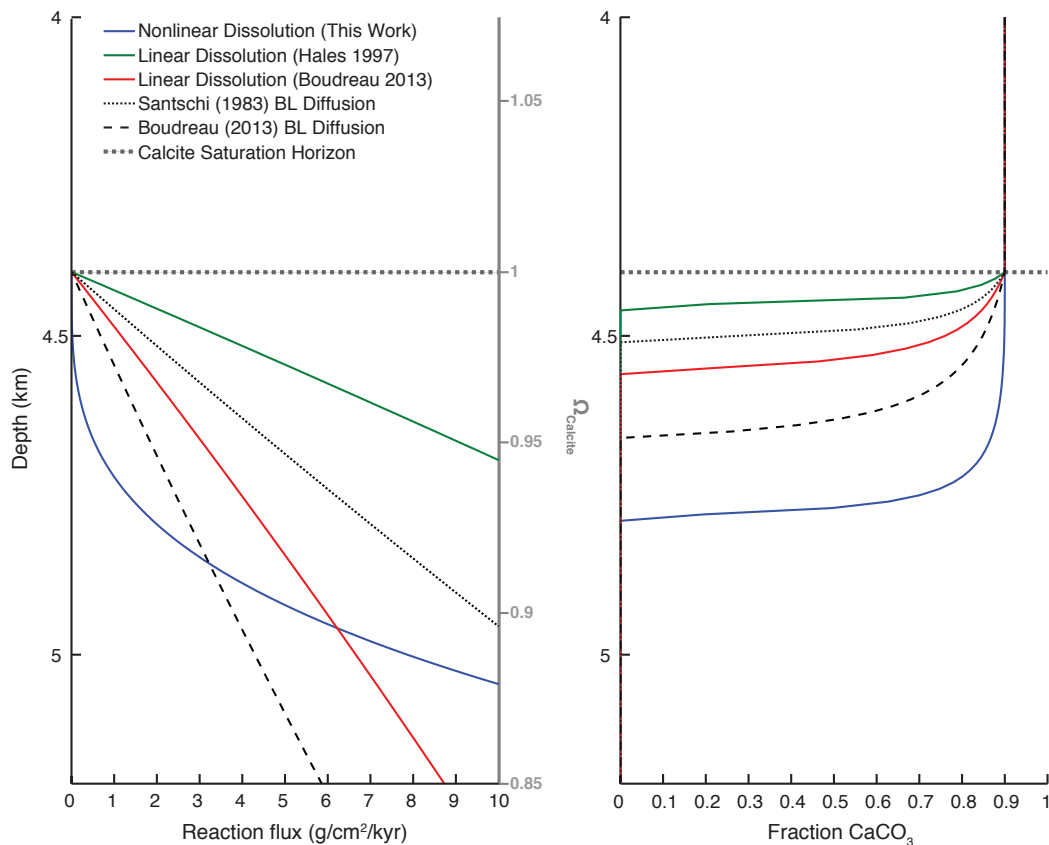


**Figure 2.10:** A simple model of the calcite lysocline (see text for the model and numbers used). **a)** dissolution fluxes paramaterized as either diffusive (dashed lines) or kinetic (solid lines). Depth is converted to $\Omega$ as in the model, and is plotted on the y-axis for reference. **b)** $\%_{CaCO_3}$ using the dissolution fluxes from **a)**.

One of the most distinctive features of ocean sediment distribution is the calcite lysocline. The lysocline is defined here as the depth range over which calcite-bearing sediments drop from $\sim 80 - 90\%$ CaCO$_3$ to $\sim 0\%$. This depth range is highly variable, and can often exceed 1 km (P E Biscaye, V Kolla, and Turekian, 1976; Venkatarathnam Kolla, Bé, and Pierre E Biscaye, 1976; Berger, 1970). The lysocline typically starts at about the calcite saturation horizon (defined as the depth

where bottom water $\Omega = 1$, but some researchers have shown that the lysocline can start above (Steven Emerson and M. Bender, 1981) or below (D. Archer, 1991; D. E. Archer, 1996) this horizon. Ever since the first measurements of %CaCO$_3$ in ocean sediments, a major question has been: What controls the shape and position of the calcite lysocline? To first order, the bottom water saturation state should exert fundamental control on the sediment composition. If calcite response to this undersaturation is fast, the sedimentary composition will be controlled by a diffusive flux between a saturated boundary layer and the undersaturated bottom water. If the response is slow, the amount of calcite in sediments will be controlled by the kinetics of dissolution itself. Kinetic control has been long-favored in the literature (J W Morse and R A Berner, 1972), but there is also recent evidence for a transport-controlled lysocline (Boudreau, Middelburg, and Meysman, 2010; Boudreau, 2013; Boudreau, Middelburg, Hofmann, et al., 2010). In his latest estimates, Boudreau, 2013 predicts lysocline thicknesses for two oceanic locations. However, his equations rely on a large diffusive boundary layer of ~ 1.2mm, and is only able to fit rather narrow lysocline thicknesses of 300-500 meters.

In order to test the influence of our current measured rates on the shape of the calcite lysocline, we constructed a simple model of %CaCO$_3$, where the fraction of calcite in the top sediment layer, $B_{\text{CaCO}_3}$ is calculated as:

$$B_{\text{CaCO}_3} = \frac{F_{rain} - F_{diss}}{F_{clay} + F_{rain} - F_{diss}}, \tag{2.7}$$

where $F_{rain}$ is the flux of calcite rain to the seafloor, $F_{diss}$ is the calcite dissolution flux, and $F_{clay}$ is the flux of non-carbonate detritus to the seafloor, all in g/cm$^2$/kyr. We tested out end-member cases of diffusive and kinetic control by applying various forms of $F_{diss}$. In the case of transport (diffusive) control:

$$F_{diss} = \beta \cdot ([CO_3^{2-}]_{btm} - [CO_3^{2-}]_{sat}) \cdot \rho_{calc} \cdot \Delta h \cdot mm_{calc}, \tag{2.8}$$

where $\beta$ is the mass transfer velocity in m/yr which relates the diffusivity of calcium and carbonate ions and the diffusive boundary layer thickness, $[CO_3^{2-}]_{btm}$ is the bottom water carbonate ion concentration which we assume to be 100 $\mu$mol/kg, and $[CO_3^{2-}]_{sat}$ is the calcite saturation value of carbonate ion, parameterized as a function of depth as in Boudreau, Middelburg, and Meysman, 2010. $\rho_{calcite} = 2.7$ g/cm$^3$ is the density of calcite, $\Delta h$ is the depth of available sediment for dissolution (here assumed to be 1 cm), and $mm_{calc}$= 100 g/mol is the molar mass of calcium carbonate. We chose to model this diffusive flux for two different boundary layer

thicknesses; one from Boudreau, 2013 ($\beta$ = 12.7 m/yr; 1.2 mm boundary layer thickness) and one from Santschi et al., 1983 (32.1 m/yr; 475 $\mu$m). The diffusive fluxes and percent calcium carbonate for these fluxes are given in Figure 2.10 a and b, respectively.

For kinetic control, the rate is parameterized as:

$$F_{diss} = [\text{CaCO}_3]_{stock} \cdot k_{diss} \cdot (1 - \Omega)^n, \qquad (2.9)$$

where $[\text{CaCO}_3]_{stock} = \frac{F_{rain}}{F_{clay}+F_{rain}} \cdot (1 - \phi) \cdot \rho_{calcite}$ is the inventory of solid calcite at the sediment-water interface. $\phi$ is the porosity, assumed to be 0.8, and $\rho_{calcite}$ is 2.7 g/cm$^3$. $k_{diss}$ in this case is in units of g/g/kyr, or kyr$^{-1}$. We compared three different rate parameterizations. First is the rate chosen by B Hales and S Emerson (1997b) that provided the best fit to Ontong-Java Plateau sediments (n = 1, $k_{diss}$ = 0.1%/day). Second is the rate constant chosen by Boudreau (2013) that provides the best linear fit to the data from Keir (1983) (60 g cm$^{-2}$ kyr$^{-1}$). Third is our rate constant data, where n=3.85 and $k_{diss}$ = 0.085 g/g/day, the best fit to our near-equilibrium 70-100 $\mu$m size fraction calcite. These dissolution fluxes and associated percent calcium carbonate curves are presented with the diffusive model results in Figure 2.10 a and b, respectively. Both transport-only fluxes produce relatively shallow lysoclines, which initiate immediately at the saturation horizon. Dissolution fluxes produce a range of behaviors, with linear rate laws producing very shallow lysoclines. Our data shows a large offset in water column depth between a drop in $B_{\text{CaCO}_3}$ and the saturation horizon.

Given the observations of %CaCO$_3$ in surface sediments, and our measured dissolution rates, there must be other factors that contribute to the shape of the lysocline. First of all, our dissolution flux crosses the transport-only flux predicted by Boudreau (2013). After this crossover at a depth of $\sim$ 4.8 km, the dissolution rate outpaces the rate of solute transport. The sediment composition would reflect this switch, and preserve more calcite than with kinetics alone, making transport the limiting term in calcite dissolution, and further deepening the lysocline.

In this simple model, we have explicitly ignored any porewater reactions taking place, such as diffusion of DIC species, sediment compaction, bioturbation, and respiration of organic matter. There is much evidence for respiration-driven dissolution in deep-sea sediments (Burke Hales, 2003; Dunne, Burke Hales, and Toggweiler, 2012; Steven Emerson and M. Bender, 1981). Respiration in sediments would drive down

the saturation state due to excess $CO_2$, which would in turn have a large effect on the dissolution rate in the case of a nonlinear rate response to undersaturation. Respiration-driven dissolution is largely ignored in the lysocline model of Boudreau, 2013. Since we have conclusively documented a nonlinear dissolution response, our results imply a potentially large role of respiration-driven dissolution, and also could allow for a switch in kinetic- to transport-controlled dynamics of the chemical lysocline.

## 2.5 Conclusions

We demonstrate here a new technique for measuring calcium carbonate dissolution rates, based on an isotopic tracer methodology. This method allows for unprecedented control on saturation state. Geometric normalization of different grain sizes aligns all data onto a single curve, although the small offset between the Aldrich and our gel-grown calcites could be due to differences is surface morphology and microstructure. The near-equilibrium dissolution rates are fit by the empirical equation:

$$\text{Rate(g/cm}^2\text{/day)} = 7.2 \pm 0.6 \cdot 10^{-4}(1 - \Omega)^{3.9 \pm 0.1}.$$

This relationship is descriptive but not informative, and implies at least two fundamental dissolution mechanisms, as well as criticality in dissolution response to undersaturation. Furthermore, our dissolution rate constants agree quite well with far-from-equilibrium dissolution rates, determined over a range of conditions and methodologies. Finally, we demonstrate for the first time agreement between our laboratory-determined dissolution rates, and those measured or extrapolated from field data. Observations of calcite sediments, paired with our rate determinations, suggest that both transport and kinetics play a role in setting $\%CaCO_3$. Respiration-driven dissolution is likely an important process as well.

*Chapter 3*

# CATALYSIS AND CHEMICAL MECHANISMS OF CALCITE DISSOLUTION IN SEAWATER

The production and dissolution of calcium carbonate minerals provide a crucial link between the marine carbon and alkalinity cycles. The ocean has absorbed about 25-30% of anthropogenic $CO_2$ emissions, dropping mean surface ocean pH since the industrial era (R A Feely, 2004). As ocean pH decreases, sedimentary carbonate minerals will dissolve to compensate for the loss of buffering capacity, eventually restoring atmospheric $p$CO$_2$ to about its pre-industrial level (D. Archer, Kheshgi, and Maier-Reimer, 1998; Ilyina and R E Zeebe, 2012). This reaction will mostly take place in the deep ocean, where the calcite saturation state $\Omega = [\text{Ca}^{2+}][\text{CO}_3^{2-}]/K'_{sp} < 1$. Most of the deep ocean is only mildly undersaturated such that pelagic dissolution is primarily a near-equilibrium phenomenon. However, attempts to quantify the relationship between calcite dissolution rate and $\Omega$ are highly variable between different studies, both in functional form and absolute value (Honjo and J Erez, 1978; Walter and J W Morse, 1985; Keir, 1980; R A Berner and J W Morse, 1974; Fukuhara et al., 2008; A. V. Subhas et al., 2015).

With the exception of very early work by R A Berner and J W Morse (1974), few studies have attempted to unpack the chemical species responsible for calcite dissolution in seawater beyond the descriptive, but not necessarily predictive, 1-$\Omega$ framework. In contrast, freshwater and dilute solution dissolution studies have made large advances in identifying key chemical species responsible for observed dissolution rates, starting from early work (L N Plummer and Wigley, 1976; Sjöberg, 1976; Sjöberg and Rickard, 1984), and culminating in a dissolution model that incorporates both aqueous species and the distribution of ion complexes on the calcite surface (Van Cappellen, Charlet, and Stumm, 1993; Arakaki and Mucci, 1995). These groups recover an essentially linear relationship between dissolution rate and saturation state.

Calcite dissolution rates in circumneutral pH conditions appear largely independent of solution pH (Cubillas et al., 2005), but instead respond nonlinearly to mineral surface processes (H Henry Teng, 2004; Rolf S Arvidson, Cornelius Fischer, and Lüttge, 2015; Rolf S Arvidson and Lüttge, 2010; J. Xu, Fan, and H Henry Teng,

2012). Dissolution rate changes are typically associated with a large increase in etch pit nucleation below some critical saturation state, $\Omega_{critical}$ (P M Dove, Han, and J J De Yoreo, 2005; Patricia M Dove et al., 2008). Even in freshwater, however, there is little understanding of which specific chemical reactions are ultimately rate-limiting in the propagation of surface features such as step edge retreat and etch pit formation and growth (J. Xu, Fan, and H Henry Teng, 2012).

In this paper, we use a novel determination of calcite dissolution kinetics to unpack their relationship to seawater chemistry (Methods and A. V. Subhas et al., 2015). In short, $^{13}$C-labeled calcites are placed in undersaturated seawater in a closed system. The evolving seawater $\delta^{13}$C traces mass transfer from solid to solution. Dissolution will add $^{13}$C to solution; precipitation will add seawater carbon (~99% $^{12}$C) to the solid surface. We first demonstrate precipitation in undersaturated solutions using secondary ion mass spectrometry (SIMS) analysis of the calcite solid. Next, we show that a box model of calcite dissolution and precipitation provides information about gross precipitation and dissolution fluxes at the calcite surface near equilibrium. The model predicts a decrease in relative importance of precipitation below $\Omega = 0.7$. Finally, we show that the enzyme Carbonic Anhydrase (CA) catalyzes the dissolution of calcite in seawater. CA is a cosmopolitan enzyme known for its rapid equilibration of carbonic acid and aqueous $CO_2$. A mechanism of dissolution through defect-assisted etch pit nucleation (P M Dove, Han, and J J De Yoreo, 2005) is proposed, which also demonstrates a distinct change in reaction energetics at $\Omega = 0.7$. Near equilibrium, CA reduces the free energy barrier to dissolution. At high [CA], this energy barrier is similar to that recovered from freshwater dissolution experiments.

### 3.1 Measuring dissolution-precipitation in the calcite solid

The net rate of $CaCO_3$ dissolution is the result of the balance between dissolution and precipitation reactions near equilibrium. Our experimental system has a strong isotopic gradient between seawater and the $^{13}$C-labeled mineral, such that the processes of precipication and dissolution will each leave distinct isotopic signatures on the calcite surface. Seawater $^{12}$C will precipitate and increase the $^{12}$C/$^{13}$C ratio of the reactive calcite surface. Dissolution will expose pure $^{13}$C-carbonate such that the surface composition approaches 100 % $^{13}$C as dissolution outpaces precipitation at lower saturation state. The same is true for cation mass balance: the calcite surface Mg/Ca ratio will change as a function of the amount of precipitated calcite from seawater with Mg/Ca = 5 and the distribution coefficient of $Mg^{2+}$ into calcite (T Oomori et al., 1987; Mucci and J W Morse, 1984). A change in Mg/Ca should

also be measurable since the initial calcite mineral contains only trace $Mg^{2+}$.

We measured the near-equilibrium balance of dissolution and precipitation by re-acting several $^{13}$C-labeled, Mg-free calcites for 48 hours in saturated and slightly undersaturated seawater. Using a secondary ion mass spectrometer (SIMS), we then measured carbon isotope and Mg/Ca profiles through this reacted surface and compared them to an unreacted control (Figure 3.1 and SI Appendix, Figure S1). The unreacted control experiments (dashed yellow) show some enrichment of $^{12}$C due to surface contamination. The supersaturated experiments (dotted blue), which will have precipitated calcite, show persistent $^{12}$C and Mg/Ca enrichment above the unreacted control. The undersaturated experiments (solid red) start at a surface composition similar to precipitated calcite, indicating that $^{12}$C has been incorporated even in undersaturated conditions. Undersaturated profiles then transition down to the composition of the unreacted control, matching the unreacted pure $^{13}$C-calcite composition. The inset in Figure 3.1 shows that all $^{12}$C/$^{13}$C compositions converge within error at about 130 nanometers deep, indicating that underlying $^{13}$C-calcium carbonate has been reached. In undersaturated experiments where dissolution is occurring, the $^{12}$C/$^{13}$C composition reaches that of the control at a depth of about 4 nanometers.

The shape of these SIMS profiles is influenced by the incorporation of $^{12}$C from precipitation, and also by the mixing of surface signals down into the calcite interior during secondary ion sputtering and excavation. To more quantitatively measure the total number of moles of seawater C and $Mg^{2+}$ incorporated into our calcites, we integrated each of the curves in Figure 3.1 and SI Appendix Figure S1 over the 140nm SIMS profile (SI Appendix equations S1-S2 and Table S2). This integral can be converted to a "reactive thickness" and compared to previous estimates. Briefly, the measured $^{12}$C/$^{13}$C mole fraction measured at each SIMS analysis cycle was converted to a number of moles of $^{12}$C. All cycles were then summed over the entire profile to estimate the total number of moles of $^{12}$C incorporated into our calcites over the 48-hour experimental period. To remove the influence of surface contamination, the control was subtracted from both the supersaturated and undersaturated experiments. The total number of moles was then converted into an effective thickness of $^{12}$C present in the supersaturated and undersaturated experiments (Table S2). This calculation estimates that 1.0-3.3 nm of $^{12}$C-calcite was incorporated in undersaturated conditions. Mg/Ca measurements also confirm the presence of new $Mg^{2+}$ in the solid (Table S2). We also found that 3.1-9.3
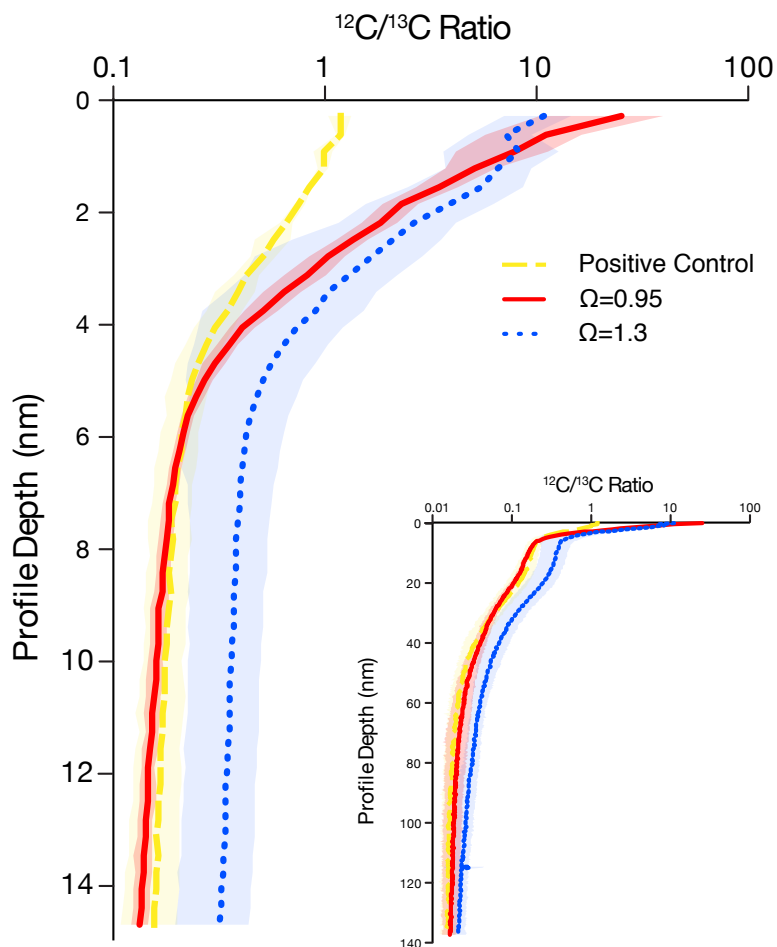
**Figure 3.1:** Vertical logarithmic $^{12}$C/$^{13}$C SIMS profiles of reacted calcite grains under three different experimental conditions. Solid lines are the mean isotope ratio of all profiles collected under each experimental condition. Shaded areas are the standard deviation of all profiles collected under each experimental condition. In the first 15 nm of these profiles, $\Omega$=0.95 profiles (solid red) transition from a supersaturated (dotted blue) composition to an unreacted (dashed yellow) composition. This $^{12}$C enrichment demonstrates that seawater carbon has incorporated into the calcite solid in undersaturated conditions. The inset shows the SIMS entire profile, with experiment ratios converging with the unreacted control run at depth. All curves are depth-corrected for the thickness of gold coating.

nm of $^{12}$C-calcite was added in supersaturated experiments, in agreement with previous precipitation experiments (Zhong and Mucci, 1989 and Figure S3). One calcite monolayer is about 0.5 nm, suggesting that even under conditions of net dissolution, seawater can react with 2-6 monolayers of calcite via gross dissolution and precipitation reactions.

Most calcite dissolution in the deep sea happens near equilibrium, where we have documented a large influence of dissolution and precipitation reactions on the com-

position of the calcite surface. Calcites in sediments, which contain primary environmental information in their oxygen isotope and/or Mg/Ca ratios, will experience similar dissolution-precipitation reactions in the deep ocean (Schrag, D J DePaolo, and Richter, 1995; Gorski and Fantle, 2017; Richter and D J DePaolo, 1987). These reactions will impart secondary porewater isotopic and chemical information, and our experiments suggest they can potentially do so deeply into the calcite surface. Future work will target understanding the extent to which these processes modify deep-sea sedimentary calcites, and should prove useful in unmixing the secondary and primary environmental signals that these calcites record.

## 3.2 Measuring and modeling dissolution-precipitation in the solution
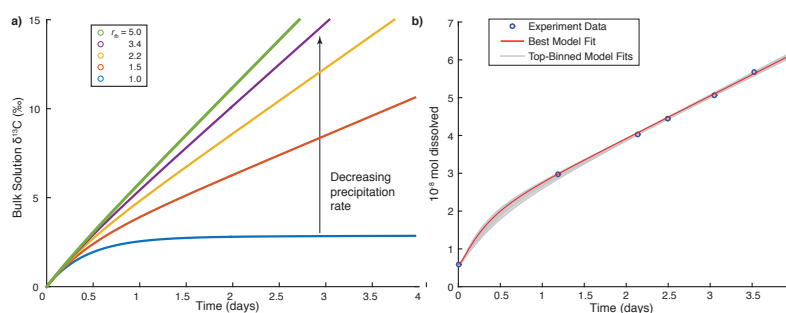


**Figure 3.2:** Results of the dissolution-precipitation model (Figure S3 and Equations S2-4). **a)** Model output of bulk solution $\delta^{13}$C under our experimental conditions, assuming a reactive calcite layer thickness of 5 monolayers. Decreasing the precipitation rate (increasing $r_f b$; see text for details) increases the net dissolution rate and decreases curvature. **b)** Model-data comparison for a dissolution experiment conducted at $\Omega = 0.87$. The red curve is the absolute best-fit $k_{diss}$ and $r_{fb}$ over the entire parameter search space; the grey curves are the next 15 best fits.

In addition to measuring dissolution-precipitation reactions in the solid, we measured the appearance of $^{13}$C in seawater dissolved inorganic carbon (DIC) using a Picarro cavity ringdown spectrometer (A. V. Subhas et al., 2015). $^{13}$C-calcite dissolution produces a straight line of seawater $\delta^{13}$C over time. The slope of this line is a direct measure of the net dissolution rate (e.g. rates in A. V. Subhas et al., 2015). However, due to the distinct isotopic boundary conditions for dissolution and precipitation, the ratio of *gross* dissolution to *gross* precipitation produces initial $\delta^{13}$C curvature over time (Figure 3.2). Because an experiment is conducted at a fixed saturation state and mineral surface area, curvature in Figure 3.2b does not represent a change in bulk solution chemistry, but instead reflects the instantaneous balance of fixed dissolution and precipitation rates at the mineral surface. Curves straighten out when the calcite surface comes into steady state with respect to dis-

solution and precipitation fluxes. Using the observation of precipitated calcite even in undersaturated conditions, we developed a box model to quantify the impact of dissolution and precipitation reactions on solution $\delta^{13}C$ versus time (SI Appendix and Figure S4 for model description).

All experimental data with sufficient data density from A. V. Subhas et al., 2015 were fit with output from the box model. We modeled a suite of dissolution rate curves over a range of gross dissolution ($R_f$) and precipitation rates ($R_b$). The ratio of these rates ($r_{fb} = R_f/R_b$), and their absolute magnitude, sets the amount of initial curvature. For example, when $r_{fb}=1$, the precipitation rate is equal to the dissolution rate and calcite is in equilibrium with solution (the blue line in Figure 3.2a). When $r_{fb}=5$, the dissolution rate is five times faster than the precipitation rate (the green line in Figure 3.2a). The size and shape of curvature observed in Figure 3.2 is also set by the volume of calcite that is allowed to react with seawater. Consistent with our SIMS results, the model gives a better fit to the data if multiple monolayers of calcite are reacting with seawater, and a best fit with 5 monolayers (SI Appendix Figure S7). An example data fit using model output is shown in Figure 3.2b and S6; details of the fitting routine are in the SI Appendix. The fitting routine output is a range of best-fit values of dissolution and precipitation rate, along with statistics on the goodness of fit. Ranges of acceptable dissolution and precipitation rates were calculated from the acceptable model fits, shown as the spread of gray curves which adequately fit the dataset in Figure 3.2b.

Dissolution studies in seawater have typically related net dissolution rate with undersaturation (1-$\Omega$; (R A Berner and J W Morse, 1974; Keir, 1980; Fukuhara et al., 2008; Honjo and J Erez, 1978; Steven Emerson and M. Bender, 1981; Boudreau, 2013)). This framework is historically linked to a derivation of net dissolution rate that assumes linear kinetics:

$$R_{diss} = R_f - R_b = k_f\{CaCO_3\} - k_b[Ca^{2+}][CO_3^{2-}], \qquad (3.1)$$

where $R$ is a rate and $k_f$ and $k_b$ are the specific dissolution and precipitation rate constants, respectively. This expression assumes that the gross dissolution rate $k_f\{CaCO_3\}$ is completely independent of solution chemistry, i.e. the activity of the solid is 1. All sensitivity of net dissolution to calcium and/or carbonate ion concentration is due to precipitation alone. Such dissolution behavior has been demonstrated in freshwater (e.g. Arakaki and Mucci, 1995), but has never been investigated directly in seawater. Model-fit gross dissolution and precipitation rates
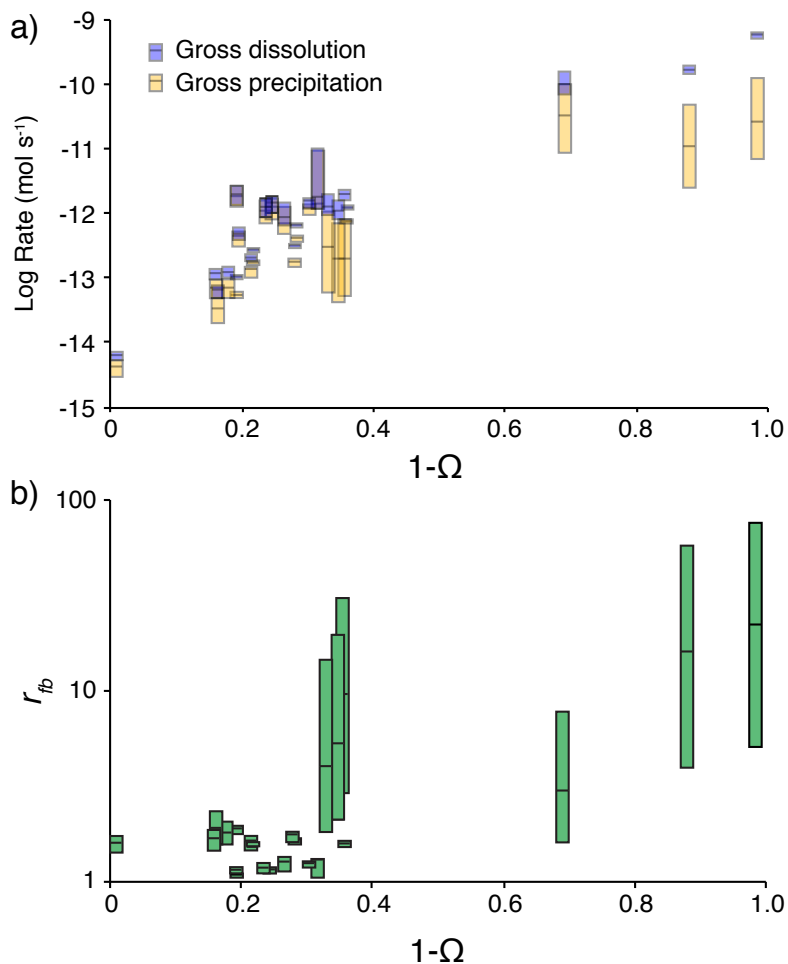
**Figure 3.3:** Results of the dissolution-precipitation model. **a)** Each net dissolution rate is represented by a pair of blue (dissolution) and yellow (precipitation) gross rates. Lines in the boxes are the median of the best fits of $R_f$; box boundaries are the 25th and 75th percentile values for $R_f$ that best fit the experimental moles dissolved versus time data. Gross precipitation rates $R_b$ are the median $R_f$ divided by the median $r_{fb}(= R_f/R_b)$ of the best fits to the experimental data; box boundaries are the 25th and 75th percentile values for $R_b$. Overall, dissolution and precipitation rates are very close to each other, leading to a net dissolution rate that is the difference between two large gross fluxes. The precipitation rate variance increases (larger box size) after $1 - \Omega \sim 0.3$. **b)** Box plot of the best-fitting $r_{fb}$ values for the dissolution data. A significant jump in $r_{fb}$ is evident after $1 - \Omega \sim 0.3$ in both the absolute value of $r_{fb}$ and the range of acceptable values.

for our seawater experiments are shown in Figure 3.3. Our data cannot be fit using a constant dissolution rate and a decreasing precipitation rate, as predicted by the linear model of Eq.(3.1). Instead, gross dissolution rates show a strong, nonlinear dependence on saturation state, changing by almost 4 orders of magnitude over the entire range of saturation states measured here. This nonlinearity implies that either the dissolution rate constant or the activity of the solid in Eq.(3.1)

changes as a function of saturation state. There is also significant information in the response of precipitation rate to saturation state. As undersaturation increases, the range of acceptable precipitation rates grows much larger than the range of acceptable dissolution rates, as shown by the size of the boxes in Figure 3.3a. The linear dissolution framework (Eq.(3.1)) predicts a continuous decline in precipitation as function of $1 - \Omega$. Our model results instead show an abrupt change in the balance of precipitation to dissolution at $\Omega = 0.7$. The ratio of gross dissolution to precipitation ($r_{fb} = R_f/R_b$) significantly increases below about $\Omega = 0.7$, suggesting a decreased contribution of precipitation to the net dissolution rate farther from equilibrium (Figure 3.3b). Because precipitation contributes less to the net rate farther from equilibrium, a larger range of $r_{fb}$ values – and thus precipitation rates – give acceptable fits to the experimental data. Such an abrupt shift in the balance of precipitation to dissolution helps to explain the strongly nonlinear dissolution rates observed in many seawater calcite dissolution studies (e.g. Keir, 1980; R A Berner and J W Morse, 1974). It also implies a distinct change in dissolution mechanism.

## 3.3 Catalysis via carbonic anhydrase and a link between solution chemistry and surface features

The nonlinearity of a gross dissolution flux brings into question the chemical reactions responsible for calcite dissolution in seawater. In dilute solution, three calcite dissolution mechanisms are proposed to operate at the calcite surface (L N Plummer and Wigley, 1976; Arakaki and Mucci, 1995):

$$CaCO_3 + H_2O \rightleftharpoons Ca^{2+} + CO_3^{2-} + H_2O, \qquad (3.2a)$$

$$CaCO_3 + H_2CO_3 \rightleftharpoons Ca^{2+} + 2HCO_3^-, \qquad (3.2b)$$

$$CaCO_3 + H^+ \rightleftharpoons Ca^{2+} + HCO_3^-. \qquad (3.2c)$$
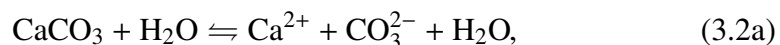
Water-catalyzed dissolution is predicted to be independent of solution chemistry (the activity of the solid is always assumed to be 1). $CO_2$ itself is thought to be relatively unreactive with $CaCO_3$, but $H_2CO_3$, produced through the hydration of $CO_2$, is an uncharged species that acts as a proton donor to promote dissolution (Arakaki and Mucci, 1995; W Dreybrodt et al., 1996; L N Plummer, Wigley, and Parkhurst, 1978). At low pH ($< 5$), calcite dissolution depends almost exclusively on the transport of hydrogen ion to the mineral surface; Eq.(3.2c) (Arakaki and Mucci, 1995; L N Plummer, Wigley, and Parkhurst, 1978; Sjöberg and Rickard, 1984). In freshwater, the reactions in Eq.(3.2) have been tied to the interaction of specific species with calcium and carbonate ion sites on the calcite surface (Arakaki
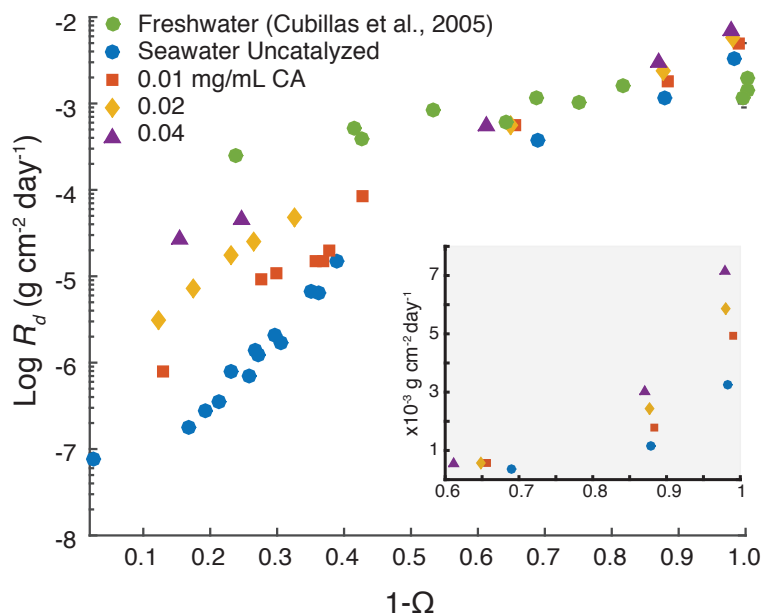
**Figure 3.4:** The relationship between saturation state, carbonic anhydrase concentration, and calcite dissolution rate in seawater. Semilog plot of dissolution rate versus undersaturation $(1-\Omega)$. The linear-linear inset at bottom right shows the far-from-equilibrium dissolution rate increase as a function of carbonic anhydrase. The x-axis $(1-\Omega)$ is the same as in the main figure; the y axis (dissolution rate) is in units of $10^{-3}$ g cm$^{-2}$ day$^{-1}$. For clarity, the inset does not show freshwater data.

and Mucci, 1995).

There is increasing evidence that Carbonic Anhydrase (CA), an enzyme which catalyzes the equilibration of $CO_2$ and $H_2CO_3$, can enhance the dissolution rate of calcium carbonate in karst systems and their analogs (Zaihua Liu, Yuan, and Wolfgang Dreybrodt, 2005; Zaihua, 2001; Thorley et al., 2014; Xie and Wu, 2013; W. Li et al., 2008). These studies used an open-system dissolution reactor, in which $CO_2$ gas was bubbled into an experimental chamber. There are two effects of CA in such a system. The first is rapidly equilibrating the bubbled gas and the solution $p$CO$_2$, resulting in an experimental system limited by the kinetics of gas exchange and with a poorly constrained saturation state, as documented by Arakaki and Mucci (1995). Secondly, CA could enhance chemical mechanisms acting at the calcite-water interface. Our results are from closed-system dissolution experiments that have no headspace and thus isolate this second chemical mechanism of CA on calcite dissolution (A. V. Subhas et al. (2015) and Methods).

Mass- and surface area-normalized dissolution rates from many $^{13}$C-dissolution experiments are plotted as a function of undersaturation $(1-\Omega)$ and CA concentration

in Figure 3.4. Calcite dissolution rates in the presence of CA are always enhanced over the uncatalyzed rates. An experiment performed in the presence of bovine serum albumin (BSA) showed no significant enhancement of dissolution rate (Figure S9), demonstrating that proteinaceous dissolved organic matter has no significant effect on dissolution rate.

Increasing [CA] enhances dissolution at all saturation states, and CA has the largest effect close to equilibrium. Far-from-equilibrium enhancement of dissolution rate in the inset of Figure 3.4 shows similar rate enhancements to values obtained in freshwater experiments (Zaihua Liu, Yuan, and Wolfgang Dreybrodt, 2005). This result is surprising since many studies in freshwater have either dismissed carbonic acid as a major proton donor (L N Plummer, Wigley, and Parkhurst, 1978; R A Berner and J W Morse, 1974), or have not found catalysis via CA in freshwater at low $p$CO$_2$ (Zaihua Liu, Yuan, and Wolfgang Dreybrodt, 2005). Our documented rate increase of ~2.5 orders of magnitude at [CA] = 0.04 mg/mL and $\Omega \sim 0.85$ suggests that, in contrast to freshwater, carbonic acid is a major proton donor close to equilibrium in seawater.

The strong nonlinearities in our dissolution rate data cannot be explained using the simple dissolution framework of Eq.(3.1). Furthermore, the addition of CA, while it increases the dissolution rate of calcite, does not produce a linear response of dissolution rate to saturation state. We were thus compelled to apply a model of dissolution to our rate data that incorporates features of the calcite solid into the control of dissolution rates P M Dove, Han, and J J De Yoreo, 2005; Patricia M Dove et al., 2008; H Henry Teng, 2004; Lasaga and Luttge, 2001. For many solid-solution systems, a description of solution chemistry alone is indeed insufficient to predict crystal growth or dissolution kinetics. In addition to saturation state and its contribution to free energy, the crystal growth theory of W. K. Burton, Cabrera, and Frank, 1951 incorporated energetics associated with the crystal itself, such as the free energy of crystal edges, faces, and lattice defects in contact with the solution. Recently, several studies have successfully mapped this theory of crystal growth and precipitation onto the dissolution of quartz, feldspar, and calcite P M Dove, Han, and J J De Yoreo, 2005; Lasaga and Luttge, 2001. In addition to the effects of saturation state, this model relates net dissolution rate ($R_{diss}$) to several physical-chemical parameters ($h$, $\omega$, $C_e$, $a$; see SI Appendix), as well as the dissolution velocity $\beta$ at defects, surface defect density $n_s$, and the interfacial energy barrier at nucleation sites $\alpha$ P M Dove, Han, and J J De Yoreo, 2005; Sangwal, 1987:

$$\ln\left(\frac{|R_d|}{(1-\Omega)^{2/3}|\sigma|^{1/6}}\right) = \ln(h\beta C_e(\omega^2 hn_s a)^{1/3}) - \frac{\pi\alpha^2\omega h}{3(k_B T)^2}\left|\frac{1}{\sigma}\right|. \qquad (3.3)$$

Saturation state control is found in the $\Omega$ and $\sigma = ln(\Omega)$ terms. $k_B T$ is the Boltzmann constant multiplied by temperature in K; i.e. the system's thermal energy.
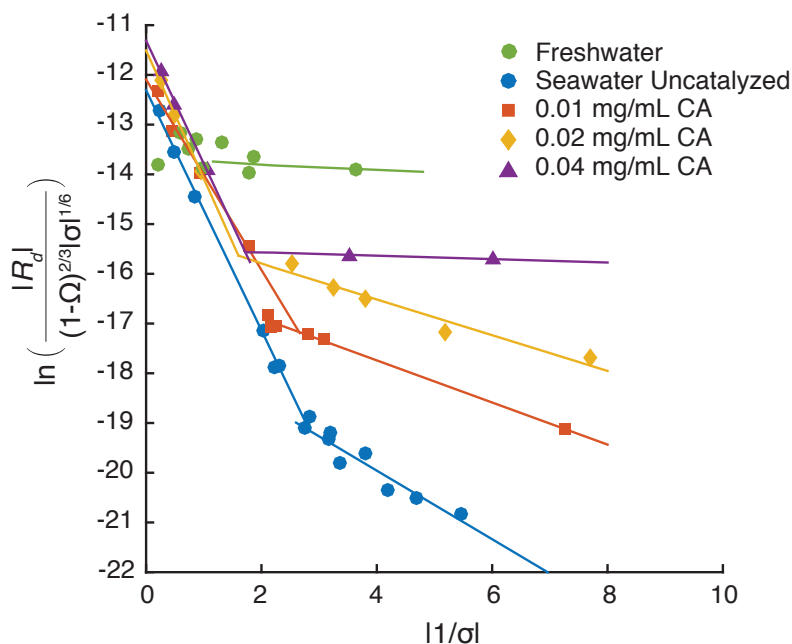


**Figure 3.5:** Dissolution rate data from Figure 3.4 plotted in the framework of Eq.(3.3). To the right of the kink (closer to equilibrium), note the decreasing slope with increasing [CA]. Freshwater data is included for comparison. Linear fits to the data in this framework are presented in Table 3.1, along with an estimate of the interfactial surface energy $\alpha$. The kink in this data represents a change in dissolution mechanism from defect-only nucleated dissolution near equilibrium to homogeneous nucleation far from equilibrium at a kink point around $\Omega = 0.65 - 0.7$.

Catalyzed and uncatalyzed dissolution rate data is plotted as the left hand side of Eq.(3.3) versus $|\frac{1}{\sigma}|$ in Figure 3.5, where $|\frac{1}{\sigma}| = 0$ is complete undersaturation. The slope of a straight line in this space gives the interfacial energy barrier $\alpha$; the intercept gives information about the kinetic rate constant $\beta$ and density of etch pit nucleation sites $n_s$. As seen in several other mineral dissolution studies (P M Dove, Han, and J J De Yoreo, 2005; Patricia M Dove et al., 2008; Malkin, Chernov, and Alexeev, 1989), our uncatalyzed data plot as two straight lines in this space with a "kink" at $|\frac{1}{\sigma}| = 3$, which corresponds to $\Omega = 0.71$. This transition in slope denotes two distinct regimes of dissolution, which has been interpreted previously as a transition from defect-assisted nucleation of etch pits near equilibrium to homogeneous etch pit nucleation farther from equilibrium (P M Dove, Han, and J J De Yoreo, 2005). It could also

be interpreted as a transition from the opening of hollow cores to the propagation of stepwaves in the framework of Lasaga and Luttge, 2001. This transition to homogeneous nucleation of etch pits is also concurrent with the saturation state at which precipitation becomes unimportant to the overall dissolution rate in our $\delta^{13}$C tracer data (Figure 3.3).

Near equilibrium (to the right in Figure 3.5), slopes decrease with increasing [CA] (Table 3.1). The slope of this line is diagnostic of the rate-limiting step in calcite dissolution near equilibrium. A decrease in the free energy barrier as a function of [CA] suggests that a greater availiability of carbonic acid effectively decreases the energetic barrier to etch pit nucleation, by increasing the concentration of carbonic acid at defects on the calcite surface. Increasing [CA] also increases the intercept (Table 3.1), changing either the density of nucleation sites ($n_s$) or the rate of step retreat ($\beta$; Eq.(3.3)). Adding [CA] does not seem to significantly change the transition between defect-assisted and homogeneous nucleation: the kink point in Figure 3.5 does not move significantly given the density of our data. The transition between these two regimes may be controlled instead by calcite saturation state (i.e. [$CO_3^{2-}$]). Since the kinetic interconversion of $CO_2$ and $H_2CO_3$ does not change the thermodynamic saturation state $\Omega$, one might not expect this kink point to change significantly due to enhanced hydration kinetics. Far from equilibrium (to the left in Figure 3.5), slopes are insensitive to [CA], indicating that interface energies at etch pit nucleation sites are insensitive to the concentration of $H_2CO_3$. Instead, transport of $H_2CO_3$ simply limits the delivery of protons to the mineral surface, limiting the overall propagation of etch pits once formed (i.e. modulating $\beta$ or $n_s$ in (3.3)).

A transition to homogeneous etch pit nucleation is also consistent with the mechanism shift diagnosed using relative dissolution and precipitation fluxes above. It is possible that precipitation limits net dissolution near equilibrium by occupying sites that would otherwise dissolve. This constraint is freed when etch pits begin to form everywhere om the solid surface. Instead of being limited to defects, dissolution is now allowed to proceed everywhere on the mineral surface, which erases the influence of precipitation reactions on the isotopic composition of the solid, and of the time-evolving solution $\delta^{13}$C.

## 3.4 Implications for the natural environment

The role of carbonic acid and CA in calcite dissolution may influence a number of outstanding problems in interface science, geochemistry, and chemical oceanog-

**Table 3.1:** Fits for dissolution rate data shown in Figure 3.5 in the framework of Eq.(3.3). Near-equilibrium fit data from $1/\sigma > 3$; far-from equilibrium fits are from $0 < 1/\sigma < 3$. Freshwater data taken from Cubillas et al., 2005. Only a single fit was performed on freshwater data due to the lack of kink.

| Experiment | Near Eq. | | | Far from Eq. | | |
|---|---|---|---|---|---|---|
| | Intercept | Slope | $\alpha$ (mJ m$^{-2}$) | Intercept | Slope | $\alpha$ (mJ m$^{-2}$) |
| SW Uncat. | -17.2 | -0.69 | 15 | -12.3 | -2.4 | 29 |
| 0.01 mg/mL CA | -16.0 | -0.42 | 12 | -12.1 | -1.9 | 26 |
| 0.02 mg/mL CA | -15.1 | -0.35 | 11 | -11.5 | -2.6 | 30 |
| 0.04 mg/mL CA | -15.5 | -0.03 | 3 | -11.3 | -2.5 | 29 |
| Freshwater Cubillas et al., 2005 | -13.7 | -0.05 | 4 | | | |

raphy. Dissolution rates measured in the Pacific ocean are highest directly at the saturation horizon, where saturation state crosses from >1 to <1 (R A Feely et al., 2002). This increased alkalinity signal has been attributed to ocean circulation transport of sediment-produced alkalinity Friis et al., 2006 or to excess water-column dissolution driven by organic matter respiration (R A Feely et al., 2002). Organic matter respiration locally increases the concentration of $CO_{2(aq)}$. If carbonic anhydrase is also expressed at the site of organic matter remineralization (Elzenga, Prins, and Stefels, 2000), then dissolution rates will be enhanced above those just driven by saturation state changes alone. Ocean acidification is leading to higher concentrations of carbonic acid (lower pH) in seawater. The direct role of carbonic acid in the kinetics of dissolution implies that minerals could be much more sensitive to ocean acidification than previously thought, since most of the ocean is close to $\Omega = 1$. Furthermore, it emphasizes the need to focus not only on water column carbonate ion concentrations, but also on carbonic acid concentrations and gradients that can influence the reactivity of carbonates in marine settings.

CA is also located at the site of calcification in many coral species (Tambutte et al., 2007; Moya et al., 2008). Several studies have also documented large diurnal variations in net calcification, to the point where some reef systems switch from net precipitating to net dissolving between day and night (Andreas J Andersson and Gledhill, 2013; Yates and Halley, 2006; J. Silverman, Lazar, and Jonathan Erez, 2007). These large swings in net calcification are thought to be mainly due to respiration-driven dissolution, both in corals themselves, and also in reef sediments (Cyronak, Santos, and Eyre, 2013; Kleypas, Anthony, and Gattuso, 2011). The presence of CA at the site of coral calcification, in reef sediments, and in reef seawater, could enhance this respiration-driven dissolution at night, providing one mechanism for these large and rapid diurnal dissolution signals seen in reef systems.

## 3.5 Conclusion

In general, calcites react much more slowly and with less predictability in seawater than freshwater, a problem that has plagued marine chemists for decades. Furthermore, calcite dissolution has been shown repeatedly to respond nonlinearly to saturation state, implying the presence of multiple dissolution mechanisms. We show here that this strongly nonlinear dissolution behavior in seawater is due to the combined effects of solution chemistry and geometric constraints on the propagation of dissolution features on the solid surface. Gross precipitation and dissolution fluxes influence the incorporation of both cation and anion tracers into the calcite solid. Treatment of bulk rate data using our box model demonstrate a change in the balance of dissolution and precipitation at $\Omega = 0.7$. In spite of the chemical complexities that arise in seawater, our results suggest that carbonic acid availability is key, such that increasing its formation using CA drastically increases calcite dissolution near equilibrium. This reaction pathway appears to be rate-limiting in seawater near equilibrium. Incorporation of geometric constraints on dissolution rates suggest that the balance of precipitation and dissolution reactions changes fundamentally once etch pits freely nucleate and propagate across the calcite surface. These findings have implications not only for the reactivity differences of calcite between freshwater and seawater, but also for how calcite dissolves in natural environments in the presence of increased $CO_2$ and carbonic anhydrase.

## 3.6 Methods and Appendix

**Calculating a reactive layer thickness using secondary ion mass spectrometry (SIMS)**

**Data Collection**

Six to eight large (300x300 $\mu$m) $^{13}$C-labeled calcite grains were embedded in 1-inch epoxy discs. Discs were then polished to 0.25 $\mu$m and reacted for 48 hours in an experimental setup similar to the dissolution experiments described in the Methods section and in A. V. Subhas et al. (2015). The alkalinity contribution of the epoxy resin to alkalinity over the course of the 48-hour experiment was minimal (at most a 4 $\mu$eq/kg increase). Omegas for the supersaturated and undersaturated experiments were 1.32±0.03 and 0.96±0.02. After reaction, discs were rinsed thoroughly with methanol and air-dried for 30 minutes before covering and storing in the dark. Methanol was used to avoid further reaction with the surface of the calcites, and for its low vapor pressure (thus low potential for carbon contamination during SIMS analyses).

SIMS profiles were collected on a Cameca 7f SIMS instrument. Carbon isotope ratios were collected in positive ion mode using a cesium beam. Mg/Ca ratios were collected as $^{24}$Mg/$^{40}$Ca in negative ion mode using an oxygen beam. A correction factor of 1.23 was applied to collected Mg/Ca ratios to account for the relative natural abundances of these isotopes. Isotope fractionation factors for both carbon and Mg/Ca incorporation into calcite were ignored as they are on the order of a permil relative and thus insignificant at our level of precision. Pertinent tuning parameters can be found in Table 3.2. Before measuring isotopic profiles, the epoxy discs were sputter-coated with 20 nm gold to ensure surface conductivity. Coated discs were then loaded into the sample evacuation chamber for ~30 hours to degas the epoxy. Dynamic transfer optics setting (DTOS) was turned off to minimize edge effects on the profile ion beam.

| Profile Type | $^{12}$C/$^{13}$C | Mg/Ca |
|---|---|---|
| Beam type | Cesium | Oxygen |
| Sample HV | -5 kV | -8.5 kV |
| Aperture | 300 $\mu$m | 300 $\mu$m |
| Raster size | 50x50 $\mu$m | 50x50 $\mu$m |
| Beam current | 0.5 nA | 3 nA |
| Incidence Angle | 24.5° | 22.5° |
| Mass Resolution $\Delta m/m$ | 3,000 | 2,000 |

**Table 3.2:** Pertinent information for SIMS profile analysis on the CAMECA 7f instrument.

Profiles were collected on at least three different grains, with at least two different spots on each grain for a total of at least six total analyses per experiment. Profiles on unreacted grains were collected in the same way without reaction in seawater. SIMS profiles in the main text show carbon isotope profiles for each epoxy disc. Solid lines are the mean of all profiles, and shaded regions depict the standard deviation of all profiles collected under each experimental condition. Proflies for Mg/Ca are shown in Figure 3.7; profiles of carbon isotope ratios are shown in Fig.1 in the main text. Carbon isotope profiles are generally cleaner and show greater separation between supersaturated and undersaturated experiments. Mg/Ca profiles are noisier, and there is less distinction between the supersaturated and undersaturated experiments. This difference can be explained by two mechanisms. First, fewer counts of Mg than Carbon-13 led to a greater relative error in each cycle, calculated using Poisson statistics. Especially deeper in the profile, this counting error manifests as noisy profiles. Second, cesium and oxygen ion beams have different properties and thus mixing dynamics during the sputtering process.

The oxygen beam was more energetic and produced rougher pits compared to the cesium beam (Figure 3.6).
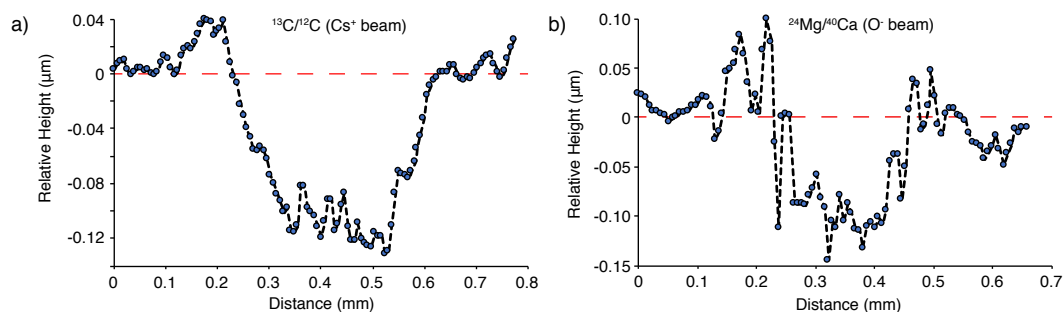


**Figure 3.6:** Example of SIMS analysis pits measured on a profilometer for the **a)** cesium beam and **b)** oxygen beam. Pits are different profiles measured on the same calcite grain. Profiles have been smoothed using a 3-point moving average for clarity, are are plotted relative to an arbitrarily designed zero height. Note the increased roughness in the oxygen profile relative to cesium.

Plots of SIMS profiles were corrected for the thickness of gold, which was burned through in about twelve cycles for C isotopes and seven cycles for Mg/Ca. The appearance of $CaCO_3$ underlying the gold coating was diagnosed by an increase in the raw counts of C and Ca ions. In order to convert mass spectrometer cycles into vertical depth, the pit depths of all profiles were measured using a profilometer, and applied as a mean value to all profiles. This mean profile depth was used to convert the number of SIMS analysis cycles to depth, corrected for the thickness of the gold coating. Examples of pit geometries are shown in Figure 3.6. Pits were in general shallower and rougher in topography for the oxygen beam (Mg/Ca) than the cesium beam (C isotope) profiles. This difference in profile shape helps to explain the different profile shapes seen between Figure 1 in the main text and Figure 3.7. Poorer resolution in the depth direction, and a more energetic oxygen beam, lead to poorer distinction between magnesium signatures in the supersaturated and undersaturated experiments in Figure 3.7.

**Analysis and data reduction**

Because SIMS sputtering is an energetic process, profiles shown in Figure 1 and 3.7 represent mixing curves, where excavated calcite is continually mixed down into the solid during the sputtering process. The number of moles in the reactive calcite layer was estimated using both cation and anion mass balances by integrating the amount of $^{12}C$ and Mg throughout the profile. Both carbon isotope and Mg/Ca intensity ratios were converted to intensity fractions for each ratio cycle, and multiplied by
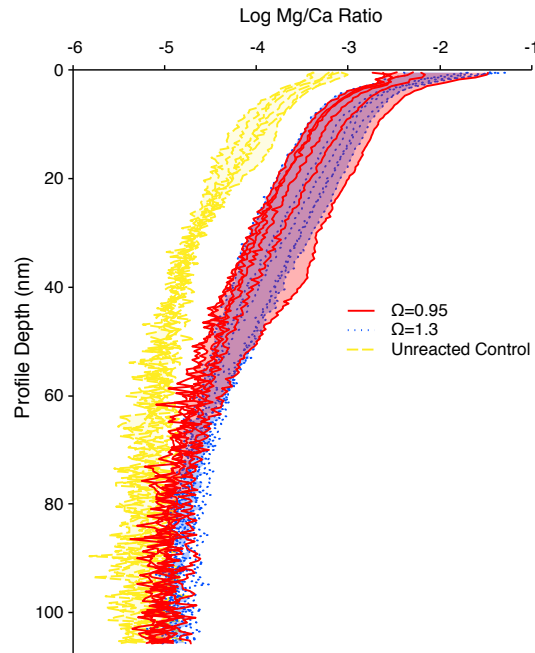
**Figure 3.7:** SIMS Mg/Ca profiles for the same experimental conditions as the main text. Ratios were collected as $^{40}\text{Mg}^{2+}/^{24}\text{Ca}^{2+}$, and demonstrate a measurable incorporation of Mg into calcite in both undersaturated and supersaturated conditions.

the number of moles in each cycle to give a number of either Mg or $^{12}$C moles in each cycle. These values were then summed to give a total number of $\text{Mg}^{2+}$ and $^{12}$C moles added in the solid:

$$
\begin{aligned}
^{12}\text{C}_{tot} &= \sum_{0}^{i} z_i \cdot \left( \frac{SA_{raster} \cdot \rho_{calcite}}{mm_{calcite}} \right) \cdot f_i^{12}, \\
\text{Mg}^{2+}{}_{tot} &= \sum_{0}^{i} z_i \cdot \left( \frac{SA_{raster} \cdot \rho_{calcite}}{mm_{calcite}} \right) \cdot f_i^{\text{Mg}^{2+}},
\end{aligned}
\tag{3.4}
$$

where the sum was taken over all cycles $i$ in the profiles. $z_i$ is the mean thickness of calcite sputtered in each cycle, estimated by dividing the measured pit depth by the total number of cycles. $f_i^{12}$ is the intensity fraction of $^{12}\text{C}/(^{13}\text{C} + {}^{12}\text{C})$ measured in SIMS cycle $i$; $f_i^{\text{Mg}^{2+}}$ is the intensity fraction of $\text{Mg}^{2+}$ measured in each SIMS cycle. $SA_{raster}$ is the SIMS raster area (50x50 $\mu m^2$); $\rho_{calcite} = 2.6 \cdot 10^6$ g m$^{-3}$ is the density of calcite and $mm_{calcite} = 100$ g mol$^{-1}$ is the molar mass of calcite. For carbon isotope balance, any $^{12}$C enrichment above the control run was assumed to represent new calcite added. Thus, the mean integrated number of moles from the control experiment was subtracted from the experimental profiles. For Mg/Ca balance, an Mg/Ca ratio of 0.08 was assumed for the newly precipitated solid (Mucci

and J W Morse, 1984; Sun et al., 2015). Thus to calculate the number of moles of new calcite added we divided by this ratio:

$$\begin{aligned}
\text{CaCO}_{3(^{12}\text{C},new)} &= {}^{12}\text{C}_{tot}; \\
\text{CaCO}_{3(Mg,new)} &= \text{Mg}^{2+}{}_{tot} \cdot \left|\frac{\text{Ca}}{\text{Mg}}\right|_{solid,eq}.
\end{aligned} \tag{3.5}$$

Here, $\text{Ca/Mg}_{solid,eq} = 1/0.08$ is taken from measurements of about 8 mole % magnesium incorporated into calcite grown in equilibrium with modern seawater (Mucci and J W Morse, 1984). Estimates for the total moles of new/exchanged calcite, as calculated by carbon and magnesium mass balances, as well as effective reactive layer thicknesses, are presented in Table 3.3. Effective layer thicknesses ($z_{eff}$) were estimated by converting the total moles of new calcite to a volume of calcite ($\rho_{calcite} = 2.63 g cm^{-3}$) and dividing by the sims raster surface area (50x50 $\mu m^2$):

$$\begin{aligned}
z_{eff,^{12}\text{C}} &= \text{CaCO}_{3(^{12}\text{C,new})} \cdot \frac{mm_{calcite}}{\rho_{calcite} \cdot SA_{raster}}, \\
z_{eff,Mg} &= \text{CaCO}_{3(Mg,new)} \cdot \frac{mm_{calcite}}{\rho_{calcite} \cdot SA_{raster}}.
\end{aligned} \tag{3.6}$$

The values for $z_{eff,Mg}$ are lower than $z_{eff,^{12}\text{C}}$. We do not know the precipitated phase in our system, and thus there is significant uncertainty in the newly precipitated solid Mg/Ca ratio. For example, there is experimental evidence that in seawater of Mg/Ca = 5, aragonite is favored to precipitate even on calcite seeds (Sun et al., 2015; John W Morse, Q. Wang, and Tsio, 1997). The distribution coefficient of $\text{Mg}^{2+}$ into aragonite is significantly lower than that in calcite by at least one order of magnitude (Zhong and Mucci, 1989). An Mg/Ca of 0.08 is thus an upper bound on the amount of Mg incorporated into our calcite. Using it in Eq.(3.5) represents a lower limit on the total carbonate precipitation in these experiments, and helps explain why layer thicknesses using Mg/Ca mass balance are thinner than those from carbon isotope mass balance.

Finally, we ground-truthed the SIMS data using the precipitation ($\Omega = 1.3$) experiment and compared to literature values of precipitation rate. At $\Omega = 1.3$, Zhong and Mucci (1989) measured a calcite precipitation rate of 1 $\mu$mol m$^{-2}$ hr$^{-1}$. Mulitplying this rate by the molar mass and dividing by the density of calcite gives a rate of 0.037 nanometers of calcite precipitated per hour. Over a 48 hour period, we should thus expect about 1.8 nm of calcite precipitated onto our SIMS disks. However, we measured that about 3-9 nm of $^{12}$C-calcite was added in our $\Omega = 1.3$ experiments

|  | $\Omega = 0.95$ | $\Omega = 1.3$ |
|---|---|---|
| ${}^{12}C_{tot}$ | $0.7\text{-}2.2 \cdot 10^{-13}$ | $2.1\text{-}6.3 \cdot 10^{-13}$ |
| $Mg^{2+}_{tot}$ | $1.5\text{-}7.8 \cdot 10^{-15}$ | $1.3\text{-}8.8 \cdot 10^{-15}$ |
| $z_{eff, {}^{12}C}$ (nm) | 1.0-3.3 | 3.1-9.3 |
| $z_{eff, Mg}$ (nm) | 0.3-1.5 | 0.2-1.7 |

**Table 3.3:** Estimates of new tracer incorporation based on integration of ${}^{12}C/{}^{13}C$ and Mg/Ca SIMS profiles. The number of moles added were determined using Eq.(3.4) of SIMS profile data. This was then converted to a thickness of calcite as described in the text.

(Table 3.3). The discrepancy between the net amount of calcite added to the surface and the amount of ${}^{12}C$ measured on the SIMS can be attributed to calcite exchange due to dissolution-precipitation reactions at the calcite surface.
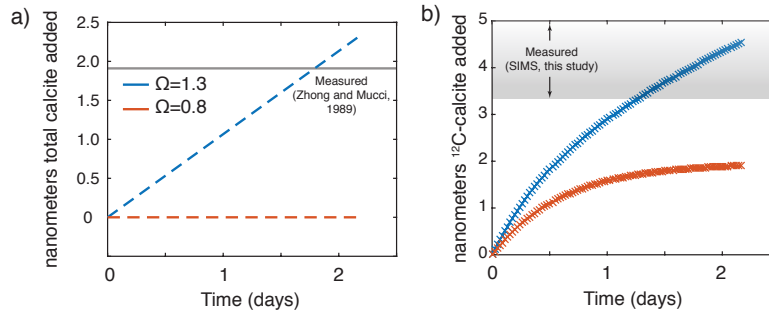


**Figure 3.8:** Plots of the dissolution-precipitation box model run in "precipitation mode" ($R_{precip}/R_{diss} = 1.3$, blue lines) over 2 days, such that calcite of seawater $\delta^{13}C$ composition was added to the surface. For comparison, a dissolution model run is also shown ($R_{precip}/R_{diss} = 0.8$, red lines). **a)** The total thickness of calcite added to the reactive surface. Net precipitation adds calcite to the reactive surface; net dissolution does not. The amount of net precipitation in 48 hours as measured by Zhong and Mucci, 1989 is shown as a grey line for reference. **b)** the effective thickness ($z_{eff}$) of pure ${}^{12}C$ calcite added to the reactive surface. Both curves add ${}^{12}C$ to the solid, due to active gross precipitation under both saturation states. Much more ${}^{12}C$ is added during net precipitation. Using a ratio of precipitation to dissolution of 1.3 and a net precipitation rate of 1 $\mu$mol m$^{-2}$ hr$^{-1}$ gives a correct total thickness of calcite added, and furthermore shows that there is more addition of ${}^{12}C - CaCO_3$ than total $CaCO_3$, due to dissolution-reprecipitation reactions. The range of ${}^{12}C - CaCO_3$ measured in SIMS experiments described above is shown in the shaded box for reference.

Assuming a linear relationship between precipitation rate and $\Omega$, similar to Eq. 1 in the main text, there should be a 30% imbalance in gross precipitation and dissolution rates at $\Omega = 1.3$. Dissolution and reprecipitation will exchange solid ${}^{13}C$ with seawater ${}^{12}C$, above and beyond the net accumulation of calcite. To estimate the amount of ${}^{12}C$ added in such dissolution-precipitation reactions, we used the box model described below, but modified it to add calcite to the reactive

surface at a rate of 1 $\mu$mol m$^{-2}$ hr$^{-1}$. We also set the balance of dissolution to precipitation of $R_{precip}/R_{diss}$ = 1.3. The results of this model, and a comparison to the model run in its "dissolution" configuration, are shown in Figure 3.8. As seen in Figure 3.8b, about 2.1 nanometers of calcite was added under precipitation conditions. Figure 3.8a further shows that about 4.4 nanometers of $^{12}$C-calcite was added to the solid through a combination of dissolution and precipitation reactions. 4.4 nanometers is within our integrated $^{12}$C measurement of 3.3-9.1 nanometers of $^{12}$C-calcite added in SIMS experiments at $\Omega$ = 1.3. The model thus confirms our SIMS measurements are accurately measuring the amount of precipitation in the solid, and gives us confidence in our measurement of the $^{12}$C enrichment in our undersaturated experiments.

**Dissolution-Precipitation Box Model and Data Fitting**

**Box Model**
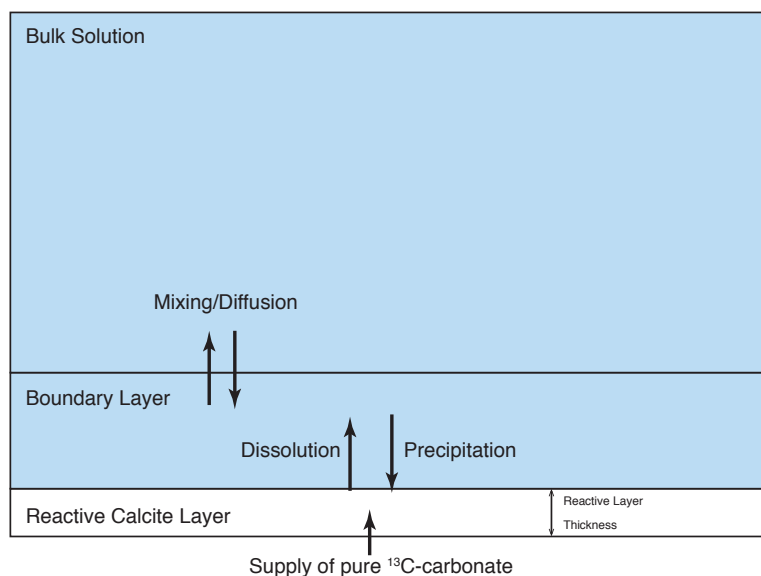


**Figure 3.9:** A schematic of our dissolution-precipitation box model. The number of monolayers changes the size of the "reactive calcite layer" reservoir. This fixed-volume reservoir is supplied with pure $^{13}$C carbon at a rate equal to the amount eroded due to net dissolution, as described in Eq.(3.7).

We developed a box model of dissolution and precipitation at the mineral surface to model our raw data of $^{13}$C versus time. A schematic of this model is shown in Figure 3.9. The model has three main reservoirs: The bulk solution, a boundary layer, and a reactive calcite layer. Carbon from the bulk solution diffuses into and out of the boundary layer. Dissolution and precipitation reactions occur between the

boundary layer and the reactive calcite layer. Because so little calcite is dissolved in our experiments, we keep the total surface area reacting with seawater fixed over time. We model this reactive calcite layer as a fixed volume "reaction front" that is constantly in contact with seawater, calculated as the fixed total surface area multiplied by a reactive layer thickness. In order to keep this volume fixed through time in the model, material removed by dissolution must be replaced by an equal flux of material from the calcite interior into the reaction front:

$$\frac{d[^{13}\text{C}]_{bulk}}{dt} = D\frac{SA}{l}\left([^{13}\text{C}]_{bl} - [^{13}\text{C}]_{bulk}\right)\frac{1}{V_{bulk}}; \tag{3.7a}$$

$$\frac{d[^{12}\text{C}]_{bulk}}{dt} = D\frac{SA}{l}\left([^{12}\text{C}]_{bl} - [^{12}\text{C}]_{bulk}\right)\frac{1}{V_{bulk}}; \tag{3.7b}$$

$$\frac{d[^{13}\text{C}]_{bl}}{dt} = \left(D\frac{SA}{l}\left([^{13}\text{C}]_{bulk} - [^{13}\text{C}]_{bl}\right) + R_{diss} \cdot f_{solid}^{13} - R_{precip} \cdot f_{bl}^{13}\right)\frac{1}{V_{bl}};$$
$$\tag{3.7c}$$

$$\frac{d[^{12}\text{C}]_{bl}}{dt} = \left(D\frac{SA}{l}\left([^{12}\text{C}]_{bulk} - [^{12}\text{C}]_{bl}\right) + R_{diss} \cdot f_{solid}^{12} - R_{precip} \cdot f_{bl}^{12}\right)\frac{1}{V_{bl}};$$
$$\tag{3.7d}$$

$$\frac{d[^{13}\text{C}]_{solid}}{dt} = R_{precip} \cdot f_{bl}^{13} - R_{diss} \cdot f_{solid}^{13} + (R_{diss} - R_{precip}) \cdot f_{interior}^{13}; \tag{3.7e}$$

$$\frac{d[^{12}\text{C}]_{solid}}{dt} = R_{precip} \cdot f_{bl}^{12} - R_{diss} \cdot f_{solid}^{12} + (R_{diss} - R_{precip}) \cdot f_{interior}^{12}. \tag{3.7f}$$

Fluxes in solution (Eqs. 3.7a-3.7d) were calculated in units of concentration per time (moles m$^{-3}$ sec$^{-1}$). The subscripts *bulk* and *bl* correspond to the bulk solution and diffusive boundary layer reservoirs, respectively. Fluxes into and out of the solid (Eqs. 3.7e-3.7f) were calculated in units of moles per time. $f^i$ represent the isotopic mole fractions of stable carbon isotope $i$. Rates of precipitation ($R_{precip}$) and dissolution ($R_{diss}$) are in units of moles per time, and represent the total amount of precipitation or dissolution. The third terms in Eqs. 3.7e and 3.7f model the supply of new calcite from the interior, at a rate equal to the net dissolution rate ($R_{diss} - R_{precip}$). This material carries an isotopic composition of the calcite interior. In this case our calcite is pure $^{13}$C, so $f_{interior}^{13} = 1$ and $f_{interior}^{12} = 0$.

The following mass balance constraints were applied to the above differential equations:

$$N_{solid,total} = \frac{m_{calcite} \cdot SA_{calcite} \cdot z_{mono} \cdot n_{mono} \cdot \rho_{calcite}}{mm_{calcite}}; \qquad (3.8a)$$

$$f_{solid}^{13} = \frac{N_{solid}^{13}}{N_{solid,total}}; \qquad (3.8b)$$

$$f_{solid}^{12} = 1 - f_{solid}^{13}; \qquad (3.8c)$$

$$V_{bl} = SA_{calcite} \cdot z_{bl}; \qquad (3.8d)$$

$$f_{bl}^{13} = \frac{[^{13}C]_{bl}}{[^{13}C]_{bl} + [^{12}C]_{bl}}; \qquad (3.8e)$$

$$f_{bl}^{12} = 1 - f_{bl}^{13}, \qquad (3.8f)$$

where $N_{solid,total}$ is the total number of moles in the reactive calcite layer; $V_{bl}$ is the volume in cubic meters of the boundary layer and is equal to the calcite surface area $SA_{calcite}$ multiplied by the boundary layer thickness $l$, assumed to be $10\mu$m. $SA_{calcite} = 0.09$ m$^2$g$^{-1}$ was measured using Kr-BET (A. V. Subhas et al., 2015). The thickness of a monolayer of calcite was assumed to be $z_{mono}$=0.5 nm, and the number of monolayers $n_{mono}$ was varied as discussed below to change the overall volume of calcite reacting with solution. $mm_{calcite} = 100$ g mol$^{-1}$ is the molar mass of calcite and $\rho_{calcite} = 2.63$ g cm$^{-3}$ is its density. The bulk volume used is identical to our experimental conditions (300 grams of seawater at density 1025 kg m$^{-3}$). $R_{precip} = R_{diss}/r_{fb}$, the ratio of dissolution to precipitation, which varied between 1.001 to 10 or more (see below for model-data fitting). The model was developed and run in MATLAB r2015a. If the boundary layer $l$ is very thick, diffusion out of the boundary layer restricts the expression of the curvature in the bulk data (not shown), because the initial burst of $^{13}$C-labeled DIC is slowly released and mixed out of the boundary layer, rather than being delivered to the bulk solution immediately. However, we expect our boundary layer to be relatively thin and do not expect diffusion to be a major component of our observed rates. This is because mixing rate does not affect our measured dissolution rates between 60-90 rpm. A $10\mu$m boundary layer and the carbonate ion diffusion coefficient in seawater ($9.55 \cdot 10^{-10}$ m$^2$s$^{-1}$, Y. H. Li and Gregory, 1974) expresses the curvature in $\delta^{13}$C versus time in both the boundary layer and the bulk solution. Example model output data, taken from the same model run as Figure 2a in the main text, is shown in Figure 3.10 for the bulk solution, boundary layer, and solid reactive calcite reservoirs. The curvature in all three plots corresponds to the solid calcite layer coming into steady state with respect to the dissolution and precipitation fluxes.

A mass balance can also be constructed for the Mg/Ca of calcite in solution using similar equations to Eq.(3.7):

$$\frac{d[\text{Mg}^{2+}]_{bulk}}{dt} = D\frac{SA}{l}\left([\text{Mg}^{2+}]_{bl} - [\text{Mg}^{2+}]_{bulk}\right)\frac{1}{V_{bulk}}; \tag{3.9a}$$

$$\frac{d[\text{Ca}^{2+}]_{bulk}}{dt} = D\frac{SA}{l}\left([\text{Ca}^{2+}]_{bl} - [\text{Ca}^{2+}]_{bulk}\right)\frac{1}{V_{bulk}}; \tag{3.9b}$$

$$\frac{d[\text{Mg}^{2+}]_{bl}}{dt} = \left(D\frac{SA}{l}\left([\text{Mg}^{2+}]_{bulk} - [\text{Mg}^{2+}]_{bl}\right) + R_{diss} \cdot f_{solid}^{\text{Mg}^{2+}} - R_{precip} \cdot f_{bl}^{\text{Mg}^{2+}}\right)\frac{1}{V_{bl}}; \tag{3.9c}$$

$$\frac{d[\text{Ca}^{2+}]_{bl}}{dt} = \left(D\frac{SA}{l}\left([\text{Ca}^{2+}]_{bulk} - [\text{Ca}^{2+}]_{bl}\right) + R_{diss} \cdot f_{solid}^{\text{Ca}^{2+}} - R_{precip} \cdot f_{bl}^{\text{Ca}^{2+}}\right)\frac{1}{V_{bl}}; \tag{3.9d}$$

$$\frac{d[\text{Mg}^{2+}]_{solid}}{dt} = R_{precip} \cdot f_{bl}^{\text{Mg}^{2+}} - R_{diss} \cdot f_{solid}^{\text{Mg}^{2+}} + (R_{diss} - R_{precip}) \cdot f_{interior}^{\text{Mg}^{2+}}, \tag{3.9e}$$

$$\frac{d[\text{Ca}^{2+}]_{solid}}{dt} = R_{precip} \cdot f_{bl}^{\text{Ca}^{2+}} - R_{diss} \cdot f_{solid}^{\text{Ca}^{2+}} + (R_{diss} - R_{precip}) \cdot f_{interior}^{\text{Ca}^{2+}}, \tag{3.9f}$$

where $f_i^{\text{Me}^{2+}}$ is the mole fraction of either $\text{Mg}^{2+}$ or $\text{Ca}^{2+}$ in the reservoir $i$. As in Eq.(3.7), solution fluxes are in terms of concentration (moles per volume), and solid fluxes are in terms of total moles. $R_{diss}$ and $R_{precip}$ are the total rates of dissolution and precipitation, respectively, in units of moles per time. Incorporation of $\text{Mg}^{2+}$ into the solid is sensitive to the ratio of magnesium to calcium in solution, and the distribution coefficient of magnesium into calcite. We modified $f_{bl}^{\text{Mg}^{2+}}$ such that it represents the mole fraction of magnesium precipitated from the solution:

$$f_{bl}^{\text{Mg}^{2+}} = \frac{D_{Mg} \cdot (\text{Mg/Ca})_{bl}}{1 + D_{Mg} \cdot (\text{Mg/Ca})_{bl}}. \tag{3.10}$$

Here, $D_{Mg} = (\text{Mg/Ca})_{solid}/(\text{Mg/Ca})_{bulk\,solution} = 0.019$ (T Oomori et al., 1987) is the distribution coefficient of $\text{Mg}^{2+}$ into calcite at room temperature, and $(\text{Mg/Ca})_{bl}$ is the Mg/Ca ratio in the model boundary layer. The quantity $D_{Mg} \cdot (\text{Mg/Ca})_{bl}$ is thus the Mg/Ca ratio of the precipitated solid in equilibrium with calcite. The right hand side of this equation converts mole ratio to mole fraction, analogous to converting carbon isotope ratios into carbon isotope mole fractions. Implicit in this equation is the assumption that, at every model time step, calcite is precipitating in equilibrium with the solution. Implementation of cation mass balance in the model is also shown in Figure 3.10. As expected, the Mg/Ca ratio of the solid decreases as dissolution overtakes precipitation. At equilibrium, the solid Mg/Ca = $D_{Mg} \cdot (\text{Mg/Ca})_{bulk}$ ~ 0.09.
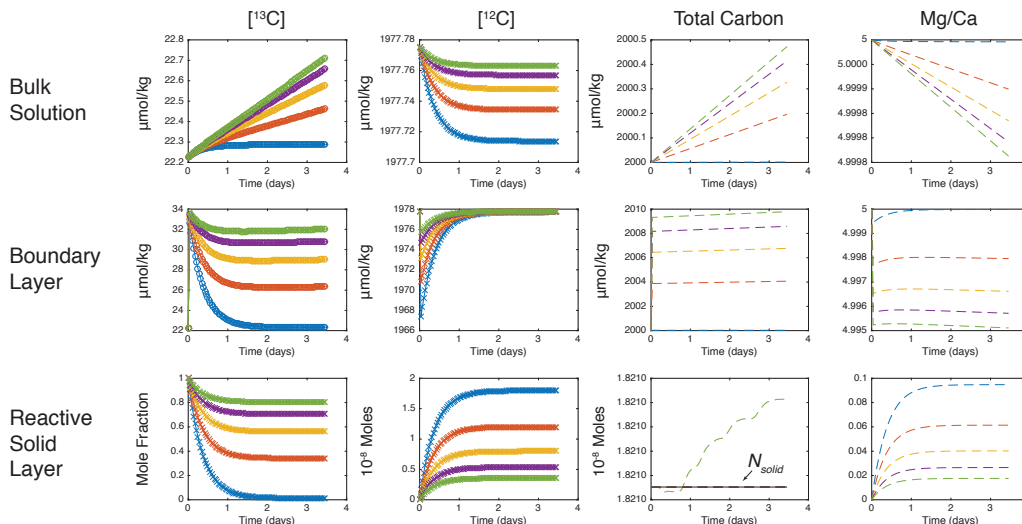
**Figure 3.10:** Example box model output showing the isotopic evolution and mass balance of the bulk solution (top row), boundary layer (middle row), and reactive calcite layer (bottom row) reservoirs. Different curves were generated by fixing $k_{diss}$ and varying $r_{fb}$ from 1 to 5. This data was taken from the same model run as the data in Figure 3.2**a**. Color key is the same as the main text figure; i.e. $r_{fb}$ for blue = 1.0; red = 1.5; yellow = 2.2; purple = 3.4; and green = 5.0. For total carbon in the reactive calcite layer, the initial number of moles in the model ($N_{solid}$) is indicated as a solid black line. With complete mass balance, all model runs should not deviate from this initial value. The green experiment showed some numerical drift; however, this drift is small (less than 0.001 nanomoles). All other experiments showed no deviation from the initial value of $N_{solid}$.

## Data fitting using the box model output

Data fitting was performed using the grid search method. A large model parameter space was generated, and data were compared to all model runs over the entire parameter range. The model was initialized and run for 400 values of $R_{diss}$ and 400 values of $r_{fb}$, spanning multiple orders of magnitude of dissolution rate ($10^{-13}$ to $10^{-8}$ moles/s), and varying $r_{fb}$ from 1.001-10 (in the framework above, 1-$\Omega$ from ~0.009 to 0.9). The time-evolution of each of these model runs (i.e. moles dissolved versus time) was then stored. Experimental data were screened to make sure that there was sufficient data density to provide good constraints on dataset curvature. For each experiment, the initial data point was set to zero moles dissolved, to eliminate excess $\delta^{13}C$ increase that may have occured due to fine particle dissolution. Model data were interpolated to the time values of the experimental data points, and the normalized fitting parameter F was calculated as:

$$nF = \frac{m_{net} - m_{m,net}}{m_{net}} + \frac{1}{i} \sum_{t=0}^{i} \frac{|n_t - n_{m,t}|}{n_t}; \qquad (3.11)$$

where in the first term, $m_{net}$ is the experimentally determined net rate, and $m_{m,net}$ is the modeled net rate, calculated as:

$$m_{m,net} = R_{diss} - R_{precip} = R_{diss} - \frac{R_{diss}}{r_{fb}} = R_{diss}(1 - \frac{1}{r_{fb}}), \qquad (3.12)$$

where $R_{diss}$ and $r_{fb}$ are defined as above. In the second term, $n_t$ are the measured number of moles dissolved at time points 0 to $i$, and $n_{m,t}$ are the model-calculated moles dissolved at the interpolated time points 0 to $i$. A normalized fitting parameter was used to avoid bias in the fitting routine arising from differences in the absolute magnitude of dissolution. The implicit assumption of these two terms is that they are both weighted equally in calculating the fitting parameter nF. The fitting parameter was calculated for each dataset at all 400x400 values of $R_{diss}$ and $r_{fb}$. The best-fitting values of $R_{diss}$ and $r_{fb}$ to each experiment dataset were then found by identifying the $R_{diss}$ and $r_{fb}$ values which gave the lowest fitting parameter $nF$. Values were chosen as acceptable fits if they fell within 0.3 log units of the global log10($nF$) minimum.

Two examples of data-model fits – one closer to equilibrium, and one farther from equilibrium – are shown in Figure 3.11. A contour plot of log $nF$ versus $F_{diss}$ and $r_{fb}$ is shown in Figure 3.11b. Panel **a** shows a profile of log$nF$ as a function of $r_{fb}$ at the best-fit value of log$R_{diss}$ (red line), and a profile of log$nF$ as a function of $r_{fb}$ along the covarying path of the local minimum through model space (black line). Panel **d** shows $nF$ across the entire model space. Panel **e** shows a profile of log$nF$ as a function of $R_{diss}$ at the best-fit value of $r_{fb}$ (red line), and a profile of log$nF$ as a function of $R_{diss}$ along the covarying path of the local minimum through model space (black line). The best model fits typically had errors on the order of 10% or less, which are comparable to the $\sim$ 5% errors in experimental dissolution rate determinations (A. V. Subhas et al., 2015). $R_{diss}$ and $r_{fb}$ values were then binned based on the goodness of fit, and statistics were collected on the top 10% of best-fit (lowest $nF$ value) model parameters, which provide the mean and standard deviations of model fit parameters in the figures in the main text. These best fits are found along the black-dashed line in Figure 3.11b. The distributions of $F_{diss}$ and $r_{fb}$ look very different for these two experiments. The high dissolution rate experiment has a much longer tail in both $F_{diss}$ and in $r_{fb}$, which indicates a large range in both of these parameters that can adequately fit the data. Comparatively,

the low undersaturation experiment demonstrates a tighter distribution of $F_{diss}$ and $r_{fb}$ values, although there are a few fliers at high dissolution rate that are paired with very low r(fb) values. We acknowledge that the fit to the lower undersaturation experiment is not as good, and there is still curvature in this dataset that is not explained by the model. There are two potential reasons for this:

1. The amount of curvature expressed in the data could be due to changing undersaturation and thus feed back on the net dissolution rate, depressing the amount of moles dissolved over time. This process should affect the high dissolution rate data more than the low dissolution rate data, and thus cannot be the source of all curvature in our data sets, as near-equilibrium data sets are more curved than far from equilibrium data sets, and these experiments will have experienced the smallest change in saturation state.

2. The amount of curvature expressed in the model is a function of the size of the fluxes relative to the size of the reactive layer. At higher dissolution rate, the fluxes quickly reset the reactive layer and thus very little curvature is expressed. Therefore, for this high net rate, there is very little curvature in the model values that can fit this data set. One explanation for this increased curvature in the data is that when the mechanism switches, the reactive layer deepens. Onset of 2D nucleation across the entire mineral surface could indeed lead to a deepening of the reaction front into the calcite lattice, as now the entire calcite surface is activated for dissolution. However, as discussed in the main text, activation of the entire surface for dissolution also means that precipitation reactions will have less of an influence on the isotopic composition of the solid, as any precipitation should be immediately removed through re-dissolution.

Given these caveats, we conclude that the data fits using our model are valid, and continue with the interpretation of our net rate data presented in the main text. All model files are available upon request to the corresponding author.

**Sensitivity to various model parameters**

Apart from $R_{diss}$ and $r_{fb}$, the main model sensitivity is in the number of monolayers of calcite (0.5 nm thick) that are allowed to react with solution. This parameter determines the shape and strength of the curvature, and also affects the ability of the model to fit the dissolution rate data. Figure 3.12 shows the goodness of fit for

several different reactive layer thicknesses (1, 3, 5, and 7 monolayers) as quartile box plots. The red line is the median of the misfit. Edges of the boxes are the 25th and 75th percentiles. The whiskers include the data extremes and outliers are plotted as red crosses. 5 monolayers provides the best overall misfit to the dataset. The box model fits are slightly skewed: they are not evenly distributed around the mean misfit value. This is partially because there is a floor at 0% misfit. But also, this skewness suggests that there are high-misfit outliers. These higher misfits are due to $\delta^{13}C$ curvature that cannot be explained using our fixed saturation-state box model and thus lead to a larger misfit in the $\delta^{13}C$ versus time data. In A. V. Subhas et al., 2015, we calculated mean $\Omega$ values and rates for these experiments; here, our model does not adjust its dissolution rate as a function of saturation state. We thus attribute these highest misfits as a consequence of small changes in $\Omega$, through either DIC loss or alkalinity generation at high rates of dissolution, leading to a changing dissolution rate over the course of the experiment. The misfit percentage does not scale with $\Omega$, suggesting that our data is not biased by an inability to sufficiently fit data as a function of saturation state. Based on the overall ability of the model to fit all of our dissolution data, we chose a reactive layer thickness of 5 monolayers in our model, which was further justified through the SIMS experiments described and discussed above and in the main text. More than 7 monolayers starts to become inconsistent with the tracer incorporation measured via SIMS, as discussed above.

**Expressions for the dissolution rate of calcite**

**The canonical derivation of a linear dissolution rate law for calcium carbonate**

Eq. 1 in the main text is a canonical representation of dissolution kinetics, and is the basis for framing dissolution in terms of undersaturation, or 1-$\Omega$:

$$R_{diss} = R_f - R_b = k_f\{CaCO_3\} - k_b[Ca^{2+}][CO_3^{2-}] = k_f - k_b[Ca^{2+}][CO_3^{2-}], \quad (3.13)$$

where $R_{diss}$ is in units of moles per time, $k_f$ is in units of moles per time, and $k_b$ is in units of length$^6$ mole$^{-1}$ time$^{-1}$. Assuming that the activity of the carbonate solid is 1, $R_f = k_f$ and $R_b = k_b[Ca^{2+}][CO_3^{2-}]$. Substitution of $K'_{sp} = \frac{[Ca^{2+}][CO_3^{2-}]_{sat}}{\{CaCO_3\}} = \frac{k_f}{k_b}$ into Eq.(3.13), and the definition of $\Omega = \frac{[Ca^{2+}][CO_3^{2-}]}{K'_{sp}}$, gives:

$$R_{diss} = k_r \cdot K'_{sp} - k_r[Ca^{2+}][CO_3^{2-}] = k_r \cdot K'_{sp}(1 - \Omega) = k_{diss}(1 - \Omega). \quad (3.14)$$

Here, $k_{diss}$ is in units of moles per time. Dividing Eq.(3.14) by surface area gives the specific dissolution rate in units of moles length$^{-2}$ time$^{-1}$. In addition, this model

suggests that the ratio of dissolution and precipitation rates is linearly proportional to $\Omega$:

$$\Omega = \frac{[\text{Ca}^{2+}][\text{CO}_3^{2-}]}{K'_{sp}} = \frac{[\text{Ca}^{2+}][\text{CO}_3^{2-}] \cdot k_r}{k_f} = \frac{R_b}{R_f}. \tag{3.15}$$

It is important to emphasize that curvature in either the gross rate of dissolution or precipitation – and thus in the net rate of dissolution – as a function of saturation state necessitates nonlinearities in either or both of these terms. For instance, curvature in the gross dissolution rate implies that either the activity of the solid is not unity at all saturation states, or that there are other terms that must be included in the rate law. The inclusion of other terms, for instance carbonic acid as a driver of dissolution, may be the way forward. A fully predictive rate law as a function of chemical speciation would thus include multiple terms, and would necessitate a speciation model of the calcite surface as a function of dissolved species and the density of calcium and carbonate surface ion sites in seawater.

**A derivation of Eq. 3 in the main text**

In the last section, we discuss a 2D-nucleation model of calcite dissolution similar to that presented by P M Dove, Han, and J J De Yoreo, 2005. This model takes elements of classical growth and nucleation theory and applies them to dissolution. The rate of dissolution initiated by etch pit formation is defined as:

$$R_n = h v^{2/3} J^{1/3}, \tag{3.16}$$

where the normal dissolution rate $R_n$ is a function of the step height $h$, the speed of a moving step $v$, and the steady-state etch pit nucleation rate, $J$. The nonlinear dependence of $R_n$ on $J$ is discussed extensively elsewhere (Sangwal, 1987; Malkin, Chernov, and Alexeev, 1989). The form of this dependence changes the absolute value of surface energies calculated in Table 1 in the main text; however, it does not impact the trends in surface energy or the location of the rate transition between defect-initiated and homogeneous etch pit nucleation shown in Figure 5 in the main text. The step retreat velocity $v$ depends on solution composition in a formulation similar to Eq.(3.13) above:

$$v = \omega\beta(C_e - C) = \omega\beta C_e(1 - \Omega); \tag{3.17}$$

where $\omega$ is the molecular volume of calcite, $\beta$ is the step kinetic coefficient cm/s, and $C_e$ is the equilibrium concentration of the species. In the case of calcite, $C_e$ is equivalent to the $K'_{sp}$ of calcite. $J$, the frequency of nucleating an etch pit, is related to saturation state $\sigma = \ln\Omega$, as nucleation is activated above some $\Delta G_{critical}$, defined by the interface free energy barrier to nucleation $\alpha$:

$$J = |\sigma|^{1/2} n_s ahC_e\beta\exp\left(\frac{\pi\alpha^2\omega h}{(k_BT)^2}\left|\frac{1}{\sigma}\right|\right). \tag{3.18}$$

New terms here are the lattice spacing $a$ and the density of nucleation sites $n_s$. Substituting Equations 3.18 and 3.17 into Eq.(3.16) and rearranging for $1/\sigma$, we recover Equation 3 in the main text.

**Carbonic anhydrase and its effect on dissolution kinetics**

The dissolution rate method from A. V. Subhas et al. (2015) allows for sensitive rate determinations in the absence of significant changes of solution chemistry or mineral surface area. For instance, using a 100% labeled $CaCO_3$ solid, we achieve a $\delta^{13}C$ sensitivity of about 20‰ per 1 $\mu$eq/kg alkalinity change. Saturation state was determined using DIC-alk pairs measured on a Picarro CRDS and a home-built titration system. Final errors on $\Omega$, calculated using alkalinity-DIC pairs, range from ≤0.01 to ~0.03 units. The $K'_{sp}$ for calcite was adjusted so that the most saturated dissolution experiments are undersaturated, requiring a correction factor of about 1.03 to the value found in J W Morse, Mucci, and Millero (1980). The alkalinity contribution of carbonic anhydrase (~30 equivalents/mol) to solutions was determined by a standard additions alkalinity experiment in natural seawater. At the same saturation state ($\Omega$=0.83), curves of $\delta^{13}C$ increase significantly in slope as CA increases (Figure 3.13).

To test the effect of other proteinaceous material on the rate of calcite dissolution, experiments were conducted in the presence of bovine serum albumin (BSA) at concentrations of 0.002 (not shown) and 0.01 mg/mL (shown in Figure 3.14 versus uncatalyzed and catalyzed dissolution rates at [CA] = 0.01 mg/mL). These experiments show no significant change in the BSA rate versus the uncatalyzed rate while dissolution experiments in the presence of CA are always faster than those without CA. If anything, rates in the presence of BSA are slightly slower. The behavior of dissolution rate versus $\Delta G$ is very similar to that described by Rolf S Arvidson and Lüttge, 2010. In their experiments, surfaces with different amounts of etching were exposed to solutions of similar undersaturation. These surfaces dissolved at signif-

icantly different rates, suggesting that the surface itself exerts significant influence on the relationship between dissolution rate and saturation state. Here, in contrast, it is the presence of CA, instead of a surface feature hysteresis, driving a different functional dependence between $\Delta G$ and dissolution rate.
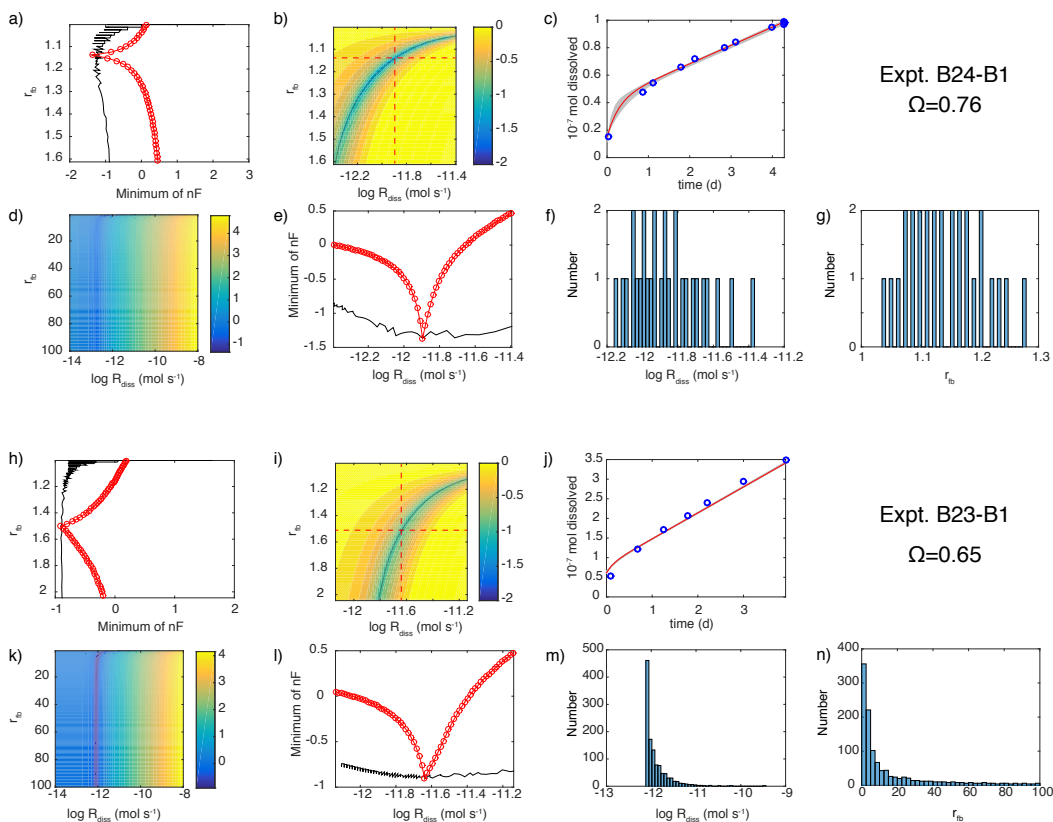
**Figure 3.11:** An example of the model-data fitting routine output for two dissolution experiments. **a-g**); data-model fits for an experiment conducted at Ω = 0.24. **b**); The surface of model-data misfit plotted as log$nF$, zoomed in on the values of $r_{fb}$ (ratio of gross dissolution to precipitation) and $F_{diss}$ (gross dissolution rate constant) that minimize log$nF$. Low values indicate a better overall misfit: -1 corresponds to a $10^{-1}$ or 10% error in the fit. Red dashed lines intersect at the global minimum pair of $F_{diss}$ and $r_{fb}$. The black dashed line follows the covarying path of the local minimum in the cost function. Values of $F_{diss}$ and $r_{fb}$ along the black traces allow for the calculation of statistics on the fit. Panel **a**) shows a profile of log$nF$ for $r_{fb}$ values at a fixed value of $F_{diss}$ (red line with points, i.e. following the dashed vertical line in panel **b**), and along the local minimum trace of $nF$ (black line, i.e. following the curved black line in panel **b**). **d**) shows the entire parameter space, with a small rectangle indicating the zoomed region in panel **b**. Note the change in color scale for values of log$nF$. Panel **e**) shows a profile of log$nF$ for the entire range of $F_{diss}$ values at a fixed value of $r_{fb}$ (red line with points) and along the local minimum trace (black line). Panel **c** shows the data-model misfit for the top model parameters $F_{diss}$ and $r_{fb}$. Panels **f** and **g** show histograms of the best-fit values for for $F_{diss}$ and $r_{fb}$, respectively. **h-n**); The same panels as above for an experiment run at Ω = 0.35. Note that the number of acceptable fits in panels **m** and **n** is much larger, as are the ranges in both $F_{diss}$ and $r_{fb}$. Also note that the large peak in $R_{diss}$ must correspond to the long tail of large $r_{fb}$ values, in order to satisfy the constraint on the net rate. This range is also evident in the relatively flat black curves in panels **h** and **l**. These distributions are the basis for the range limits in Figure 3 in the main text.
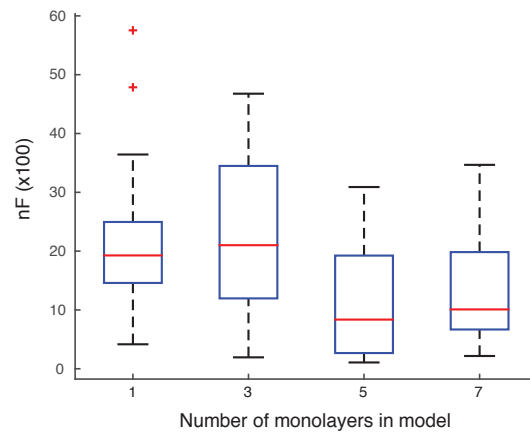
**Figure 3.12:** Sensitivity test of mean model goodness of fit (%) for all experiments as a function of the number of monolayers in the reactive calcite reservoir, plotted as box plot quartiles. The red line is the median of the misfit. Edges of the boxes are the 25th and 75th percentiles. The whiskers include the data extremes and outliers are plotted as red crosses. There is a minimum in the misfit error if five monolayers of calcite are used.
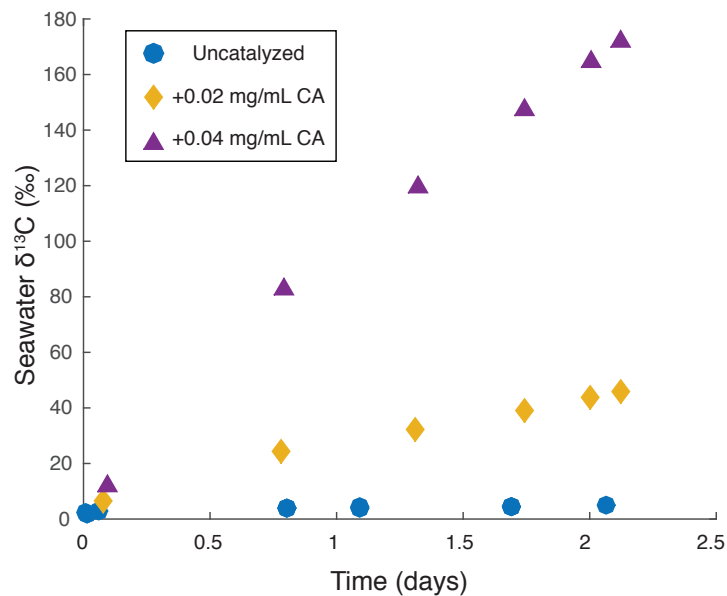


**Figure 3.13:** Plots of $\delta^{13}C$ versus time for several dissolution experiments at the same saturation state and different [CA].
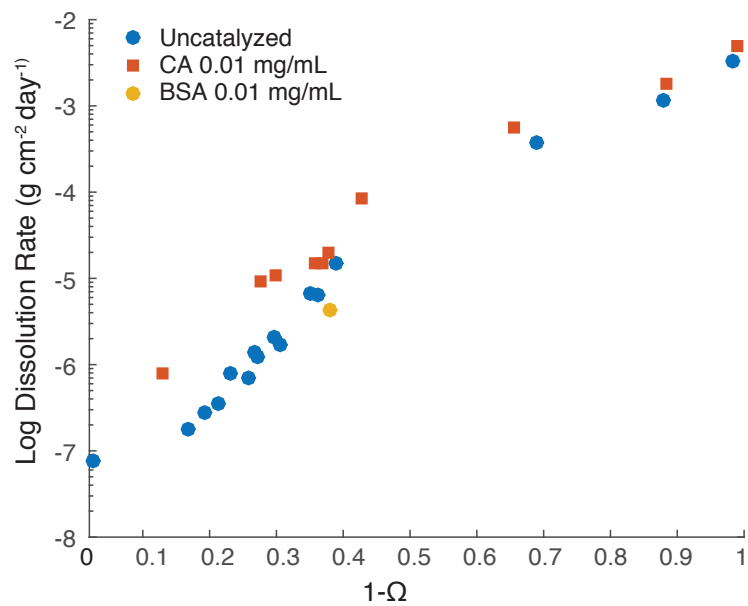
**Figure 3.14:** Dissolution rates in the presence of BSA compared to uncatalyzed dissolution rates at the same undersaturation. The similarity in rate indicates that unreactive dissolved organic matter has no influence on dissolution rate.

# THE ROLES OF MAGNESIUM AND ORGANIC CARBON IN CONTROLLING THE DISSOLUTION RATE OF BIOGENIC CALCITES IN SEAWATER

## 4.1  Introduction

Most of the open-ocean calcium carbonate is produced by coccoliths and foraminifera J Erez, 2003. Carbonate production in the open ocean exceeds the $CaCO_3$ sink needed to balance alkalinity inputs from continental weathering, resulting in a large alkalinity flux from dissolution of carbonate-rich sediments back into seawater (Milliman, 1993; Arrhenius, 1988; Sigman and Boyle, 2000). This alkalinity flux plays a key role in mediating atmospheric $CO_2$ on 5-10,000 year timescales (Richard E Zeebe, 2012; Andy Ridgwell, 2005; Robert A Berner and Kothavala, 2001)).

The ocean's response to $CO_2$ perturbations on such timescales is determined by the deep ocean's saturation state with respect to calcite, $\Omega = [Ca^{2+}][CO_3^{2-}]/K'_{sp}$. If $\Omega < 1$, dissolution is thermodynamically favored. The current invasion of anthropogenic $CO_2$ into surface ocean waters will eventually reach the deep ocean, driving down $\Omega$ and promoting more dissolution of calcium carbonate sediments D. Archer, Kheshgi, and Maier-Reimer (1998). The rate at which we are emitting $CO_2$ has reinvigorated interest into the marine $CaCO_3$ cycle and its regulation of $CO_2$ perturbations (Orr et al., 2005; Doney et al., 2009; Richard A Feely et al., 2012).

However, the kinetic response of calcites to undersautration depends on more than just saturation state. Studies over the last half-century have failed to establish a linear rate law for calcite dissolution in seawater as a function of undersaturation (i.e. Rate $\propto$ 1-$\Omega$; (Keir, 1980; R A Berner and J W Morse, 1974; A. V. Subhas et al., 2015; Truesdale, 2015)). Saturation state alone is thus insufficient to predict the kinetics of calcite dissolution in seawater. Furthermore, dissolution rates of many biogenic calcites normalized by surface area often do not agree with each other (Honjo and J Erez, 1978; Walter and J W Morse, 1985; Pickett and A J Andersson, 2014; Cubillas et al., 2005). This observation has led some authors to conclude that gas adsorption measurements of surface area are not an appropriate quantification of the available reactive surface area (John W Morse, Rolf S Arvidson, and Lüttge, 2007; Walter and J W Morse, 1985). Instead, these authors hypothesized that there

must be microstructural or subtle chemical differences between biogenic calcites of similar bulk composition which are not captured by the BET measurement of surface area. This reactive surface area would then control the reactivity of a given calcite in seawater; however, a method to measure this reactive surface area has not been established.

The geometry of a mineral's surface has indeed been shown to alter its reactivity. For example, Rolf S Arvidson and Lüttge (2010) measured significant differences in dissolution rate across a range of saturation states for the same mineral and different amounts of etching. Surface observations of silicate and carbonate minerals have indicated that structural changes due to dissolution, such as step edge retreat, and etch pit opening and spreading, can be described as a function of saturation state using models of crystal growth and nucleation (P M Dove, Han, and J J De Yoreo, 2005; Patricia M Dove et al., 2008; Lasaga and Luttge, 2001; A. Subhas, Adkins, J. Erez, Rollins, et al., Under Review). Despite of the wide array of biogenic calcite structures, and the lack of agreement among dissolution rate determinations, there has been little effort to link such surface features with dissolution mechanisms in biogenic calcites.

Biogenic calcites present two further complications compared to the inorganic mineral. First, organic matter has long been implicated in the dissolution rates of calcites in the ocean. Organic matter packaged with carbonates is often suggested to enhance dissolution rates, because respired $CO_2$ decreases the local saturation state (Milliman, Troy, et al., 1999; Steven Emerson and M. Bender, 1981; Burke Hales, 2003; D. Archer, 1991). Conversely, organic coatings surrounding coccoliths have been suggested to suppress their dissolution rate in sediments by protecting the underlying lith calcite from corrosive seawater (Honjo and J Erez, 1978; Keir, 1980). Why these specific organic moieties would be protective, rather than destructive, to the underlying calcite, is not explained.

Organic molecules are also often involved in the calcification process (John W Morse, Rolf S Arvidson, and Lüttge, 2007; Hemleben, Spindler, and O. R. Anderson, 1989; Shmuel Bentov, Brownlee, and Jonathan Erez, 2009; Branson et al., 2016). In many planktonic foraminifera, the primary organic membrane provides a template for the initial calcification of a new chamber (Hemleben, Spindler, and O. R. Anderson, 1989; S Bentov and J Erez, 2005; Branson et al., 2016; Mass et al., 2014; Drake et al., 2013). Recently, soluble macromolecules bound in the lattice of coccolith calcite have also been shown to actively recruit calcium ions from solution

*in vitro* (Gal et al., 2016). These organic matrices become embedded within the calcite lattice as carbonate is precipitated, and thus are spatially distinct from organic coatings or organic matter packaged with sinking carbonate particles. Because these organic matrices are intimately involved in the precipitation process, they should act to prevent or slow dissolution. However, the role of organic matrices within the carbonate lattice in the dissolution process has not been directly investigated.

Secondly, the presence of $Mg^{2+}$ in biogenic calcites adds additional uncertainties to thermodynamic variables such as the solubility product ($K'sp$) of magnesian calcites (L Niel Plummer and Mackenzie, 1974). Low Mg calcites in the range of 0-5 mol % Mg show no significant relationship between Mg content and solubility product (John W Morse, Rolf S Arvidson, and Lüttge, 2007). Above this value, solubility increases significantly with mole % Mg. In contrast to bulk solubility data, planktonic foraminiferal tests, which contain low amounts of magnesium ($O$ mmol mol$^{-1}$) show measurable decreases in Mg/Ca as a function of bottom water saturation state when picked from coretop sediments (Brown and Elderfield, 1996). These Mg/Ca decreases have also been empirically related to the amount of mass loss and density change (Johnstone, Schulz, et al., 2010; Johnstone, Jimin Yu, et al., 2011) and an increase in crystallinity (Nouet and Bassinot, 2007) of foraminiferal tests.

Magnesium is heterogeneously distributed in foraminiferal calcite, typically as bands normal to the growth direction of the test (A. Y. Sadekov, Stephen M Eggins, and Patrick De Deckker, 2005). These bands make up only about 5% of the total calcite, such that differences in reactivity due to heterogeneous Mg content may not manifest as different species-specific solubilities. However, we lack a deep understanding of the kinetic processes responsible for preferential Mg removal, and how these processes may or may not relate to bulk thermodynamic solubility.

We show here dissolution rates from four different biogenic calcites using a newly developed isotope tracer method (A. V. Subhas et al., 2015; A. Subhas, Adkins, J. Erez, Rollins, et al., Under Review). This method traces small amounts of dissolution from $^{13}$C-labeled carbonates into seawater by measuring the change in the $\delta^{13}$C of seawater over time. Plots of $\delta^{13}$C versus time measure the net rate of dissolution, and also diagnose the balance of gross dissolution and precipitation fluxes at the mineral surface (A. Subhas, Adkins, J. Erez, Rollins, et al., Under Review). This method has the advantage of being sensitive to small amounts of dissolution, such that very low solid:solution ratios can be used.

We cultured an assemblage of planktonic and benthic foraminifera, the soft coral *Rhythismia fulvum*, and the coccolith *E. huxleyi* in $^{13}$C-labeled seawater and then used these labeled materials in dissolution experiments across a large range of seawater saturation states. We measured dissolution rates on whole shells, in order best replicate oceanic conditions. After surface area normalization, there are still significant differences in dissolution rate between biominerals. We find a strong correlation near equilibrium between dissolution rate and Mg content. We also find a strong correlation between far-from-equilibrium dissolution rate and the amount of organic carbon bound in the calcite lattice. These results begin to quantify the differences between coccoliths, foraminifera, and high-Mg soft corals in a framework that should be applicable to biogenic calcites broadly. These results deepen our understanding of the chemical controls on calcite dissolution in seawater.

## 4.2 Methods

### Culturing of marine calcifiers

Planktonic foraminifera, Benthic foraminifera, high-Mg soft corals, and coccoliths were cultured in $^{13}$C-labeled seawater for use in dissolution experiments. These cultured calcites were compared to dissolution experiments conducted using synthetic $^{13}$C-calcite. With the exception of coccoliths, marine calcifiers were cultured in two sessions at the Inter-University Institute in Eilat, Israel. Precipitation of calcium carbonate in culturing experiments was periodically checked with the alkalinity anomaly method. Alkalinities were either measured by hand on small (15 gram) samples using a Radiometrics America ABU91 Autoburette and the Gran method, or using a Metrohm Dosimat with an autosampler and an endpoint determination. Both instruments were calibrated with standard seawater reference materials.

Seawater labeled in $^{13}$C was prepared for culturing experiments using unfiltered surface seawater retrieved from the Gulf of Eilat several kilometers from the shore. This seawater was stored for at most one week in the dark prior to use as a culturing medium. All dissolved inorganic carbon (DIC) was stripped out through addition of HCl and vigorous bubbling with air for several hours. Acidified, DIC-free seawater was then transferred to a 5L Supelco bag for storage and DI$^{13}$C addition. A concentrated stock solution of Na$_2$H$^{13}$CO$_3$ and NaOH was then injected into the acidified seawater reservoir, in a ratio that restored DIC and alkalinity to their typical surface values of 2000 $\mu$mol kg$^{-1}$ and 2500 $\mu$eq kg$^{-1}$ respectively. These labeled seawaters were stored cold and in the dark prior to use.

The soft coral species *Rhythismia fulvum* was collected from ~ 3m water depth in the Gulf of Eilat. Pieces of this coral were cut from the main colony and glued to glass slides using store-bought super glue. These glass slides were then transferred to gas-tight plastic containers with a stir-bar, described in Taubner et al., 2012. Culture vessels were filled with $^{13}C$ seawater and exposed to a 12h/12h light-dark cycle at a light intensity of ~250 $\mu$mol photons m$^{-2}$ s$^{-1}$. Viability of colonies was monitored through daily visual examination of colony color and polyp extension under lighted conditions. Labeled seawater was exchanged weekly, or more frequently if the rate of alkalinity drawdown was particularly fast. At the end of the culturing session, coral colonies were removed from the culturing vessels and were gently shaken in a 2% sodium hypochlorite solution until all organic matter was dissolved away. The resulting spicules were then rinsed three to five times with ultrapure (Milli-Q) water, dried, and stored in plastic test tubes for analysis and dissolution experiments.

Assemblages of mixed benthic foraminifera were collected from stones at 2-3m water depth in the Gulf of Eilat. These assemblages were mostly *Amphistegina* species, although there were some other high-Mg calcite Milliolid species as well. Stones were scrubbed using a toothbrush to liberate foraminifera into a bucket containing fresh surface seawater. Low-density organic matter and floating material was poured off. Foraminifera at the bottom of the bucket were then transferred to an aquarium tank with fresh surface seawater devoid of debris. Only healthy forams then climbed up glass slides suspended from floating styrofoam islands in the aquarium, over a period of one to two days. These healthy individuals were then collected, sieved into size fractions, and placed in ground-glass stoppered 250 mL Erlenmeyer flasks filled with the $^{13}C$-labeled seawater culturing medium. Forams were left in a darkened corner of the laboratory with the natural diurnal light cycle, at a maximum light intensity of ~ 10$\mu$mol photons m$^{-2}$ s$^{-1}$. Precipitation rates for these assemblages were measured weekly, and water was exchanged at most every two weeks. In two of the five culturing vessels, large foraminifera spawned offspring, which were cultured along with the others in the Erlenmeyer. These smaller individuals became very strongly labeled with $^{13}C$ since they spawned in the culturing medium. At the end of the culturing sessions, foraminifera were removed from the Erlenmeyer flasks, rinsed with natural seawater, treated with 2% bleach, rinsed three to five times with Milli-Q water, and dried. These shells were then sieved into multiple size fractions and stored in plastic sample tubes for analysis and dissolution experiments.

Planktonic foraminifera were collected from surface plankton towns conducted in

deep (> 300m) water in the Gulf of Eilat. A 200 $\mu$m net was used, towed behind the boat at about 15-20 meters depth. The most viable foraminifera were recovered from "drift tows", where the boat was simply allowed to drift at about 1 knot maximum speed. Species collected were *G. ruber*, *G. siphonifera*, and *O. universa*. Foraminifera were manually separated from the rest of the plankton mass and placed in culturing dishes containing fresh seawater under full light for rehabilitation. Healthy individuals were then transferred in groups of two or three to clear glass jars sealed with Parafilm and plastic lids, filled with the labeled seawater culturing medium. Foraminifera were cultured under a 12h/12h light-dark cycle with a light intensity of ~250 $\mu$mol photons m$^{-2}$ s$^{-1}$. Forams were fed freshly hatched *Artemia* every day or every other day. The health and size of forams was assessed at each feeding by spine length, cytoplasm color, and symbiont density (Hemleben, Spindler, and O. R. Anderson, 1989). Foraminifera that underwent gametogenesis, or otherwise died, were collected, dried, and stored in paleontological slide cases. The relative yield of foraminifera that underwent gametogenesis was about 90%.

Need to get method from Patrizia/Gerald about culturing coccoliths.

**Dissolution rate experiments**
**Experimental setup**

Dissolution experiments were conducted in a similar way to A. V. Subhas et al. (2015) for all biogenic materials measured. Briefly, undersaturated seawaters were made by adjusting the alkalinity of UV-treated, 0.2 $\mu$m filtered, HgCl$_2$ - poisoned, standard seawater using 0.1N HCl. Gas-impermeable foil bags (Supelco part no. 30336-U or Sorbent Systems PAKVF4C) were fitted with sampling ports, and labeled calcite (1-5 mg) was weighed out and quantitatively poured in. Open bags were heat-sealed shut, and then evacuated to remove all headspace. Undersaturated fill waters of known saturation state were siphoned from large foil bag reservoirs into these experimental bags. Grains were rinsed with 50 mL of this fill water, which was then removed and discarded. Then, about 300 grams of fill water was siphoned in, bags were weighed to obtain the exact mass of water added, and the experiment was considered started once the bags were subsequently placed on a shaker table at 60-90 rpm. At each sampling point, the experimental bags were weighed. Samples were withdrawn every four to twelve hours depending on the rate of dissolution and amount of material in the experiment. Total experiment duration lasted six to twelve samplings over one to ten days. We measured DIC

and $\delta^{13}C$ simultaneously using a home-built Picarro CRDS system (A. V. Subhas et al., 2015). Alkalinity measurements were also taken roughly every day to check for alkalinity consistency and to calibrate the isotopic ratio of the dissolving solid, as discussed below. Dissolution experiments were conducted on *E. huxleyi* both bleached and unbleached, bleached benthic foraminifera of multiple size classes, bleached planktonic foraminifera, and bleached *Rhythismia fulvum* spicules.

**Calculation of dissolution rate through time series of seawater $\delta^{13}C$**

In A. V. Subhas et al., 2015, we dissolved 100% $^{13}C$-labeled material, and tracked the number of moles dissolved as a function of the time-evolving isotope ratio of seawater DIC:

$$\Delta^{13}C_{2-1} = m_1 \cdot \frac{[DIC]}{1 + R_{init}} \cdot (R^{13}_2 - R^{13}_1),\qquad(4.1)$$

where $m_1$ is the seawater mass of time point 1, $[DIC]/(1 + R_{init})$ is the initial $^{12}C$ concentration of the seawater (which remains unchanged while dissolving 100% labeled materials) and $R^{13}_i$ is the $^{13}C/^{12}C$ ratio measured at time point $i$. $\Delta^{13}C_{2-1}$ is then the total number of moles dissolved between time points 1 and 2.

Not all cultured materials were completely labeled with $^{13}C$, and thus added both $^{13}C$ and $^{12}C$ to solution as they dissolved. The isotope ratio measured at time 2 in an experiment with incompletely labeled solid is defined in terms of the total moles of $^{12}C$ and $^{13}C$ in solution from two sources:

$$R_2^{13} = \frac{[^{13}C]_2}{[^{12}C]_2} = \frac{[^{13}C]_1 + [^{13}C]_{diss}}{[^{12}C]_1 + [^{12}C]_{diss}},\qquad(4.2)$$

where the subscript *diss* represents the number of moles of carbon that have dissolved between time points 1 and 2. The isotopic composition of the dissolving solid $R_s = \frac{[^{13}C]_{diss}}{[^{12}C]_{diss}}$. Substituting $^{12}C_{diss} = {}^{13}C_{diss}/R_s$ and $R_1 = {}^{13}C_1/{}^{12}C_1$ into Eq.(4.2), and rearranging for $[^{13}C]_{diss}$, allows for calculation of the number of moles dissolved in terms of measured isotope ratios and DIC concentration:

$$^{13}C_{diss} = [DIC] \cdot m_{sw} \left(\frac{R_s}{R_1 + 1}\right)\left(\frac{R_1 - R_2}{R_2 - R_s}\right);$$

$$^{12}C_{diss} = \frac{^{13}C_{diss}}{R_s};\qquad(4.3)$$

$$C_{diss,tot} = {}^{13}C_{diss} + {}^{12}C_{diss} = [DIC] \cdot m_{sw}\left(1 + \frac{1}{R_s}\right)\left(\frac{R_s}{R_1 + 1}\right)\left(\frac{R_1 - R_2}{R_2 - R_s}\right).$$

At the limit of a 100% labeled material (very large $R_s$), Eq.(4.3) reduces to Eq.(4.1). A numerical analysis of this equation as a function of $R_s$ is shown in Figure 4.1. In 300 g of seawater with a typical DIC = 2000 $\mu$mol/kg, the number of moles dissolved corresponding to a 10 ‰ signal in the bag $\delta^{13}C_{DIC}$ increases strongly with decreasing $R_s$ (Figure 4.1a). Similarly, propagating a 10% relative error on $R_s$ through Eq.(4.3) shows that the error on the number of moles dissolved also grows strongly when $R_s < 1$ (Figure 4.1b). This strong dependence means that the dissolution rate of materials labeled < 50% is very sensitive to the ratio of the solid. Above $R_s = 1$, the error on the number of moles dissolved is relatively insensitive to $R_s$, because of the larger contribution of $^{13}$C to the changing $\delta^{13}$C of seawater.
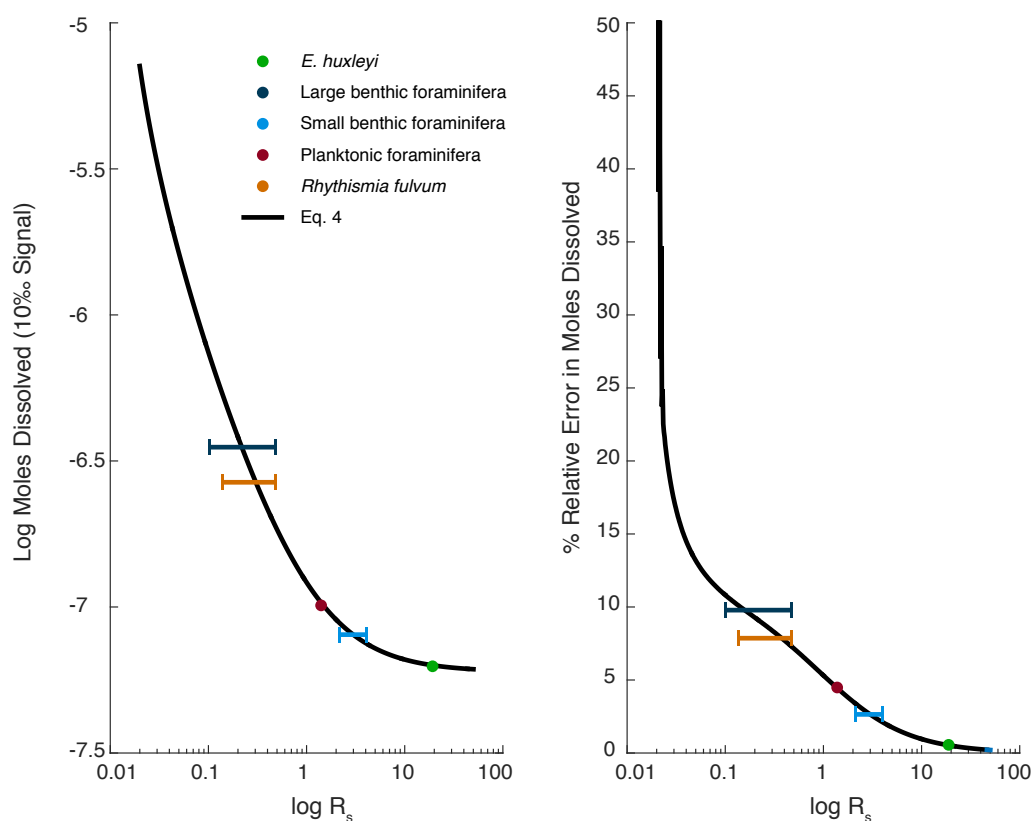


**Figure 4.1:** Numerical analysis of Eq.(4.3). The extent of labeling as determined through Eq.(4.4) and bulk analysis is also shown for reference. Numerical values of $R_s$ for these materials are shown in Table 4.1. **a)** Total moles dissolved as a function of the $\log(R_s)$, given a $\delta^{13}$C signal in an experiment of 10 ‰. This plot assumes 300 g of seawater with DIC = 2000$\mu$mol/kg. **b)** Relative error of the number of moles dissolved as a function of $\log(R_s)$. For reference, an $R_s$=1 means the sample is 50% $^{13}$C.

Figure 4.1 also shows the measured isotopic composition of the biominerals cultured in this study. Culturing of biogenic carbonates does not necessarily lead to a 100% $^{13}$C solid. In many cases, $^{13}$C-labeled calcite overgrows previously precipitated

calcite, leading to isotopic heterogeneity in the final cultured biomineral. If seawater only dissolves the outer layers of calcite, which are also the most strongly labeled, the isotopic composition of the *dissolving* solid will be different than the isotopic composition of the *bulk* solid.

The amount of $^{13}$C labeling in cultured materials was therefore assessed in two ways. First, the bulk solid isotopic composition was measured. Small (~0.1 mg) samples of whole carbonate shells were weighed out and transferred into 12 mL AutoMate glass vials with screw-on plastic septum caps. Vials were then evacuated, and then acidified with 3 mL 10% phosphoric acid. Acidified samples were then analyzed for their total $CO_2$ and $\delta^{13}$C using the Picarro CRDS system described in A. V. Subhas et al., 2015, standardized against gravimetric mixtures of natural abundance optical-grade calcite and pure $^{13}$C calcite from Sigma Aldrich. The response of the Picarro over large isotope ratio changes ($^{13}$C/$^{12}$C = 0.01 - 20) was linear.

Secondly, the amount of labeling of the *dissolving* solid was determined by measuring the alkalinity change in dissolution experiments. For each biogenic material presented here, at least one dissolution experiment was allowed to proceed long enough to generate measurable changes in alkalinity. These experiments provide the strongest constraint on the instantaneous value of $R_s$ in Eq.(4.3). Dissolution adds two equivalents of alkalinity for every mole of carbonate dissolved:

$$C_{diss,tot} = \frac{1}{2}\left(m_2 Alk_2 - m_1 Alk_1\right), \qquad (4.4)$$

where $m_i$ is the mass of seawater at time point $i$. The amount of dissolution measured using Eq.(4.3) was used to estimate alkalinity at every time point, and was compared against the measured alkalinity. $R_s$ was then varied until the measured and estimated alkalinities matched. An example of this type of analysis is shown for dissolution of benthic foraminifera in Figure 4.2, where the benthic foraminiferal $R_s$ was adjusted to a value of 4 to match the measured alkalinity values. Alkalinity and $\delta^{13}$C data demonstrated good agreement using a single value of $R_s$, indicating that the $^{13}$C content of dissolving carbonate did not change significantly over the course of an experiment. Only one dissolution experiment using poorly labeled benthic foraminifera ($R_s = 0.1$) showed a significant deviation from a single $R_s$ calibration curve, and this deviation manifested itself after about 15 % mass loss.

Moles dissolved calculated in this way, using alkalinity-calibrated $R_s$, were plotted versus time and then fit with straight lines to determine the dissolution rate (Figure 4.5). As in A. V. Subhas et al., 2015, straight lines after 24 hours were typically
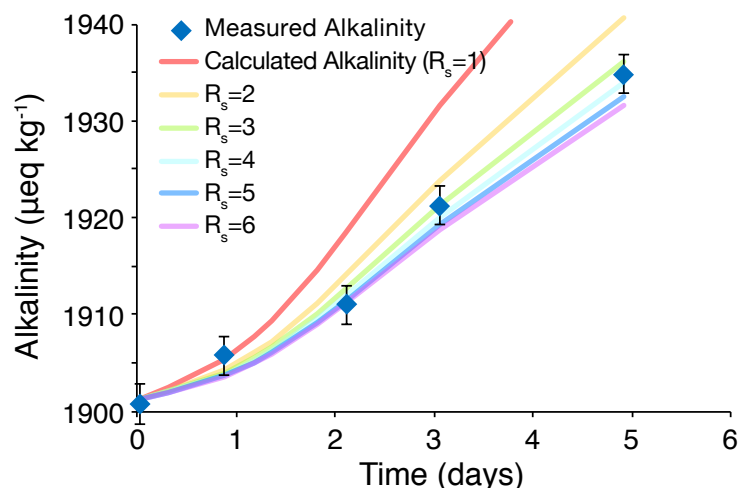
**Figure 4.2:** An example of measured versus calculated alkalinity for a dissolution experiment using benthic foraminifera (125-300$\mu$m; expt. no. B63-B3). Error bars on measured alkalinities are the standard error of the in-house standard measured in the same analytical session. The measured $\delta^{13}$C values for this experiment were transformed into a calculated alkalinity using integer values of $R_s$ from 1-6, propagated through Equations 4.3 and 4.4. These alkalinity curves are shown as solid lines for comparison to the data. An $R_s$ of 4 was chosen based on this analysis.

chosen to provide fits. Changes from this 24-hour cutoff will be described in detail below.

**Sample characterization**

Specific surface areas were determined by the BET method Brunauer, Emmett, and Teller, 1938 using Kr as the analysis gas on at least 0.05 square meters of calcite (A. V. Subhas et al., 2015; Kanel and J W Morse, 1979). Analysis was performed on a Micromeritics ASAP 2010 instrument. Surface areas were performed on all samples for which sufficient material was available: Aldrich calcite, untreated coccoliths, large (710-1000$\mu$m) size fraction benthic foraminifera, and well-preserved single-species planktonic foraminifera specimens picked from core tops (*G. ruber, G. sacculifer*, and *O. universa* species), sieved into multiple size fractions. Cultured planktonic foraminifera were not used directly due to small samples. The core top values were used instead to normalize rate data.

Organic matter content was established by measuring the total carbon and organic carbon content of cultured carbonates, bleached and untreated, using a Costech elemental analyzer attached to a Picarro CRDS. (can we cite Joyce's paper for this? Need details on EA make and model). Total carbon samples were measured into either 4x6mm or 5x9mm tin capsules, and standardized against an optical-

grade calcite standard material of known isotopic composition. The organic matter fraction of bleached and untreated carbonate samples was measured by the vapor-decarbonation method (e.g. Harris, Horwath, and Kessel, 2001). Samples were standardized against Optical calcite and the USGS-1 Urea standard.

Metal-calcium ratios were measured on an Agilent 7500 quadrupole ICP-MS. Samples were dissolved in 5% trace-metal clean HCl and diluted to 1 mM total calcium concentration. These solutions were then run on the ICP-MS, bracketed by blanks and an in-house standard that was calibrated for accuracy to reference materials. Relative standard deviations for the in-house standard in a single run were $\leq 1\%$.

## 4.3 Results

### Sample characterization
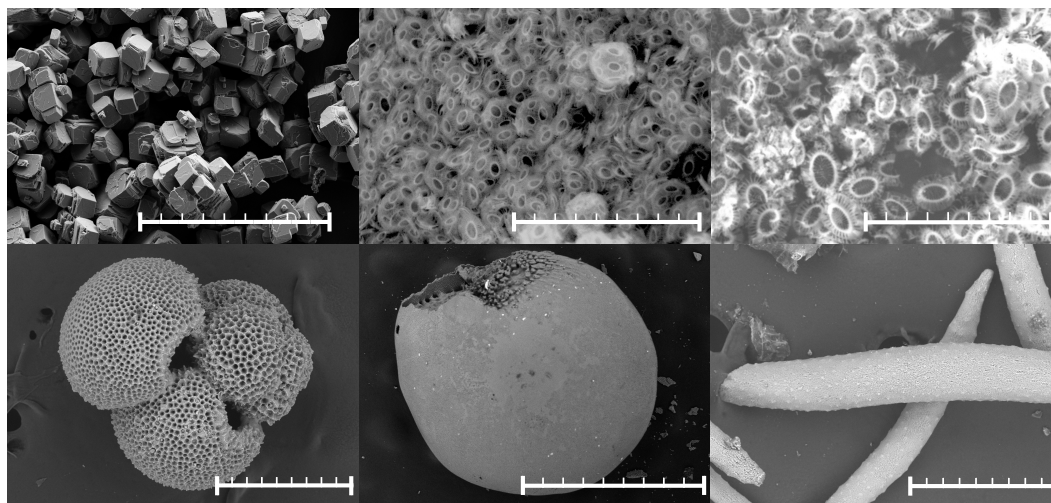


**Figure 4.3:** SEM images of materials used in this study. Clockwise, from top left, with scale bar lengths in parentheses: Aldrich calcite (200 $\mu$m); untreated *E. huxleyi* liths (20 $\mu$m); bleached *E. huxleyi* liths (10 $\mu$m); spicules from the soft coral *Rhythismia fulvum* (200 $\mu$m); a large Amphistegina test (1,000 $\mu$m); a test of the planktonic foraminifera *G. ruber* (300 $\mu$m).

Secondary electron microscope (SEM) images of all materials are shown in Figure 4.3. Measurements of Kr-BET surface area, organic carbon content, Mg/Ca, and $R_s$ for all materials presented here are shown in Table 4.1. Bleached *E. huxleyi* contained less $C_{org}$ by weight than untreated coccoliths, decreasing from 6% before treatment to 1.5%. *E. huxleyi* have the highest specific surface area as determined by Kr-BET (10.5 m$^2$g$^{-1}$). Planktonic foraminifera had a mean surface area of 4.7 m$^2$ g$^{-1}$ and did not show any relationship between measured surface area and sieving fraction (Chapter B). Large benthic foraminifera had the smallest specific surface

| Material | Size ($\mu$m) | SSA (m$^2$ g$^{-1}$) | mol% $C_{org}$ | wt% Mg/Ca (mole %) | $R_s$ |
|---|---|---|---|---|---|
| Aldrich Calcite | 70-100 | 0.09 | 0 | 0 | $\geq$ 99 |
| *Rhythismia fulvum* | | 0.69 | 0.90 | 12 | 0.15-0.5 |
| *E. huxleyi* | | 10.4 | 6.0 | 0.01* | 20 |
| *E. huxleyi* bleached | | 10.4 | 1.5 | 0.01 | 20 |
| Planktonic Foraminifera | | 4.0 | 0.29 | 0.5* | 1.5 |
| Benthic Foraminifera | 710-1000 | 0.11 | 0.18 | 3.5 | 0.1-0.5 |
| | 300-500 | | | | 2-3 |
| | 125-300 | | | | 4-6 |

**Table 4.1:** Compilation of pertinent data collected on the biogenic carbonates cultured for dissolution experiments. Asterisks indicate values taken from the literature because of the lack of sufficient sample material. Soft corals, coccoliths, and planktonic foraminifera were not separated into size classes due to the homogeneity of lith sizes (for coccoliths) and the scarcity of material (for planktonics). Foraminiferal and soft coral organic content is reported for bleached specimens only, and thus represents only the organic matter intimately associated with the carbonate lattice.

area of all biogenic calcites at 0.1 m$^2$ g$^{-1}$.

Measured Mg/Ca values for the benthic foraminifera and the soft coral *Rhythismia fulvum* were 3.5 and 12 mol %, respectively. Due to sample size limitations, For coccoliths and planktonic foraminifera, values were taken from the literature (e.g. H M Stoll et al., 2001; Anand, Elderfield, and Conte, 2003). Samples ranged from almost no Mg (inorganic calcite, *E. huxlyei*) to 12 mol% Mg (*Rhysthismia fulvum*). Planktonic and benthic foraminifera contained intermediate Mg content.

All foraminifera used in this study are of the perforate group. Perforate foraminifera typically precipitate low-Mg calcite and form consecutive chambers, adding calcite laminations to older chambers during new chamber formation (J Erez, 2003; Shmuel Bentov, Brownlee, and Jonathan Erez, 2009). Because new generations of planktonic foraminifera cannot be cultured in the laboratory, we could not completely label planktonic foraminifera tests. However, alkalinity calibrations of the dissolving ratio of our cultured foraminifera show a dissolving $R_s$ of 1.5 (Table 4.1 and Figure 4.1), indicating that about 60 % of dissolving foraminiferal calcite was labeled with $^{13}$C. This ratio indicates that on average, cultured foraminifera more than doubled in mass between plankton tow collection and gametogenesis in culture.

Benthic *Amphistegina* species show a much wider range of $R_s$ compared to planktonic foraminifera. Large individuals are only weakly labeled, with a bulk $R_s$ = 0.1. In other words, the large *Amphistegina* only increased their shell mass by about 10 % during culturing, consistent with very slow growth rates observed in larger individuals (Kuile and Jonathan Erez, 1984). The $R_s$ calibrated on these same individuals using Eq.(4.4) produced a dissolving ratio of about 0.5. The difference

between bulk (0.1) and dissolution-calibrated (0.5) $R_s$ is because the most recently precipitated – and thus strongest labeled – calcite overgrows previously deposited calcite, and is thus the most exposed to seawater.

There was a spawning event in the benthic foraminifera culture vessels, leading to many small foraminifera that grew up from gametes in culture. Many of these small individuals were thus completely labeled in $^{13}$C. In some cases, the calibrated $R_s$ deviated from the bulk $R_s$, but as demonstrated in Figure 4.1 and Eq.(4.3), an $R_s > 1$ does not significantly impact the total number of moles dissolved. In all dissolution rate calculations, we used the alkalinity-calibrated $R_s$.

*E. huxleyi* were the most strongly labeled in $^{13}$C as measured by bulk analysis and verified through alkalinity measurements during experiments. The soft coral *Rhythismia fulvum* was also rather weakly labeled ($R_s$=0.15). The range of $R_s$ values in Table 4.1 reflects the range between the bulk measurement (typically the lower bound) and the alkalinity-calibrated values (typically higher than the bulk measurement). No range means that the bulk and alkalinity-calibrated $R_s$ were the same. If these two values differed, the alkalinity-calibrated $R_s$ was used to calculate the amount of total dissolution.

**Dissolution experiments**

Slopes of moles dissolved versus time were taken and normalized to the mass of carbonate in each experiment. Coccolith dissolution rates were calculated after the initial curvature (e.g. after 0.3 days in Figure 4.5). Because soft coral and foraminiferal curves were straight for the entire dissolution experiment, the rate calculation was insensitive to the time interval over which the rate was taken. For these samples, rates were typically calculated over the first 1-2 days of experiment to minimize mass loss and changing seawater saturation state. If alkalinity changed significantly over the duration of an experiment, saturation state was calculated from the mean and standard deviation (rather than standard error) of the alkalinity over the pertinent time interval.
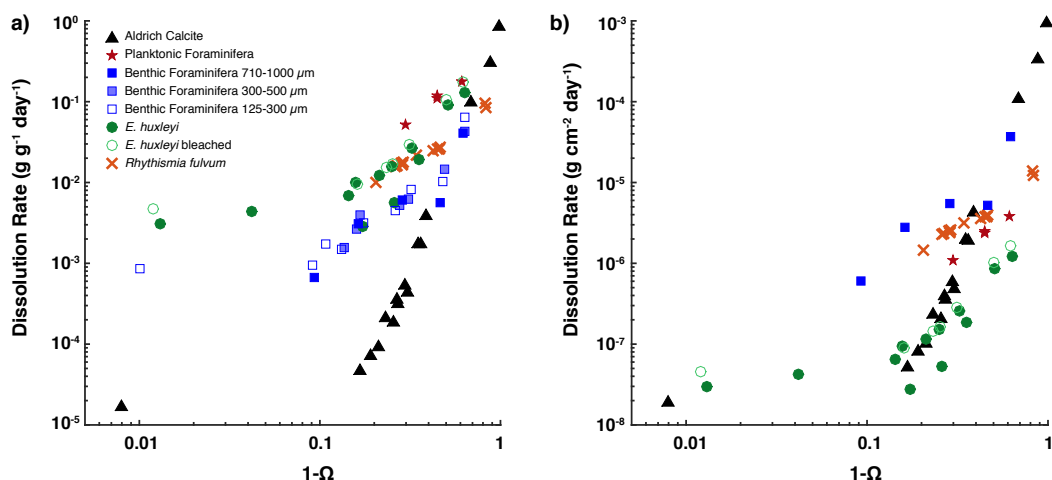
**Figure 4.4: a)** Mass- and **b)** surface area-normalized dissolution rate data for all biogenic and inorganic calcites measured, plotted on logarithmic axes. All materials have a nonlinear relationship to saturation state: slopes of all materials are greater than 1. Regression parameters of log(dissolution rate) versus log(1-$\Omega$) are shown in Table 4.2.

Dissolution rates at multiple saturation states for all biogenic materials are shown normalized by mass in Figure 4.4a and by mass and specific surface area in Figure 4.4b. There are fewer benthic foraminiferal curves in Figure 4.4b because SSA was only measured on the 710-1000 $\mu$m size fraction. Regressions of log(Rate) versus log(1-$\Omega$) were performed on all materials. The slope $n$ and intercept $k$ for these regressions are presented in Table 4.2. For Aldrich and *E. huxleyi* regressions, only data after $\Omega$=0.85 were used because of the strongly kinked data evident in Figure 4.4.

| Material | $n$ | $\log k_{mass}$ ($\frac{g}{g\,day}$) | $\log k_{sa}$ ($\frac{g}{cm^2\,day}$) |
|---|---|---|---|
| Aldrich Calcite | 5.7±0.2 | -0.17±0.1 | -2.6±0.1 |
| *Rhythismia fulvum* | 1.5±0.1 | -0.99±0.04 | -4.83±0.04 |
| Planktonic Foraminifera | 1.8±0.1 | -0.35±0.05 | -5.0±0.2 |
| Benthic Foraminifera | | | |
| 125-300$\mu$m | 1.8±0.2 | -1.1±0.2 | n/a |
| 300-500$\mu$m | 1.8±0.2 | -1.2±0.1 | n/a |
| 710-1000$\mu$m | 1.8±0.4 | -1.8±0.4 | -4.3±0.3 |
| *E. huxleyi* | 2.3±0.1 | -0.31±0.05 | -5.44±0.05 |
| *E. huxleyi* bleached | 2.1±0.1 | -0.3±0.1 | -5.5±0.1 |

**Table 4.2:** Regression fits of log(rate) versus log(1-$\Omega$) for all materials $n$ is the slope of this regression, and $k$ is the intercept. Surface-area normalized dissolution rate constants are shown for materials with BET surface area measurements.

Very close to equilibrium, the dissolution rates of inorganic calcite, benthic foraminifera,

and coccoliths show a very weak dependence on saturation state (Figure 4.4). Below about $\Omega = 0.9$, dissolution rate increases nonlinearly as a function of undersaturation. The $n$ for aldrich calcite (Table 4.2) is different from that in A. V. Subhas et al. (2015) because far-from-equilibrium data are also included in these fits, which increases $n$ significantly. Biogenic calcite dissolution rates also exhibit a nonlinear response to saturation state, but with a smaller $n$ than inorganic calcite. The $n$ values calculated here ($n$ = 1.8 - 2.3) are consistent with recent measurements of bulk sediment dissolution ($n$ = 1.4-2.8; Gehlen et al., 2005b. This similarity indicates that our biogenic dissolution data should reflect more accurately how carbonate sediments might respond to changing seawater saturation state.

The soft coral *Rhythismia fulvum* is the only material in this study that can be classified as a high-magnesium calcite. It has an Mg content of 13-14 mole % Mg as determined by ICP-MS analysis on whole spicules. The $K'_{sp}$ of high-Mg biogenic carbonates is highly variable, and thus it is difficult to constrain the x-axis on plots like Figure 4.4. Instead, we used the method of Keir (1980) and extrapolated our dissolution rate data to zero-rate. The carbonate ion concentration at zero-rate was then used to calculate a new $K'_{sp}$. Data from John W Morse and Mackenzie (1990) suggest that the $K'_{sp}$ for 12-14 mole % calcites is very similar to that of Aragonite. Our extrapolated zero-rate $K'_{sp}$ is almost identical to that of aragonite, giving us confidence in our choice.

Normalized by mass, the dissolution rates of all biogenic materials are faster than inorganic calcite (Figure 4.4a). This is especially evident near equilibrium. Farther from equilibrium, rates begin to converge with each other. Planktonic foraminifera dissolve slighly faster than coccoliths. Coccolith and soft coral rates are similar, and benthic foraminifera dissolve the most slowly. There is no significant separation betwen the dissolution rates of three different size classes of benthic foraminifera. Bleached and unbleached coccolith dissolution rates also show no significant difference.

Normalized by surface area, the trends between materials change significantly, due to the large range in measured specific surface areas (Table 4.1 and Figure 4.4b). Near equilibrium, coccoliths dissolve at a similar rate to inorganic calcite. Farther from equilibrium, however, they dissolve significantly more slowly than inorganic calcite. Both planktonic foraminifera and soft corals also dissolve more slowly than inorganic calcite far from equilibrium. Planktonic foraminifera and soft corals exhibit intermediate dissolution rates, and benthic foraminifera exhibit the fastest

specific dissolution rates. The benthics also appear to follow inorganic calcite dissolution rates far from equilibrium.

## 4.4 Discussion

Dissolution rates of biogenic carbonates are often offset from each other, sometimes by orders of magnitude (Keir, 1980; Gehlen et al., 2005a; Pickett and A J Andersson, 2014; Walter and J W Morse, 1985; Ries et al., 2016). We observe similar offsets in rates, normalized by both mass and surface area (Figure 4.4 and Table 4.2). These significant differences in the *n* and *k* values between different calcites imply that the mineral itself exerts strong control on its dissolution behavior: seawater $\Omega$ alone cannot predict how fast a given calcite will dissolve. Despite these large offsets, both mass- and surface area- normalization schemes give useful information about the reactivity of these biogenic calcites. Below, we discuss mass-and surface area-normalized dissolution rates of our biogenic materials, and attempt to build an understanding of what controls their behavior as a function of saturation state. Along the way, we also touch on the usefulness of BET surface area measurements for interpreting trends in dissolution rates. In particular, we use surface area-normalized coccolith and inorganic calcite dissolution rates to show the importance of organic matrices within the calcite lattice for dissolution rates. We then use the dissolution behavior of benthic foraminifera to show the importance of $Mg^{2+}$ on dissolution rates. Finally, we incorporate these two ideas into a basic framework in which $Mg^{2+}$ content enhances dissolution near equilibrium, and organic matrices within the carbonate lattice retard dissolution rates far from equilibrium.

**Mass-normalized dissolution rates of biogenic calcites**

Mass-normalized rates are often used in ocean models which incorporate $CaCO_3$ dissolution (Friis et al., 2006; Dunne, Burke Hales, and Toggweiler, 2012; Jokuls-dottir and D. Archer, 2016). Mass is a useful denominator in models because of its direct translation to a quantity of sediment or particulate matter in the water column (Keir, 1980; Fukuhara et al., 2008; Honjo and J Erez, 1978; Keir, 1983). Our dissolution rates show that planktonic foraminifera dissolve the fastest per gram. Coccoliths are slightly slower. Therefore, per gram, foraminifera will deliver alkalinity slightly more rapidly back to the water column than coccoliths. These results are borne out in deep sea sediments, where coccolith calcite is preferentially preserved (W. Broecker and Clark, 2009). Benthic foraminifera, on the other hand, deliver the least alkalinity per gram of sediment, and soft corals deliver a similar

amount as coccoliths. The mass normalized trend of dissolution is thus planktonic foraminifera >coccoliths ≥ soft corals > benthic foraminifera. This trend, while useful for predicting sedimentary preservation, does not correspond only to the magnesium content of these biominerals (Table 4.1), as has been suggested by Pickett and A J Andersson (2014).

Organic carbon has also been suggested to control dissolution rates of deep-sea particles, through respiration-driven dissolution (Milliman, Troy, et al., 1999; Steven Emerson and M. Bender, 1981). Our experiments are conducted in poisoned, filtered, and UV-treated seawater. Thus, we do not have any respiration during the course of our experiments, an assertion borne out by the very tight control of alkalinity and DIC over the course of an experiment (A. V. Subhas et al., 2015). Organic coatings on coccoliths have also been suggested to suppress their dissolution rate (Keir, 1980; Honjo and J Erez, 1978). This hypothesis was made based on the faster dissolution of bleached coccoliths compared to untreated coccoliths. In this study, we removed organic matter in the same way as both Keir (1980) and Honjo and J Erez (1978) by treating with 2% sodium hypochlorite. This process decreased the organic matter content by 75% (Table 4.1), and disaggregated intact coccospheres (Figure 4.3). The earlier studies did not report the organic carbon contents of their bleached coccoliths, and thus it is difficult to directly compare our results with theirs. However, we observe no difference in dissolution rate between bleached and untreated *E. huxlyei* liths over a wide range of saturation states (Figure 4.4), suggesting that organic coatings do not affect coccolith dissolution rates.

One possible difference here is the amount of available surface area for dissoultion between bleached and unbleached coccoliths. While not immediately apparent in Figure 4.4a, there are two unbleached points that show slow dissolution rates compared to the rest of the curve, at $\Omega \sim 0.82$ and 0.7 in Figure 4.4b. The untreated coccoliths formed a thick, flaky, cake-like consistency when dried, instead of a fine powder. This caking has been observed before in sediment trap samples (Heather M Stoll and Patrizia Ziveri, 2002; Bairbakhish et al., 1999), and could contribute to a lower available surface area for dissolution compared to completely disaggregated coccospheres. Bleached coccoliths, on the other hand, behave like a fine calcite powder. It is possible that a similar effect is responsible for the discrepancy in dissolution rates observed by Honjo and J Erez (1978) and Keir (1980).

Inorganic and biogenic dissolution data also suggests that rates should scale with inverse grain size (A. V. Subhas et al., 2015; Keir, 1980; Cubillas et al., 2005).

Mass normalization should show an inverse grain size relationship with larger grains dissolving more slowly than smaller ones. However, our dissolution data of multiple size classes of benthic foraminifera, from 125 $\mu$m - 1 mm, show the same dissolution rates when normalized by mass. This data suggest that the surface area available for dissolution is not controlled by test size, but by microstructural features instead. This explanation implies that different size classes of *Amphistegina* species have the same specific surface area (m$^2$ g$^{-1}$). In other words, the area of calcite exposed per gram of *Amphistegina* test does not change with the test diameter. In support of this argument are our measurements of planktonic foraminiferal BET surface area (Appendix B). These measurements show no significant relationship to foraminiferal size, again suggesting that there are microstructural features controlling available surface area instead of the size of the test itself.

**Surface area normalization**

The surface areas presented here were measured using multi-point Kr-BET, which has been shown to provide much more accurate surface area measurements on small samples than Nitrogen-BET (A. V. Subhas et al., 2015; Kanel and J W Morse, 1979). To our knowledge, these surface area measurements are the first made on *Rhythismia fulvum* spicules and *Amphistegina* tests. We cannot compare these values to the literature. We recover the same surface area as previous studies for coccoliths (Honjo and J Erez, 1978). The surface areas measured for planktonic foraminifera is about a factor of two larger than those measured previously (Honjo and J Erez, 1978; Keir, 1980). We used the multi-point method to calculate BET surface areas, with a minimum of six points to constrain the slope and intercept of our pressure data. A one-point calculation of surface area can also be made on a single $p/p_0$ value. One-point BET surface areas of planktonic foraminifera are about 2 m$^2$g$^{-1}$, similar to those reported by Honjo and J Erez (1978). The multi-point method is more robust, as it regresses all of the pressure-volume data to calculate the amount of gas adsorbed (Brunauer, Emmett, and Teller, 1938). Additionally, our surface area determination agrees with the surface areas measured on large size-fraction carbonate-rich sediment, which is mostly made up of foraminifera (Gehlen et al., 2005a; Gehlen et al., 2005b). We are thus confident in our surface area determinations and conclude that they accurately reflect the area of calcite exposed to Krypton gas.

Normalization by surface area changes the relative trends in dissolution rate between the biogenic calcites presented here (Figure 4.4). Because coccoliths have the

largest specific area, they exhibit the largest offset between mass- and surface area-normalized dissolution rates. Near equilibrium, surface area-normalized coccolith rates are nearly identical to the dissolution rate of inorganic calcite. As undersaturation increases, inorganic rates increase much more rapidly than coccolith rates. Coccolith dissolution rates have long been observed to be slower than inorganic calcite (Honjo and J Erez, 1978; Keir, 1980). Farther from equilibrium, our findings are consistent with these earlier studies. However, we show that close to equilibrium, surface area-normalized dissolution rates of coccolith and inorganic calcite are very similar. These curves diverge significantly from each other at about $\Omega = 0.7$.

When normalized by surface area, planktonic foraminifera dissolve faster than coccoliths, by a factor of the ratio of their specific surface areas (10.5/4.5 = 2.2). There was no measurable relationship between sieving size fraction and specific surface area in planktonic foraminifera, suggesting no relationship between test size and specific surface area (Appendix B). The Kr-BET surface area of planktonic foraminifera more probably measures the surface area of microstructural features. The lack of relationship between test size and surface area should not be surprising, given the complexity of foraminiferal test ultrastructure. The dissolution flux of foraminiferal-rich sediment should thus be insensitive to the size of foraminifera present. Instead, dissolution will be sensitive to microstructural features and other characteristics of the foraminiferal test. Planktonics demonstrate a slightly shallower slope $n$ versus $1-\Omega$ (Table 4.2) from coccoliths, although this relationship is only based on four points.

Once normalized by specific surface area, the benthic foraminifera *Amphistegina* tests dissolve more quickly than both planktonic foraminifera and *E. huxleyi* (Figure 4.4b), especially near equilibrium. Their surface area is a factor of 20 smaller than that of planktonic foraminifera, and this difference is enough to switch their relative dissolution rates. We only plot the surface area normalized dissolution rates for the 710-1000 $\mu$m size class of *Amphistegina*, because this is the only sample for which we had sufficient material to measure specific surface area (Table 4.1). However, given the discussion above of planktonic foraminiferal surface area measurements, and the lack of separation of mass-normalized *Amphistegina* dissolution rates, it is likely that all size fractions have a similar specific surface area.

With the exception of near-equilibrium coccolith and inorganic calcite dissolution rates, BET surface areas fail to collapse the dissolution rates of biogenic calcites onto a single curve. This lack of agreement between calcites has been used as evidence

for the inadequacy of BET to capture "reactive" surface areas of biogenic calcites (John W Morse, Rolf S Arvidson, and Lüttge, 2007). Instead of stopping here, however, we show below that our $\delta^{13}C$ data allows for a more detailed investigation of dissolution rates, and we show that these differences are related to both $Mg^{2+}$ and organic matter content in the calcite lattice.

**Mechanistic insights from curves of $\delta^{13}C$ versus time**

In undersaturated seawater, we measure the net rate of dissolution by constraining the slope of the number of moles dissolved versus time, typically after some initial curvature in our $\delta^{13}C$ data. Previously, we have shown that this initial curvature is related to the small imbalance gross dissolution and precipitation (A. V. Subhas et al., 2015; A. Subhas, Adkins, J. Erez, Rollins, et al., Under Review). In undersaturated solutions, the amount of dissolution is greater than the amount of precipitation, although both processes are still exchanging mass between the solid and solution. A larger gross dissolution flux leads to an initially steep increase in seawater $\delta^{13}C$, until the mineral surface comes into steady state with respect to both gross dissolution and gross precipitation (A. Subhas, Adkins, J. Erez, Rollins, et al., Under Review). Once steady state is reached, the net rate can be estimated by taking the slope of the straight line after this initial curvature.
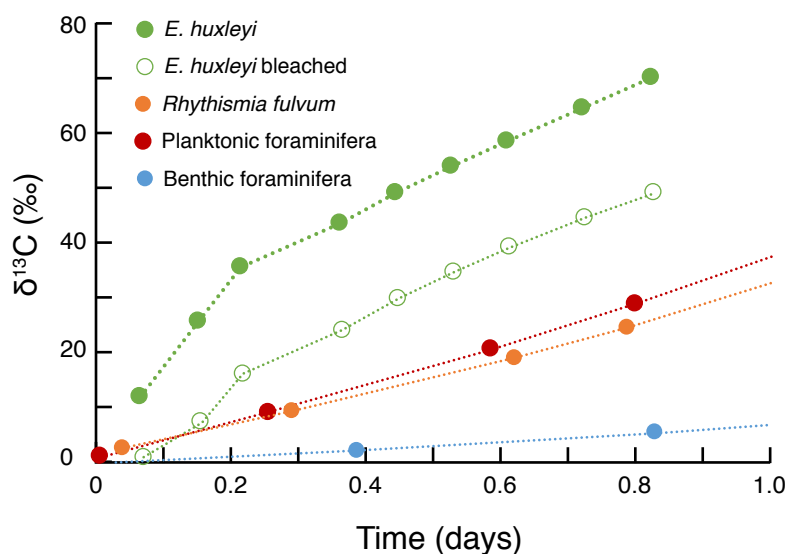


**Figure 4.5:** The first 24 hours of $\delta^{13}C$ versus time for various biogenic materials. Coccolith experiments shown here were terminated after 20 hours. Differences between different materials' curves are discussed below. Note the strong curvature in coccolith curves versus the essentially straight lines for most other materials.

Dissolution experiments conducted with cultured biogenic materials showed two distinct behaviors of $\delta^{13}$C versus time (Figure 4.5). Coccolith calcite exhibited curvature of $\delta^{13}$C over time, similar to Aldrich calcite (A. Subhas, Adkins, J. Erez, Rollins, et al., Under Review; A. V. Subhas et al., 2015). Bleached and untreated *E. huxleyi* samples showed different initial $\delta^{13}$C enrichments, but leveled off to the same slope after about 7 hours (0.3 days in Figure 4.5). In contrast, foraminiferal and soft coral curves were essentially straight for the entire dissolution experiment.

Time traces of $\delta^{13}$C can lend insight into the divergence of coccolith and inorganic dissolution rates farther from equilibrium. Figure 4.6 shows $\delta^{13}$C data for coccolith and Aldrich dissolution experiments close to equilibrium (Figure 4.6a) and far from equilibrium (Figure 4.6b). The y-axes of these plots have been normalized to the final $\delta^{13}$C value of the experiment for ease of comparison. At Ω=0.78, coccolith and inorganic calcite demonstrate nearly identical curvature, and their net rates normalized by surface area are also comparable. Farther from equilibrium, net dissolution of inorganic calcite is dominated by gross dissolution such that there is little to no curvature (e.g. Figure 4.6b). At Ω = 0.35, coccolith $\delta^{13}$C is much more curved than Aldrich calcite. This strong curvature suggests that there is a strong precipitation flux at the lith surface which considerably decreases the net dissolution rate, even very far from equilibrium.
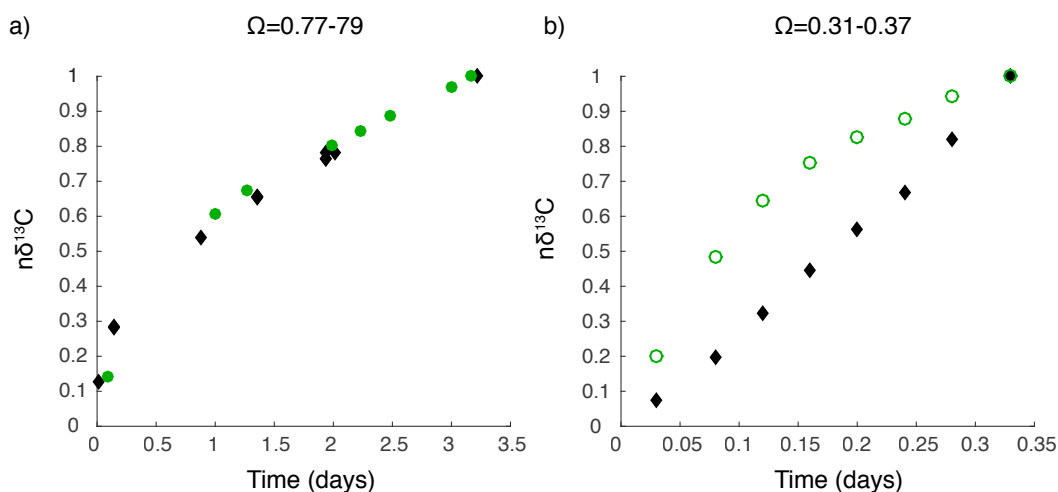


**Figure 4.6:** Curves of normalized $\delta^{13}$C ($\delta^{13}$C$_t$/$\delta^{13}$C$_{final}$) versus time for coccoliths (closed and open green circles) and Aldrich calcite (black diamonds) at two saturation states. **a)** Dissolution curves of Aldrich and untreated (closed circle) coccoliths at Ω = 0.77 − 0.79. Note the similarity in curvature between the two materials. **b)** Dissolution curves of Aldrich and bleached (open circle) coccoliths at Ω = 0.31 − 0.37. There is significantly more curvature in the first 8 hours of dissolution for coccoliths compared to Aldrich calcite.

Bleached and untreated coccoliths show similar net dissolution rates far from equilibrium (Figure 4.4b). Bleached coccoliths still retain 1.5 % by weight organic carbon, and extreme curvature is noticeable in the bleached coccolith dissolution data in Figure 4.6b. Such depression of dissolution rates cannot be due to external coatings of organic matter, because they were removed during bleaching. Instead, the organic material in question may be embedded in the calcite lattice, such that a surficial treatment of bleach does not remove it. Rather than a masking effect of surficial organic matter, we propose that specific (but as yet unidentified) organic molecules embedded within the calcite lattice enhance precipitation reactions at the lith surface, even in undersaturated conditions. This enhanced precipitation leads to extreme $\delta^{13}$C curvature.

Such a role for lith-bound organics in the mediation of dissolution-precipitation reactions is consistent with the findings of Gal et al. (2016), and also with the observation that coccoliths persist in deep-sea sediments much longer than other biogenic calcites (A. McIntyre and R. McIntyre, 1971). The presence of organic matrices in coccolith calcite is an active area of research (Gal et al., 2016; Young and Henriksen, 2003; Mackinder, Wheeler, and Schroeder, 2010). Recently, Gal et al. (2016) found that soluble macromolecules bound in the calcite lattice of *P. carterae* liths bound to calcium ions in solution and nucleated calcium clusters around the organic base plate framework. Similar to this finding, the liths dissolved here could release their lattice-bound soluble macromolecules into solution, which in turn would bind to calcium (10 mM in seawater), increasing local supersaturation, and enhancing the reprecipitation of calcite. This organic mediation of dissolution-reprecipitation reactions is a different mechanism for coccolith preservation than has been previously suggested. It also provides the hypothesis that the observed sensitivity of different coccolith species to dissolution (e.g. Berger, 1973) will be related to the amount and type of organic matrix trapped within the lith calcite.

Although coccoliths show very strong curvature, it is surprising that foraminiferal and soft coral calcite do not demonstrate this behavior. Dissolution curves of $\delta^{13}$C versus time for the foraminifera in this study are linear over the entire dissolution experiment, unlike both coccolith and inorganic calcite curves (see Figure 4.5, Figure 4.6, and A. V. Subhas et al. (2015) and A. Subhas, Adkins, J. Erez, Rollins, et al. (Under Review)). This linearity, even in the first 24 hours, suggests that dissolution processes vastly outweigh precipitation processes, even near equilibrium where dissolution and precipitation should be closely balanced. Such an imbalance leads

to linear curves of $\delta^{13}$C versus time, like that seen for Aldrich calcite far from equilibrium in Figure 4.6b.

There are two potential reasons for fast dissolution rates near equilibrium. First is the effect of changing surface area as foraminiferal shells dissolve. Even at very small amounts of mass loss, SEM images of the smooth top of *Amphistegina* tests show significant alteration of the surface (Figure 4.7). Pits, channels, and surface roughness develop as more mass is lost from the test, all of which act to increase the surface area in contact with seawater. Surface areas have indeed been shown to grow under extreme amounts of dissolution (Honjo and J Erez, 1978). Increased surface area with a relatively unchanged shell mass would lead to a higher dissolution rate over time, which would counteract any curvature in our plots of $\delta^{13}$C versus time.
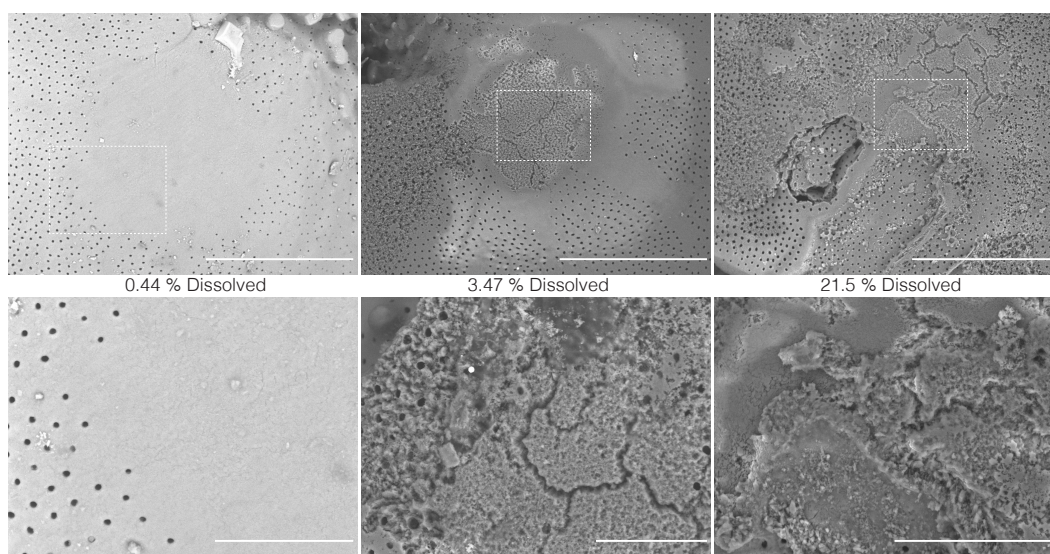


**Figure 4.7:** SEM images of the top of *Amphistegina* tests (the smooth center of the test in Figure 4.3) after increasing amounts of mass loss. Scale bars in the top row are 300 $\mu$m; scale bars in the bottom row are 30 $\mu$m. Note the large texture change as mass loss increases.

The second potential cause for fast dissolution rates near equilibrium is the high Mg content of *Amphistegina* species (3.5 mole %). *Amphistegina* tests have a higher Mg content compared to planktonic foraminifera by about one order of magnitude (Shmuel Bentov, Brownlee, and Jonathan Erez, 2009; S Bentov and J Erez, 2005; A. Y. Sadekov, Stephen M Eggins, and Patrick De Deckker, 2005). Bulk solubility products measured on calcites with 0-4 mole % Mg do not demonstrate an increase in solubility with Mg content (John W Morse and Mackenzie, 1990). Bulk thermodynamics, however, do not necessarily dictate the kinetic response of Mg-bearing carbonates to undersaturated seawater. Indeed, several studies have

found that the kinetics of dissolution are influenced by Mg content, even below 8 mole % (Pickett and A J Andersson, 2014; Walter and J W Morse, 1985; Ries et al., 2016), the Mg content of calcite in equilibrium with seawater (T Oomori et al., 1987).

The effect of Mg on dissolution rate also depends on the location of magnesium within the test. In fact, Mg/Ca heterogeneity is a common feature in many foraminiferal species (A. Y. Sadekov, Stephen M Eggins, and Patrick De Deckker, 2005; S Bentov and J Erez, 2005). High-Mg bands are observed normal to the test growth axis (A. Y. Sadekov, Stephen M Eggins, and Patrick De Deckker, 2005; S M Eggins, A. Sadekov, and P De Deckker, 2004), and there are many hypotheses as to the physiological signficance of these bands (S Bentov and J Erez, 2005; J Erez, 2003; Branson et al., 2016; Evans, Jonathan Erez, et al., 2015; Evans, Müller, et al., 2013). Analyses of core-top foraminifera have shown a decrease in bulk Mg/Ca as bottom water undersaturation increases, suggesting that Mg-rich bands dissolve disporportionately faster than Mg-poor phases (Johnstone, Jimin Yu, et al., 2011; Johnstone, Schulz, et al., 2010; Brown and Elderfield, 1996). In this study, we have strong constraints on the total mass loss measured from $\delta^{13}$C and alkalinity changes in our experiments. If mass is lost congruently, we should expect no change in calcite Mg/Ca after dissolution. If high-Mg bands are dissolved preferentially, calcite Mg/Ca should decrease as a function of the amount of mass lost.

Metal-Calcium analyses performed on benthic foraminiferal tests recovered from quenched dissolution experiments show a decrease in Mg/Ca as function of mass dissolved (Figure 4.8a; all Me/Ca data can be found in Appendix C). These measurements were made on single large (710-1000$\mu$m, closed symbols) and multiple small (125-300$\mu$m, open symbols) foraminifera. There is one outlier in Figure 4.8, which could be due to the mixture of individuals with a range of Mg-contents. However, the overall trends in Figure 4.8 cannot be explained solely by mixing, since individual large foraminifera also show a decrease in Mg/Ca with increasing mass loss.

Although bulk shell $K'_{sp}$ may not change significantly with mole % Mg, the trend in Figure 4.8 suggests that more soluble Mg-rich phases dissolve first, leaving behind Mg-poor phases. Such dissolution behavior could explain the straight lines of $\delta^{13}$C versus time (Figure 4.5), as these phases will dissolve very quickly without concomitant reprecipitation due to their higher solubility. Mg-rich calcite dissolution could also help explain the fissuring and textural changes observed on the top of the

fist of *Amphistegina* tests (Figure 4.7), if these features are nucleated at high-Mg bands. Mg-rich phases will also be disproportionately sensitive to dissolution close to calcite equilibrium, where Mg-free calcite reacts very slowly. As a result, near-equilibrium dissolution increases very strongly as mole % Mg increases (see below and Figure 4.9).

Figure 4.8b shows B/Ca ratios in dissolved *Amphistegina* shells as a function of percent dissolved. Boron content also decreases as more shell is dissolved, such that at 27% dissolution, the B/Ca has decreased from 600 to 200 $\mu$mol/mol. Even at very small amounts of dissolution – 0.2 to 1 % dissolution – B/Ca decreases by 30% to about 400 $\mu$mol/mol. Moreover, there is a strong relationship between Mg/Ca and B/Ca (Figure 4.8c). This relationship of B/Ca to Mg/Ca suggests that B and Mg dissolve out preferentially, that these shell components are related to each other, and that they are possibly co-located in the test. B/Ca in foraminiferal shells is currently being developed as a useful and powerful proxy for reconstructing past ocean seawater carbonate system parameters (Henehan et al., 2013; J Yu, Elderfield, and Honisch, 2007; Rae et al., 2011). The strong relationship between B/Ca and % dissolution implies that strong care must be taken to choose well-preserved foraminifera for B/Ca analysis, as any primary signal could be modified through preferential dissolution of B- and Mg- rich phases out of the foraminiferal test.
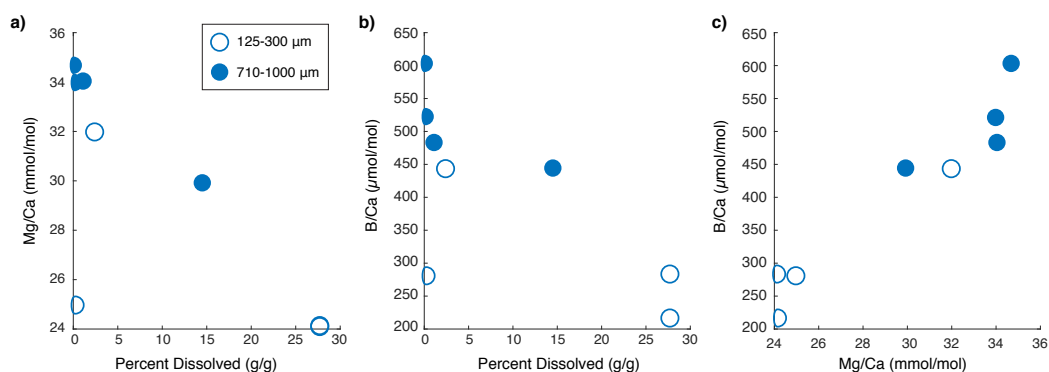


**Figure 4.8:** Measurements from a suite of metal-calcium ratio measurements conducted on *Amphistegina* tests retrieved from quenched dissolution experiments. **a)** Mg/Ca in mmol/mol. The x-axis was calculated from $\delta^{13}$C data in each dissolution experiment; the y-axis was measured independently. **b)** B/Ca in $\mu$mol/mol. **c)** cross-plot of B/Ca versus Mg/Ca.

**The combined effects of Mg and Corg on dissolution rates**

Two significant differences between inorganic and biogenic calcites are 1) their Mg content and 2) the amount of organic carbon bound in the calcite lattice. When

normalized by specific surface area, biogenic dissolution rates are more linear than inorganic calcite, such that closer to equilibrium, rates are generally faster, and farther from equilibrium rates are generally slower (Figure 4.4). As discussed above, Mg preferentially dissolves from benthic foraminiferal shells, which could lead to the observed enhanced reactivity close to equilibrium. Organic matter bound in coccoliths, on the other hand, seems to supress dissolution rates far from equilibrium by promoting reprecipitation. Mg increases reactivity, and organic matter decreases it. The relative importance of Mg and $C_{org}$ on specific dissolution rate is investigated in Figure 4.9. Dissolution rates of all biogenic and inorganic calcites at $\Omega = 0.84$ and $\Omega = 0$ were plotted as a function of Mg and organic matter content. We chose to plot these two effects as Arrhenius relationships:

$$R = R_0 \exp(-x). \tag{4.5}$$

This functional form assumes a relationship between the inorganic rate ($R_0$), and the measured rate ($R$), such that $log(R/R_0)$ is a linear function of some quantity -$x$. In the Arrhenius and Eyring equations, $x = \Delta G/RT$. In our case, $x$ is either Mg content (mole %) or organic carbon content (wt %). By plotting our rates in this form, we assume a relationship between Mg and organic matter content and the free energy ($\Delta G$) of the calcite-seawater system. The 4-quadrants in Figure 4.9 demonstrate a relationship between Mg/Ca and dissolution rate close to equilibrium (top left panel), and a relationship between organic carbon content and dissolution rate far from equilibrium (bottom right panel). Neither $Mg^{2+}$ nor organic matter exhibit linear relationships in the framework of Eq.(4.5). Therefore, there is no straightforward link between these two calcite components and $\Delta G$.

Near equilibrium, there is a nonlinear relationship between Mg content and $\log(R/R_0)$ (upper left panel of Figure 4.9). Rate increases sharply with Mg content, and then plateaus between 5-10 mol % Mg. The strongest effect on rate is seen between 0 and 5 mol % Mg, where $K'_{sp}$ is least sensitive to Mg content, at least given the current literature solubility data. We should not expect a straightforward relationship between dissolution rate and Mg content: high-Mg carbonates have been shown to dissolve quickly and contribute significant alkalinity to reef and shelf carbonate systems (Andreas J Andersson, Bates, and Mackenzie, 2007; Pickett and A J Andersson, 2014; John W Morse, Andreas J Andersson, and Mackenzie, 2006). Conversely, Mg has also been shown to inhibit dissolution and precipitation in far-from-equilibrium dissolution experiments (R S Arvidson et al., 2006; M. Xu and Higgins, 2011). These competing relationships lead to a complicated relationship between Mg content and

calcite solubility (John W Morse, Rolf S Arvidson, and Lüttge, 2007; John W Morse and Mackenzie, 1990). These results only underscore this complicated relationship, and suggest that more careful studies of low-Mg calcite dissolution in seawater are needed.

Far from equilibrium, there is a strong relationship between % $C_{org}$ and dissolution rate (lower right panel of Figure 4.9), such that at 1.5% organic matter content, the dissolution rate is almost 2.5 orders of magnitude slower than the inorganic dissolution rate. The strong effect of organic matter on dissolution rate is not a new idea in the literature. Organic coatings have long been hypothesized as the reason for retarded dissolution rates of coccoliths (Keir, 1980; Honjo and J Erez, 1978). Our results show that it is not the organic "sheath" that protects the coccolith, but instead the organic matter intimately associated with the calcite lattice. This organic matter actively recruits ions responsible for precipitation, and thus slows down the overall dissolution rate. This hypothesis is supported by the presence of strong curvature in plots of $\delta^{13}C$ verusus time in coccolith dissolution rate data. The same process could be occurring in foraminiferal shells, although we do not observe similar curvature in the raw $\delta^{13}C$ data versus time, most likely because this curvature is being masked by changes in surface area and incongruous dissolution of Mg-rich phases (also discussed above). There is also less organic matter in foraminiferal tests, which would decrease the importance of this mechanism to the overall dissolution rate in forams.
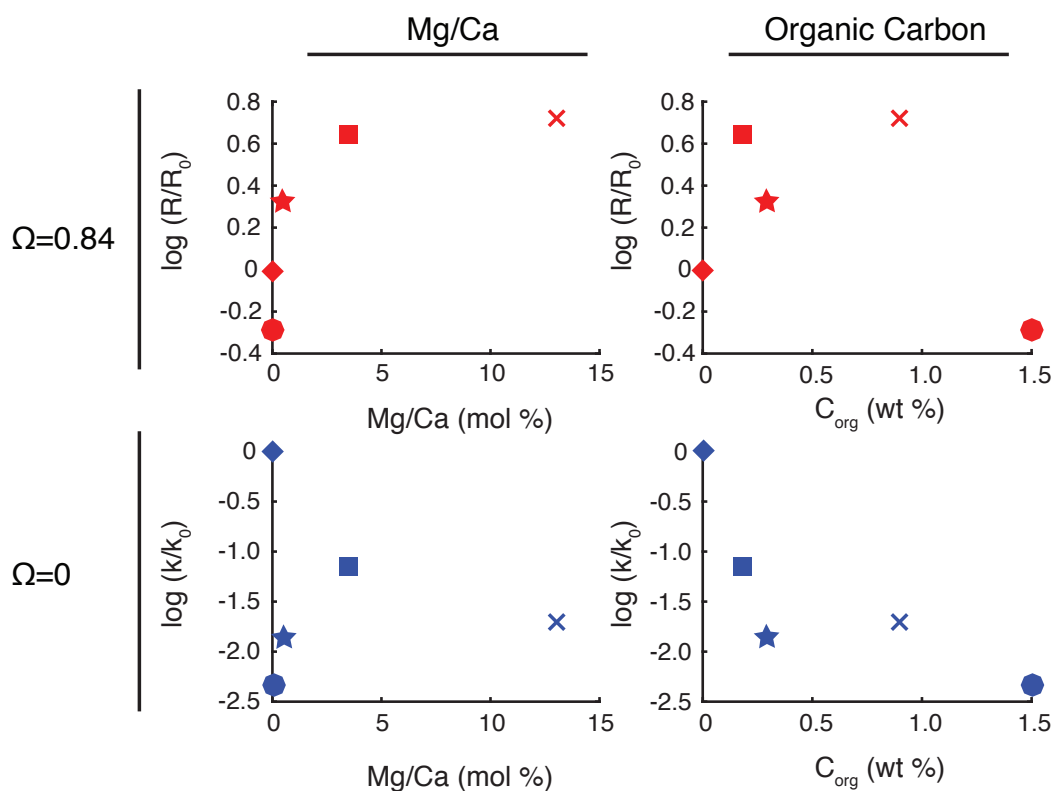
**Figure 4.9:** A 4-quadrant plot of dissolution rate versus Mg/Ca and organic carbon content for five different calcite types: inorganic (◆), coccolith (●), planktonic foraminiferal (★), benthic foraminiferal (■), and soft coral (**X**). The top two plots show the logarithmic ratio of rates at $\Omega = 0.84$. Rates for planktonic forams and soft corals were extrapolated to this saturation state using the regression parameters shown in Table 4.2. The bottom two plots show the logarithmic ratio of rates at $\Omega = 0$, or in other words, the rate constants shown in Table 4.2. Near-equilibrium rates show a relationship with Mg/Ca; far-from-equilibrium rates show a relationship with $\%C_{org}$.

## Surface features and a geometric model of dissolution

A lack of agreement between surface area normalized rates has long confounded chemical oceanographers and geochemists. In fact, crystal growth models based on the theory of W. K. Burton, Cabrera, and Frank (1951) provide a theoretical basis why specific surface features might react differently to the same saturation state. This theory imposes geometric constraints on the rate of crystal growth as a function of supersaturation, and allows for the development of several key features such as step edges, crystal defects, and 2-dimensional growth features (Malkin, Chernov, and Alexeev, 1989; L. C. Nielsen, Donald J DePaolo, and James J De Yoreo, 2012; H H Teng, P M Dove, and J J De Yoreo, 2000). Models of crystal growth have also been applied to mineral dissolution, and such models have successfully described the dissolution behavior of silicate minerals, and their transition between different

dissolution modes, such as step edge retreat, nucleation of etch pits at crystal defects, and nucleation of etch pits everywhere (P M Dove, Han, and J J De Yoreo, 2005; Patricia M Dove et al., 2008; Sangwal, 1987). The theory allows for crystal geometry to modify terms that are traditionally based on saturation state alone, ending in a final description of dissolution rate (P M Dove, Han, and J J De Yoreo, 2005):

$$\ln\left(\frac{|R_d|}{(1-\Omega)^{2/3}|\sigma|^{1/6}}\right) = \ln(h\beta C_e(\omega^2 h n_s a)^{1/3}) - \frac{\pi\alpha^2\omega h}{3(k_B T)^2}\left|\frac{1}{\sigma}\right|. \qquad (4.6)$$

Here, the left side is the normalized dissolution rate $R_d$ in units of moles m$^{-2}$ s$^{-1}$. $\Omega$ is the saturation state of calcite, and $\sigma = ln(\Omega)$. On the left hand side, $k_B T$ is the Boltzmann constant multiplied by temperature in K; i.e. the system's thermal energy. The physical parameters related to calcite are the step height $h$, molecular volume $\omega$, lattice spacing $a$, and $C_e$, which is equivalent to the $K'_{sp}$ for calcite. Terms that specifically involve a rate of dissolution are the dissolution velocity $\beta$ at defects, surface defect density $n_s$, and the interfacial energy barrier at nucleation sites $\alpha$. The product $\beta n_s^{1/3}$ is found in the intercept of Eq.(4.6), while the interfacial energy is found in the slope of Eq.(4.6).

When plotting the left hand side of Eq.(4.6) versus $|1/\sigma|$, P M Dove, Han, and J J De Yoreo (2005) described three regions of behavior. A positive slope describes step edge retreat (Region 1). Negative slopes indicate 2D nucleation of etch pits, and typically there is a transition between 2D nucleation at surface defects (Region 2) and homogeneous 2D nucleation (Region 3).

In Figure 4.10, we show all of our biogenic data plotted in this space. It is hard to say much about planktonic dissolution rates because of the lack of data density, and its proximity to the transition between Regions 2 and 3. However, we see all three regions in our dissolution data, with Aldrich, coccolith, and benthic foraminiferal calcite all demonstrating positive slopes near equilibrium (at high $1/\sigma$; Region 1 in Figure 4.10a). This suggests that, near equilibrium, biogenic and inorganic calcite dissolves by step edge retreat. Furthermore, the similarity between coccolith and inorganic rates in this region suggests that these two calcites have a similar rate of step edge retreat.

Rates switch to negative slopes in (Region 2) at $1/\sigma = 6 = 12(\Omega = 0.85 - 0.92)$. Biogenic calcite slopes in Region 2 are generally more shallow than Aldrich calcite, consistent with the smaller $n$ values measured in the $1 - \Omega$ framework (Figure 4.10b and Table 4.2). This region has been previously hypothesized to represent

the formation of etch pits at surface defects (P M Dove, Han, and J J De Yoreo, 2005), and is also consistent with the opening of screw dislocations in the model of Lasaga and Luttge (2001). A shallower slope compared to inorganic calcite reflects a smaller value of $\alpha$, the interfacial energy at defects. Therefore, biogenic calcites demonstrate a lower barrier to dissolution at defect sites than inorganic calcite.
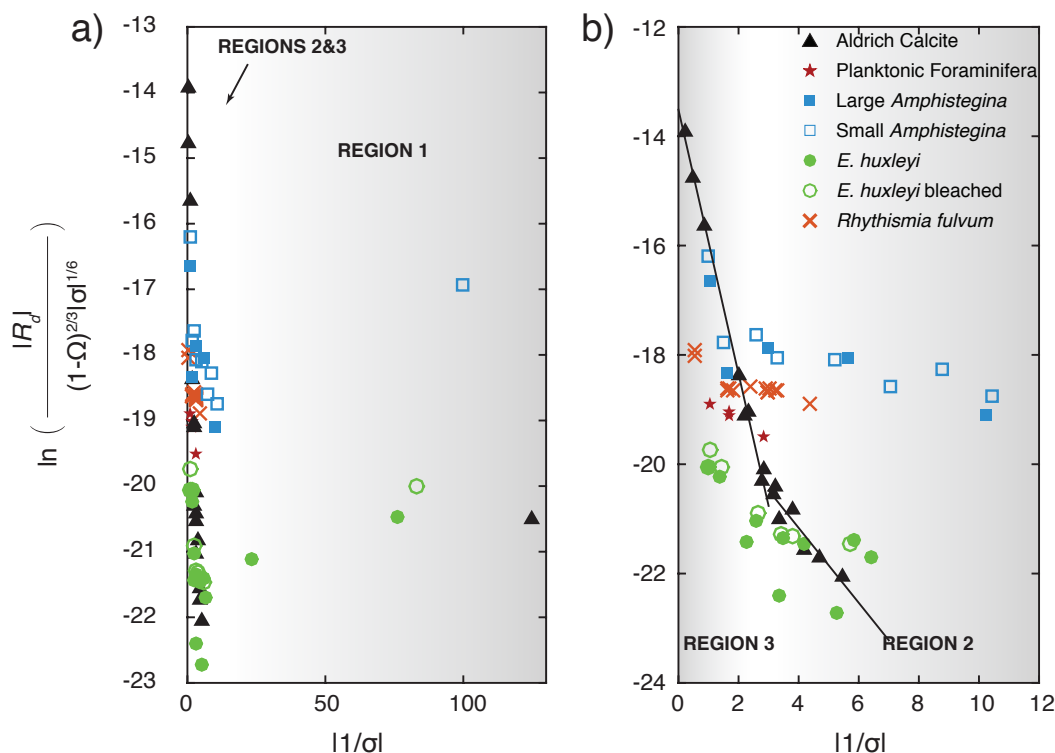


**Figure 4.10:** Dissolution rate data for all calcites measured in this study, presented in the framework of P M Dove, Han, and J J De Yoreo (2005). **a)** Dissolution rate data for all biominerals plotted as the left hand side of Eq.(4.6) versus $|1/\sigma|$. **b)** the same data blown up in the region $0 \leq |1/\sigma| \leq 12$. Note the shift from a postitive slope in Region 1 to negative slopes in Regions 2 and 3.

The transition between Regions 2 and 3 occur for all biogenics once their rates intersect with the inorganic reference frame, between $1/\sigma = 2 - 3(\Omega = 0.7 - 0.6)$. This behavior suggests that, even given the large variation in rates for these different minerals, the inorganic reference frame is dictating the underlying behavior of these biogenic calcites. In Region 3, *Amphistegina* dissolution rates actually fall on top of the inorganic dissolution curve (Figure 4.10b). *Amphistegina* calcite has high Mg content, but also relatively low organic matter content. Thus, far from equilibrium, we might expect the rate of benthic dissolution to be similar to inorganic calcite. Soft coral, planktonic, and coccolith dissolution rates all fall below the inorganic curve.

Coccolith dissolution rates are also the lowest, consistent with their high organic matter content suppressing dissolution rates far from equilibrium. Soft coral calcite falls in between coccolith and inorganic calcite, again consistent with the general trends between organic carbon content and dissolution rate.

The framework described above does not explicitly include terms for $Mg^{2+}$ or organic templates. In fact, it was developed for a single component crystal such as quartz (P M Dove, Han, and J J De Yoreo, 2005; Patricia M Dove et al., 2008). More work must therefore be done to adapt this model to a two component crystal such as $CaCO_3$, not to mention the incorporation of other components applicable to biogenic calcite dissolution. However, it is a promising descriptor of the differences between different biominerals and inorganic calcite.

## 4.5 Conclusion

The use of a $^{13}$C-tracer method grants unprecedented insights into the dissolution rates of biogenic calcites in seawater. Coupled with high-precision measurements of BET surface area using Kr gas, rates presented here show trends with saturation state, calcite Mg content, and calcite organic matter content. Analysis of curves of $\delta^{13}$C versus time from coccolith dissolution experiments leads us to the hypothesis that molecules released from the lith lattice actively promote re-precipitation of coccolith calcite, even far from equilibrium. This process retards dissolution far from equilibrium, and provides a mechanism for the preservation of coccoliths in seafloor sediments. Analysis of the Mg/Ca content of foraminiferal calcite before and after dissolution shows that Mg is preferentially leached out of calcite as it dissolves. In *Amphistegina* species, dissolution also preferentially leaches out boron. A compilation of all dissolution rates shows trends with Mg content near equilibrium, suggesting that more soluble Mg-rich calcite phases dissolve out quickly, over and above the effects of Mg content on bulk thermodynamic solubility. The leaching of these phases may help explain specific textural changes observed in foraminiferal tests from sediments. The compilation also shows trends with organic matter far from equilibrium, highlighting the effect of organics in recruiting ions from seawater for precipitation – a vestige of the original biomineralization process. We also apply a geometric dissolution model with our data that separates rates into three regions, consistent with step edge retreat, nucleation of etch pits at surface defects, and homogeneous nucleation of etch pits. This framework is also broadly consistent with our previous findings that organic matrices supress dissolution far from equilibrium, although more work is needed to fully explain the data in this framework. These

results help to quantify diagenetic changes in calcites due to dissolution, and move the field towards a quantitative understanding of how calcites dissolve in seawater.

*Chapter 5*

# 2D AND 3D ANALYSIS OF DISSOLVING BENTHIC FORAMINIFERA

## 5.1 Introduction

The shells of marine benthic foraminifera are a key paleoceanographic archive. In particular, the oxygen isotopic composition and Mg/Ca ratio of foraminiferal calcite have been used to constrain seawater chemistry composition, deep ocean temperature, and global ice volume over the Cenozoic (Lear, Elderfield, and Wilson, 2000; Lear, Rosenthal, and Slowey, 2002; Barker et al., 2005). Many individual species require their own calibrations however, speaking to our lack of understanding about how different physiologies mask underlying environmental signals (Anand, Elderfield, and Conte, 2003; J Erez, 2003). It has also been recognized from early on that Mg is not distributed homogeneously throughout the foraminiferal test (M. L. Bender, Lorens, and Williams, 1975). Closer analysis of calcite bands that run perpendicular to the growth direction have identified distinct banding in chemistry as well, with alternating high- and low-Mg layers (A. Y. Sadekov, Stephen M Eggins, and Patrick De Deckker, 2005).

Depending on their location in deep sea sediments, foraminiferal tests are also significantly altered by early diagenesis, through dissolution in the water column and on the seafloor. The presence or absence of intact foraminiferal tests, as well as specific morphological features linked to dissolution, have been used with various levels of success to quantify the corrosiveness of seawater (Dittert et al., 1999). In addition to visual and physical changes in test morphology (Corliss and Honjo, 1981; Honjo and J Erez, 1978; Berger, 1970; Kotler, R. E. Martin, and Liddell, 1992), bulk shell Mg/Ca also appears to decrease as a function of mass loss (Johnstone, Jimin Yu, et al., 2011; Brown and Elderfield, 1996).

Because Mg content has been shown to increase the solubility of calcite (John W Morse and Mackenzie, 1990), it has been proposed that dissolution disproportionately affects Mg-rich bands in foraminifera (Nouet and Bassinot, 2007; Johnstone, Jimin Yu, et al., 2011; A. Subhas, Adkins, J. Erez, P. Ziveri, et al., in prep.). We looked at the shallow-dwelling benthic foraminifera *Amphistegina lobifera* to investigate the link between shell chemistry effects to visible changes in morphology. We

used SEM images and high-resolution ($\leq 1\mu$m voxel size) CT scans to identify the regions responsible for mass loss, and attempt to tie those to specific morphological features of the test – and also to shell chemistry variations. CT scanning has been used to elucidate large-scale interior structures of benthic foraminifera (Hohenegger and Briguglio, 2012; Briguglio and Hohenegger, 2014), and a study by Johnstone, Schulz, et al., 2010 showed that CT scans could be used to qualitatively assess the extent of dissolution in planktonic foraminifera. SEM imagery has also been used for many years to identify patterns of dissolution in benthic foraminifera (Gonzales et al., 2017; Corliss and Honjo, 1981; Kotler, R. E. Martin, and Liddell, 1992). We attempt to use both techniques to quantify the effects of dissolution on *Amphistegina* test morphology. This work provides a potential tool to use in identifying preservation potential in benthic foraminifera. Finally, we propose a hypothesis for the morphological changes we see, related to the selective dissolution high-Mg bands in *Amphistegina* tests.

## 5.2   Materials and Methods

The large benthic foraminifera *Amphistegina* was collected from shallow (1-3 meter water depth) sediments in the Gulf of Aqaba, in the Red Sea. Foraminifera were then cultured as described in A. Subhas, Adkins, J. Erez, P. Ziveri, et al., in prep. Once culturing experiments were finished, foraminifera were washed three times with milli-Q water and dried at 60°C overnight. Some of these foraminifera were used in dissolution experiments, described in A. V. Subhas et al. (2015) and A. Subhas, Adkins, J. Erez, P. Ziveri, et al. (in prep.). Dissolution experiments were quenched by removing the foraminifera from the experimental apparatus, rinsing them with milli-Q water, and drying them at 60°C overnight. All foraminifera were stored in plastic vials at room temperature for further analysis. Both unreacted and dissolved specimens were used in this study.

### SEM imagery and analysis

SEM images of unreacted and dissolved benthic foraminifera were taken using a Hitachi TM-1000 Environmental SEM. Dissolved specimens were removed from quenched ^{13}C-dissolution experiments, such that the amount of mass loss was tightly constrained for each specimen (A. V. Subhas et al., 2015; A. Subhas, Adkins, J. Erez, P. Ziveri, et al., in prep.). In order for a true comparison across several images, all grayscale histograms were normalized to their full dynamic range using ImageMagick's "normalize" command. This command stretches the range of

grayscale intensities in the image to the full dynamic range, blacks out at most 2% of the lowest intensities and whites out at most 1% of the top intensities. Images were then imported into MATLAB, and the program "psd_2D" (included below) was used to calculate the radially-averaged power spectrum of surface topography in each image. Here we assume that grayscale is a proxy for surface topography in SEM images. The algorithm receives a grayscale image and a pixel size in meters. It converts pixels to area elements, and then computes a fast Fourier-transform for each element's grayscale value. It then radially averages these values, and plots this Fourier analysis as a power spectrum as a function of radial frequency $q$ ($m^{-1}$), which here has been converted to roughness wavelength $\lambda_z = 2\pi/q$. The resulting plot is a power spectrum of grayscale roughness as a function of wavelength $\lambda_z$.

## 3D imagery and volume analysis

Micro-CT scans were collected on one undissolved *Amphistegina* sp. benthic foraminifera, and one specimen from experiment B63-B1 (11.7% dissolved). Both foraminifera were from the 700-1000 $\mu$m sieving fraction. Scans were collected using a Rigaku Nano3DX CT scanner at USC's Molecular Imaging Center. Scans were collected at both 1.05 $\mu$m and 0.52 $\mu$m voxel resolution using a molybdenum source. The instrument then ran a reconstruction of the X-ray data to generate a z-stack of .tiff image files. Stacks of .tiff files from the reconstructed image were normalized using ImageMagick in order to reduce brightness-contrast differences between scanned specimens. These normalized stacks were then imported into the ImageJ package FIJI to make ortho-sections and 3D reconstructions. 2D-power spectra were once again collected on all images in each .tiff stack. In addition, the "local thickness" plugin of ImageJ was used to calculate the thickness of the shell (Dougherty, 2007). Local thickness is a measure of 3D thickness. Therefore, for each z-slice, the thickness map takes into account the thickness in the z-direction as well. The thickness map shows essentially the volume of the largest sphere whose center and entire volume is inside the object. The algorithm calculates local thickness for the entire 3D object, and z-slices show a single slice of the computed local thickness in three dimensions at that particular z-horizon.

Volume and surface area data on reconstructed foraminifera were collected using the software VGStudioMAX 3.0. Image stacks were imported from z-stacks that had been brightness-corrected to remove CT background noise. Surface areas and volumes were collected under three different data treatments: 1) Reconstructions without further adjustment; 2) Reconstructions using the "surface correction" algo-

rithm and a manual threshold for noise; 3) Reconstructions using the "surface correction" algorithm and an automated noise detection scheme based on user-specified regions of "material" and "background" to compute a background threshold. From these three surfaces, the software then computed total volume, object volume, and surface area. Sample weight was calculated by multiplying the object by the mean density of calcite: $m_{obj} = V_{obj} \cdot \rho_{calcite}$. Specific surface area, in units of square meters per gram, was calculated by dividing the surface area by the object's mass: $SSA = SA/m_{obj}$.

## 5.3 Results

**2D imagery and analysis**
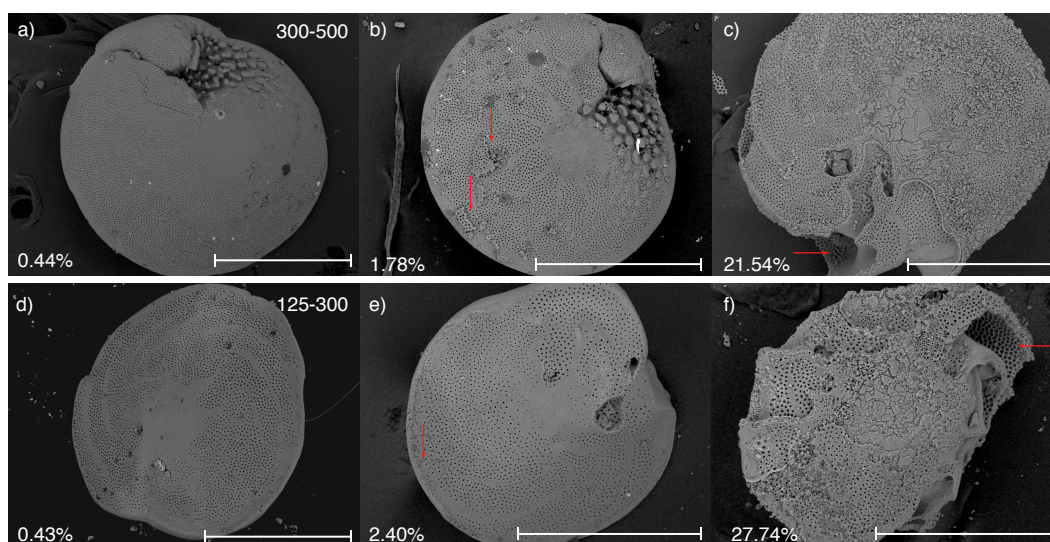


**Figure 5.1:** SEM images of benthic foraminifera after different amounts of mass loss. The amount of mass loss, shown in the bottom left hand corner of each image, increases from left to right. **a-c)** foraminifera from the 300-500 $\mu$m sieving fraction retrieved from quenched dissolution experiments. **d-f)** foraminifera from the 125-300 $\mu$m sieving fraction. Note the large texture change and loss of chambers under extreme mass loss. Specific dissolution features mentioned in the text are marked with red arrows. Scale bars in microns: **a)** 300, **b)** 300, **c)** 200, **d)** 200, **e)** 200, **f)** 200.

SEM images of whole dissolved benthic foraminifera are shown in Figure 5.1. The effects of dissolution are most obvious in the heavily dissolved specimens (**c** and **f**). The smooth centers of foraminifera under different amounts of mass loss are shown in Figure 5.2. Images **b-d** are the same as those in Chapter 4.
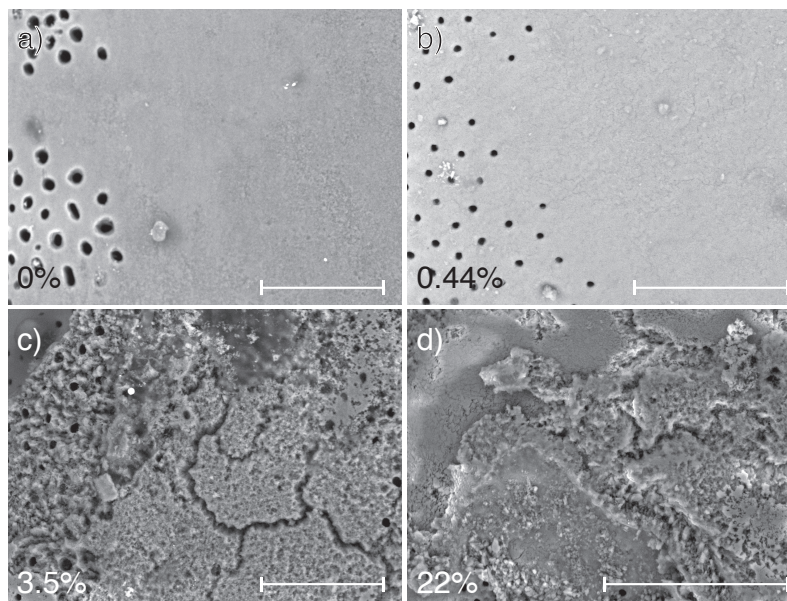
**Figure 5.2:** The smooth tops of large (700-1000 $\mu$m) benthic foraminifera *Amphistegina*, recovered from quenched dissolution experiments. The amount of total mass loss is shown in the bottom left corner of each image. Scale bars for all images are 30 $\mu$m.

## 3D Imagery and Analysis

A single z-slice from the 1.05 $\mu$m resolution CT scan of an undissolved *Amphistegina* test, and its computed local thickness, is shown in Figure 5.3. From the full set of z-slices, the entire test was reconstructed in 3D using ImageJ. Reconstructions for both unreacted and dissolved specimens are shown in Figure 5.4, in front- and side-view. There is significantly more surface texture on the dissolved specimen. In side view, more of the knobby textures at the chamber aperture are exposed. Surface areas and volumes for dissolved and undissolved specimens are shown in Table 5.1.

## 5.4 Discussion

### Dissolution-generated surface features

The *Amphistegina* tests studied here show a distinct pattern of mass loss as dissolution proceeds. *Amphistegina* grows a new chamber and adds an extra layer of calcite over previous chambers, leading to a laminated structure and a thickly calcified central knob. Tests with very small amounts of mass loss (Figure 5.1a,d), and no mass loss (Figure 5.4a,c and Figure 5.2a), show a relatively smooth surface, with pore structures and the unadorned central calcite knob. Several suture-like features can also be seen radiating from this central surface. The test aperture is adorned with knob-like features, which aid in pseudopod extension and feeding (J. Erez, *personal communication*). Specific dissolution patterns in SEM images and in 3D
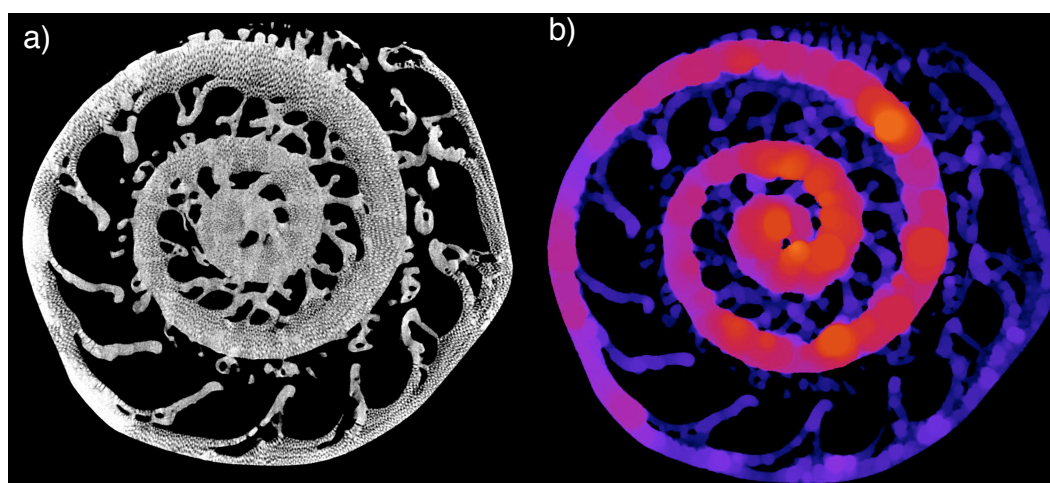
**Figure 5.3:** A z-slice from a 1.05-$\mu$m-resolution CT scan of an unreacted *Amphistegina* test. **a)** 8-bit grayscale image showing chamber whorls. The outermost chamber is the most recent addition to the test. The spots along the test surface are pores, many of which penetrate through the test walls. **b)** Local thickness map, showing test thickness for the z-slice in **a)** in all three dimensions. Warmer colors are thicker; cooler colors are thinner. This image shows the decrease in thickness moving from inside to the most recent chamber.

| | **Dissolved** | | | **Undissolved** | | |
|---|---|---|---|---|---|---|
| | uncorr. | Manual corr. (iso 19000) | ROI corr. (iso 15000) | uncorr. | manual corr. (iso 25995) | ROI corr (iso 23280) |
| Total Volume (mm$^3$) | 1.47 | 1.47 | 1.47 | 1.5 | 1.5 | 1.5 |
| Object Volume (mm$^3$) | 0.34 | 0.3 | 0.33 | 0.38 | 0.34 | 0.35 |
| Surface Area (mm$^2$) | 69.1 | 100.9 | 79.2 | 57.8 | 76.0 | 71.2 |
| | | | | | | |
| calc. wt (mg) | 0.89 | 0.79 | 0.87 | 1.00 | 0.89 | 0.92 |
| calc. SSA (m$^2$g$^{-1}$) | 0.077 | 0.128 | 0.091 | 0.058 | 0.085 | 0.077 |
| Emtpy volume (mm$^3$) | 1.13 | 1.17 | 1.14 | 1.12 | 1.16 | 1.15 |
| | | | | | | |
| meas. wt (mg) | 0.95 | | | 1.03 | | |
| Roughness change (%) | 33 | 51 | 18 | | | |

**Table 5.1:** Surface areas and volumes as calculated from VG Studio Max. Values are presented using three different image treatments. Surfaces were either not adjusted ("uncorr."), or adjusted using the software's "surface correction" algorithm, which allows for the resolution of sub-pixel features. These surface corrections were applied with both a manual threshold ("Manual corr.") and with an automated threshold ("ROI corr") in order to correct for the image background. ISO values for the thresholds are listed. Weights and specific surface areas were calculated from the volume and surface area estimates. The measured weight is also shown for comparison to calculated values. Roughness is calculated as the relative change in specific surface area between the dissolved and undissolved specimens for each image treatment (i.e. ($SSA_d/SSA_u$ -1)·100). In all cases, roughness is greater in the dissolved specimen compared to the undissolved specimen.
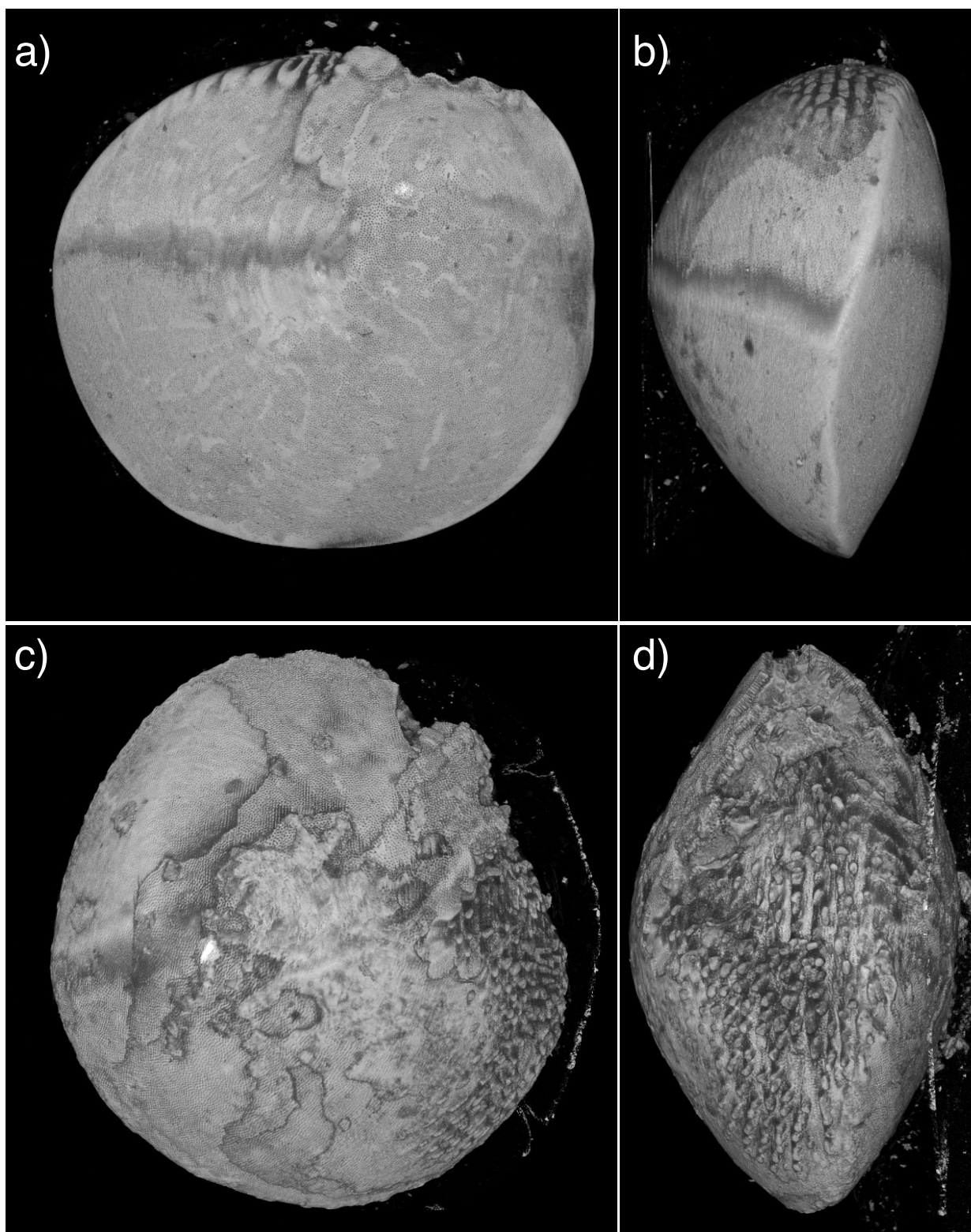
**Figure 5.4:** CT-scanned three-dimensional reconstructions of unreacted (**a-b**) and ~12% dissolved (**c-d**) *Amphistegina* tests. Front and side views are presented; tests are about 1 mm in diameter. Note the large increase in roughness in the dissolved specimen. Also note that the most recent, outermost chamber appears to have fully dissolved and come off.

micro-CT reconstructions begin to emerge which modify the test's initial structure (Figures 5.1, 5.2, and 5.4). Initial roughness and etching is not immediately apparent under very small amounts of mass loss (Figure 5.1a,d). After only 2% dissolution, however, large-scale features of dissolution can be seen, such as remnant "islands" of chamber laminae in Figure 5.1b and etching around the test perimeter in Figure 5.1e. The formation of etching channels and the development of surface roughness is even more evident in Figure 5.2: at only 3.5% dissolution, large etching channels have developed on the central knob.

Subsequent mass loss leads to the removal of calcite layers and the formation of larger etched channels (Figure 5.1c,f). These patterns are also evident in CT-reconstructions of the dissolved shell in Figure 5.4c and d. Notably in all of these specimens, the final chamber is often partially or completely missing, exposing the test interior. Loss of the final chamber has been used as a preservation metric in other benthic foraminiferal species (Corliss and Honjo, 1981; Gonzales et al., 2017). The remaining calcite layers also appear much more fragmented and etched (Figure 5.1c,f,Figure 5.4c,d), with a terraced pattern exposing multiple laminations.

The head-on and side view of a ~12% dissolved *Amphistegina* test (Figure 5.4c and d) also show significant effects from dissolution. Compared to the undissolved specimen in Figure 5.4a and b, the knobby features at the test aperture are much more exposed. This exposure suggests that the final chamber is significantly eroded in this specimen, with as little as 10% of mass lost. Such sensitivity to mass loss may be due to the fact *Amphistegina* species are particularly suceptible to dissolution compared to deep-sea benthic foraminifera (Corliss and Honjo, 1981). Additionally, Figure 5.3b shows that this final chamber wall is also the thinnest region of the test. Thus, it should be the most fragile compared to other chambers. The local thickness of other benthic foraminiferal species' chambers may give further insights into why certain species retain or lose their final chambers as they dissolve.

Given the striking visual differences between the unreacted and dissolved specimens observed in Figure 5.4, one might expect that the surface area to volume ratio (and the specific surface area; SSA) increases with mass loss. Calculations of SSA were compared for the unreacted and dissolved CT reconstructions in Figure 5.4. These results, presented in Table 5.1, show a modest increase in SSA by a factor of 1.18-1.51, or an 18-51% increase in specific surface area with 12% mass loss. The SSA increase is smallest when the software used its own "ROI" algorithm to subtract the background, and is highest when no correction is applied to the images. One way to

ground-truth these different image treatments is to compare their computed object volume (and thus object mass) with the object's measured mass. Measured masses are most similar to those calculated without any image correction. However, the dissolved/unreacted mass ratio (0.92) is most similar to the mass ratio calculated using the "ROI" algorithm (0.94). The other corrections produce different mass ratios: 0.89 for uncorrected, and 0.89 for manually corrected. Thus, in terms of comparing the two objects, the "ROI" algorithm calculations are probably the most accurate.
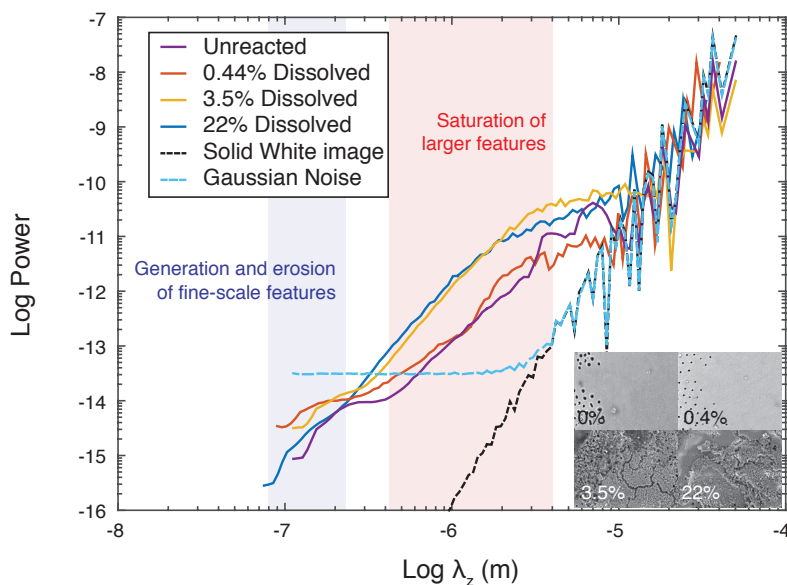


**Figure 5.5:** Radially averaged surface roughness power spectra as a function of length scale for the images in Figure 5.2. Features at about 0.4-3 $\mu$m, shaded in red, appear to reach maximum roughness after about 3.5% dissolution, and correspond to the larger fissures and channels seen in Figure 5.2**c** and **d**. Sub-micron features, shaded in blue, appear to increase in power at very small amounts of dissolution, and then disappear as dissolution proceeds, in favor of larger channels.

These calculations suggest that surface roughness increases by about 20% with 11% mass loss. Assuming a linear relationship between surface area and dissolution rate, a 20% increase in roughness would only increase the dissolution rate by a factor of 1.2. Such a rate increase is relatively minor, and should not have a major impact on the rate of reactivity of benthic foraminiferal calcite. In contrast, Honjo and J Erez (1978) found that planktonic foraminifera dissolved for 60 days in the deep ocean increased their SSA by a factor of up to 2 or 3 after only 30% dissolution. This discrepancy suggests that there may be a significant feedback between a test's initial structure, its dissolution rate, and the generation and propagation of surface

roughness as dissolution proceeds. For instance, in the same study, samples of *E. huxleyi* lost about 11% of their mass and showed only a 20% increase in SSA. Our results are broadly consistent with this large range in dissolution-generated roughness, and imply that benthic foraminifera do not increase in roughness significantly as a function of increasing mass loss. Instead, their reactivity should be driven by the initial surface features and structures of the test, which are then modified through the dissolution process. It is possible that once a majority of the inner test is exposed, such as in Figure 5.1c and f, SSA starts to change dramatically. However, up to about 10% mass loss, the surface features seen in Figures 5.1, 5.2, and 5.4, while visually striking, are more likely responders to dissolution, and their appearance does not significantly modify the shell's bulk SSA.

A well-defined progression of visual changes as a function of mass loss begs the question: can we quantify these changes and define some metric for dissolution-generated diagenetic features? To this end, 2D-power spectra of the images shown in Figure 5.2 were analyzed and are presented in Figure 5.5. This analysis assumes that grayscale variations across the image directly reflect surface topography. Although the TM-1000 collects both backscattered and secondary electrons, the calcite surface should be very similar between images and thus backscatter intensity due to elemental variations should be relatively small compared to secondary electron intensity due to surface topography. The smooth central knobs of benthic foraminifera are ideal surfaces for this analysis, because they are relatively flat, and have no underlying topography that could bias these power spectra.

Spectra of *Amphistegina* are compared to the power spectra of a solid white image and an image of purely Gaussian noise. The white image $\lambda_z$ falls constantly, demonstrating the red-shifted background spectrum of a completely flat spectrum. The noisy image $\lambda_z$ also falls sharply at first, and then plateaus to a typical white noise power spectrum at about $\lambda_z$=2.5 $\mu$m. The spectra of *Amphistegina* tops show several features. First, roughness power generally increases as a function of $\lambda_z$. Secondly, spectra are very noisy at length scales greater than 10 microns. This noise is consistent with noisier reference spectra as well, suggesting that limited spectral information can be gleaned at these length scales. Below this length scale, several patterns emerge. First, at the 0.4-3 $\mu$m length scale, all dissolved spectra exhibit greater roughness than the unreacted surface. The 0.44%-dissolved surface shows only modest roughness increases, whereas the 3.5% and 22% dissolved spectra show a large and similar enhancement in roughness compared to the unreacted surface.

This length scale is consistent with the size of surface channels which first appear in the 3.5%-dissolved image.

Below a length scale of about 0.25 $\mu$m, a different pattern emerges. All dissolved spectra are still enriched over the unreacted control. However, the order of enhancement switches. Here, the 0.44% and 3.5% spectra show a similarly large enhancement over the unreacted control. At these length scales, the 22% spectrum is only slightly enhanced over the unreacted surface. In combination, the patterns of roughness at these two length scales suggest a hypothesis for how dissolution affects foraminiferal calcite. At first, small (sub-micron) features are generated. These features then grow to large micron-scale channels and pits, which quickly saturate the surface with micron-scale roughness at about 3.5% mass loss. With more mass loss, roughness at the small scale is subsequently lost as small-scale features develop into larger features.
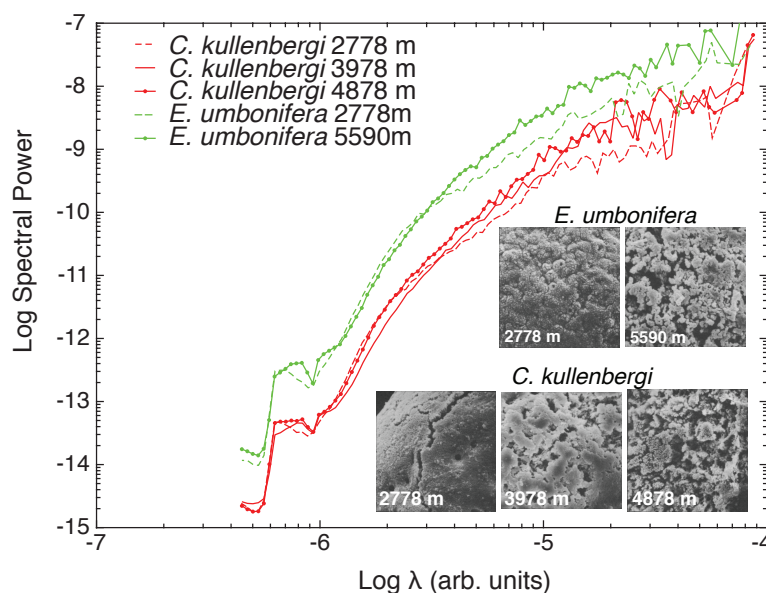


**Figure 5.6:** SEM images from several dissolved benthic foraminifera, described in Corliss and Honjo, 1981. Images corresponding to the curves are shown as insets at the bottom right. The power spectra of all images are color-coded by species. The spectra for *E. umbonifera* (green lines) are shifted to higher powers for figure clarity. The x-axis for this figure is in arbitrary units because the pixel size for these images is unknown. Listed magnification for these images is "479x".

Ideally, samples collected from the field would show similar patterns to those observed on specimens analyzed after laboratory experiments. However, few studies have collected images that meet the criteria necessary to perform the analysis presented here. The closest comparison in the literature is the study of Corliss and

Honjo (1981), which suspended several species of benthic foraminifera at multiple depths in the deep ocean for 60 days, recovered the shells, and used microscopy to investigate the effects of dissolution on test morphology. Several of these images were collected on the smooth tops of the shells. Two species of benthic foraminifera from this study – *C. kullenbergi* and *E. umbonifera* – had images of suitable quality and magnification to attempt a power spectrum analysis. The images, copied from an electronic copy of the Corliss and Honjo (1981) manuscript, along with their power spectra, are shown in Figure 5.6. One downside to this analysis is that the authors did not provide a scale bar for these images, and so the x-axis only provides a relative scale for wavelength. Given these complications, it is clear that in both species, between $\log(\lambda)$ = -4 and -6, the specimens suspended deeper in the water column exhibit a higher roughness than those suspended shallower in the water column. The "power reversal" evident in all dissolved *Amphistegina* specimens in Figure 5.5 at low $\lambda_z$ is harder to resolve here. For instance, the 5590m *E. umbonifera* specimen displays lower power than the 2778m specimen. However, the deep *C. kullenbergi* specimen does display lower power than the shallower specimen, indicating that the loss of surface roughness at these small length scales may be occurring. There is thus some hope that a more careful study of foraminiferal samples retrieved from the field could be used to further calibrate the use of roughness spectra as a metric for the extent of dissolution.

**The propagation of surface features into the shell's interior**

Evidence of dissolution, while present on the surface of these foraminifera, has also been documented by other researchers in the interior of foraminiferal calcite. For instance, Johnstone, Schulz, et al., 2010 showed that the tests of planktonic foraminifera lose density along dissolution surfaces parallel to the outer test wall. Furthermore, Nouet and Bassinot, 2007 showed that different phases are present within a single foraminiferal test, which contain different Mg contents and different crystallinities. Dissolution preferentially removes the more disordered, Mg-rich phase, leaving behind the more ordered, Mg-poor phase.

Similarly, A. Subhas, Adkins, J. Erez, P. Ziveri, et al. (in prep.) showed a decrease in Mg content with increased mass loss in the same *Amphistegina* tests presented in this study. Ion microprobe maps of foraminiferal calcite show distinct bands of Mg parallel to the test surface (A. Y. Sadekov, Stephen M Eggins, and Patrick De Deckker, 2005), suggesting that the distribution of Mg in foraminifera is related to specific layers deposited during biomineralization. Johnstone, Jimin Yu, et al.
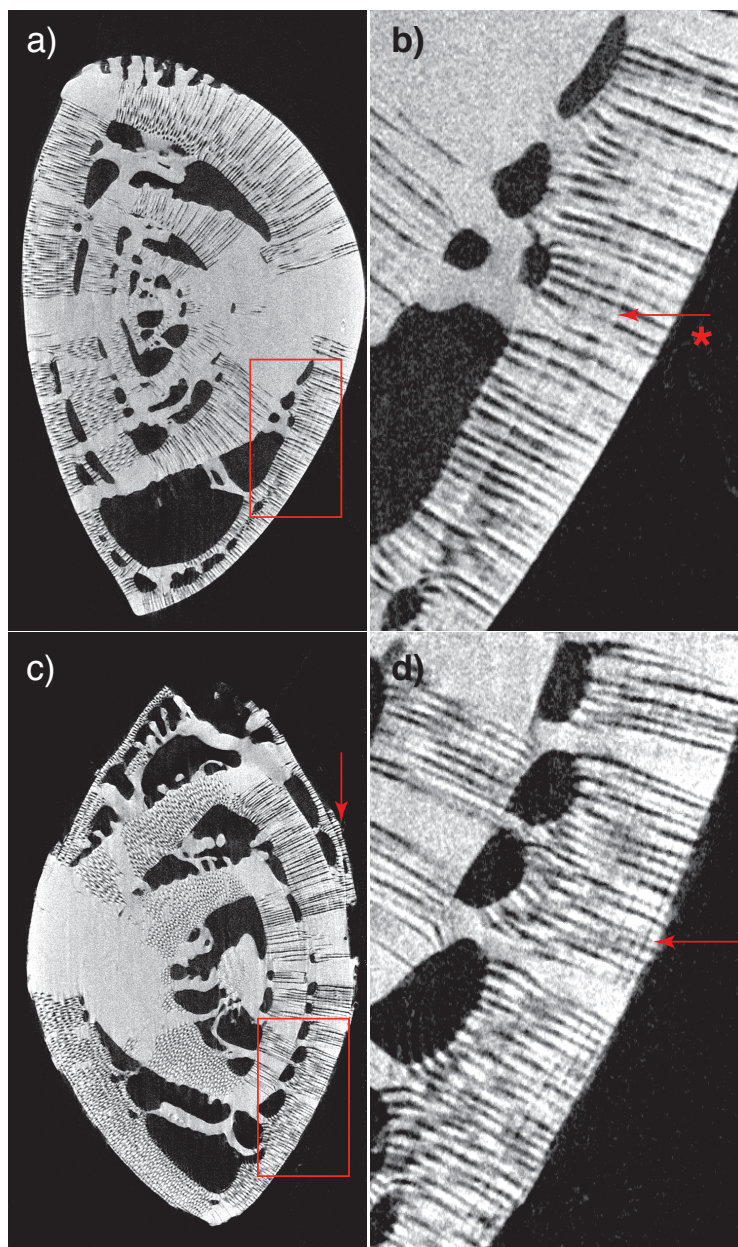
**Figure 5.7:** Slices in the YZ plane through the 3D-reconstructed foraminiferal specimens. **a)** unreacted specimen, with a detailed area shown in **b)**. The asterisk indicates where a grayscale intensity profile along this lamination feature was taken for Figure 5.9 below. The dissolved specimen is shown in **c-d**. Detail shows the dissolution along surfaces parallel to the foraminiferal surface, showing that dissolution penetrates deeper than the outer surface.

(2011) used CT scans in conjunction with trace element analysis to devise a scheme to correct the Mg/Ca of planktonic foraminifera for the effects of dissolution. They also showed SEM evidence for dissolution along layers within the test. All of these studies suggest that the reactivity of foraminiferal calcite is tied to its Mg content, and this reactivity can selectively affect certain layers within the test. We thus investigated in detail our CT scans in an attempt to locate where Mg-rich phases might be dissolving out preferentially from *Amphistegina* tests.
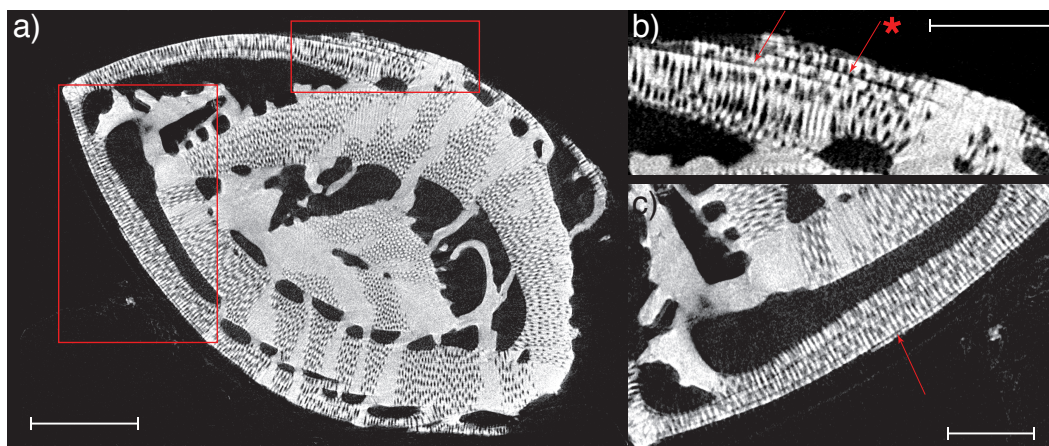


**Figure 5.8: a**); Ortho-slice in the XZ plane of the dissolved test. Scale bar is 200 $\mu$m. The red boxes in **a**) are blown up for clarity in panels **b**) and **c**), where scale bars are 100 $\mu$m. These panels show several truncated laminations, removed due to dissolution. Dissolution surfaces are indicated by arrows, penetrating deeper into the test along a lamination boundary. The asterisk indicates where a grayscale intensity profile along this lamination boundary was taken for Figure 5.9 below.

Slices from the CT reconstructions show evidence of laminations that could be related to Mg/Ca variability. The unreacted specimen in Figure 5.7a and b appears whole, with large chamber voids and pores traversing the chamber walls. In Figure 5.7b, laminations are evident, running parallel to the outer test surface. These laminations have been shown to represent growth bands in *Nummulites* and *Operculina* species (Evans, Müller, et al., 2013). In a YZ slice of the 11% dissolved specimen shown in Figure 5.7c and d, dissolution features are most noticeable at the surface, with a bumpy surface reflecting the terminated, terraced laminations evident in Figure 5.4. Looking in detail at Figure 5.7d, laminations are more obvious than in Figure 5.7b, with dark lines running parallel to the test surface. These bands are evidence that dissolution is selectively affecting certain laminations.

These patterns are more noticeable in Figure 5.8. On the right hand side of Figure 5.8a, the inner test wall is exposed, also seen as the loss of the final chamber in
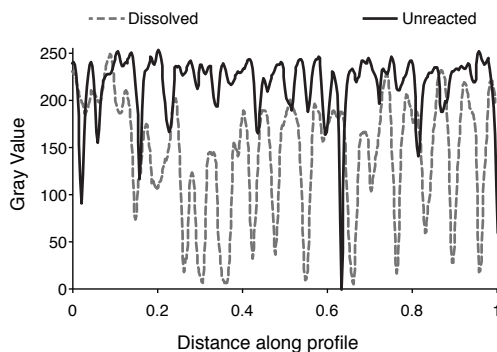
**Figure 5.9:** Profiles of grayscale intensity along the lamination features indicated by asterisks in Figures 5.7 and 5.8. The x-axis is normalized to the total distance, and is expressed as a fraction along the profile. The unreacted surface is from Figure 5.7 and shows almost complete saturation except when traversing pores. The dissolved surface is from Figure 5.8 and shows distinctly lower intensity across almost the entire profile, indicating the absence of mass.

Figure 5.4. In Figure 5.8b, several dissolution surfaces are evident, penetrating deep inside, originating at the surface from a terminated lamination. These dissolution surfaces even cut into the more solid mass of calcite in the far right of Figure 5.8b, which is part of the test's central core – the surface of which is exposed as the smooth white top. At least three dissolution surfaces can be counted, starting at the outermost layer. Similar dissolution features along laminations can be seen in Figure 5.8c. The fact that three distinct surfaces can be seen suggests that seawater is accessing more soluble features deeper into the test.
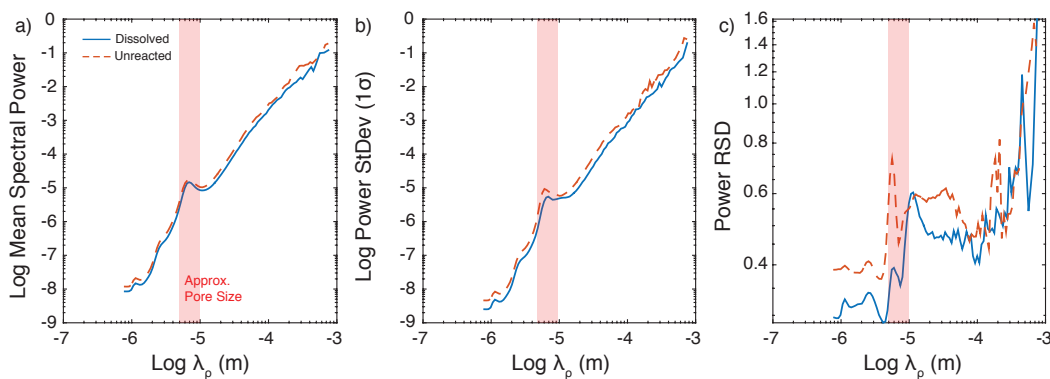


**Figure 5.10:** Statistics on radially averaged 2D power spectra collected on all images from the CT scan reconstructions for unreacted (red) and dissolved (blue) foraminifera. **a**) Mean spectral power as a function of $\lambda_\rho$. **b**) Standard deviation ($1\sigma$) of spectral power. **c**) Relative standard deviation (standard deviation divided by the mean). In particular, the peak in spectral power at $\lambda_{rho}$=4-10 $\mu$m is characteristic of the foraminiferal pore width (see Figure 5.7). The RSD this band is higher for the unreacted specimen than for the dissolved specimen.
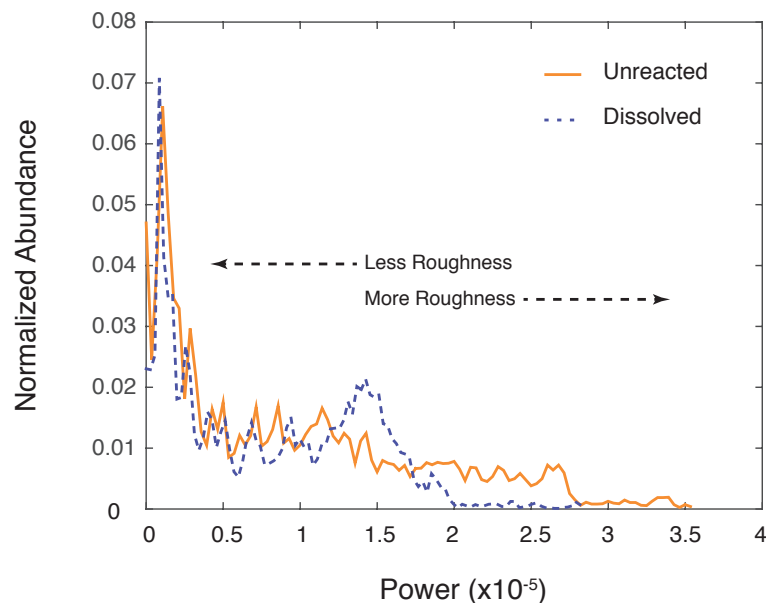
**Figure 5.11:** Histograms of power from the $4 \cdot 10^{-6} \leq \lambda_\rho \leq 10 \cdot^{-6}$ spectral band, highlighted in red in Figure 5.10. Dissolved (blue) power shows two distinct peaks in spectral power at ~0.2 and $1.5 \cdot 10^{-5}$. Unreacted (orange) power shows one peak at $0.2 \cdot 10^{-5}$, with a longer tail at high power extending to over $3.5 \cdot 10^{-5}$.

In an attempt to quantify the changes seen qualitatively in Figures 5.7 and 5.8, a roughness power spectrum analysis was conducted on all z-slices from CT scans of dissolved and unreacted foraminiferal tests, shown in Figure 5.10. Because these slices contain chamber voids and many pores, these spectra should have a different shape than those in Figure 5.5 and Figure 5.6. The grayscale here also does not reflect topography as it did in SEM images. Instead, grayscale in CT scans reflects density, and therefore less intense gray values correspond to less dense areas. Black areas indicate zero density, and gray areas could reflect some density from neighboring layers during slicing and image processing. We distinguish the power spectrum analysis from above ($\lambda_z$) as a density frequency ($\lambda_\rho$).

Statistics on all power spectra are shown in Figure 5.10. Mean power of all spectra increase in power as a function of wavelength (Figure 5.10a). In contrast to Figure 5.5, the mean spectral power in the unreacted specimen is consistently higher than that of the dissolved specimen. There is a distinct peak in spectral power at the 4-10 $\mu$m wavelength, highlighted as the approximate pore diameter. However, the shapes of the unreacted and dissolved spectra show very little difference between them. In other words, the dissolution features observed in Figure 5.8 and 5.7 do not show up as first-order features in the roughness spectrum of the dissolved test.

However, there are features in these roughness spectra that are obscured by plotting mean power instead of looking at the shape of the power distributions. The standard deviation of all power spectra also decrease as a function of wavelength (Figure 5.10b). When plotted as the relative standard deviation in Figure 5.10c, peaks in RSD are evident. These peaks do not directly correspond to peaks in mean spectral power, and they also appear at different wavelengths for the unreacted and dissolved specimens. These differences suggest that the algorithm is identifying distinct patterns of roughness.

Instead of plotting statistics, histograms of spectral power for the 4-10 $\mu$m wavelength band are plotted in Figure 5.11. These histograms took only the $4 \cdot 10^{-6} \leq \lambda_{rho} \leq 10^{\cdot -6}$ spectral power from all dissolved and unreacted z-slices (about 1600 total images). The distribution of power in this spectral band shows one discernable peak at~$0.1 \cdot 10^{-5}$, with a long, large-roughness tail. In contrast, the dissolved specimen shows two distinct peaks in power, at ~0.1 and $1.5 \cdot 10^{-5}$. An explanation of the shapes of these distributions is only speculative at this point. They suggest two things: First, the unreacted specimen's pores have a large range in roughness. There are a few locations with very rough surfaces, but also many with much smoother surfaces as well. Second, dissolution smooths out the large-roughness features, shortening the high-roughness tail observed in the unreacted specimen. The dissolved specimen also contains a smaller peak at even lower roughness. The appearance of two peaks here could due to two features with a similar lengthscale – such as pores and laminations – being dissolved and smoothed out. However, this hypothesis requires more CT scans of samples with a range of mass losses, or a single specimen getting scanned periodically during a dissolution time series.

The dissolution surfaces noticeable in Figures 5.8 and 5.7, combined with the observations of previous studies, provide a hypothesis for how dissolution propagates through the test. High-Mg calcite (~20 mol %) has been observed as the initial phase that precipitates during *Amphistegina* chamber formation (S Bentov and J Erez, 2005). This calcite is made up of small ($\leq 10\mu$m) microspheres, closely associated with the primary organic matrix which serves as a template for chamber structure. Thicker low-Mg calcite is then precipitated on either side of this high-Mg layer. Although circumstantial at this stage, the bimodal distribution in Figure 5.11 shows up in the 4-10 $\mu$m wavelength band, suggesting that these features in the power spectra could be related to these high-Mg microspheres.

High-Mg calcites are more soluble than low-Mg calcites (John W Morse, Rolf S

Arvidson, and Lüttge, 2007; John W Morse and Mackenzie, 1990), such that at the same seawater carbonate ion concentration, a high-Mg calcite will dissolve out preferentially (L Niel Plummer and Mackenzie, 1974; A. Subhas, Adkins, J. Erez, P. Ziveri, et al., in prep.). Seawater could access high-Mg bands in *Amphistegina* tests initially through the pores, which traverse the test perpendicular to these laminations. These bands will then dissolve out preferentially, leaving behind the low-Mg secondary calcite layers. The laminations which remain, now only loosely connected to the rest of the test, are easily sloughed off, leaving terminated laminations and isolated islands on the test surface.

Interior dissolution features thus help explain the surficial patterns of dissolution observed here and in other studies (Corliss and Honjo, 1981; Kotler, R. E. Martin, and Liddell, 1992), and could help to tie these changes to measurable trends in test chemistry. Bulk Mg/Ca should change as a function of mass loss, which has been well documented in plakntonic foraminifera (Johnstone, Jimin Yu, et al., 2011; Brown and Elderfield, 1996) and in *Amphistegina* (A. Subhas, Adkins, J. Erez, P. Ziveri, et al., in prep.). Heterogeneity in Mg/Ca across calcite laminations is also well-documented in several species of foraminifera (Evans, Jonathan Erez, et al., 2015; Evans, Müller, et al., 2013; A. Y. Sadekov, Stephen M Eggins, and Patrick De Deckker, 2005). The hypothesis presented here should be validated by making ion probe or SIMS measurements of Mg/Ca, and potentially also organic matter content, across multiple laminations of *Amphistegina* tests.

## 5.5   Conclusion

We investigated images taken of a suite of *Amphistegina* tests that underwent different amounts of dissolution. These tests demonstrate a consistent morphological pattern of dissolution. The smooth test center is a useful location for tracking dissolution features, because its initial surface is unornamented. Initial small-scale features further develop into larger etch pits and channels, which then lead to the removal of laminations and the destruction of the final chamber. The saturation of the smooth top with dissolution features can be traced and quantified using 2D power spectra of surface roughness, and samples analyzed from *in situ* deep ocean dissolution experiments show similar trends in roughness to those seen in *Amphistegina* tests. A calibration of surface roughness spectra as a dissolution index should prove to be a useful tool in assessing the diagenetic preservation of benthic foraminifera in deep sea sediments.

Finally, high-resolution CT scans show that dissolution also penetrates into the test's subsurface, initiating dissolution of specific lamination planes parallel to the test surface. These dissolution surfaces structurally weaken overlying laminations, allowing for the removal of entire sheets from the test. These dissolution features also penetrate into the thicker calcified central column. Further work will show if these surfaces correspond to a more soluble, Mg-rich, calcite phase.

*Chapter 6*

# IDENTIFYING CARBONIC ANHYDRASE ACTIVITY IN THE NATURAL ENVIRONMENT

## 6.1 Introduction

The enzyme carbonic anhydrase (CA) is ubiquitous. It plays a role in the interconversion of $CO_2$ and $HCO_3^-$ by catalyzing the hydration of $CO_2$:

$$CO_2 + H_2O \underset{k_{-2}}{\overset{k_{+2}}{\rightleftharpoons}} H_2CO_3 \rightleftharpoons HCO_3^- + H^+. \tag{6.1}$$

At high pH, the hydroxylation of $CO_2$ also becomes important:

$$CO_2 + OH^- \underset{k_{-4}}{\overset{k_{+4}}{\rightleftharpoons}} HCO_3^-. \tag{6.2}$$

Here, $k_{+2}$ is the rate of $CO_2$ hydration and $k_{-2}$ is the rate of $H_2CO_3$ dehydration. Similarly, $k_{+4}[OH^-]$ is the rate of $CO_2$ hydroxylation and $k_{-4}$ is the rate of $HCO_3^-$ dehydroxylation. The uncatalyzed rates of hydration to dehydration are different by about 2.5 orders of magnitude, such that the formation of $HCO_3^-$ through $CO_2$ hydration is much slower than the dehydration reaction (Johnson, 1982; Pinsent, Pearson, and Roughton, 1956; X. Wang et al., 2010). For example, at pH 7 and room temperature, the residence time of $CO_2$ is on the order of $1/k_{+2} \sim 54$ seconds (Pinsent, Pearson, and Roughton, 1956). Compared to essentially instantaneous acid-base kinetics which can rapidly equilibrate $H_2CO_3$, $HCO_3^-$, and $CO_3^{2-}$, the hydration of $CO_2$ is the rate-limiting step in equilibrating all DIC species in solution.

Because many biological systems are pH-buffered, the concentrations of $CO_{2(aq)}$ are often very low, and processes which require either rapid production or consumption of $CO_2$ require enzymatic catalysis of this hydration reaction. CA is used in diverse physiological processes, from calcification (Tambutte et al., 2007; Rahman, Tamotsu Oomori, and Uehara, 2007; Miyamoto et al., 1996) to photosynthesis (C. L. Martin and Tortell, 2008; Y. Xu et al., 2008; Moroney, Bartlett, and Samuelsson, 2001; Elzenga, Prins, and Stefels, 2000) to the exchange of respiratory $CO_2$ in humans (C. Tu et al., 1978). It is known to exist intracellulary and extracellularly, bound to outer cell walls or membranes (Elzenga, Prins, and Stefels, 2000; C. L. Martin and Tortell, 2008; Mustaffa, Striebel, and Wurl, 2017).

In addition to its effects *in vivo*, CA has also been shown to affect the dissolution kinetics of calcium carbonate, both in karst environments far from equilibrium (Zaihua Liu, Yuan, and Wolfgang Dreybrodt, 2005), and in seawater near equilibrium (Ch. 2 of Thesis). The consequence of this catalysis is that CA affects the rate of alkalinity production in the ocean through $CaCO_3$ dissolution, adding yet another component of the ocean-atmosphere $CO_2$ cycle to those in which CA plays a part. The diverse and pervasive nature of CA brings up the question: can we identify CA in the environment? Where is it being expressed, and is it associated with $CaCO_3$ production/dissolution cycles?

We investigated several assays in order to evaluate their applicability to measuring CA activity in natural samples. The requirements for such an assay are different from those in a laboratory, where many studies are performed on purified enzyme (Z. Yu et al., 2006; Miyamoto et al., 1996). The assay must have a low limit of detection, perform robustly in the field, and have the potential to work in natural seawater. We investigated the classic pH-drop method of Wilbur and N. G. Anderson, 1948, and the esterase activity assay of Pocker and Stone, 1967. We also developed an *ad hoc* assay using a $H^{13}CO_3^-$ spike in natural seawater, which traces the appearance of $^{13}CO_2$ in the assay headspace. Finally, we tested the membrane inlet mass spectrometry (MIMS) method of measuring the rate of depletion of $^{18}O$ from $CO_{2(aq)}$, which is proportional to the rate of hydration in solution.

We measured CA activity in several natural samples to assess the performance of these four different assays. CA activity was measured in oyster larvae, the alga *Picocystis* isolated from Mono Lake water, human saliva, and finally natural seawater collected from the San Pedro Ocean Time Series (SPOT). We show that the pH-drop and MIMS methods are suitable for low-concentration CA measurements, with the MIMS technique being more sensitive and quantitative. It is also robust and compact and thus appropriate for field-based studies.

## 6.2 Materials and Methods

Four methods were investigated to measure the CA activity of natural samples, and are detailed below. The "pH-drop" method was modified from Wilbur and N. G. Anderson, 1948. The ability of CA to catalyze the hydrolysis of esters has also been exploited as an assay for general enzymatic activity (Pocker and Stone, 1967; Tashian, Shows, and Plato, 1963), and was tested here. In addition to assays based on chemical transformations, two isotope-based assays were used. A new system

was developed that measures the appearance of $^{13}CO_2$ in the headspace over a stirred solution containing excess $^{13}HCO_3^-$. Finally, the oxygen isotope exchange method, first proposed by Mills and Urey, 1940, was also used. This method is further described by D. N. Silverman and C. K. Tu, 1976, is reviewed in D. N. Silverman, 1982, and has been used extensively since.

Bovine carbonic anhydrase (BCA) was purchased as a lyophilized powder from Sigma Aldrich. This powder was stored at 4°C. Solutions of carbonic anhydrase were made up either in 20 mM Tris-HCl buffer at pH 8.0 or in natural, filtered seawater. Enzyme solutions were also stored cold. Solutions were periodically checked for their activity, and retained their activity for up to three weeks. Solutions left for several months lost their catalytic activity. A "blank" enzyme solution of Bovine Serum Albumin was made up in the same way, to test the effect of extra proteinaceous material on assay sensitivity.

Solutions of two known carbonic anhydrase inhibitors, acetazolamide (AZ) and ethoxzolamide (EZ), were also prepared for use in assays. A saturated solution of AZ was prepared by dissolving powdered AZ into deionized water for a saturated solution concentration of 4.4 mmol/L. EZ is even more sparingly soluble in water, and was dissolved in DMSO to a concentration of 216 mmol/L. Unless otherwise noted, inhibition experiments were conducted with 10 $\mu$L AZ and 1 $\mu$L EZ solution, leading to inhibitor concentrations in a 5 mL assay of 9 $\mu$M and 43 $\mu$M, respectively.

Natural samples measured here were either analyzed for their enzymatic activity directly following their collection, or were stored frozen at -20°C before analysis. Oyster and urchin larvae were received frozen from Christina Ann Frieder of the Manahan lab. These larvae were removed from live culturing experiments and immediately frozen for storage. Oysters contained about 0.03 $\mu$g of protein per individual; urchins contained about 0.11 $\mu$g protein per individual.

Samples of *picocystis* were taken from Mono Lake surface water. Approximately 8L of lake water was centrifuged in 50 mL increments at 10,000 rpm for 15 minutes each. The resulting pellets were then resuspended in Tris buffer and aggregated in two 50 mL Falcon tubes containing 10 mL each. Thus, *picocystis* was concentrated by a factor of 400:1. These Falcon tubes were then split into 10 aliquots of 1 mL each and frozen at -20 °C.

When indicated, some samples were lysed to measure their internal carbonic anhydrase activity. Samples were sonicated on ice for a varying amount of time, from

10 seconds to several minutes. All sonication was done in 10-30s bursts to ensure that the cellular material did not heat up and proteins did not denature. In some preparations, lysed samples were then centrifuged at 6,000 rpm for 10 minutes, and the supernatant was sampled for its enzymatic activity.

**pH method**

This method involves measuring the time taken for a $CO_2$-saturated solution to reach an equilibrium pH. A beaker containing 12 mL ice-cold Tris-HCl buffer (20 mM, pH 8) was submerged in ice. To this gently stirred solution was added 8 mL ice-cold, $CO_2$-saturated deionized water. The pH of this solution was continuously monitored at 2 Hz using a pH electrode (Metrohm 6.0262.100) attached to a Keysight 34972A data acquisition unit. The output of the pH electrode was conditioned using an Omega model PHTX-22 high-impedance preamplifier. The time taken for the assay solution to reach pH ~6.5 was used to estimate the equilibration timescale of $CO_2$ via dehydration into the other DIC species. Enzymatic activity was assessed by adding the sample to the initial Tris buffer solution, prior to $CO_2$ addition. A sample's timescale to equilibration was then compared to the "blank" using the W-A (or E.U.) unit measurement:

$$E.U. = \frac{t_{blank} - t_{smp}}{t_{smp}}, \tag{6.3}$$

where $t_{blank}$ is the timescale of equilibration between Tris-buffer and $CO_2$-saturated water only, and $t_{smp}$ is the same timescale in the presence of free BCA or an unknown sample.

**Esterase method**

In general, this method exploits CA's nonspecific ester hydrolysis catalysis as a proxy for $CO_2$ hydratioon catalysis. The assay measures the hydrolysis of para-nitrophenyl acetate (p-NPA) to form para-nitrophenol (p-NP) and acetate. A 1.5 mg/mL solution of BCA in phosphate buffer was used as a standard. The reagent stock solution was 140 mM p-NPA in acetonitrile. The assay was conducted in either 1 mL or 100 $\mu$L phosphate buffer (pH 8, 100 mM) and an initial p-NPA concentration of between 0.28 and 0.7 mM. A BCA standard solution or a natural sample was stirred into phosphate buffer and then transferred into a plastic spectrophotometric cuvette. p-NPA was then added to the cuvette via pipette, and the measurement sequence was initiated. The rate of appearance of p-NP was calculated by measuring the rate of increase in absorbance at $\lambda$ =420 nM on a Beckman-Coulter DU 800 spectrophotometer at a

frequency of 0.13 Hz for 5 minutes. The rate of absorbance was converted to rate of substrate production using the extinction coefficient for p-NP of 18,500 absorbance units/ M p-NP. Background hydrolysis rates were collected by introducing p-NPA to buffer. Background rates were subtracted from all rates to calculate the net rate of catalyzed hydrolysis.

**Picarro method**

A new method was established to measure CA activity in seawater. In general, CA activity was assessed in a solution of natural seawater spiked with $H^{13}CO_3^-$ by continuously sampling the headspace $CO_2$ $\delta^{13}C$ using a Picarro cavity ringdown spectrometer. A stream of air was flowed into the solution headspace and then into the Picarro analysis chamber. This gas mixture's $CO_2$ concentration and its $\delta^{13}C$ was recorded at a frequency of 1 Hz. This assay assumes that the headspace $CO_2$ $\delta^{13}C$ will be sensitive to the steady state reached between hydration/dehydration kinetics in solution, headspace-solution gas exchange, and the flow rate of gas through the system.
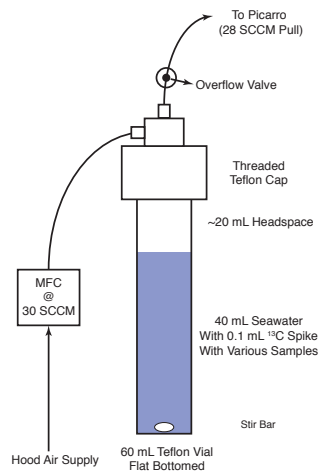


**Figure 6.1:** A schematic of the Picarro assay for CA activity.

Specifically, a teflon reaction chamber consisting of a flat-bottomed, 60 mL vial with a stir bar and a threaded cap with two inlets was filled with 40 mL natural seawater. This solution was stirred gently. Lab air was fed into the reaction chamber via one inlet at a mass-flow-controlled rate of 30 standard cubic centimeters per minute (SCCM). The Picarro sampled the reaction chamber headspace via the second chamber inlet. The Picarro G2131-*i* was used, which has a 40 mL analysis chamber and a gas draw of 28 SCCM. The residence time of $CO_2$ in the Picarro chamber is thus 28/40 = 0.7 minutes. A small three-way "overflow valve" was placed in

between the chamber and Picarro inlet to ensure that the entire reaction occurred at atmospheric pressure. A diagram of this system is shown in Figure 6.1. Samples or standard BCA solutions were added to seawater before the spike addition.

The isotopic spike was made up by dissolving 100%-$^{13}$C sodium bicarbonate (CAS 87081-58-1) in natural seawater with natural abundance DIC. The concentration of added H$^{13}$CO$_3^-$ was 6 mM, with background natural abundance seawater DIC at a concentration of 2 mM. The total spike DIC concentration was thus 6+2=8 mM and a 13/12 ratio of ~6/2=3. A typical assay run consisted of adding 100 $\mu$L of this spike to 40 mL of natural seawater.

After an initial period of 5-10 minutes, the steady-state $\delta^{13}$C enrichment relative to the blank was calculated as a measure of catalytic activity, in permil notation:

$$\epsilon_{pic} = \left( \frac{\delta^{13}C_{smp} + 1000}{\delta^{13}C_{blank} + 1000} - 1 \right) * 1000, \tag{6.4}$$

where $\delta^{13}C_{smp}$ is the headspace $\delta^{13}$C with a sample or CA standard solution, and $\delta^{13}C_{blank}$ is the headspace $\delta^{13}$C with only seawater and spike.

**MIMS method**

The MIMS method measures the depletion of $^{18}$O from aqueous $^{13}$CO$_2$ using membrane inlet mass spectrometry. Isotopes of oxygen are exchanged between labeled HCO$_3^-$ and natural abundance water:

$$^{13}CO^{18}O + H_2^{16}O \rightleftharpoons H^+ + H^{13}COO^{18}O^- \rightleftharpoons\, ^{13}CO_2 + H_2^{18}O. \tag{6.5}$$

The oxygen isotope spike is infinitely diluted into the large background of water (55M) at a rate proportional to the rate of hydration/dehydration and the proportion of total DIC as CO$_2$ in solution (D. N. Silverman, 1982; J Uchikawa and R E Zeebe, 2012). The isotopic spike was prepared by equilibrating a 2M solution of NaH$^{13}$CO$_3$ in labeled water ($\geq$ 97 mol% $^{18}$O) for at least 24 hours. The resulting bicarbonate spike was almost completely labeled in $^{13}$C and, given the ratio of natural abundance oxygen from bicarbonate ($\frac{3\text{moles O}}{1\text{mole HCO}_3^-} \cdot$ 2 Moles HCO$_3^-$ = 6M Oxygen) to labeled oxygen from water (55 M), was about 6/55 = 89% labeled in $^{18}$O.

A Pfeiffer QMG 220 mass spectrometer with a closed-type source and a mass range of 1-200 AMU was used for data collection. All isotopologues of CO$_2$ were collected during a measurement ($m/z$ = 44,45,46,47,48,49). This mass spectrometer

was fitted with a membrane inlet sensor consisting of a 4 cm-length of 0.23 mm thick silastic tubing, sealed by a knot at one end. This tubing was gently slid over a length of threaded copper wire, which provided structural support against the mass spectrometer's high vacuum. This sensor was connected to the mass spectrometer inlet via a 1/16" O.D. stainless steel tube.

The membrane sensor was introduced to the mass spectrometer's high vacuum by slowly opening a shutoff valve, reaching an operating pressure of about $4 \cdot 10^{-6}$ mbar. The membrane was then immersed in the gently stirred assay solution (5 mL 20 mM Tris-HCl buffer, pH 8). Samples or standard BCA solutions were then added via pipette to this assay solution. Doubly labeled spike solution was then added directly via pipette. The response time of the mass spec to spike addition was $\leq 2$ seconds. Depletion of oxygen-18 from the DIC pool was measured as the intensity fraction of $^{18}$O isotopologues of $^{13}CO_2$:

$$f^{18} = \frac{2 \cdot (49) + (47)}{2[(45) + (47) + (49)]},$$ (6.6)

where (45), (47) and (49) are measured ion currents at those $m/z$ values. Isotopes of $^{13}CO_2$ were used to minimize the background and thus increase the signal to noise ratio. The fraction of $^{13}$C was also monitored during a measurement in a similar fashion:

$$f^{13} = \frac{(45)}{(44) + (45)}.$$ (6.7)

The rate of hydration/dehydration was measured by taking the slope of $\log(f^{18})$ versus time (D. N. Silverman, 1982; Mills and Urey, 1940; Joji Uchikawa et al., 2015; Y. Xu et al., 2008). In most experiments, a CA inhibitor (either AZ or EZ) was added to the assay after 5-10 minutes of reaction. This allowed for a direct comparison of inhibited and uninhibited $^{18}$O depletion rates for the same sample.

The slope of $\log(f^{18})$ versus time ($\lambda$) was converted to the kinetic rate of reaction by a correction factor related to the fraction of DIC as $CO_2$ (Y. Xu et al., 2008; J Uchikawa and R E Zeebe, 2012; D. N. Silverman, 1982):

$$\lambda = 0.5 \cdot k^* \cdot \left(1 + f_{CO_2} - \sqrt{1 + \frac{2}{3} f_{CO_2} + (f_{CO_2})^2}\right);$$

$$k^* = \left(k_{+2} + \frac{k_{cat}}{K_M}[CA] + k_{+4}[OH^-]\right);$$ (6.8)

where $k_{+2}$ is the uncatalyzed rate of $CO_2$ hydration, $\frac{k_{cat}}{K_M}$ is the rate in $M^{-1}s^{-1}$ of catalyzed hydration, and $k_{+4}[OH^-]$ is the uncatalyzed rate of hydroxylation. The fraction of DIC as $CO_2$ in solution is represented as $f_{CO_2}$. Values from Pinsent, Pearson, and Roughton (1956) were used for $k_{+2}$ and $k_{+4}$. The $k^*$ of natural samples was converted to an "effective BCA activity" by subtracting $(k_{+2} + k_{+4}[OH^-])$ from $k^*$ and dividing by the measured $\frac{k_{cat}}{K_M}$ for BCA, yielding units of moles/liter effective concentration. The effective mass of enzyme was calculated by multiplying effective molar concentrations by the molar mass of bovine CA ($30{,}000$ g mol$^{-1}$).

## 6.3   Results

Results from assay experiments are shown below, categorized by assay type. A summary and comparison of assay performance is provided in the Discussion.

**pH Drop Results**
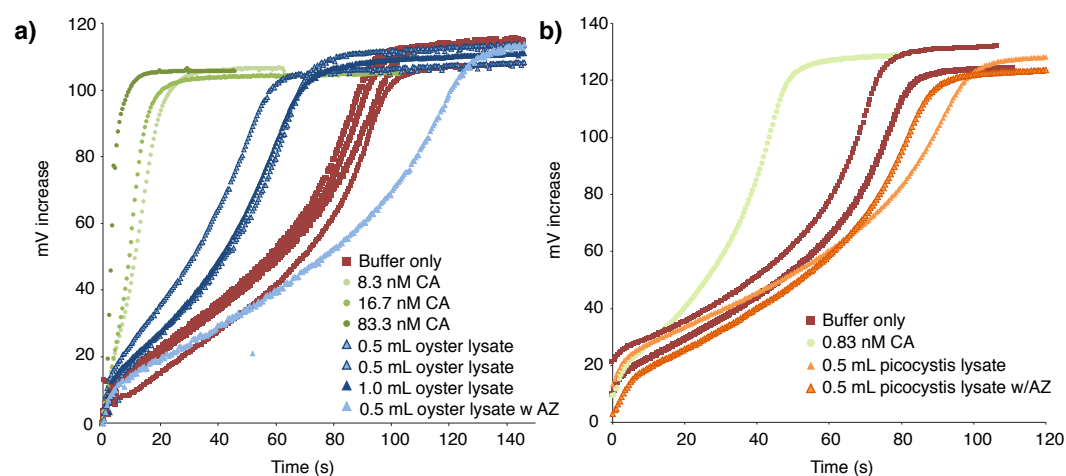


**Figure 6.2:** Traces of pH electrode voltage versus time for **a)** standard BCA and oyster lysate and **b)** standard BCA and *picocystis* lysate. Uncatalyzed runs with Tris buffer only are shown as well.

Traces of pH electrode voltage versus time are presented in Figure 6.2. Upon addition of $CO_2$-saturated water, the pH decreases (voltage increases) until it reaches its equilibrium pH. The time between $CO_2$ addition and this plateau is used to calculate $E.U.$ in Eq.(6.3). Corresponding E.U. values are presented in Table 6.1. There is about 5% blank variability ($1\ \sigma$) in the time needed to reach equilibrium in Figure 6.2a. Also note the significantly different buffer-only equilibration time between Figure 6.2a ($95\pm4$ s) and Figure 6.2b ($\sim$ 65 s). This is because it is difficult to maintain $CO_2$ saturation with an atmosphere of 400 ppm $CO_2$. When bubbling with pure $CO_2$ gas, the solution can rapidly become supersaturated, leading to a very

138

short equilibration time even in the absence of CA. When left for too long without $CO_2$, the solution degasses and is no longer saturated with $CO_2$. Thus, the baseline must be constantly checked.

CA solutions equilibrate buffer and $CO_2$ solutions consistently faster than buffer-only equilibration. Oyster lysates, presented graphically Figure 6.2a, equilibrate buffer and $CO_2$ solutions consistently faster than buffer-only equilibration. The oyster lysate is also completely inhibited by the addition of 1 $\mu$M AZ. Assay results for lysates of *Picocystis* are shown in Figure 6.2b. There was no measurable activity above the buffer-only system from *Picocystis* lysate. In fact, the inhibited *Picocystis* lysate sample showed a slightly faster equilibration than the uninhibited lysate.

BCA activity in E.U. from Figure 6.2a and b are plotted versus the amount of BCA added in Figure 6.3. There is a significant change in slope in E.U. versus [BCA] between 0 and 5 $\mu$g BCA, indicating that there is a nonlinear response of pH at low [CA]. This nonlinear response complicates the use of the pH assay as a quantitative measure of CA activity, especially at low [CA].
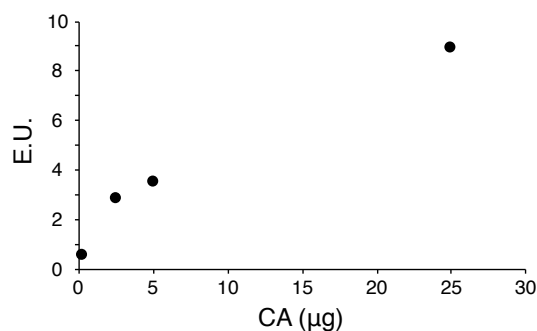


**Figure 6.3:** The enzyme activity in E.U. of bovine CA versus the amount of BCA present in the pH-drop assay. Note the change in slope after about 5 $\mu$g CA. This nonlinearity complicates the use of this pH-drop assay to quantify the amount of CA activity in natural samples.

*E.U.* values calculated for Oyster samples are presented in Table 6.1. In order to convert lysate activity to effective BCA concentration, the slope between 0 and 8.3 nM BCA (2.92 E.U./nM BCA) was used. The amount of activity in oyster samples does not directly scale with lysate amount (Table 6.1). The standard calibration predicts that somewhere between 0.11 and 0.38 % of oyster protein by weight is Carbonic Anhydrase.

| BCA STANDARDS | time (s) | CA (μg) | E.U. | Error | nM CA | |
|---|---|---|---|---|---|---|
| Blanks | 94±4 | | | | | |
| 8.3 nM CA | 25 | 2.5 | 2.9 | 0.1 | 8.3 | |
| 16.7 nM CA | 21 | 5 | 3.5 | 0.2 | 16.7 | |
| 83.3 nM CA | 9.5 | 25 | 8.9 | 0.4 | 83.3 | |
| | | | | | | |
| *OYSTER SAMPLES* | | | | | | *g/g oyster protein (%)* |
| 0.5 mL lysate | 58 | 0.55 | 0.6 | 0.03 | 1.8 | 0.38 |
| 0.5 mL lysate | 69 | 0.33 | 0.4 | 0.02 | 1.1 | 0.11 |
| 1.0 mL lysate | 69 | 0.32 | 0.4 | 0.02 | 1.1 | 0.11 |
| 0.5 mL lysate w/AZ | 121 | | -0.22 | -0.01 | | |

**Table 6.1:** Summary of pH-drop measurements of CA activity in BCA standards and oyster larval samples. The amount of CA present in oysters was calculated from their E.U. values and the slope of BCA E.U. versus [BCA] between 0 and 8.3 nM BCA (Figure 6.3). Note that the inhibited oyster sample showed no CA activity.
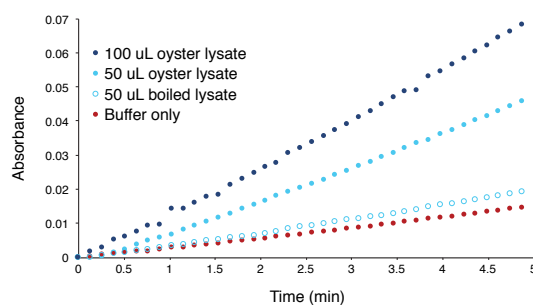


**Figure 6.4:** Traces of absorbance versus time for oyster lysate samples analyzed using the esterase assay. Absorbance measures the appearance of the product para-nitrophenol (p-NP) at a wavelength of 420 nm. Oyster lysates demonstrate a measurable activity over the uncatalyzed (buffer only) assay. The boiled oyster lysate shows similar activity to the uncatalyzed (buffer only) assay.

**Esterase assay results**

Esterase assay traces of absorbance versus time for oyster lysate samples are presented in Figure 6.4. All natural sample lysates showed faster rates of ester hydrolysis than buffer-only hydrolysis, and the amount of hydrolysis scaled linearly with the amount of lysate added. Lysates boiled to denature proteins showed a similar rate of hydrolysis to the buffer alone, implying that the rate enhancement is due to intact proteins.

| p-NPA (mM) | Esterase rate (mM/min) | [BSA] (μmol/L) |
|---|---|---|
| 0.56 | 0.0017 | 0.50 |
| 0.28 | 0.0011 | 0.50 |
| 0.7 | 0.0025 | 0.25 |

| Picocystis lysate (μL) | p-NPA (mM) | Esterase rate (mM/min) | eff. [BSA] (μmol/L) | nM in lysate |
|---|---|---|---|---|
| 100 | 0.28 | 1.87E-05 | 0.008 | 8.4 |
| 500 | 0.28 | 8.37E-05 | 0.039 | 38.8 |
| 800 | 0.28 | 2.28E-04 | 0.105 | 105 |
| 1000 | 0.7 | 4.53E-04 | 0.045 | 45.2 |

| Oyster lysate (μL) | | | | g/g total protein |
|---|---|---|---|---|
| 50 | 0.28 | 3.1E-04 | 0.089 | 0.18 |
| 100 | 0.28 | 5.4E-04 | 0.160 | 0.16 |
| 50 | 0.28 | 2.8E-04 | 0.082 | 0.16 |
| 50 | 0.28 | 2.9E-04 | 0.083 | 0.17 |

**Table 6.2:** Compiled rates of ester hydrolysis measured on BCA and natural samples. All rates shown have had the uncatalyzed (buffer-only) rate subtracted from them. Effective BCA activity in natural samples was calculated by comparing to the measured BCA rate at the listed substrate concentration. The amount of *picocystis* CA in lake water was calculated by applying the 1:400 concentration factor mentioned in the Methods section. The amount of oyster larval CA, in grams per gram of total protein, was calculated by converting effective activity to an amount of BCA using a molar mass of 30 kDa. This BCA mass was then divided by the amount of total protein in the lysate present (300 μg/mL).

Rates of hydrolysis for all BCA standards, oyster lysates, and *Picocystis* lysates are shown in Table 6.2. Lysates of *Picocystis* also showed enhanced rates of hydrolysis, unlike in the pH assay, which showed no measurable CA activity. Boiled *Picocystis* lysates also showed negligible esterase activity. However, the rate of hydrolysis does not scale linearly with the amount of lysate added. The amount of "effective BCA activity" in these samples was calculated by normalizing the lysate hydrolysis rate to the rate of BCA:

$$[BCA]_{eff,lys} = [BCA]\frac{R_{hyd,lys}}{R_{hyd,BCA}}. \tag{6.9}$$

Essentially this is a one-point calibration to calculate the lysate $[BCA]_{eff,lys}$ using the measured BCA hydrolysis rate ($R_{hyd,lys}$). BCA rates used were at the same substrate concentration as the lysate assays. These values are presented in Table 6.2 as well. Estimates of oyster lysate effective BCA activity (0.17 g/g total protein) are about two orders of magnitude greater than the activity measured by the pH assay (0.001 g/g total protein). The assay also predicts that *Picocystis* lysates contain between 8-100 nM CA.
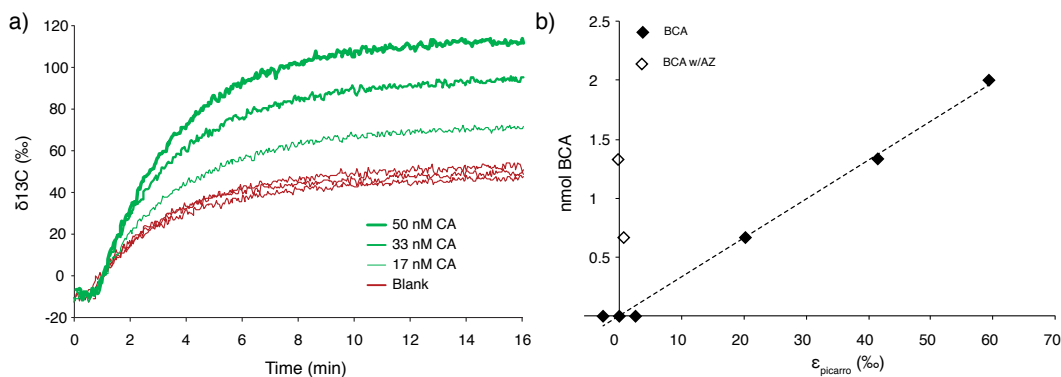
**Figure 6.5:** A calibration of the Picarro-$^{13}$C CA assay. **a)** shows traces of headspace $\delta^{13}$C versus time for blanks (seawater plus spike) and standard additions of BCA. Thicker lines denote higher [BCA]. **b)** plots the steady-state $\delta^{13}$C at 12 minutes against [BCA]. The x-axis is plotted as the $\epsilon$ relative to the blank. Linearity is achieved from about 10-50 nM (0.5-2.5 nmol total) CA.
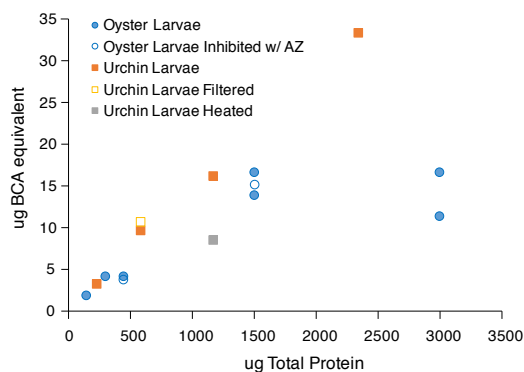


**Figure 6.6:** Using the calibration from Figure 6.5, $\epsilon_{picarro}$ values for cell lysates are converted to effective BCA concentrations, plotted here versus the total amount of larval protein present in the assay. Both oyster and urchin larvae demonstrate linearity until about 1500 $\mu$g total protein in the assay; oyster larvae deviate from this linearity at high protein concentration. Filtering does not affect the observed CA activity. Heating the lysate decreases its observed activity by about half.

**Picarro $^{13}$C assay results**

Calibration curves for the Picarro-$^{13}$C CA assay are presented in Figure 6.5. With the addition of 0.1 mL H$^{13}$CO$_3^-$, the headspace CO$_2$ $\delta^{13}$C increases to a steady state of 40±1.5‰ vs. PDB. Steady state is reached after about 10 minutes of measurement. Solutions of carbonic anhydrase are consistently enriched over the blank. Figure 6.5b shows that the enrichment ($\epsilon_{picarro}$) scales linearly with the amount of BCA in solution. Furthermore, AZ fully inhibits measured enrichments in free BCA solutions, as shown by the open symbols in Figure 6.5b. Given the blank variability of about 1.5 ‰ and the calibration curve shown here, the limit of detection is a

signal of about 5 ‰, or 4.25 nM BCA.

Various oyster and urchin larvae were also measured using this assay. Results from these assays are plotted in Figure 6.6. The x-axis here is the total amount of protein added to the assay; the y-axis is the effective BCA amount in $\mu$g, using the calibration of Figure 6.5b and a BCA mass of 30 kDa. The slopes of oyster and urchin lysates indicate that about 1% of the total protein is BCA. Filtering urchin larvae at 0.2$\mu$m produces the same CA activity as the unfiltered sample, suggesting that all CA in the assay is free and not associated with solid material.

However, Figure 6.6 also highlights several issues with the Picarro-$^{13}$C assay. After about 1500 $\mu$g of total protein, oyster lysates cease to produce a linear relationship between total protein and CA activity. The presence of inhibitor does not reduce the observed CA activity. Finally, heating at 80°C for 20 minutes failed to remove all CA activity from the sample. This assay also failed to show any CA activity in *Picocystis* lysates (not shown).

## MIMS double-label assay results
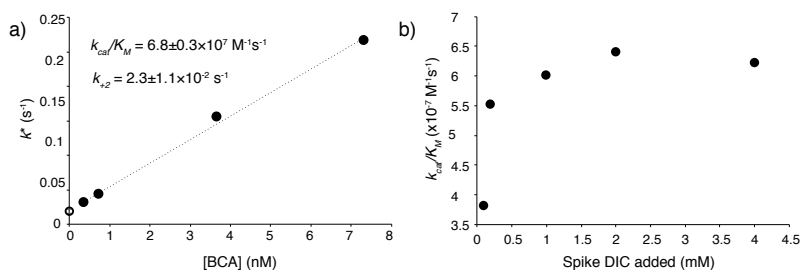


**Figure 6.7:** Determinations of kinetic constants for the DIC+CA system in 0.02M Tris-HCl buffer at pH 8. **a)** A plot of bovine carbonic anhydrase (BCA) concentration versus the rate constant $k^*$, calculated using Eq.(6.8). The slope of this line gives $\frac{k_{cat}}{K_M}$ and the intercept can be converted to $k_{+2}$ using Eq.(6.8). **b)** A plot of $\frac{k_{cat}}{K_M}$ versus spike amount added to the assay. The slope of **a)** is the value of the y-axis here. This plot plateaus after about 1.5 mM DIC added.

Results of BCA solutions and natural samples run on the MIMS assay are presented in Figure 6.8. Both $f^{13}$ and $f^{18}$ traces are shown. After spike addition, and initial isotopic increase, the value of $f^{13}$ versus time generally increases; the $f^{18}$ decreases with time. This is because the rate of appearance of mass 45 ($^{13}$C$^{16}$O$_2$) is related to the rate of disappearance of masses 47 and 49 ($^{13}$C$^{16}$O$^{18}$O and $^{13}$C$^{18}$O$_2$, respectively), through the dilution of $^{18}$O-DIC via hydration/dehydration reactions. However, traces of $f^{18}$ are much cleaner. The noisiness of $f^{13}$ data is attributed to a contribution of contaminating $^{12}$CO$_2$ from breathing and natural CO$_2$ variations
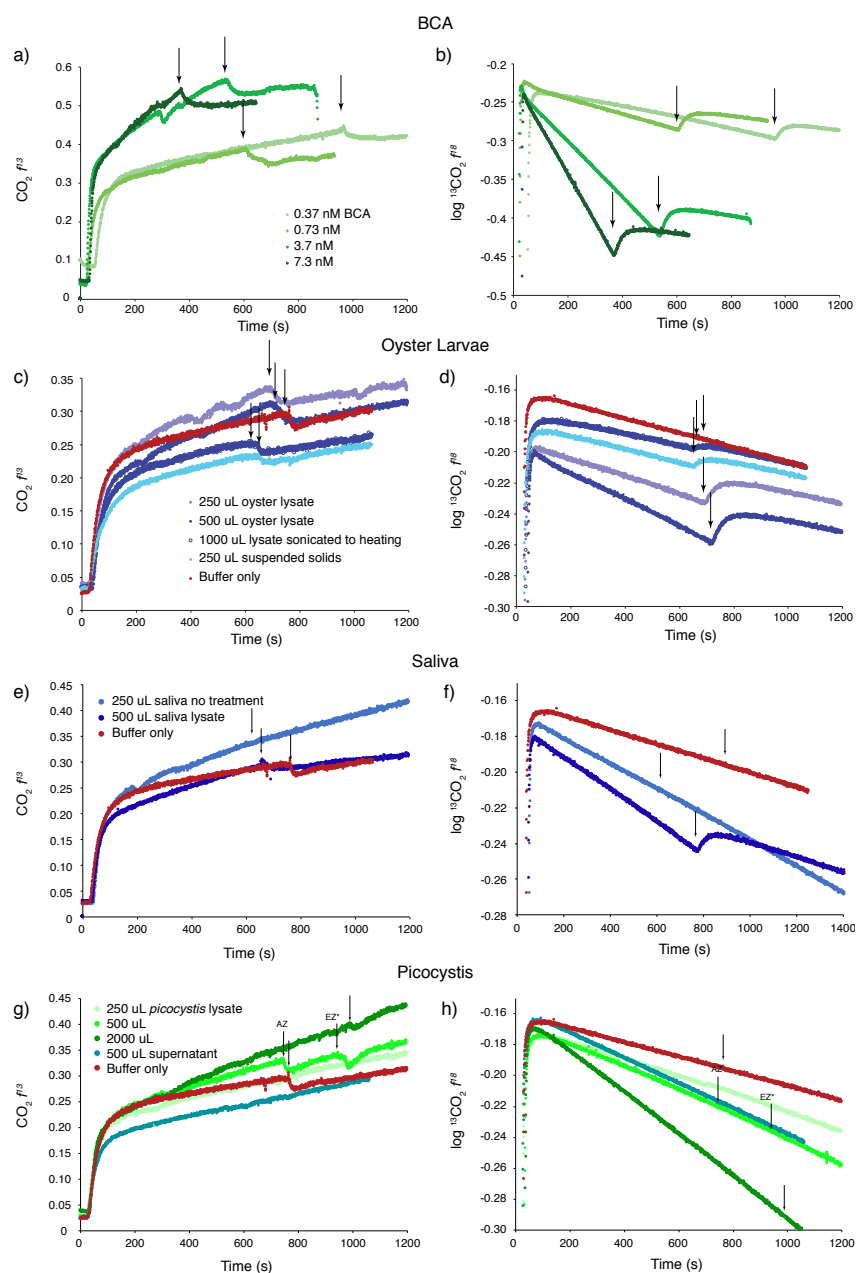
**Figure 6.8:** Traces of MIMS data from standard BCA experiments (**a**,**b**), oyster larvae (**c**,**d**), saliva (**e**,**f**), and *picocystis* (**g**,**h**). The left column shows MIMS $f^{13}$ versus time; the right column shows MIMS $f^{18}$ versus time. Arrows indicate the addition of 1 $\mu$M AZ inhibitor to the assay, except for the one arrow denoting the addition of the membrane-permeable EZ inhibitor. Note the change in slope after AZ addition in BCA samples, except for the buffer only $f^{18}$ curve in **d**). Note that not all natural samples show a change in slope after inhibition.

that affect the $^{13}CO_2$ signal much less strongly. Thus, we focus on the rate of $^{18}O$ depletion as a tracer of hydration/dehydration rate.

Results from standard additions of BCA are shown in Figure 6.8a-b. Rates of $f^{18}$ loss increase with increasing [BCA]. Arrows indicate the addition of inhibitor (AZ or EZ) into the assay. Following a brief rise in $f^{18}$ after the inhibitor is added, slopes are in general much more shallow than before, indicating that the rate of hydration/dehydration is slower in the presence of inhibitor. All BCA slopes are significantly shallower after the addition of inhibitor (Figure 6.8a-b). Slopes of $f^{13}$ also decrease after inhibitor addition for BCA runs.

Oyster lysates also show some CA activity (Figure 6.8c-d). When sonicated to heating, the $f^{18}$ slope is similar to that of the blank. Addition of the inhibitor changes the $f^{18}$ slopes of all lysates, indicating that oyster lysate CA activity can be inhibited using the MIMS assay. The buffer-only run shows a dip in $f^{13}$ after inhibitor addition, but the $f^{18}$ slope remains unchanged. Saliva assays are shown in Figure 6.8e-f. Both assays show increased activity over the blank. However, in the untreated sample, addition of inhibitor had no effect on either $f^{13}$ or $f^{18}$ slopes. The lysate, however, was effectively inhibited using AZ. MIMS assays run with *Picocystis* lysates are shown in Figure 6.8g-h. These lysates also show measurable CA activity. However, all $f^{18}$ traces were unaffected by the addition of AZ and EZ inhibitors.

A calibration of activity versus [BCA] can be more quantitative using the MIMS method through use of Eq.(6.8). The slope of $f^{18}$ versus time ($\lambda$) was converted to a rate constant of $CO_2$ hydration, which was then plotted against [BCA], allowing for the calcluation of specific rate parameters for the $CO_2 - H_2O$ system. Figure 6.7 shows determinations of $\frac{k_{cat}}{K_M}$ for BCA using the MIMS technique in two different methods. First, the concentration of CA was varied (Figure 6.7a). The slope of $k^*$ versus [CA] gives $\frac{k_{cat}}{K_M}$; the intercept gives $k_{+2}$. The slope gives a value of $\frac{k_{cat}}{K_M} = 6.8 \pm 0.3 \cdot 10^7$ $M^{-1}s^{-1}$, in good agreement with previous determinations between 2.3 and $8.3 \cdot 10^7$ $M^{-1}s^{-1}$ (J Uchikawa and R E Zeebe, 2012; Dodgson et al., 1990). The intercept gives a value of $k_{+2} = 2.3 \pm 1.1 \cdot 10^{-2}$ $s^{-1}$. Pinsent, Pearson, and Roughton (1956) measured $k_{+2}=1.86 \cdot 10^{-2}$ $s^{-1}$ at 21°C, in excellent agreement with our determination. The value measured by Johnson (1982) ($2.58 \cdot 10^{-2}$ $s^{-1}$), is also consistent with our results, given our rather large error bars. The $k^*$ measured from AZ-inhibited slopes ($\lambda = 9.8 \pm 1.5 \cdot 10^{-5}$ $s^{-1}$) in Figure 6.8a are also plotted as open circles in Figure 6.7a, giving $k_{+2} = 1.89 \pm 0.57 \cdot 10^{-2}$ $s^{-1}$. This value is lower

than that of Johnson (1982), and in good agreement with that of Pinsent, Pearson, and Roughton (1956).
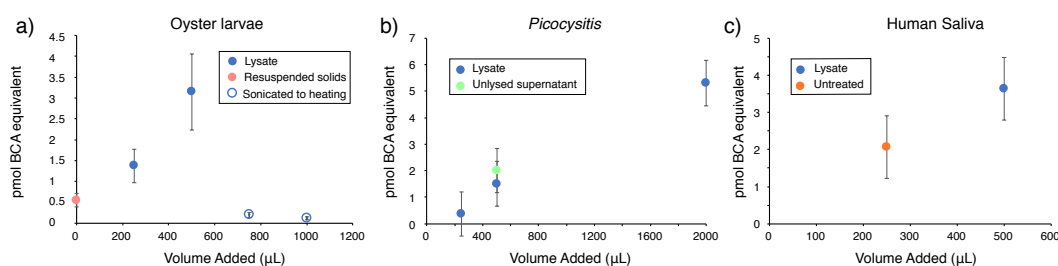


**Figure 6.9:** CA activity versus lysate amount for three natural samples. **a)** Oyster lysates. Lysed solids, including larval shells, were resuspended in buffer and showed some CA activity. Lysates that were sonicated to heating showed almost no CA activity, indicating that the proteins had denatured. **b)** *Picocystis* lysates. The supernatant removed from unlysed cells prior to sonication shows CA activity. **c)** human saliva samples show linearity despite the fact that one sample was not treated before adding to the assay.

Calculation of $\frac{k_{cat}}{K_M}$ was also made at multiple spike DIC concentrations and a single [CA] of 3.67 nM. These experiments are presented in Figure 6.7b. The $k_{+2}$ and $k_{+4}$ from Pinsent, Pearson, and Roughton (1956) were used. The experiment at very low DIC (0.1 mM) gives a low $\frac{k_{cat}}{K_M} = 3.8 \cdot 10^7$ M$^{-1}$s$^{-1}$. The mean of all $\frac{k_{cat}}{K_M}$ is $5.6 \pm 1.0 \cdot 10^7$ M$^{-1}$s$^{-1}$; excluding the low DIC point gives $\frac{k_{cat}}{K_M} = 6.0 \pm 0.4 \cdot 10^7$ M$^{-1}$s$^{-1}$. This value is just outside of the error envelope for the value calculated from Figure 6.7a, but is consistent with previous measurements, as discussed above.
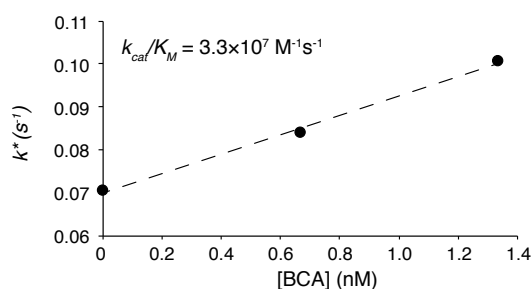


**Figure 6.10:** Calibration of the MIMS assay in 0.2$\mu$m filtered poisoned natural seawater. This seawater medium was assumed to be free of all biological activity and enzymes.

The amount of CA in natural samples was determined by running the MIMS assay with cell lysate material. The slopes from Figure 6.8 are plotted versus lysate amount in Figure 6.9. All materials showed a linear correlation between the amount of lysate and CA activity. The oyster samples in Figure 6.9a, when sonicated to denaturation, lost all activity. Also, as evident from Figure 6.8b, inhibition of activity was achieved

using 1 $\mu$M AZ. The solid pellet after sonication was also resuspended in buffer and run for its CA activity. It showed a small but measurable amount of activity.

*Picocystis* lysates showed a linear relationship between the amount of lysate and the amount of CA. In addition to the lysate, the supernatant was collected after sample thawing and before lysing and run on the assay. This supernatant also showed CA activity. Standard results for the assay run in $0.2\mu$m filtered poisoned natural seawater are shown in Figure 6.10. The slope of [CA] versus $k^*$ gives $\frac{k_{cat}}{K_M} = 3.3 \pm \cdot 10^7$ M$^{-1}$s$^{-1}$, significantly lower than the value in 0.02M Tris buffer. Fresh, unfiltered seawater from the San Pedro Ocean Time Series (SPOT) location was also tested using the assay. Slopes of $\log f^{18}$ are presented in Table 6.3, along with effective BCA concentrations, using the $\frac{k_{cat}}{K_M}$ calculated for seawater.

| Seawater type | $\lambda$ (x10$^2$ s$^{-1}$) | inhibited $\lambda$ (x10$^2$ s$^{-1}$) | $\frac{k_{cat}}{K_M}$[CA] (x10$^{-7}$ s$^{-1}$) | effective [CA] (nM) |
|---|---|---|---|---|
| SPOT unfiltered | 1.57±0.02 | 1.47±0.01 | 3.66 | 0.11 |
| SPOT 0.7 $\mu$m filtered | 1.53±0.02 | 1.48±0.01 | 1.76 | 0.05 |

**Table 6.3:** Results of MIMS assays conducted on natural, unfiltered seawater from SPOT. The assay was conducted with 420 $\mu$M total DIC. Errors on slopes were calculated directly from the scatter in $f^{18}$ data versus time. $\frac{k_{cat}}{K_M}$[CA] was calculated by subtracting the inhibited slope and dividing by the $f_{CO_2}$ correction factor in Eq.(6.8). Thus, the inhibited $\lambda$ was assumed to represent the uncatalyzed $k_{+2} + k_{+4}$[OH$^-$] in SPOT seawater. The $\frac{k_{cat}}{K_M}$ of BCA in seawater from Figure 6.10 was then used to calculate the effective [CA]. The unfiltered seawater shows more CA activity than the filtered seawater, suggesting that while there may be free CA in surface seawater, most is probably bound to the outside of cells and organisms as eCA.

## 6.4 Discussion

Three of the methods tested here – pH-drop, esterase, and MIMS – have been used extensively in the literature to estimate CA activity. The Picarro-$^{13}$C method was developed *ad-hoc* for the measurement of CA in seawater, and has never been described before in the literature. We include a summary of the results for all assays in Table 6.4. We also summarize the sensitivity range of these four assays, and their applicability to natural samples, in Table 6.5. These methods all have their strengths and weaknesses, which are outlined below.

The pH-drop method was one of the first assays developed (Wilbur and N. G. Anderson, 1948), and has been used extensively on oyster lysates and protein extracts (Miyamoto et al., 1996; Medakovic, 2000), organic matrices of corals (Tambutte et al., 2007; Rahman, Tamotsu Oomori, and Wörheide, 2011), human saliva (Murakami and Sly, 1987), bacterial CA, (Z Liu et al., 2009), and lake water filtrates

|  | Oyster | Picocystis | Saliva | Seawater |
|---|---|---|---|---|
| *pH* | | | | |
| [CA] | 0.001 g/g | 0 | N.T. | N.T. |
| Inhibited? | Yes | N/A | N.T. | N.T. |
| *Esterase* | | | | |
| [CA] | 0.18 g/g | 10-45nM in lysate | N.T. | N.T. |
| Inhibited? | N.T. | N.T. | N.T. | N.T. |
| *Picarro* $^{13}$C | | | | |
| [CA] | 0.01 g/g | 0 | 10 nM in lysate | 0 |
| Inhibited? | No | N/A | No | N/A |
| *MIMS* | | | | |
| [CA] | 0.001 g/g | 1.5-3 nM in lysate | 7-8 nM in lysate | 0.11 nM |
| Inhibited? | Yes | No | Yes | Yes |

**Table 6.4:** A summary table of all data collected on natural samples using the four different assay techniques. Although the pH-drop method has a low limit of detection, it did not detect any activity in *Picocystis* lysates, while the esterase and MIMS assays did. The MIMS assay also detected CA activity in natural seawater.

(Berman-Frank et al., 1994; E V Kupriyanova et al., 2003; Elena V Kupriyanova et al., 2016). The method is fast, with measurements taking only a few minutes; reagents are inexpensive; and it requires only a pH electrode for the measurement. It has a relatively low limit of detection, with solutions containting $\leq$ 1 nM CA showing definite rate enhancement (Figure 6.2b). The pH-drop method suggests that very small amounts of CA are present in oyster lysate material, which were successfully inhibited with AZ.

| Method | Sensitivity Range | Sample Size | Suitable for natural samples? |
|---|---|---|---|
| pH drop | 1-100 nM | 12 mL | Yes |
| Esterase | 10-100 nM | 0.1-1mL | No |
| Picarro | 5-50 nM | 40 mL | No |
| MIMS | 0.1-10 nM | 5 mL | Yes |

**Table 6.5:** A summary of the methods and their requirements. The MIMS method has the lowest limit of detection and can also work on relatively small sample sizes.

However, this method does not allow for the extraction of real kinetic information. Instead, the E.U. scale is a measure of the relative instantaneous hydration rate of $CO_2$ as it is mixed into the buffer solution. $CO_2$-saturated water is unstable given an atmospheric $p$CO$_2$=400 ppm (in 2017), and therefore there is significant blank variability from run to run (Figure 6.2). Therefore, this technique is probably best suited for presence-absence or semi-quantitative CA measurements only.

Although CA was first thought to be highly specific to the interconversion of $CO_2$ and $H_2CO_3$, it was discovered that the enzyme can also hydrolyze ester linkages in organic molecules (Pocker and Stone, 1967; Tashian, Shows, and Plato, 1963). From this discovery, Pocker and Stone (1967) developed an esterase assay, which has been used successfully on purified CA extracts (Z. Yu et al., 2006; S. A. Nielsen and Frieden, 1972a; S. A. Nielsen and Frieden, 1972b). Furthermore, this promiscuity of CA has helped elucidate mechanistic information about the method of hydration at the enzyme's active site (Lopez et al., 2011; Fisher et al., 2005). The method requires only a spectrophotometer and basic reagents, which make it a cost-effective screener for CA activity, especially when the enzyme can be purified.

There are some documented inconsistencies between traditional $CO_2$-based assays and esterase assays in the literature. For example, S. A. Nielsen and Frieden (1972b) measured both esterase and $CO_2$ hydration activity in purified bovine and oyster CA. They found that the ratio of esterase activity to $CO_2$ hydration activity in bovine CA was 1:1000, and that this ratio in oyster CA was 2.6:1000. This factor of 2.6 difference between the two suggests that CA's esterase activity is not directly scalable to its catalysis of $CO_2$ hydration. Z. Yu et al. (2006) was also only able to achieve 50% inhibition of purified oyster CA using AZ. One possibility for these results is that different CA molecules catalyze ester hydrolysis and $CO_2$ hydration slightly differently. Another possibility is that these purified enzyme extracts contained other proteins that also possess esterase activity.

Similar to these reported inconsistencies, our results of esterase activity on whole cell lysates seem to grossly overestimate the activity of CA. For example, the esterase assay predicts that 17% of oyster larval protein is CA – an unreasonable result. This activity is most likely protein-related, because we removed almost all excess esterase activity through heating. Thus, it is entirely possible that whole cell lysates contain other esterases which obscure the esterase activity of CA. Given the difference between the pH assay result of 0.001 g/g total protein CA activity in oysters, and the esterase result of 0.17 g/g total protein esterase activity in oysters, we would be searching for a 1:100 signal in the observed ester hydrolysis rate. This signal to noise ratio is untenable for low concentrations of CA in natural samples. Thus, we conclude that the esterase method is poorly suited for measuring CA activity in whole natural samples.

The Picarro-^{13}C method described here was designed *ad hoc* by the authors to measure CA activity in seawater samples. A similar method was attempted using a

$H^{13}CO_3^-$ spike, measuring the rate of appearance of $^{13}C$ in $CO_{2aq}$, sampled using a MIMS (Dieter F Sültemeyer et al., 1989). Our method is slightly different, since it samples $^{13}C$ gas derived from the dehydration of $^{13}CO_3^{2-}$ in solution, transferred to the headspace via gas exchange, and mixed into the natural abundance carrier gas at atmospheric $pCO_2$. This mixture, delivered to the Picarro, was expected to give an enriched $\delta^{13}C$ in the presence of CA, due to the increased rate of $^{13}CO_2$ production via dehydration in solution. Indeed, our experiments with purified BCA indicate that the assay works effectively in about 10 minutes, gives resolvable signals, and can be completely inhibited using AZ.

The Picarro-$^{13}C$ technique does not appear to perform well with natural samples and cell lysates. First, the sensitivity of the method is about one order of magnitude lower than the pH-drop and MIMS methods. This sensitivity is driven primarily by the variance in the blank of 1‰, and also by the relatively large amount of $CO_2$ needed to make a measurement on the Picarro. The analysis chamber is about 40 mL, and given a mass flow of 28 sccm, the chamber has a maximum response time of 1.4 minutes. The chamber operates at 15 torr and 40°C, requiring about 12 nmol of $CO_2$ being constantly supplied to the analyzer. For comparison, a typical MIMS response time is 1-2 seconds and operates at $10^{-6}$ torr (D F Sültemeyer, Fock, and Canvin, 1990; Delacruz et al., 2010).

Secondly, the amount of CA in oyster lysate (0.01 g/g total protein) was about one order of magnitude above the amount measured using the pH drop method (Table 6.4). Neither heating nor addition of inhibitor was able to eliminate the $\delta^{13}C$ enrichments measured in assays of cell lysates, indicating that the enrichments observed may not be exclusively due to CA activity. These enrichments may thus be due to other proteins which enhance the gas transfer rate, or perhaps manipulate the $CO_2$ chemistry in other ways. It should also be noted that the authors of Dieter F Sültemeyer et al., 1989 reverted to the $^{18}O$-MIMS technique in their subsequent publication (D F Sültemeyer, Fock, and Canvin, 1990). The complications involving cell lysates in the Picarro assay, in addition to the high detection limit, make it poorly suited for the measurement of CA activity in natural samples.

Carbonic anhydrase activity measured by the exchange of $^{18}O$ between DIC and $H_2O$ dates back to pioneering experiments by Mills and Urey, 1940. Some researchers then realized that they could use heavily enriched sodium bicarbonate, and measure against the lower $^{13}C$ background for better sensitivity (D. N. Silverman and C. K. Tu, 1976; D. N. Silverman, 1982). These authors measured the depletion of $^{18}O$ label

from $^{13}$C species using a membrane inlet connected to a mass spectrometer. This method, then, requires the most costly set of equipment out of all of those described here. First, enriched isotopic spikes are needed, including $H^{13}CO_3^-$ and $H_2^{18}O$. Secondly, a quadrupole mass spectrometer is needed to make the measurement, which, while relatively inexpensive relative to magnetic sector instruments, is much more expensive than a pH electrode.

The price tag does come with benefits. The isotopic exchange method is the only assay to work at equilibrium: bulk DIC species are fully equilibrated, and the assay measures the exchange of isotopes between these species. Secondly, because of the extensive theory built from isotope exchange studies, rate constants can be extracted from the slopes of $^{18}O$ depletion versus time (D. N. Silverman, 1982; D. N. Silverman and Lindskog, 1988; J Uchikawa and R E Zeebe, 2012). The results shown in Figure 6.7 demonstrate that we can extract rate constants for the uncatalyzed and catalyzed hydration of $CO_2$, validating our application of the method in the laboratory.

This technique has also been applied to the CA activity in natural samples, from purified CA and cell lysates (Y. Xu et al., 2008; Dodgson et al., 1990), cultured diatoms and cyanobacteria (Dieter F Sültemeyer et al., 1989; D F Sültemeyer, Fock, and Canvin, 1990; Murray R Badger and Price, 1989; M R Badger and Andrews, 1982), spinach photosystems (Hillier et al., 2006; McConnell et al., 2007), extracellular CA (Delacruz et al., 2010), and particles filtered from natural seawater (Tortell, C. L. Martin, and Corkum, 2006). Thus, we had confidence in our ability to measure the CA activity in natural samples using this method.

Indeed, we have successfully detected CA activity in several natural samples using the MIMS technique. The MIMS results for CA activity show broadly similar results to the pH drop method for oyster lysates (Table 6.4), predicting that CA represents about 0.001 g/g total protein in oyster larvae. This CA activity was successfully inhibited by AZ. About 0.1 % of total protein as CA is much more reasonable than the other assays' estimates of CA activity. Our results are hard to compare with other studies, because every study chooses to normalize CA activity by a different metric (wet weight (Medakovic, 2000), purified protein amount (Miyamoto et al., 1996), or not specified (Z. Yu et al., 2006)). However, future work including a CA activity assay as a function of life cycle stage in oysters is being planned, and will hopefully yield useful insights into the nature of CA expression during growth and shell development in oysters.

Interestingly, the MIMS technique also identified CA activity in *Picocystis* lysates,

which the pH assay did not detect. However, the addition of both EZ and AZ did not inhibit the observed CA activity. It could be that the type of CA found in *Picocystis* is quite different from the erythrocyte form, and thus is less affected by traditional CA inhibitors. In fact, the genes for multiple carbonic anhydrases, and CA activity, have been measured in microbes isolated from soda lakes (E V Kupriyanova et al., 2003; Elena V Kupriyanova et al., 2016). Genetic analysis showed that genes for all three isoforms currently known – $\alpha$, $\beta$, and $\gamma$ – are present in these alkaphilic bacteria (Elena V Kupriyanova et al., 2016). These isoforms are structurally quite different from each other and thus may not behave similarly in the presence of inhibitors (Moroney, Bartlett, and Samuelsson, 2001). Furthermore, some of the soluble forms of CA isolated by E V Kupriyanova et al. (2003) had very high tolerances to inhibitors – as high as 1-10 mM total inhibitor concentration. It is thus possible that *Picocystis* CA is insensitive to traditional CA inhibitors.

Given the extremely high DIC and alkalinity measured in Mono Lake (0.3 and 0.6 moles/kg and eq/kg, respectively), $CO_2$ is expected to be quite low and thus primary producers may indeed be $CO_2$-limited. The presence of CA is also implicated in a long-standing controversy regarding the $^{14}C$ budget of Mono Lake (W S Broecker et al., 1988; Rachel Oxburgh, Wallace S Broecker, and Wanninkhof, 1991). *Picocystis* is the dominant primary producer in Mono Lake (Oremland, Miller, and Whiticar, 1987; Roesler et al., 2002; Oremland, 2013), and is thus a prime candidate for the production of CA in the lake. The fact that we measured CA activity in the supernatant of unlysed cells could mean that these algae produce extracellular CA. This extracellular CA would more rapidly equilibrate the $^{14}C$-enriched atmospheric $CO_2$ with lake water $CO_2$, producing a larger $^{14}C$ anomaly in the lake than would be expected given traditional gas exchange rates (W S Broecker et al., 1988). However, more measurements of CA activity in *Picocystsis* cultures and the media they are grown in are needed to fully address this mystery.

The MIMS assay technique has also been applied here to natural seawater. While the values of $k_{+2}$ were extracted in buffer (Figure 6.7), this analysis was not successful in seawater because the DIC and alkalinity of the seawater medium was not measured. Therefore the $f_{CO_2}$ and pH were not known. An $f_{CO_2}$ of 0.008 was assumed for the seawater-spike mixture in order to calculate $k^*$, but this value gives abnormally high values of $k_{2+} \sim 0.07$ s$^{-1}$ (Figure 6.10). However, the plot of $k^*$ versus [CA] still gives information about the rate of catalysis due to CA, and yields a $\frac{k_{cat}}{K_M} = 3.8 \cdot 10^7$ M$^{-1}$s$^{-1}$. This value is significantly lower than the $\frac{k_{cat}}{K_M}$ calculated in buffer. S. A.

Nielsen and Frieden (1972b) reported the inhibition of bovine CA activity in the presence of chloride ion, with 50% inhibition achieved at only 0.2 M NaCl. Thus, it is not unreasonable that BCA should also be less effective in seawater, which contains about 0.5 M NaCl.

We also attempted to measure the CA activity of natural, unfiltered seawater. These results, while barely above the detection limit, show a significantly greater slope of $f^{18}$ versus time compared to the inhibited slope (Table 6.3). There is more CA associated with the particles than free in seawater, presumably because most CA is bound to the membranes of marine microorganisms (Mustaffa, Striebel, and Wurl, 2017; Elzenga, Prins, and Stefels, 2000). Recently, Mustaffa, Striebel, and Wurl (2017) described a method of measuring extracellular CA concentrations in natural seawater, by a fluorometric method. This method measures the fluorescent-sensitive binding of a dye to the zinc in the active site of CA, and estimates about 0.2 nM CA in samples taken from the Baltic Sea. This result is broadly consistent with our MIMS finding of $\sim$ 0.11 nM CA in SPOT seawater. This method needs to be refined, but could provide robust measurements of CA activity in natural samples. A study of the CA activity in surface seawater, in falling particles, and in surface sediments will matter not only for the effect of CA on gas exchange and primary productivity, but also for elucidating its role in accelerating calcite dissolution in the ocean (A. Subhas, Adkins, J. Erez, Rollins, et al., Under Review).

## 6.5 Conclusion

Four different assays of CA activity were tested here to investigate their potential for measuring CA activity in natural samples. The esterase assay, while relatively inexpensive, was not suitable for cell lysates because of the presence of significant esterase activity not specifically associated with the presence of CA. The Picarro assay similarly showed good response in the presence of pure BCA, but recorded $^{13}$C enrichments in cell lysates that could not be inhibited with known CA inhibitors. The pH drop method successfully detected CA activity in oyster lysates, but not in *Picocystis*. It also demonstrated a large blank variability. The MIMS method, on the other hand, was able to provide robust rate data for uncatalyzed and catalyzed $CO_2$ hydrolysis and measured CA activity in oyster, saliva, and *Picocystis* lysates. It also measured a small but significant CA activity in natural seawater. The MIMS method will therefore be used in the future to measure the CA activity in a number of settings moving forward. A growth series of CA activity will be attempted on oysters grown in the laboratory. The presence of extracellular CA in *Picocystsis* will

be tested more thoroughly. Finally, the presence of CA in natural seawater, falling particles, and seafloor sediments will also be attempted.

# BIBLIOGRAPHY

Anand, P, H Elderfield, and M H Conte (2003). "Calibration of Mg/Ca thermometry in planktonic foraminifera from a sediment trap time series". In: *Paleoceanography*.

Andersson, Andreas J, Nicholas R Bates, and Fred T Mackenzie (2007). "Dissolution of Carbonate Sediments Under Rising $pCO_2$ and Ocean Acidification: Observations from Devil's Hole, Bermuda". In: *Aquatic Geochemistry* 13.3, pp. 237–264.

Andersson, Andreas J and Dwight Gledhill (2013). "Ocean Acidification and Coral Reefs: Effects on Breakdown, Dissolution, and Net Ecosystem Calcification". In: *Annual Review of Marine Science* 5.1, pp. 321–348.

Arakaki, T and A Mucci (1995). "A continuous and mechanistic representation of calcite reaction-controlled kinetics in dilute solutions at 25 C and 1 atm total pressure". In: *Aquatic Geochemistry* 1, pp. 105–130.

Archer, David (1991). "Modeling the calcite lysocline". In: *Journal of Geophysical Research: Oceans (1978–2012)* 96.C9, pp. 17037–17050.

Archer, David E (1996). "An atlas of the distribution of calcium carbonate in sediments of the deep sea". In: *Global Biogeochemical Cycles* 10.1, pp. 159–174.

Archer, David, Haroon Kheshgi, and Ernst Maier-Reimer (1998). "Dynamics of fossil fuel $CO_2$ neutralization by marine $CaCO_3$". In: *Global Biogeochemical Cycles* 12.2, pp. 259–276.

Arrhenius, G (1988). "Rate of Production, Dissolution and Accumulation of Biogenic Solids in the Ocean". In: *Palaeogeography, Palaeoclimatology, Palaeoecology* 67.1-2, pp. 119–146.

Arvidson, R S et al. (2006). "Magnesium inhibition of calcite dissolution kinetics". In: *Geochimica et Cosmochimica Acta* 70, pp. 583–594.

Arvidson, Rolf S, Cornelius Fischer, and Andreas Lüttge (2015). "Calcite Dissolution Kinetics". In: *Aquatic Geochemistry*, pp. 1–8.

Arvidson, Rolf S and Andreas Lüttge (2010). "Mineral dissolution kinetics as a function of distance from equilibrium – New experimental results". In: *Chemical Geology* 269.1-2, pp. 79–88.

Badger, M R and T J Andrews (1982). "Photosynthesis and Inorganic Carbon Usage by the Marine Cyanobacterium, Synechococcus Sp". In: *Plant Physiology* 70.2, pp. 517–523.

Badger, Murray R and G Dean Price (1989). "Carbonic Anhydrase Activity Associated with the Cyanobacterium Synechococcus PCC7942". In: *Plant Physiology* 89.1, pp. 51–60.

Badillo-Almaraz, V E and J Ly (2003). "Calcium sorption on hydroxyapatite in aqueous solutions: reversible and nonreversible components". In: *Journal of colloid and interface science* 258.1, pp. 27–32.

Bairbakhish, Ahmed N et al. (1999). "Disintegration of aggregates and coccospheres in sediment trap samples". In: *Marine Micropaleontology* 37.2, pp. 219–223.

Barker, Stephen et al. (2005). "Planktonic foraminiferal Mg/Ca as a proxy for past oceanic temperatures: a methodological overview and data compilation for the Last Glacial Maximum". In: *Quaternary Science Reviews* 24.7-9, pp. 821–834.

Bednarsek, N et al. (2014). "Limacina helicina shell dissolution as an indicator of declining habitat suitability owing to ocean acidification in the California Current Ecosystem". In: *Proceedings of the Royal Society B: Biological Sciences* 281.1785, pp. 20140123–20140123.

Bender, M L, R B Lorens, and D F Williams (1975). "Sodium, magnesium and strontium in the tests of planktonic foraminifera". In: *Micropaleontology* 21.4, p. 448.

Bentov, S and J Erez (2005). "Novel observations on biomineralization processes in foraminifera and implications for Mg/Ca ratio in the shells". In: *Geology* 33.11, pp. 841–844.

Bentov, Shmuel, Colin Brownlee, and Jonathan Erez (2009). "The role of seawater endocytosis in the biomineralization process in calcareous foraminifera". In: *Proceedings of the National Academy of Sciences* 106.51, pp. 21500–21504.

Berelson, W M et al. (2007). "Relating estimates of $CaCO_3$ production, export, and dissolution in the water column to measurements of $CaCO_3$ rain into sediment traps and dissolution on the sea floor: A revised global carbonate budget". In: *Global Biogeochemical Cycles* 21.1.

Berger, W H (1970). "Planktonic Foraminifera - Selective Solution and Lysocline". In: *Marine Geology* 8.2, pp. 111–&.

– (1973). "Deep-sea carbonates: evidence for a coccolith lysocline". In: *Deep Sea Research and Oceanographic Abstracts* 20.10, pp. 917–921.

Berman-Frank, Ilana et al. (1994). "$CO_2$ availability, carbonic anhydrase, and the annual dinoflagellate bloom in Lake Kinneret". In: *Limnology and Oceanography* 39.8, pp. 1822–1834.

Berner, R A and J W Morse (1974). "Dissolution kinetics of calcium carbonate in sea water; IV, Theory of calcite dissolution". In: *American Journal of Science* 274, pp. 108–134.

Berner, Robert A and Zavareth Kothavala (2001). "Geocarb III: A Revised Model of Atmospheric $CO_2$ over Phanerozoic Time". In: *American Journal of Science* 301.2, pp. 182–204.

Bilinski, H et al. (1991). "Trace metal adsorption on inorganic solid phases under estuarine conditions". In: *Marine Chemistry* 32.2-4, pp. 225–233.

Biscaye, P E, V Kolla, and K K Turekian (1976). "Distribution of calcium carbonate in surface sediments of the Atlantic Ocean". In: *Journal of Geophysical Research: Oceans (1978–2012)* 81.15, pp. 2595–2603.

Boudreau, Bernard P (2013). "Carbonate dissolution rates at the deep ocean floor". In: *Geophysical Research Letters* 40.4, pp. 744–748.

Boudreau, Bernard P, Jack J Middelburg, Andreas F Hofmann, et al. (2010). "Ongoing transients in carbonate compensation". In: *Global Biogeochemical Cycles* 24.4.

Boudreau, Bernard P, Jack J Middelburg, and Filip J R Meysman (2010). "Carbonate compensation dynamics". In: *Geophysical Research Letters* 37.L03603, pp. 1–5.

Branson, Oscar et al. (2016). "Nanometer-Scale Chemistry of a Calcite Biomineralization Template: Implications for Skeletal Composition and Nucleation". In: *Proceedings of the National Academy of Sciences* 113.46, pp. 12934–12939.

Briguglio, Antonino and Johann Hohenegger (2014). "Growth oscillation in larger foraminifera". In: *Paleobiology* 40.3, pp. 494–509.

Broecker, W S et al. (1988). "The Radiocarbon Budget for Mono Lake - an Unsolved Mystery". In: *Earth and Planetary Science Letters* 88.1-2, pp. 16–26.

Broecker, Wallace and Elizabeth Clark (2009). "Ratio of coccolith $CaCO_3$ to foraminifera $CaCO_3$ in late Holocene deep sea sediments". In: *Paleoceanography* 24.3, pp. 1–11.

Brown, S J and H Elderfield (1996). "Variations in Mg/Ca and Sr/Ca ratios of planktonic foraminifera caused by postdepositional dissolution: Evidence of shallow Mg-dependent dissolution". In: *Paleoceanography* 11.5, pp. 543–551.

Brunauer, S, P H Emmett, and E Teller (1938). "Adsorption of gases in multimolecular layers". In: *Journal of the American Chemical Society* 60, pp. 309–319.

Burton, W K, N Cabrera, and F C Frank (1951). "The Growth of Crystals and the Equilibrium Structure of Their Surfaces". In: *Philosophical Transactions of the Royal Society of London. Series A, Mathematical and Physical Sciences* 243.866, pp. 299–358.

Chou, LEI, R M Garrels, and R Wollast (1989). "Comparative study of the kinetics and mechanisms of dissolution of carbonate minerals". In: *Chemical Geology* 78.3-4, pp. 269–282.

Corliss, B H and S Honjo (1981). "Dissolution of Deep-Sea Benthonic Foraminifera". In: *Micropaleontology* 27.4, pp. 356–378.

Cubillas, Pablo et al. (2005). "Experimental determination of the dissolution rates of calcite, aragonite, and bivalves". In: *Chemical Geology* 216.1-2, pp. 59–77.

Cyronak, T, I R Santos, and B D Eyre (2013). "Permeable coral reef sediment dissolution driven by elevated $pCO_2$ and pore water advection". In: *Geophysical Research Letters*, n/a–n/a.

Delacruz, J et al. (2010). "Detecting extracellular carbonic anhydrase activity using membrane inlet mass spectrometry". In: *Analytical Biochemistry* 403, pp. 74–78.

Dickson, A G and F J Millero (1987). "A comparison of the equilibrium constants for the dissociation of carbonic acid in seawater media". In: *Deep Sea Research* 34.10, pp. 1733–1743.

Dittert, N et al. (1999). "Carbonate Dissolution in the Deep-Sea: Methods, Quantification and Paleoceanographic Application". In: *Use of Proxies in Paleoceanography*. Berlin, Heidelberg: Springer Berlin Heidelberg, pp. 255–284.

Dixit, Suvasis and Susan A Carroll (2007). "Effect of solution saturation state and temperature on diopside dissolution". In: *Geochemical Transactions* 8.1, pp. 3–14.

Dodgson, S J et al. (1990). "Comparison of $^{18}O$ exchange and pH stop-flow assays for carbonic anhydrase". In: *Journal of Applied Physiology* 68.6, pp. 2443–2450.

Doney, Scott C et al. (2009). "Ocean Acidification: The Other $CO_2$ Problem". In: *Annual Review of Marine Science* 1.1, pp. 169–192.

Dougherty, Robert P. (2007). *Computing Local Thickness of 3D Structures with ImageJ*. http://www.optinav.info/LocalThicknessEd.pdf.

Dove, P M, N Z Han, and J J De Yoreo (2005). "Mechanisms of classical crystal growth theory explain quartz and silicate dissolution behavior". In: *Proceedings of the National Academy of Sciences* 102.43, pp. 15357–15362.

Dove, Patricia M et al. (2008). "Kinetics of amorphous silica dissolution and the paradox of the silica polymorphs". In: *Proceedings of the National Academy of Sciences* 105.29, pp. 9903–9908.

Drake, Jeana L et al. (2013). "Proteomic analysis of skeletal organic matrix from the stony coral Stylophora pistillata". In: *Proceedings of the National Academy of Sciences* 110.10, pp. 3788–3793.

Dreybrodt, W et al. (1996). "The kinetics of the of the reaction $CO_2+H_2O -> H^+ + HCO_3^-$ as one of the rate limiting steps for the dissolution of calcite in the system $H_2O$-$CO_2$-$CaCO_3$". In: *Geochimica et Cosmochimica Acta* 60.18, pp. 3375–3381.

Dunne, John P, Burke Hales, and J R Toggweiler (2012). "Global calcite cycling constrained by sediment preservation controls". In: *Global Biogeochemical Cycles* 26.3.

Eggins, S M, A Sadekov, and P De Deckker (2004). "Modulation and daily banding of Mg/Ca in Orbulina universa tests by symbiont photosynthesis and respiration: a complication for seawater thermometry?" In: *Earth and Planetary Science Letters*.

Elzenga, J Theo M, Hidde B A Prins, and Jacqueline Stefels (2000). "The role of extracellular carbonic anhydrase activity in inorganic carbon utilization of Phaeocystis globosa (Prymnesiophyceae): A comparison with other marine algae using the isotopic disequilibrium technique". In: *Limnology and Oceanography* 45.2, pp. 372–380.

Emerson, Steven and M Bender (1981). "Carbon fluxes at the sediment-water interface of the deep-sea: calcium carbonate preservation." In: *Journal of Marine Research*.

Erez, J (2003). "The source of ions for biomineralization in foraminifera and their implications for paleoceanographic proxies". In: *Reviews in Mineralogy and Geochemistry*.

Evans, David, Jonathan Erez, et al. (2015). "Mg/Ca-temperature and seawater-test chemistry relationships in the shallow-dwelling large benthic foraminifera Operculina ammonoides". In: *Geochimica et Cosmochimica Acta* 148.C, pp. 325–342.

Evans, David, Wolfgang Müller, et al. (2013). "Eocene seasonality and seawater alkaline earth reconstruction using shallow-dwelling large benthic foraminifera". In: *Earth and Planetary Science Letters* 381.C, pp. 104–115.

Feely, R A (2004). "Impact of Anthropogenic $CO_2$ on the $CaCO_3$ System in the Oceans". In: *Science* 305.5682, pp. 362–366.

Feely, R A et al. (2002). "In situ calcium carbonate dissolution in the Pacific Ocean". In: *Global Biogeochemical Cycles* 16.4, pp. 91–1–91–12.

Feely, Richard A et al. (2012). "Decadal changes in the aragonite and calcite saturation state of the Pacific Ocean". In: *Global Biogeochemical Cycles* 26.3.

Fischer, Cornelius, Rolf S Arvidson, and Andreas Lüttge (2012). "How predictable are dissolution rates of crystalline material?" In: *Geochimica et Cosmochimica Acta* 98.C, pp. 177–185.

Fisher, Z et al. (2005). "Structural and kinetic characterization of active-site histidine as a proton shuttle in catalysis by human carbonic anhydrase II". In: *Biochemistry* 44.4, pp. 1097–1105.

Friis, K et al. (2006). "Possible overestimation of shallow-depth calcium carbonate dissolution in the ocean". In: *Global Biogeochemical Cycles* 20.4.

Fukuhara, Tatsuo et al. (2008). "An in situ experiment of calcium carbonate dissolution in the central Pacific Ocean". In: *International Journal of Greenhouse Gas Control* 2.1, pp. 78–88.

Gal, A et al. (2016). "Macromolecular recognition directs calcium ions to coccolith mineralization sites". In: *Science* 353.6299, pp. 590–593.

Gehlen, M et al. (2005a). "Reassessing the dissolution of marine carbonates: I. Solubility". In: *Deep Sea Research Part I: Oceanographic Research Papers* 52.8, pp. 1445–1460.

– (2005b). "Reassessing the dissolution of marine carbonates: II. Reaction kinetics". In: *Deep Sea Research Part I: Oceanographic Research Papers* 52.8, pp. 1461–1476.

Gonzales, Mariane V et al. (2017). "HelP Index: Hoeglundina elegans Preservation Index for Marine Sediments in the Western South Atlantic". In: *The Journal of Foraminiferal Research* 47.1, pp. 56–69.

Gorski, Christopher A and Matthew S Fantle (2017). "Stable mineral recrystallization in low temperature aqueous systems: A critical review". In: *Geochimica et Cosmochimica Acta* 198, pp. 439–465.

Hales, B and S Emerson (1997a). "Calcite dissolution in sediments of the Ceara Rise: In situ measurements of porewater $O_2$, pH, and $CO_{2(aq)}$". In: *Geochimica et Cosmochimica Acta* 61.3, pp. 501–514.

– (1997b). "Evidence in support of first-order dissolution kinetics of calcite in seawater". In: *Earth and Planetary Science Letters* 148, pp. 317–327.

Hales, Burke (2003). "Respiration, dissolution, and the lysocline". In: *Paleoceanography* 18.4.

Hamm, L M et al. (2014). "Reconciling disparate views of template-directed nucleation through measurement of calcite nucleation kinetics and binding energies". In: *Proceedings of the National Academy of Sciences* 111.4, pp. 1304–1309.

Harris, D, W R Horwath, and C van Kessel (2001). "Acid fumigation of soils to remove carbonates prior to total organic carbon or carbon-13 isotopic analysis". In: *Soil Science Society of America Journal* 65.6, pp. 1853–1856.

Heberling, Frank et al. (2011). "Structure and reactivity of the calcite–water interface". In: *Journal of colloid and interface science* 354.2, pp. 843–857.

Hemleben, C, M Spindler, and O R Anderson (1989). *Modern Planktonic Foraminifera*. Springer-Verlag.

Henehan, Michael J et al. (2013). "Calibration of the boron isotope proxy in the planktonic foraminifera *Globigerinoides ruber* for use in palaeo-$CO_2$ reconstruction". In: *Earth and Planetary Science Letters* 364.C, pp. 111–122.

Hillier, Warwick et al. (2006). "Quantitative Assessment of Intrinsic Carbonic Anhydrase Activity and the Capacity for Bicarbonate Oxidation in Photosystem II †". In: *Biochemistry* 45.7, pp. 2094–2102.

Hohenegger, Johann and Antonino Briguglio (2012). "Axially Oriented Sections of Nummulitids: a Tool to Interpret Larger Benthic Foraminiferal Deposits". In: *The Journal of Foraminiferal Research* 42.2, pp. 134–142.

Honjo, S and J Erez (1978). "Dissolution rates of calcium carbonate in the deep ocean; an in-situ experiment in the North Atlantic Ocean". In: *Earth and Planetary Science Letters* 40, pp. 287–300.

Ilyina, T and R E Zeebe (2012). "Detection and projection of carbonate dissolution in the water column and deep-sea sediments due to ocean acidification". In: *Geophysical Research Letters* 39.

Johnson, K S (1982). "Carbon-Dioxide Hydration and Dehydration Kinetics in Sea-Water". In: *Limnology and Oceanography* 27.5, pp. 849–855.

Johnstone, Heather J H, Michael Schulz, et al. (2010). "Inside story: An X-ray computed tomography method for assessing dissolution in the tests of planktonic foraminifera". In: *Marine Micropaleontology* 77.1-2, pp. 58–70.

Johnstone, Heather J H, Jimin Yu, et al. (2011). "Improving temperature estimates derived from Mg/Ca of planktonic foraminifera using X-ray computed tomography–based dissolution index, XDX". In: *Paleoceanography* 26.1, PA1215–17.

Jokulsdottir, Tinna and David Archer (2016). "A stochastic, Lagrangian model of sinking biogenic aggregates in the ocean (SLAMS 1.0): model formulation, validation and sensitivity". In: *Geoscientific Model Development* 9.4, pp. 1455–1476.

Kanel, J de and J W Morse (1979). "A simple technique for surface area determination". In: *Journal of Physics E Scientific Instruments* 12, pp. 272–273.

Keir, R S (1980). "The dissolution kinetics of biogenic calcium carbonates in seawater". In: *Geochimica et Cosmochimica Acta* 44, pp. 241–252.

– (1983). "Variation in the carbonate reactivity of deep-sea sediments: determination from flux experiments". In: *Deep Sea Research* 30.3A, pp. 279–296.

Kleypas, Joan A, Kenneth R N Anthony, and Jean-Pierre Gattuso (2011). "Coral reefs modify their seawater carbon chemistry - case study from a barrier reef (Moorea, French Polynesia)". In: *Global Change Biology* 17.12, pp. 3667–3678.

Kolla, Venkatarathnam, Allan W H Bé, and Pierre E Biscaye (1976). "Calcium carbonate distribution in the surface sediments of the Indian Ocean". In: *Journal of Geophysical Research: Oceans (1978–2012)* 81.15, pp. 2605–2616.

Kontoyannis, Christos G and Nikos V Vagenas (2000). "Calcium carbonate phase analysis using XRD and FT-Raman spectroscopy". In: *The Analyst* 125.2, pp. 251–255.

Kotler, E, R E Martin, and W D Liddell (1992). "Experimental analysis of abrasion and dissolution resistance of modern reef-dwelling foraminifera: implications for the preservation of biogenic carbonate". In: *Palaios* 7.3, pp. 244–276.

Kuile, Benno ter and Jonathan Erez (1984). "In situ growth rate experiments on the symbiont-bearing foraminifera Amphistegina lobifera and Amphisorus hemprichii". In: *The Journal of Foraminiferal Research* 14.4, pp. 262–276.

Kupriyanova, E V et al. (2003). "Carbonic Anhydrase Activity of Alkalophilic Cyanobacteria from Soda Lakes". In: *Russian Journal of Plant Physiology* 50.4, pp. 532–539.

Kupriyanova, Elena V et al. (2016). "The complete genome of a cyanobacterium from a soda lake reveals the presence of the components of $CO_2$-concentrating mechanism". In: *Photosynthesis Research* 130.1, pp. 151–165.

Lasaga, A C and A Luttge (2001). "Variation of crystal dissolution rate based on a dissolution stepwave model". In: *Science* 291.5512, pp. 2400–2404.

Lear, C H, H Elderfield, and P A Wilson (2000). "Cenozoic deep-sea temperatures and global ice volumes from Mg/Ca in benthic foraminiferal calcite". In: *Science* 287.5451, pp. 269–272.

Lear, C H, Y Rosenthal, and N Slowey (2002). "Benthic foraminiferal Mg/Ca-paleothermometry: A revised core-top calibration". In: *Geochimica et Cosmochimica Acta* 66.19, pp. 3375–3387.

Li, Wei et al. (2008). "Limestone Dissolution Induced by Fungal Mycelia, Acidic Materials, and Carbonic Anhydrase from Fungi". In: *Mycopathologia* 167.1, pp. 37–46.

Li, Y H and S Gregory (1974). "Diffusion of Ions in Sea-Water and in Deep-Sea Sediments". In: *Geochimica et Cosmochimica Acta* 38.5, pp. 703–714.

Liu, Zaihua, Daoxian Yuan, and Wolfgang Dreybrodt (2005). "Comparative study of dissolution rate-determining mechanisms of limestone and dolomite". In: *Environmental Geology* 49.2, pp. 274–279.

Liu, Z et al. (2009). "Production, purification, and characterization of a fusion protein of carbonic anhydrase from *Neisseria gonorrhoeae* and cellulose binding domain from *Clostridium thermocellum*". In: *Biotechnology Progress* 25.1, pp. 68–74.

Lopez, Marie et al. (2011). "Promiscuity of Carbonic Anhydrase II. Unexpected Ester Hydrolysis of Carbohydrate-Based Sulfamate Inhibitors". In: *Journal of the American Chemical Society* 133.45, pp. 18452–18462.

Lueker, T J, A G Dickson, and C D Keeling (2000). "Ocean $pCO_2$ calculated from dissolved inorganic carbon, alkalinity, and equations for $K_1$ and $K_2$: validation based on laboratory measurements of $CO_2$ in gas and seawater at equilibrium". In: *Marine Chemistry* 70.1-3, pp. 105–119.

Luttge, A, R S Arvidson, and C Fischer (2013). "A Stochastic Treatment of Crystal Dissolution Kinetics". In: *Elements* 9.3, pp. 183–188.

MacInnis, I N and S L Brantley (1992). "The role of dislocations and surface morphology in calcite dissolution". In: *Geochimica et Cosmochimica Acta* 56.3, pp. 1113–1126.

Mackinder, L, G Wheeler, and D Schroeder (2010). "Molecular mechanisms underlying calcification in coccolithophores". In: *Geomicrobiology* . . .

Malkin, A I, A A Chernov, and I V Alexeev (1989). "Growth of Dipyramidal Face of Dislocation-Free Adp Crystals - Free-Energy of Steps". In: *Journal of Crystal Growth* 97.3-4, pp. 765–769.

Martin, C L and P D Tortell (2008). "Bicarbonate transport and extracellular carbonic anhydrase in marine diatoms". In: *Physiologia plantarum.*

Martin, W R and F L Sayles (1996). "CaCO$_3$ dissolution in sediments of the Ceara Rise, western equatorial Atlantic". In: *Geochimica et Cosmochimica Acta* 60.2, pp. 243–263.

Mass, T et al. (2014). "Immunolocalization of skeletal matrix proteins in tissue and mineral of the coral Stylophora pistillata". In: *Proceedings of the National Academy of Sciences* 111.35, pp. 12728–12733.

McConnell, I L et al. (2007). "A quantitative assessment of the carbonic anhydrase activity in photosystem II". In: *Biochimica et Biophysica Acta (BBA) - Bioenergetics* 1767.6, pp. 639–647.

McIntyre, Andrew and R McIntyre (1971). "Coccolith concentrations and differential solution in oceanic sediments". In: *The Micropaleontology of Oceans. Cambridge Univ. Press, London*, pp. 253–261.

Medakovic, D (2000). "Carbonic anhydrase activity and biomineralization process in embryos, larvae and adult blue mussels *Mytilus edulis* L". In: *Helgoland Marine Research* 54, pp. 1–6.

Mehrbach, C et al. (1973). "Measurement of the apparent dissociation constants of carbonic acid in seawater at atmospheric pressure". In: *Limnology and Oceanography* 18.6, pp. 897–907.

Millero, F J (1995). "Thermodynamics of the carbon dioxide system in the oceans". In: *Geochimica et Cosmochimica Acta* 59.4, pp. 661–667.

Milliman, J D (1993). "Production and accumulation of calcium carbonate in the ocean: budget of a nonsteady state". In: *Global Biogeochemical Cycles.*

Milliman, J D and A W Droxler (1995). "Calcium carbonate sedimentation in the global ocean: linkages between the neritic and pelagic environments". In: *Oceanography.*

Milliman, J D, P J Troy, et al. (1999). "Biologically mediated dissolution of calcium carbonate above the chemical lysocline?" In: *Deep Sea Research* 46.10, pp. 1653–1669.

Mills, G A and H C Urey (1940). "The Kinetics of Isotopic Exchange between Carbon Dioxide, Bicarbonate Ion, Carbonate Ion and Water". In: *Journal of the American Chemical Society* 62, pp. 1019–1026.

Miyamoto, H et al. (1996). "A carbonic anhydrase from the nacreous layer in oyster pearls". In: *Proceedings of the National Academy of Sciences* 93.18, pp. 9657–9660.

Moroney, J V, S G Bartlett, and G Samuelsson (2001). "Carbonic anhydrases in plants and algae". In: *Plant Cell and Environment* 24.2, pp. 141–153.

Morse, J W and R A Berner (1972). "Dissolution kinetics of calcium carbonate in seawater; II, A kinetic origin for the lysochne". In: *American Journal of Science* 272, pp. 840–851.

Morse, J W, A Mucci, and F J Millero (1980). "The solubility of calcite and aragonite in seawater of 35‰ salinity at 25°C and atmospheric pressure". In: *Geochimica et Cosmochimica Acta* 44, pp. 85–94.

Morse, John W, Andreas J Andersson, and Fred T Mackenzie (2006). "Initial responses of carbonate-rich shelf sediments to rising atmospheric $pCO_2$ and "ocean acidification": Role of high Mg-calcites". In: *Geochimica et Cosmochimica Acta* 70.23, pp. 5814–5830.

Morse, John W, Rolf S Arvidson, and Andreas Lüttge (2007). "Calcium Carbonate Formation and Dissolution". In: *Chemical Reviews* 107.2, pp. 342–381.

Morse, John W and Fred T Mackenzie (1990). *Geochemistry of sedimentary carbonates*. Vol. 48. Elsevier.

Morse, John W, Qiwei Wang, and Mai Yin Tsio (1997). "Influences of temperature and Mg:Ca ratio on $CaCO_3$ precipitates from seawater". In: *Geology* 25.1, pp. 85–87.

Moya, A et al. (2008). "Carbonic Anhydrase in the Scleractinian Coral *Stylophora pistillata*: Characterization, localization, and role in biomineralization". In: *Journal of Biological Chemistry* 283.37, pp. 25475–25484.

Mucci, A (1983). "The solubility of calcite and aragonite in seawater at various salinities, temperatures, and one atmosphere total pressure". In: *American Journal of Science* 283, pp. 780–799.

Mucci, A and J W Morse (1984). "The solubility of calcite in seawater solutions of various magnesium concentration, It= 0.697 m at 25 C and one atmosphere total pressure". In: *Geochimica et Cosmochimica Acta*.

Murakami, H and W S Sly (1987). "Purification and characterization of human salivary carbonic anhydrase." In: *Journal of Biological Chemistry* 262.3, pp. 1382–1388.

Mustaffa, Nur Ili Hamizah, Maren Striebel, and Oliver Wurl (2017). "Extracellular carbonic anhydrase: Method development and its application to natural seawater". In: *Limnology and Oceanography: Methods* 39, pp. 215–16.

Nickl, H J and H K Henisch (1969). "Growth of calcite crystals in gels". In: *Journal of the Electrochemical Society Solid State Science* 116.9, pp. 1258–1260.

Nielsen, Laura C, Donald J DePaolo, and James J De Yoreo (2012). "Self-consistent ion-by-ion growth model for kinetic isotopic fractionation during calcite precipitation". In: *Geochimica et Cosmochimica Acta* 86.C, pp. 166–181.

Nielsen, S A and E Frieden (1972a). "Carbonic anhydrase activity in molluscs". In: *Comparative Biochemistry and Physiology* 41B.3, pp. 461–468.

– (1972b). "Some Chemical and Kinetic Properties of Oyster Carbonic-Anhydrase". In: *Comparative Biochemistry and Physiology* 41B.4, pp. 875–889.

Nouet, Julius and Franck Bassinot (2007). "Dissolution effects on the crystallography and Mg/Ca content of planktonic foraminifera *Globorotalia tumida* (Rotaliina) revealed by X-ray diffractometry". In: *Geochemistry, Geophysics, Geosystems* 8.

Oomori, T et al. (1987). "Distribution Coefficient of $Mg^{2+}$ Ions Between Calcite and Solution at 10-50 Degrees C". In: *Marine Chemistry* 20.4, pp. 327–336.

Oremland, R S (2013). "A random biogeochemical walk into three soda lakes of the western USA: With an introduction to a few of their microbial denizens". In: *Polyextremophiles*.

Oremland, R S, L G Miller, and M J Whiticar (1987). "Sources and Flux of Natural Gases From Mono Lake, California". In: *Geochimica et Cosmochimica Acta* 51.11, pp. 2915–2929.

Orr, James C et al. (2005). "Anthropogenic ocean acidification over the twenty-first century and its impact on calcifying organisms". In: *Nature* 437.7059, pp. 681–686.

Oxburgh, R and W S Broecker (1993). "Pacific carbonate dissolution revisited". In: *Palaeogeography* 103.1-2, pp. 31–40.

Oxburgh, Rachel, Wallace S Broecker, and Richard H Wanninkhof (1991). "The carbon budget of Mono Lake". In: *Global Biogeochemical Cycles* 5.4, pp. 359–372.

Pickett, M and A J Andersson (2014). "Dissolution Rates of Biogenic Carbonates in Natural Seawater at Different $pCO_2$ Conditions: A Laboratory Study". In: *Aquatic Geochemistry*.

Pinsent, B R W, L Pearson, and F J W Roughton (1956). "The kinetics of combination of carbon dioxide with hydroxide ions". In: *Transactions of the Faraday Society* 52, pp. 1512–9.

Plummer, L N and TML Wigley (1976). "The dissolution of calcite in $CO_2$-saturated solutions at 25 C and 1 atmosphere total pressure". In: *Geochimica et Cosmochimica Acta* 40.2, pp. 191–202.

Plummer, L N, TML Wigley, and D L Parkhurst (1978). "The kinetics of calcite dissolution in $CO_2$-water systems at 5 to 60 degrees C and 0.0 to 1.0 atm $CO_2$". In: *American Journal of Science* 278.2, pp. 179–216.

Plummer, L Niel and Fred T Mackenzie (1974). "Predicting mineral solubility from rate data; application to the dissolution of magnesian calcites". In: *American Journal of Science* 274.1, pp. 61–83.

Pocker, Y and J T Stone (1967). "Catalytic Versatility of Erythrocyte Carbonic Anhydrase .3. Kinetic Studies of Enzyme-Catalyzed Hydrolysis of P-Nitrophenyl Acetate". In: *Biochemistry* 6.3, pp. 668–&.

Rae, James W B et al. (2011). "Boron isotopes and B/Ca in benthic foraminifera: Proxies for the deep ocean carbonate system". In: *Earth and Planetary Science Letters* 302.3-4, pp. 403–413.

Rahman, M Azizur, Tamotsu Oomori, and Tsuyoshi Uehara (2007). "Carbonic Anhydrase in Calcified Endoskeleton: Novel Activity in Biocalcification in Alcyonarian". In: *Marine Biotechnology* 10.1, pp. 31–38.

Rahman, M Azizur, Tamotsu Oomori, and Gert Wörheide (2011). "Calcite Formation in Soft Coral Sclerites Is Determined by a Single Reactive Extracellular Protein". In: *Journal of Biological Chemistry* 286.36, pp. 31638–31649.

Richter, F M and D J DePaolo (1987). "Numerical-Models for Diagenesis and the Neogene Sr Isotopic Evolution of Seawater From DSDP Site 590b". In: *Earth and Planetary Science Letters* 83.1-4, pp. 27–38.

Ridgwell, A and R E Zeebe (2005). "The role of the global carbonate cycle in the regulation and evolution of the Earth system". In: *Earth and Planetary Science Letters* 234, pp. 299–315.

Ridgwell, Andy (2005). "A Mid Mesozoic Revolution in the regulation of ocean chemistry". In: *Marine Geology* 217.3-4, pp. 339–357.

Riebesell, U et al. (2010). *Guide to best practices for ocean acidification research and data reporting*. Publications Office of the European Union.

Ries, J B et al. (2016). "Impacts of seawater saturation state ($\Omega$ A= 0.4–4.6) and temperature (10, 25 C) on the dissolution kinetics of whole-shell biogenic carbonates". In: *Geochimica et Cosmochimica Acta* 192, pp. 318–337.

Roesler, Collin S et al. (2002). "Distribution, production, and ecophysiology of Picocystis strain ML in Mono Lake, California". In: *Limnology and Oceanography* 47.2, pp. 440–452.

Sabine, C L et al. (2004). "The oceanic sink for anthropogenic $CO_2$". In: *Science* 305.5682, pp. 367–371.

Sadekov, Aleksey Yu, Stephen M Eggins, and Patrick De Deckker (2005). "Characterization of Mg/Ca distributions in planktonic foraminifera species by electron microprobe mapping". In: *Geochemistry, Geophysics, Geosystems* 6.12, pp. 1–14.

Sangwal, K (1987). *Etching of Crystals: Theory, Experiment, and Application*. North Holland.

Santschi, P H et al. (1983). "Estimates of the Resistance to Chemical-Transport Posed by the Deep-Sea Boundary-Layer". In: *Limnology and Oceanography* 28.5, pp. 899–912.

Sarmiento, Jorge and Nicolas Gruber (2006). *Ocean Biogeochemical Dynamics*. Princeton University Press.

Schrag, D P, D J DePaolo, and F M Richter (1995). "Reconstructing Past Sea-Surface Temperatures - Correcting for Diagenesis of Bulk Marine Carbonate". In: *Geochimica et Cosmochimica Acta* 59.11, pp. 2265–2278.

Schwartz, A et al. (1971). "Growth of vaterite and calcite crystals in gels". In: *Materials Research Bulletin* 6, pp. 1341–1344.

Shiraki, R, P A Rock, and W H Casey (2000). "Dissolution kinetics of calcite in 0.1 M NaCl solution at room temperature: an atomic force microscopic (AFM) study". In: *Aquatic Geochemistry* 6, pp. 87–108.

Sigman, D M and E A Boyle (2000). "Glacial/interglacial variations in atmospheric carbon dioxide". In: *Nature* 407.6806, pp. 859–869.

Silverman, D N (1982). "Carbonic anhydrase: Oxygen-18 exchange catalyzed by an enzyme with rate-contributing Proton-transfer steps". In: *Methods in enzymology* 87, pp. 732–752.

Silverman, D N and S Lindskog (1988). "The Catalytic Mechanism of Carbonic-Anhydrase - Implications of a Rate-Limiting Protolysis of Water". In: *Accounts of Chemical Research* 21.1, pp. 30–36.

Silverman, D N and C K Tu (1976). "Carbonic anhydrase catalyzed hydration studied by $^{13}$C and $^{18}$O labeling of carbon dioxide". In: *J Am Chem Soc* 98.4, pp. 978–984.

Silverman, Jacob, Boaz Lazar, and Jonathan Erez (2007). "Effect of aragonite saturation, temperature, and nutrients on the community calcification rate of a coral reef". In: *Journal of Geophysical Research* 112.C5.

Sjöberg, E L (1976). "A fundamental equation for calcite dissolution kinetics". In: *Geochimica et Cosmochimica Acta* 40.4, pp. 441–447.

Sjöberg, E L and D T Rickard (1984). "Calcite Dissolution Kinetics - Surface Speciation and the Origin of the Variable pH-Dependence". In: *Chemical Geology* 42.1-4, pp. 119–136.

– (1985). "The effect of added dissolved calcium on calcite dissolution kinetics in aqueous solutions at 25 C". In: *Chemical Geology* 49.4, pp. 405–413.

Stockner, T.F. et al. (2013). *Climate Change 2013: The Physical Science Basis. Contribution of Working Group I to the Fifth Assessment Report of the Intergovernmental Panel on Climate Change*. Tech. rep., p. 1535.

Stoll, H M et al. (2001). "A first look at paleotemperature prospects from Mg in coccolith carbonate: Cleaning techniques and culture measurements". In: *Geochemistry, Geophysics, Geosystems* 2.5,

Stoll, Heather M and Patrizia Ziveri (2002). "Separation of monospecific and restricted coccolith assemblages from sediments using differential settling velocity". In: *Marine Micropaleontology* 46.1-2, pp. 209–221.

Subhas, Adam V et al. (2015). "A novel determination of calcite dissolution kinetics in seawater". In: *Geochimica et Cosmochimica Acta* 170.C, pp. 51–68.

Subhas, A.V., J.F. Adkins, J. Erez, N.E. Rollins, et al. (Under Review). "Catalysis and Chemical Mechanisms of Calcite Dissolution in Seawater". In: *Under Review at the Proceedings of the National Academy of Sciences*.

Subhas, A.V., J.F. Adkins, J. Erez, P. Ziveri, et al. (in prep.). "Controls on the Dissolution Kinetics of Biogenic Calcites in Seawater". In: *in preparation*.

Sültemeyer, D F, H P Fock, and D T Canvin (1990). "Mass-Spectrometric Measurement of Intracellular Carbonic-Anhydrase Activity in High and Low Ci Cells of Chlamydomonas - Studies Using $^{18}O$ Exchange with $^{13}C/^{18}O$ Labeled Bicarbonate". In: *Plant Physiology* 94.3, pp. 1250–1257.

Sültemeyer, Dieter F et al. (1989). "Active $CO_2$ Transport by the Green Alga Chlamydomonas reinhardtii". In: *Plant Physiology* 89.4, pp. 1213–1219.

Sun, Wenhao et al. (2015). "Nucleation of metastable aragonite $CaCO_3$ in seawater". In: *Proceedings of the National Academy of Sciences* 112.11, pp. 3199–3204.

Tambutte, S et al. (2007). "Characterization and role of carbonic anhydrase in the calcification process of the azooxanthellate coral *Tubastrea aurea*". In: *Marine Biology* 151, pp. 71–83.

Tang, Ruikang, Christine A Orme, and George H Nancollas (2004). "Dissolution of Crystallites: Surface Energetic Control and Size Effects". In: *ChemPhysChem* 5.5, pp. 688–696.

Tashian, R E, T B Shows, and C C Plato (1963). "Inherited Variant of Erythrocyte Carbonic Anhydrase in Micronesians From Guam and Saipan". In: *Science* 140.356, pp. 53–54.

Taubner, I et al. (2012). "Uptake of alkaline earth metals in Alcyonarian spicules (Octocorallia)". In: *Geochimica et Cosmochimica Acta* 84.C, pp. 239–255.

Teng, H H, P M Dove, and J J De Yoreo (2000). "Kinetics of calcite growth: surface processes and relationships to macroscopic rate laws". In: *Geochimica et Cosmochimica Acta* 64.13, pp. 2255–2266.

Teng, H Henry (2004). "Controls by saturation state on etch pit formation during calcite dissolution". In: *Geochimica et Cosmochimica Acta* 68.2, pp. 253–262.

Tertre, E et al. (2010). "Methodology to obtain exchange properties of the calcite surface—Application to major and trace elements: Ca(II), $HCO_3^-$, and Zn(II)". In: *Journal of colloid and interface science* 347.1, pp. 120–126.

Thorley, Rachel M S et al. (2014). "The role of forest trees and their mycorrhizal fungi in carbonate rock weathering and its significance for global carbon cycling". In: *Plant Cell and Environment* 38.9, pp. 1947–1961.

Tortell, P D, C L Martin, and M E Corkum (2006). "Inorganic carbon uptake and intracellular assimilation by subarctic Pacific phytoplankton assemblages". In: *Limnology and Oceanography*.

Truesdale, Victor W (2015). "Evidence and Potential Implications of Exponential Tails to Concentration Versus Time Plots for the Batch Dissolution of Calcite". In: *Aquatic Geochemistry*, pp. 1–32.

Tu, C et al. (1978). "$CO_2$ kinetics in red cell suspensions measured by $^{18}O$ exchange." In: *Journal of Biological Chemistry* 253.22, pp. 8178–8184.

Uchikawa, J and R E Zeebe (2012). "The effect of carbonic anhydrase on the kinetics and equilibrium of the oxygen isotope exchange in the $CO_2$–$H_2O$ system: Implications for $\delta^{18}O$ vital effects in biogenic carbonates". In: *Geochimica et Cosmochimica Acta* 95, pp. 15–34.

Uchikawa, Joji et al. (2015). "Experimental evidence for kinetic effects on B/Ca in synthetic calcite: Implications for potential $B(OH)_4^-$ and $B(OH)_3$ incorporation". In: *Geochimica et Cosmochimica Acta* 150.C, pp. 171–191.

Van Cappellen, P, L Charlet, and W Stumm (1993). "A surface complexation model of the carbonate mineral-aqueous solution interface". In: *Geochimica et Cosmochimica Acta* 57.15, pp. 3505–3518.

Walter, L M and E A Burton (1986). "The effect of orthophosphate on carbonate mineral dissolution rates in seawater". In: *Chemical Geology* 56, pp. 313–323.

Walter, L M and J W Morse (1985). "The Dissolution Kinetics of Shallow Marine Carbonates in Seawater - a Laboratory Study". In: *Geochimica et Cosmochimica Acta* 49.7, pp. 1503–1513.

Wang, Xiaoguang et al. (2010). "Comprehensive Study of the Hydration and Dehydration Reactions of Carbon Dioxide in Aqueous Solution". In: *The Journal of Physical Chemistry A* 114.4, pp. 1734–1740.

Wilbur, Karl M and Norman G Anderson (1948). "Electrometric and colorimetric determination of carbonic anhydrase". In: *Journal of Biological Chemistry* 176.1, pp. 147–154.

Xie, Tengxiang and Yanyou Wu (2013). "The role of microalgae and their carbonic anhydrase on the biological dissolution of limestone". In: *Environmental Earth Sciences* 71.12, pp. 5231–5239.

Xu, Jie, Chunfang Fan, and H Henry Teng (2012). "Calcite dissolution kinetics in view of Gibbs free energy, dislocation density, and $pCO_2$". In: *Chemical Geology* 322-323.C, pp. 11–18.

Xu, M and S R Higgins (2011). "Effects of magnesium ions on near-equilibrium calcite dissolution: Step kinetics and morphology". In: *Geochimica et Cosmochimica Acta* 75, pp. 719–733.

Xu, Yan et al. (2008). "Structure and metal exchange in the cadmium carbonic anhydrase of marine diatoms". In: *Nature* 452.7183, pp. 56–61.

Yates, K K and R B Halley (2006). "Diurnal variation in rates of calcification and carbonate sediment dissolution in Florida Bay". In: *Estuaries and Coasts* 29.1, pp. 24–39.

York, D (1966). "Least-squares fitting of a straight line". In: *Canadian Journal of Physics* 44.5, pp. 1079–1086.

Young, Jeremy R and Karen Henriksen (2003). "Biomineralization Within Vesicles: The Calcite of Coccoliths". In: *Reviews in Mineralogy and Geochemistry* 54.1, pp. 189–215.

Yu, J, H Elderfield, and B Honisch (2007). "B/Ca in planktonic foraminifera as a proxy for surface seawater pH". In: *Paleoceanography*.

Yu, Zhenyan et al. (2006). "A novel carbonic anhydrase from the mantle of the pearl oyster (Pinctada fucata)". In: *Comparative Biochemistry and Physiology Part B: Biochemistry and Molecular Biology* 143.2, pp. 190–194.

Zaihua, Liu (2001). "Role of Carbonic Anhydrase as an Activator in Carbonate Rock Dissolution and Its Implication for Atmospheric $CO_2$ Sink". In: *Acta Geologica Sinica (English Edition)* 75.3, pp. 275–278.

Zeebe, R E and P Westbroek (2003). "A simple model for the $CaCO_3$ saturation state of the ocean: The "Strangelove," the "Neritan," and the "Cretan" Ocean". In: *Geochemistry*.

Zeebe, Richard E (2012). "History of Seawater Carbonate Chemistry, Atmospheric $CO_2$, and Ocean Acidification". In: *Annual Review of Earth and Planetary Sciences* 40.1, pp. 141–165.

Zhang, J and G H Nancollas (1998). "Kink Density and Rate of Step Movement during Growth and Dissolution of an AB Crystal in a Nonstoichiometric Solution". In: *Journal of colloid and interface science* 200.1, pp. 131–145.

Zhong, S and A Mucci (1989). "Calcite and aragonite precipitation from seawater solutions of various salinities: Precipitation rates and overgrowth compositions". In: *Chemical Geology* 78.3-4, pp. 283–299.

*A p p e n d i x   A*

# DISSOLUTION BOX MODEL CODE

These codes loop through the ratio of gross dissolution to gross precipitation only. They are easily modified to loop through the dissolution rate, F$_{diss}$, as well.

## A.1   Constants and definitions

```matlab
%%%%%%%%%%%%%%%%%%%%%%%%%%%%%%%%%%%%%%%%%%
%
% Definitions for use with solution_d13c_equations.m
    ↪ and
% solution_d13c_solver.m
%
% Goal is to make a 3 box model for dissolution of 100%
    ↪  pure 13C caco3
% into seawter
%
% AVS and JN
%%%%%%%%%%%%%%%%%%%%%%%%%%%%%%%%%%%%%%%%%%

seconds_per_day = 86400; %seconds per day


%%%%%%%%%%
% Define properties of the solid
%%%%%%%%%%

mass_caco3 = 5e-3; %mass of powder used in g
SA = 0.09*mass_caco3; %total surface area of calcite m2
    ↪  (m2/g from BET * g powder used)
density_caco3 = 2.7e6; %density of calcite in g/m3;
    ↪ (2.7g/cm3 according to http://www.mindat.org/min
    ↪ -859.html
calcite_diameter = 85e-6; %average diameter of 70-100um
    ↪   particles in meter
```

```matlab
particle_vol = 4/3*pi*(calcite_diameter/2)^3; %volume
    of individual spherical particle in m3
particle_mass = particle_vol*density_caco3; %mass of 1
    particle in g
total_particles = mass_caco3/particle_mass; %total
    number of calcite particles

caco3_MM = 100.08; %molar mass of calcite in g/mol
layer_thickness = 5e-10; %thickness in m of reactive
    layer
layer_vol = layer_thickness*SA; %volume of caco3 active
    layer in m3
number_of_monolayers = 5; %SI says 5 monolayers, (
    should be 1<x<10)

mols_13c_solid_initial = layer_vol*density_caco3/
    caco3_MM*number_of_monolayers; %initial mols 13C
    in solid, assuming it 100% 13C
mols_12c_solid_initial = 0; %assume no 12C in solid
    initially
mols_total_solid_initial = mols_13c_solid_initial +
    mols_12c_solid_initial;

%%%%%%%%
% Define properties of the solution
%%%%%%%%
Vbulk = 0.3; %mass of water used in kg
seawater_density = 1.026; %in kg/m3
Vbulk = Vbulk/seawater_density; %convert volume to m^3
bl_thickness = 1e-5; %boundary layer thickenss in m (10
    um)
Vbl=SA*bl_thickness; %Boundary layer volume defined by
    mineral SA and the boundary layer thickness

Ca_init = 1e-2; %Ca conc. in mol/kg
Mg_init = 5e-2; %Mg conc. in mol/kg
```

```
46
47  D_mg = 0.019; %D for calcite at 25C from Oomori et al.
        ↪ 1987
48
49  DIC = 2e-3; %DIC in mol/kg
50  Alk = 2e-3; %Alk in mol/kg.... this is really just a
        ↪ test.  The Omega for Alk=DIC is basically 1.  It
        ↪ shouldn't feed back at all on dissolution rate.
51
52  %DIC = DIC*seawater_density; %convert to mol/m3
53  R13_PDB = 0.0112372; %13C/12C in PDB std
54  d13c_initial = 0;% set initial d13c to 1 permil
55  R13_initial = (d13c_initial/1000+1)*R13_PDB;
56
57  f13_init = R13_initial/(1+R13_initial); %fraction of
        ↪ total C that is 13C in PDB
58  f12_init = 1-f13_init; %fraction of total C that is 12C
        ↪   in PDB
59
60  bulk_c13_initial = DIC*f13_init; %in mols/m3
61  bulk_c12_initial = DIC*f12_init;
62
63  bl_c13_initial = DIC*f13_init;
64  bl_c12_initial = DIC*f12_init;
65
66  %%%%%%%
67  % Define rate constants
68  %%%%%%%
69
70  D = 9.55e-10; %molecular diffusion coefficient in m2/s
        ↪ (Lee & Gregory 1974 has 9.55e-6 cm2/s for CO32-
        ↪ in water at 25C)
71
72  F_diss = 5e-13; %adam's value for diss in mol/s 1e-11
        ↪ to 1e-13
73
```

```
74 l_r = 5; %length of ratio vector
75 log_ratio = linspace(0.001,1,l_r); %Here going from
     ↪ 1.002 to 10.
76 offset_ratio = 10.^log_ratio; %factor relating k_diss
     ↪ to k_precip. arbitrarily assigned
77
78 F_precip = F_diss./offset_ratio; %Precip rate defined
     ↪ by F_diss and offset_ratio
```

## A.2   Equations script

```
1 function dcdt = solution_d13c_equations_bl_dependence_r
     ↪ (t,c,F_p)
2
3 solution_d13c_definitions_bl_dependence_r;
4
5 %dcdt(1) 13DIC of bulk solution (mols/m3)
6 %dcdt(2) 12DIC of bulk solution (mols/m3)
7 %dcdt(3) 13DIC of boundary layer (mols/m3)
8 %dcdt(4) 12DIC of boundary layer (mols/m3)
9 %dcdt(5) mols 13C of reactive solid volume (mols)
10 %dcdt(6) mols 12C of reactive solid volume (mols)
11
12 %dcdt(7) is [Ca++] of bulk
13 %dcdt(8) is [Mg++] of bulk
14 %dcdt(9) is [Ca++] of boundary layer
15 %dcdt(10) is [Mg++] of boundary layer
16 %dcdt(11) is [Ca++] of solid
17 %dcdt(12) is [Mg++] of solid
18
19 %dcdt(13) is Alk of bulk
20 %dcdt(14) is Alk of boundary layer
21
22 %Set Definitions of flux ratios
23     f12_caco3 = c(6)./(c(5)+c(6)); %N12/(N12+N13)
           ↪ fraction of mols 12C/totalC in caco3 solid
```

```matlab
24      f12_bl = c(4)./(c(3)+c(4));% DIC12_bl/(DIC13_bl+
           ↪ DIC12_bl) fraction of mols 12C/totalC in bl;

25

26      R12_diss = F_diss*f12_caco3; %units of 1/s
27      R13_diss = F_diss*(1-f12_caco3); %units of 1/s

28

29      R12_precip = F_p*(f12_bl); %F_precip formerly
           ↪ k_precip. Now in units of 1/s
30      R13_precip = F_p*(1-f12_bl); %units of 1/s

31

32      R_lower = (R13_diss+R12_diss)-(R13_precip+
           ↪ R12_precip); %flux from lower layers to caco3
           ↪  to active layer
33      R_lower(R_lower<0) = 0;

34

35      %R_lower reduces to (F_diss - F_precip) so it is a
           ↪ constant
36      y=0; %ratio of 12C to 13C coming up from inside
           ↪ CaCO3 crystal. Set to 0 (so it all 13C)

37

38

39  %Set flux equations

40

41  dcdt(1) = D*SA/bl_thickness*(c(3) - c(1))./Vbulk;
42  dcdt(2) = D*SA/bl_thickness*(c(4) - c(2))./Vbulk;

43

44  dcdt(3) = (D*SA/bl_thickness*(c(1) - c(3)) +  R13_diss
         ↪ - R13_precip)./Vbl;
45  dcdt(4) = (D*SA/bl_thickness*(c(2) - c(4)) +  R12_diss
         ↪ - R12_precip)./Vbl;

46

47  dcdt(5) = R13_precip - R13_diss + (1-y)*R_lower;
48  dcdt(6) = R12_precip - R12_diss + y*R_lower;

49

50  %% Cation section

51
```

```matlab
%Fmg_bulk = c(8)./(c(8)+c(7));
%Fca_bulk = 1-Fmg_bulk;
%Fmg_bl = c(10)./(c(10)+c(9));
%Fca_bl = 1-Fmg_bl;
Rmg_bl = c(10)./c(9);
Fmg_solid = c(12)./(c(12)+c(11));
Fca_solid = 1-Fmg_solid;

dcdt(7) = D*SA/bl_thickness.*(c(9) - c(7))./Vbulk;
dcdt(8) = D*SA/bl_thickness.*(c(10)- c(8))./Vbulk;

dcdt(9) = (D*SA/bl_thickness.*(c(7) - c(9)) + F_diss.*
    Fca_solid - F_p.*(1-D_mg.*Rmg_bl./(1+D_mg.*Rmg_bl
    )))./Vbl;
dcdt(10) = (D*SA/bl_thickness.*(c(8) - c(10)) + F_diss
    .*Fmg_solid - F_p.*D_mg.*Rmg_bl./(1+D_mg.*Rmg_bl)
    )./Vbl;

dcdt(11) = F_p.*(1-D_mg.*Rmg_bl./(1+D_mg.*Rmg_bl)) -
    F_diss.*Fca_solid + (1-y).*(F_diss-F_p);
dcdt(12) = F_p.*D_mg.*Rmg_bl./(1+D_mg.*Rmg_bl) - F_diss
    .*Fmg_solid + y.*(F_diss-F_p);

%% Alkalinity section

%Just do bulk alkalinity in solution and boundary layer
    .  No need to do
%anything with the solid, and can treat everything
    without isotopes.

dcdt(13) = D*SA/bl_thickness*(c(14) - c(13))./Vbulk;
dcdt(14) = (D*SA/bl_thickness*(c(13) - c(14)) +  2.*(
    F_diss - F_p))./Vbl;

dcdt = dcdt';
```

```
79  end
```

**A.3  Solver script**

```
1   clc
2   close all
3   clear all
4
5   solution_d13c_definitions_bl_dependence_r;
6
7   %dcdt(1) 13DIC of bulk solution (mols/time)
8   %dcdt(2) 12DIC of bulk solution (mols/time)
9   %dcdt(3) 13DIC of boundary layer (mols/time)
10  %dcdt(4) 12DIC of boundary layer (mols/time)
11  %dcdt(5) mols 13C of reactive solid volume (mols/time)
12  %dcdt(6) mols 12C of reactive solid volume (mols/time)
13
14  %set initial concentrations
15  %Set c0 in mols/m3
16  c0(1) = bulk_c13_initial;
17  c0(2) = bulk_c12_initial;
18  c0(3) = bl_c13_initial;
19  c0(4) = bl_c12_initial;
20  c0(5) = mols_13c_solid_initial;
21  c0(6) = mols_12c_solid_initial;
22  c0(7) = Ca_init;
23  c0(8) = Mg_init;
24  c0(9) = Ca_init;
25  c0(10) = Mg_init;
26  c0(11) = mols_13c_solid_initial;
27  c0(12) = 0;
28  c0(13) = Alk;
29  c0(14) = Alk;
30
31  tend = 2.5*seconds_per_day;  %Length of experiment
        duration.
32
```

```matlab
33  options = odeset('RelTol',1e-8,'AbsTol',1e-11,'
       ↪  InitialStep',0.1);

34

35  for  i=1:l_r

36

37      F_p = F_precip(i);

38

39  a = ode15s(@(t,c)
       ↪  solution_d13c_equations_bl_dependence_r(t,c,F_p)
       ↪  ,[0 tend],c0,options);

40

41  t0 = linspace(0,tend,100);

42

43  Y = deval(a,t0);

44

45  time(:,i) = t0;
46  bulk_13DIC(:,i) = Y(1,:).*1e6; %This is in umol/kg
47  bulk_12DIC(:,i) = Y(2,:).*1e6;
48  %bulk_DIC(:,i) = bulk_13DIC(:,i) + bulk_12DIC;

49

50  %bulk_delta13c(:,i) = (bulk_13DIC(:,i)./bulk_12DIC(:,i)
       ↪  ./R13_PDB-1).*1000;

51

52  bl_13DIC(:,i) = Y(3,:).*1e6; %in umols/kg
53  bl_12DIC(:,i) = Y(4,:).*1e6; %in umols/kg;
54  %bl_DIC(:,i) = bl_13DIC + bl_12DIC;

55

56  %bl_delta13c(:,i) = (bl_13DIC./bl_12DIC./R13_PDB-1)
       ↪  .*1000;

57

58  solid_13C(:,i) = Y(5,:); %in mols
59  solid_12C(:,i) = Y(6,:);

60

61  bulk_Ca(:,i) = Y(7,:).*1e3;
62  bulk_Mg(:,i) = Y(8,:).*1e3;

63
```

```
64  bl_Ca (: , i )  =  Y(9 ,:) .∗1 e3 ;
65  bl_Mg (: , i )  =  Y(10 ,:) .∗1 e3 ;

66

67  solid_Ca (: , i )  =  Y(11 ,:) ;
68  solid_Mg (: , i )  =  Y(12 ,:) ;

69

70  bulk_Alk (: , i )  =  Y(13 ,:) .∗1 e6 ;
71  bl_Alk (: , i )  =  Y(14 ,:) .∗1 e6 ;

72

73  end

74

75  %% Define  carbon  isotope  ratios

76

77  bulk_DIC  =  bulk_13DIC  +  bulk_12DIC ;
78  bulk_delta13c  =  (bulk_13DIC ./ bulk_12DIC ./ R13_PDB −1)
       ↪  .∗1000;
79  bl_DIC  =  bl_13DIC  +  bl_12DIC ;
80  bl_delta13c  =  (bl_13DIC ./ bl_12DIC ./ R13_PDB −1).∗1000;

81

82  f13_solid  =  solid_13C ./( solid_13C+solid_12C ) ;

83

84  %% Define  cation  ratios

85

86  bulk_MgCa  =  bulk_Mg ./ bulk_Ca ;
87  bl_MgCa  =  bl_Mg ./ bl_Ca ;
88  solid_MgCa  =  solid_Mg ./ solid_Ca ;

89

90  %% Do  carbonate  system  parameters  NEED THE PROGRAM
       ↪  CO2SYS  FOR  THIS  PART  OF  THE  CODE.

91

92  par1type  =     1; % The  first  parameter  supplied  is  of
       ↪  type  "1",  which  is  "alkalinity"
93  par2type  =     2; % The  first  parameter  supplied  is  of
       ↪  type  "1",  which  is  "DIC"
94  sal      =     35; % Salinity  of  the  sample
95  tempin   =     21; % Temperature  at  input  conditions
```

```
 96 presin    =     0; % Pressure      at input conditions
 97 tempout   =    21; % Temperature at output conditions -
        ↪ doesn't matter in this example
 98 presout   =     0; % Pressure      at output conditions -
        ↪ doesn't matter in this example
 99 sil       =    50; % Concentration of silicate  in the
        ↪ sample (in umol/kg)
100 po4       =     0; % Concentration of phosphate in the
        ↪ sample (in umol/kg)
101 pHscale   =     1; % pH scale at which the input pH is
        ↪ reported ("1" means "Total Scale")  - doesn't
        ↪ matter in this example
102 k1k2c     =     4; % Choice of H2CO3 and HCO3-
        ↪ dissociation constants K1 and K2 ("4" means "
        ↪ Mehrbach refit")
103 kso4c     =     1; % Choice of HSO4- dissociation
        ↪ constants KSO4 ("1" means "Dickson")
104
105 % Do the calculation. See CO2SYS's help for syntax and
        ↪ output format.
106 % Making things into a long file format
107
108 A_bulk = CO2SYS(bulk_Alk(:),bulk_DIC(:),par1type,
        ↪ par2type,sal,tempin,tempout,presin,presout,sil,
        ↪ po4,pHscale,k1k2c,kso4c);
109 A_bl = CO2SYS(bl_Alk(:),bl_DIC(:),par1type,par2type,sal
        ↪ ,tempin,tempout,presin,presout,sil,po4,pHscale,
        ↪ k1k2c,kso4c);
110
111 bulk_Omega = A_bulk(:,15);
112 bl_Omega = A_bl(:,15);
113
114 bulk_Omega = reshape(bulk_Omega,[],l_r);
115 bl_Omega = reshape(bl_Omega,[],l_r);
116
117 figure(1)
```

```matlab
118
119 % Bulk plots
120 subplot(3,4,1)
121 plot(time, bulk_13DIC,'o-')
122 xlabel('Time (days)')
123 ylabel('Bulk 13C (umols/kg)')
124
125 subplot(3,4,2)
126 plot(time, bulk_12DIC,'x-')
127 xlabel('Time (days)')
128 ylabel('Bulk 12C (umols/kg)')
129
130 subplot(3,4,3)
131 plot(time,bulk_DIC,'--')
132 xlabel('Time (days)')
133 ylabel('Bulk DIC (umols/kg)')
134
135 subplot(3,4,4)
136 plot(time, bulk_MgCa,'--')
137 xlabel('Time (days)')
138 ylabel('Bulk Mg/Ca')
139
140 %Boundary layer plots
141
142 subplot(3,4,5)
143 plot(time, bl_13DIC,'o-')
144 xlabel('Time (days)')
145 ylabel('Bl 13C (umols/m3)')
146
147 subplot(3,4,6)
148 plot(time, bl_12DIC,'x-')
149 xlabel('Time (days)')
150 ylabel('Bl 12C (umol/m3)')
151
152 subplot(3,4,7)
153 plot(time,bl_DIC,'--')
```

```matlab
154  xlabel('Time (days)')
155  ylabel('Bl DIC (umol/kg)')
156
157  subplot(3,4,8)
158  plot(time, bl_MgCa,'--')
159  xlabel('Time (days)')
160  ylabel('Boundary Mg/Ca')
161
162  % Solid plots
163
164  subplot(3,4,9)
165  plot(time, f13_solid,'x-')
166  xlabel('Time (days)')
167  ylabel('Fraction 13C Solid')
168
169  subplot(3,4,10)
170  plot(time, solid_12C.*caco3_MM./density_caco3./SA,'x-')
171  xlabel('Time (days)')
172  ylabel('Mols 12C in Solid')
173
174  subplot(3,4,11)
175  plot(time,(solid_12C+solid_13C).*caco3_MM./
        ↪ density_caco3./SA,'--')
176  hold on
177  plot([time(1) time(end)],[mols_total_solid_initial
        ↪ mols_total_solid_initial].*caco3_MM./
        ↪ density_caco3./SA,'k--')
178  xlabel('Time (days)')
179  ylabel('Total mols in solid')
180
181  subplot(3,4,12)
182  plot(time,solid_MgCa,'--')
183  xlabel('Time (days)')
184  ylabel('Solid Mg/Ca')
185
186  figure(2)
```

```matlab
187  subplot(2,1,1)
188  plot(time, bulk_delta13c ,'-o')
189  xlabel('Time (days)')
190  ylabel('d13C of bulk')
191
192  subplot(2,1,2)
193  plot(time, bl_delta13c ,'v-')
194  xlabel('Time (days)')
195  ylabel('d13C of bl')
196
197  figure(3)
198  plot(time./seconds_per_day, bulk_delta13c ,'-')
199  xlabel('Time (days)')
200  ylabel('d13C of bulk')
201  ylim([0  15])
202
203  figure(4)
204  subplot(3,3,1)
205  plot(time, bulk_Mg ,'o-')
206  xlabel('Time (days)')
207  ylabel('Bulk Mg (mmols/kg)')
208
209  subplot(3,3,2)
210  plot(time, bulk_Ca ,'x-')
211  xlabel('Time (days)')
212  ylabel('Bulk Ca (umols/kg)')
213
214  subplot(3,3,3)
215  plot(time,bulk_MgCa ,'--')
216  xlabel('Time (days)')
217  ylabel('Bulk Mg/Ca')
218
219  subplot(3,3,4)
220  plot(time, bl_Mg ,'o-')
221  xlabel('Time (days)')
222  ylabel('Bl Mg (mmols/m3)')
```

```
223
224   subplot(3,3,5)
225   plot(time, bl_Ca,'x-')
226   xlabel('Time (days)')
227   ylabel('Bl Ca (mmols/m3)')
228
229   subplot(3,3,6)
230   plot(time,bl_MgCa,'--')
231   xlabel('Time (days)')
232   ylabel('Bl DIC (umol/kg)')
233
234   subplot(3,3,7)
235   plot(time, solid_Mg,'o-')
236   xlabel('Time (days)')
237   ylabel('Mols Mg in solid')
238
239   subplot(3,3,8)
240   plot(time, solid_Ca,'x-')
241   xlabel('Time (days)')
242   ylabel('Mols Ca in Solid')
243
244   subplot(3,3,9)
245   plot(time,solid_MgCa,'--')
246   xlabel('Time (days)')
247   ylabel('Solid Mg/Ca')
248
249   figure(5)
250   subplot(2,2,1)
251   plot(time,bulk_Alk,'o-')
252   xlabel('Time (days)')
253   ylabel('Bulk alkalinity')
254
255   subplot(2,2,2)
256   plot(time,bl_Alk,'o-')
257   xlabel('Time (days)')
258   ylabel('bl Alk')
```

```
259
260  subplot (2 ,2 ,3)
261  plot (time , bulk_Omega , 'o-')
262  xlabel ('Time (days)')
263  ylabel ('Bulk \Omega_{Ca}')
264
265  subplot (2 ,2 ,4)
266  plot (time , bl_Omega , 'o-')
267  xlabel ('Time (days)')
268  ylabel ('Bl \Omega_{Ca}')
```

# BET MEASUREMENTS OF PLANKTONIC FORAMINIFERA

Planktonic foraminiferal samples for BET analysis were picked from sediment cores by Carina Fish. These samples were then sent to Adam Subhas for measurement on a Micromeritics ASAP 2010 gas adsorption instrument. Species were picked based on morphology, and were sent in splits by size fraction, to determine if there was any control of test size on the measured specific surface area.

**Table B.1:** Weights of planktonic foraminifera samples collected from core tops, used for Kr-BET analysis in this study.

| Session | Species | Size fraction ($\mu$m) | wt. (mg) |
|---|---|---|---|
| 1 | *O. universa* | 515-600 | 6.01 |
|   | *G. ruber* | 425-500 | 5.38 |
|   | *G. sacculifer* | 425-500 | 11.49 |
|   | *G. sacculifer* | 515-600 | 16.31 |
| 2 | *O. universa* | 425-515 | 12.47 |
|   | *O. universa* | 600-825 | 15.36 |
|   | *G. ruber* | 355-425 | 13.95 |
|   | *G. sacculifer* | 355-425 | 18.11 |
| 3 | *G. sacculifer* | 425-515 | 47.46 |
|   | *G. ruber* | 425-515 | 5.31 |
|   | *G. ruber* | 250-355 | 30.42 |

**Table B.2:** Mean Kr-BET surface areas collected from three different analytical sessions shown below. Numbers in bold were collected with $> 0.1$ square meters of total surface area and are thus highly reliable. Numbers in italic are collected with $\leq 0.05$ square meters of total surface area, and are thus not as reliable, due to the small sample size. On average, there is very little trend with sieving fraction, and all species of planktonic foraminifera show a similar specific surface area of about 4-4.5 square meters per gram of sample.

| Size fraction ($\mu$m) | SSA ($m^2\ g^{-1}$) | | |
|:---:|:---:|:---:|:---:|
| | *O. universa* | *G. sacculifer* | *G. ruber* |
| 250-355 | – | – | **4.1** |
| 355-425 | – | *4.4* | **4.9** |
| 425-515 | 4.3 | **3.3** | 5.5 |
| 515-600 | 4.3 | 4.4 | – |
| 600-840 | 4.7 | – | – |
| Total | 4.5 | 4.0 | 4.5 |

**Table B.3:** First run of the Kr-BET analysis of planktonic foraminifera. All foraminifera and standard materials are presented for several replicate runs.

| Sample | Size Fraction ($\mu$m) | wt (g) | Run 1 SSA (m$^2$ g$^{-1}$) | Run 1 SA$_{tot}$ (m$^2$) | Run 2 SSA (m$^2$ g$^{-1}$) | Run 2 SA$_{tot}$ (m$^2$) | Mean SSA (m$^2$ g$^{-1}$) | Stdev (1$\sigma$) |
|---|---|---|---|---|---|---|---|---|
| *O. universa* | 515-600 | 0.00601 | 4.4 | 0.05 | 4.2 | 0.05 | 4.3 | – |
| *G. ruber* | 425-515 | 0.00538 | 7.6 | 0.03 | 8.6 | 0.03 | 8.1 | – |
| *G. sacculifer* | 425-515 | 0.01149 | 5.2 | 0.05 | 5.3 | 0.05 | 5.3 | – |
| *G. sacculifer* | 515-600 | 0.01631 | 4.5 | 0.10 | 4.4 | 0.09 | 4.4 | – |
| Anorthosite | | | 4.6 | 0.73 | 4.8 | 0.77 | 4.7 | – |
| Alumina Std | | | 0.43 | 0.16 | 0.41 | 0.15 | 0.42 | – |

**Table B.4:** Second run of the Kr-BET analysis of planktonic foraminifera. All foraminifera and standard materials are presented for several replicate runs.

| Sample | Size Fraction ($\mu$m) | wt (g) | Run 1 SSA (m$^2$ g$^{-1}$) | Run 1 SA$_{tot}$ (m$^2$) | Run 2 SSA (m$^2$ g$^{-1}$) | Run 2 SA$_{tot}$ (m$^2$) | Run 3 SSA (m$^2$ g$^{-1}$) | Run 3 SA$_{tot}$ (m$^2$) | Mean SSA (m$^2$ g$^{-1}$) | Stdev (1$\sigma$) |
|---|---|---|---|---|---|---|---|---|---|---|
| Alumina Std | | 0.2459 | 0.4 | 0.10 | 0.4 | 0.10 | | | 0.4 | |
| Anorthosite | | 0.3195 | 4.7 | 1.49 | | | | | 4.7 | |
| *O. universa* | 425-515 | 0.0125 | 4.9 | 0.06 | 4.0 | 0.05 | 4.1 | 0.05 | 4.3 | 0.5 |
| *O. universa* | 600-800 | 0.0154 | 5.2 | 0.08 | 4.8 | 0.07 | 4.2 | 0.06 | 4.7 | 0.5 |
| *G. ruber* | 355-425 | 0.0139 | 5.2 | 0.07 | 4.6 | 0.06 | 4.8 | 0.07 | 4.9 | 0.3 |
| *G. sacculifer* | 355-425 | 0.0181 | 4.8 | 0.09 | 4.4 | 0.08 | 4.0 | 0.07 | 4.4 | 0.4 |

**Table B.5:** Third run of the Kr-BET analysis of planktonic foraminifera. All foraminifera and standard materials are presented for several replicate runs.

| Sample | Size Fraction ($\mu$m) | wt (g) | Run 1 SSA (m$^2$ g$^{-1}$) | SA$_{tot}$ (m$^2$) | Run 2 SSA (m$^2$ g$^{-1}$) | SA$_{tot}$ (m$^2$) | Run 3 SSA (m$^2$ g$^{-1}$) | SA$_{tot}$ (m$^2$) | Run 4 SSA (m$^2$ g$^{-1}$) | SA$_{tot}$ (m$^2$) | Mean SSA (m$^2$ g$^{-1}$) | Stdev ($1\sigma$) |
|---|---|---|---|---|---|---|---|---|---|---|---|---|
| Alumina Std | | 0.2085 | 0.46 | 0.10 | 0.46 | 0.09 | 0.44 | 0.09 | | | 0.45 | 0.01 |
| G. sacc | 425-515 | 0.0475 | 3.9 | 0.19 | 3.2 | 0.15 | 3.0 | 0.17 | 3.1 | 0.17 | 3.3 | 0.4 |
| G. ruber | 425-515 | 0.0053 | 9.1 | 0.05 | 5.5 | 0.05 | 5.4 | 0.05 | | | 5.5 | 0.1 |
| G. ruber | 250-355 | 0.0304 | 4.7 | 0.14 | 4.1 | 0.13 | 3.9 | 0.12 | 3.7 | 0.11 | 4.1 | 0.4 |

# METAL-CALCIUM RATIO MEASUREMENTS IN DISSOLVED BIOGENIC CALCITES

**Table C.1:** Metal-calcium ratios measured in benthic foraminifera and soft coral spicules before and after dissolution experiments. These measurements are the basis of Figure 4.8 in Chapter 4.

| Sample | Li/Ca $\mu$mol mol$^{-1}$ | B/Ca $\mu$mol mol$^{-1}$ | Na/Ca mmol mol$^{-1}$ | Al/Ca mmol mol$^{-1}$ | Mn/Ca $\mu$mol mol$^{-1}$ | Zn/Ca $\mu$mol mol$^{-1}$ | Sr/Ca mmol mol$^{-1}$ | Cd/Ca $\mu$mol mol$^{-1}$ | Ba/Ca $\mu$mol mol$^{-1}$ | Nd/Ca $\mu$mol mol$^{-1}$ | U/Ca nmol mol$^{-1}$ | Mg/Ca mmol mol$^{-1}$ | % Dissolution | Size fraction |
|---|---|---|---|---|---|---|---|---|---|---|---|---|---|---|
| **FORAMS** | | | | | | | | | | | | | | |
| B62-B1.D | 24.3 | 281 | 17.6 | 42.1 | 4.74 | 17.7 | 1.49 | 0.91 | 1.64 | 0.22 | 21.7 | 25.0 | 0.2 | 125-300 |
| B58-B4.D | 24.7 | 443 | 33.0 | 54.2 | 5.10 | 22.1 | 1.52 | 1.15 | 1.86 | 0.22 | 32.0 | 32.0 | 2.4 | 125-300 |
| B63-B3.D | 23.5 | 217 | 9.6 | 51.1 | 5.66 | 12.7 | 1.51 | 1.02 | 1.38 | 0.27 | 29.0 | 24.1 | 27.7 | 125-300 |
| B59-B1.D | 29.7 | 521 | 15.3 | 55.1 | 4.69 | 3.1 | 1.80 | 0.20 | 1.31 | 0.13 | 17.6 | 34.0 | 0.1 | 710-1000 |
| B60-B1.D | 27.6 | 483 | 13.2 | 31.7 | 6.10 | 0.8 | 1.75 | 0.03 | 1.35 | 0.25 | 19.9 | 34.0 | 1.1 | 710-1000 |
| B63-B1.D | 28.4 | 444 | 13.6 | 51.7 | 4.36 | 2.2 | 1.83 | 0.14 | 1.36 | 0.16 | 17.2 | 29.9 | 14.5 | 710-1000 |
| 710-1000.D | 29.4 | 603 | 13.2 | 39.8 | 8.73 | 9.2 | 1.88 | 1.01 | 1.36 | 0.17 | 19.7 | 34.7 | 0.0 | 710-1000 |
| B63-B3A.D | 22.2 | 283 | 9.7 | 52.1 | 5.33 | 12.5 | 1.51 | 0.98 | 1.37 | 0.23 | 30.9 | 24.1 | 27.7 | 125-300 |
| **CORALS** | | | | | | | | | | | | | | |
| B41-B4-6.D | 20.7 | 373 | 14.8 | 50.2 | 7.72 | 5.6 | 3.11 | 0.03 | 4.85 | 12.72 | 42.2 | 133.4 | 3.3 | N/A |
| B41-B13.D | 21.4 | 358 | 16.3 | 160.3 | 9.53 | 20.8 | 3.09 | 0.07 | 5.99 | 3.05 | 74.6 | 132.6 | 2.2 | N/A |
| B41-B13A.D | 22.2 | 452 | 16.4 | 167.4 | 9.42 | 20.5 | 3.08 | 0.09 | 6.01 | 3.05 | 72.7 | 132.7 | 2.2 | N/A |
| Avg | 21.4 | 395 | 15.8 | 125.95 | 8.89 | 15.6 | 3.09 | 0.06 | 5.61 | 6.27 | 63.18 | 132.9 | | |
| STD | 0.7 | 50.3 | 0.9 | 65.7 | 1.0 | 8.7 | 0.0 | 0.0 | 0.7 | 5.6 | 18.2 | 0.4 | | |

# IMAGES OF DISSOLVED BIOGENIC CALCITES

## D.1  Plates of dissolved planktonic foraminifera

Ω=0.57, 1 day　　　　　　　　　Ω=0.57, 2.5  days
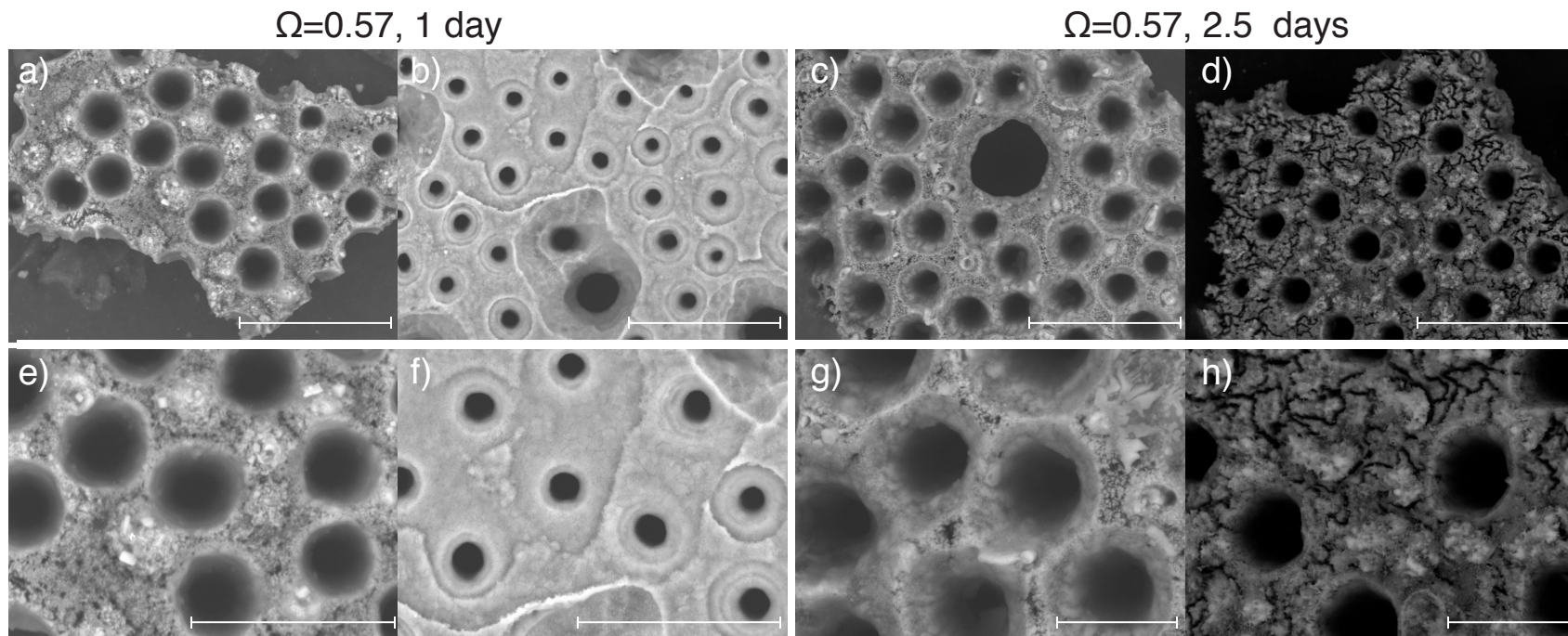


**Figure D.1:** Images of dissolved foraminiferal tests from experiments B54-B1 and B54-B2. The saturation state and length of experiment are listed above the plates. **a,b,e,f)** 24 hours of dissolution at Ω = 0.57. **c,d,g,h)** 60 hours of dissolution at Ω = 0.57. Scale bars in microns: **a-b)** 30; **c-d)** 20; **e-h)** 10.

## Ω=0.40, 1 day
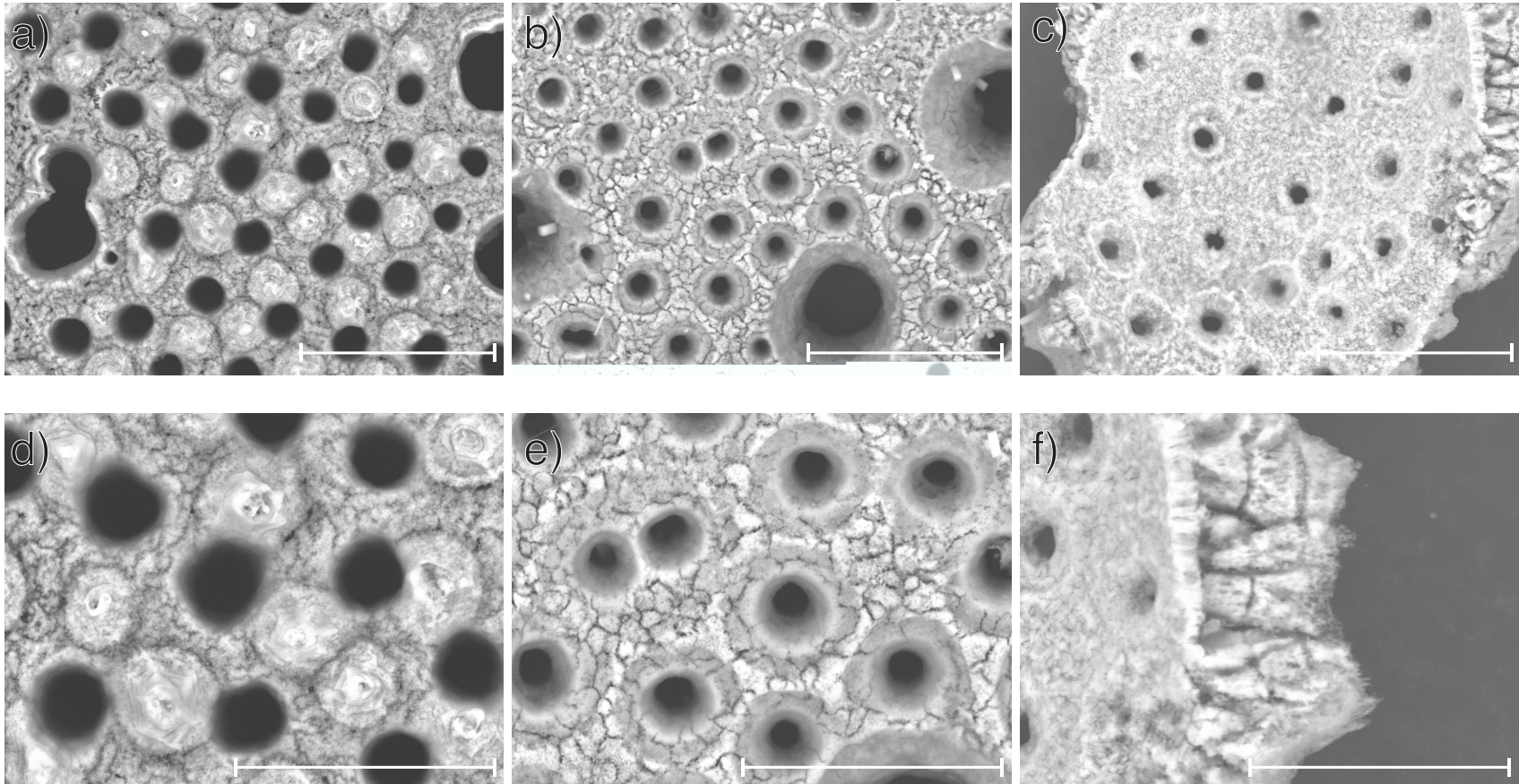


**Figure D.2:** Images of dissolved foraminiferal tests from experiments B54-B3. The saturation state and length of experiment are listed above the plate. Scale bars in microns: **a-c)** 30; **e-f)** 20.

Ω=0.68, 2.5 days
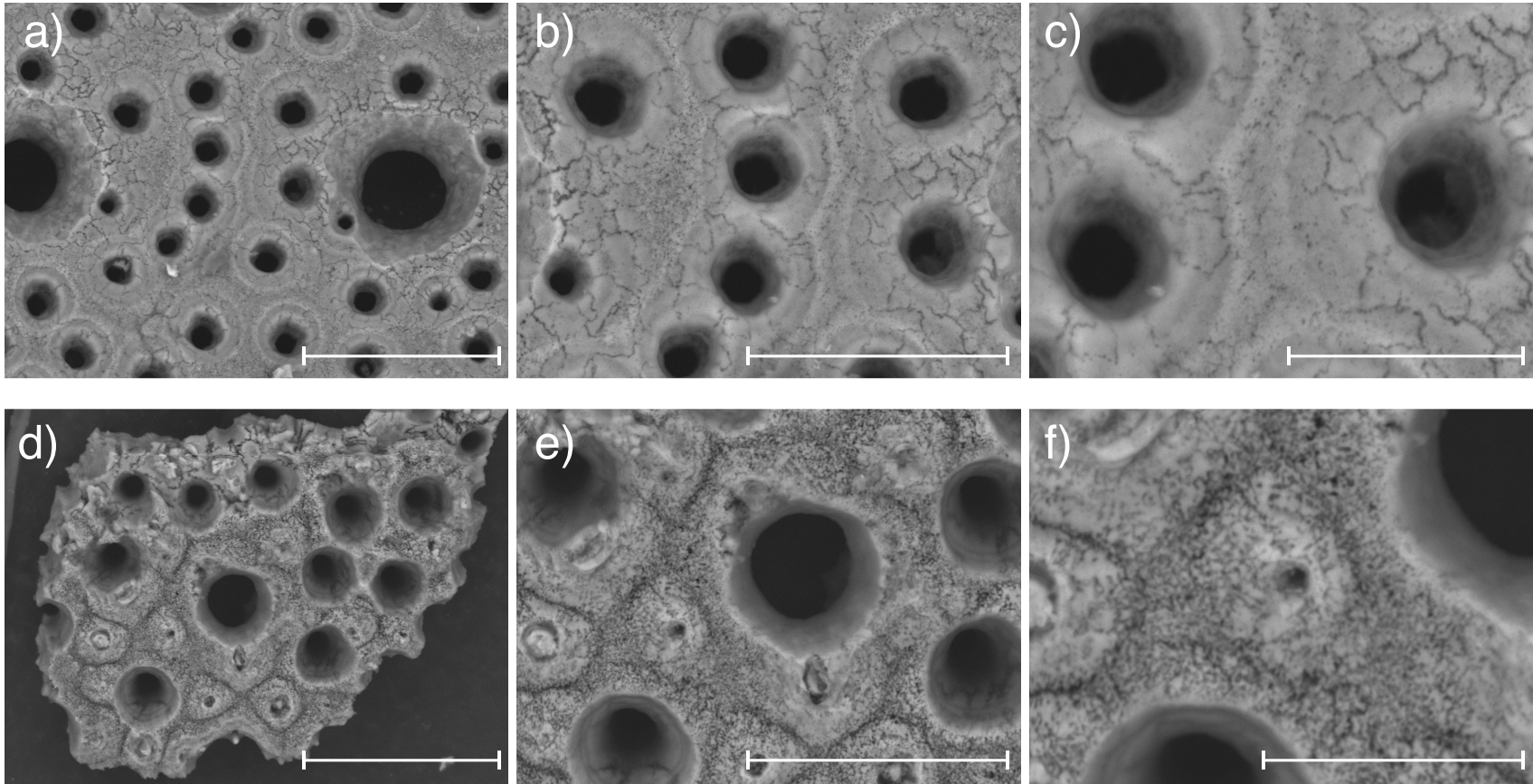
**Figure D.3:** Images of dissolved foraminiferal tests from experiments B54-B4. The saturation state and length of experiment are listed above the plate. Scale bars in microns: **a-f**: 30,20,10,30,20,10.

## D.2 Plates of dissolved soft coral spicules
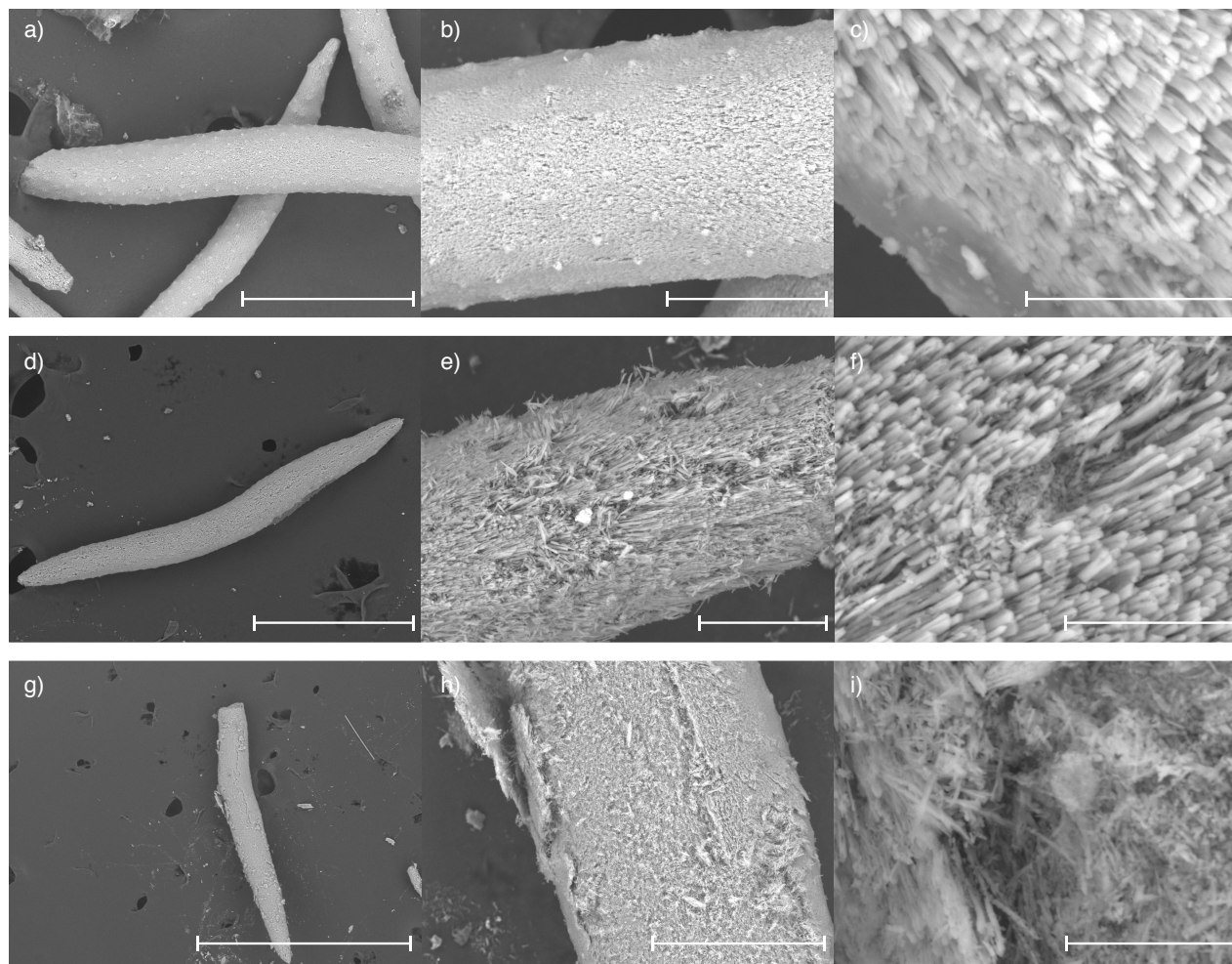


**Figure D.4:** Soft coral spicules under different stages of dissolution. **a-c)** unreacted spicules. **d-f)** soft corals after about 2% dissolution. **g-i)** soft corals after about 3% of dissolution. Scale bars in microns: **a-i)** 200,50,10,300,30,10,1000,100,10.

*A p p e n d i x   E*

# THE 2D - PSD SCRIPT

This script was taken from the Matlab File Exchange (`https://www.mathworks.com/matlabcentral/fileexchange/54297-radially-averaged-surface-roughness-topography-power-spectrum--psd-`). It was written by Mona Mahoob Kanafi and last updated on December 16, 2016.

```matlab
function [q , C, PSD] = psd_2D(z , PixelWidth)
% Calculates radially averaged 2D power spectrum.
% It is better to remove mean and tilt in your
    ↪ topography before applying
% this function
% Here, same pixelwidth in x and y direction is assumed
    ↪  which is typical
% of measurement instruments.

% ===
% inputs:
% z : height topography, a matrix of n*m size (SI units
    ↪ , i.e. meters)

% PixelWidth: size of each Pixel in topography/image (
    ↪ SI units, i.e.
% meters). If you don't know your pixelwidth just
    ↪ devide topography length by
% number of pixels in length.

% ===
% outputs:
% q: wavevectors, which is 2pi/lambda. lambda is
    ↪ wavelength of your
% roughness components.

% C: Radially averaged power spectrum (2D PSD)
```

```matlab
22
23 % PSD: this structure contain any other interesting
   ↪ information you may
24 % need.
25
26 % in order to plot final result just use:
27 % loglog(q,C)
28
29 % 2D FFT of surface topography could be seen by:
30 % imagesc(1+log10(abs(PSD.Hm)))
31
32 % ================
33 % make the size an even number (For PSD)
34 [n,m] = size(z);
35 if mod(n,2)
36     z = z(2:end,:);
37     n = n -1;
38 end
39 if mod(m,2)
40     z = z(:,2:end);
41     m = m -1;
42 end
43
44 Ln = n * PixelWidth; % width of image
45 Lm = m * PixelWidth; % length of image
46
47 a = PixelWidth; % lattice spacing in meter
48
49 % ================
50 % Window function (up to user)
51 % win = tukeywin(n,0.25)*tukeywin(m,0.25)';
52 % win = hann(n)*hann(m)';
53 % win = kaiser(n,10)*kaiser(m,10)';
54 % win = bartlett(n) * bartlett(m)';
55 win = (1 - (((0:n-1)-((n-1)/2))/((n+1)/2)).^2)'*(1 -
   ↪ (((0:m-1)-((m-1)/2))/((m+1)/2)).^2); % Welch
```

```matlab
                 ↪ window
56
57 recInt = trapz (0:n-1,trapz (0:m-1,(( rectwin (n)* rectwin (
     ↪ m) ').^2) ,2) ,1); % integral of squared rectangular
     ↪ window
58 winInt = trapz (0:n-1,trapz (0:m-1,(win.^2) ,2) ,1); %
     ↪ integral of square of selected window function
59 U = ( winInt / recInt ); % Normalization constant
60
61 z_win = z.*win ;
62 % ===============
63 % Calculate 2D PSD
64 Hm = fftshift ( fft2 ( z_win , n ,m) );
65 Cq = (1/U)*(a^2/((n*m)*((2* pi )^2)) .*(( abs ((Hm))) .^2));
66 Cq( n/2+1 ,m/2+1) = 0; % remove the mean
67
68 % ===============
69 % corresponding wavevectors to Cq values after fftshift
     ↪ has been applied
70 qx_1=zeros (m,1) ;
71 for k =0:m-1
72     qx_1 (k+1)=(2* pi /m)*(k) ;
73 end
74 qx_2 = fftshift ( qx_1 );
75 qx_3 = unwrap ( qx_2 -2* pi );
76 qx = qx_3 / a ;
77
78
79 qy_1=zeros (n,1) ;
80 for k =0:n-1
81     qy_1 (k+1)=(2* pi /n)*(k) ;
82 end
83 qy_2 = fftshift ( qy_1 );
84 qy_3 = unwrap ( qy_2 -2* pi );
85 qy = qy_3 / a ;
86
```

```matlab
87
88 % ================
89 % Radial Averaging
90 [qxx,qyy] = meshgrid(qx,qy);
91 [~,rho] = cart2pol(qxx,qyy);
92 rho = floor(rho);
93 J = 100; % resolution in q space (increase if you want)
94 qrmin = log10(sqrt((((2*pi)/Lm)^2+((2*pi)/Ln)^2)));
95 qrmax = log10(sqrt(qx(end).^2 + qy(end).^2)); % Nyquist
96 q = floor(10.^linspace(qrmin,qrmax,J));
97
98 % ================
99 % Averaging Cq values
100 C_AVE = zeros(1,length(q));
101 ind = cell(length(q)-1 , 1);
102 for j = 1:length(q)-1
103     ind{j} = find( rho > q(j) & rho <=(q(j+1)));
104     C_AVE(j) = nanmean(Cq(ind{j}));
105 end
106 ind = ~isnan(C_AVE);
107 C = C_AVE(ind);
108 q = q(ind);
109
110 % ================
111 PSD.Hm = Hm; % 2D FFT
112 PSD.C = C;
113 PSD.q = q;
114 PSD.Cq = Cq;
115 PSD.qx = qx;
116 PSD.qy = qy;
117 PSD.z_win = z_win; % z profile after window function
        applied
```